DEVELOPMENT AND MOLECULAR UNDERSTANDING OF PLASMONIC PHOTOTHERMAL THERAPY (PPTT) IN COMBATING CANCER

A Dissertation
Presented to
The Academic Faculty

By

Moustafa R. K. Ali

In Partial Fulfillment
of the Requirements for the Degree
Doctor of Philosophy in the
School of Chemistry & Biochemistry

Georgia Institute of Technology
May 2017

DEVELOPMENT AND MOLECULAR UNDERSTANDING OF PLASMONIC PHOTOTHERMAL THERAPY (PPTT) IN COMBATING CANCER

Approved by:

Dr. Mostafa A. El-Sayed, Advisor
School of Chemistry & Biochemistry
Georgia Institute of Technology

Dr. John F. McDonald
School of Biology
Georgia Institute of Technology

Dr. Loren Williams
School of Chemistry & Biochemistry
Georgia Institute of Technology

Dr. Zhong Lin Wang
School of Materials Science and Engineering
Georgia Institute of Technology

Dr. Ronghu Wu
School of Chemistry & Biochemistry
Georgia Institute of Technology

Date Approved: [March 13, 2017]

To my mom, dad, sisters, brother, nephews and nieces, without you in my life I will never have the stamina to get a doctoral degree from Georgia Tech.

ACKNOWLEDGEMENTS

First, I would like to acknowledge my advisor, Prof. Mostafa A. El-Sayed, for whom I am grateful to for the opportunities he provided me with and for his guidance, support, and encouragement during my time at Georgia Tech. He always encouraged me to pursue my dream of being a scientist. His great enthusiasm and dedication to science continues to inspire me.

I would also like to thank my thesis committee members, Prof. Loren Williams, Prof. Ronghu Wu, Prof. John F. McDonald, and Prof. Zhong Lin Wang for their guidance and constructive feedback on my thesis. I would especially like to thank Prof. Ronghu Wu and his student, Haopeng Xiao, for their collaboration on mass spectrometry research. I would like to thank Prof. Dong M. Shin and Dr. Mohammad Aminur Rahman at Emory University for their collaboration during the application studies conducted on mice. I greatly appreciate Dr. Tiegang Han and Dr. Yan Tang for their work on bio-informatics analysis. I would like to acknowledge Prof. Todd. Sulchek and his student, Bian H. Do, for their collaboration in Atomic Force Microscopy. I would like to thank Prof. Ning Fang and his postdoc, Dr. Kuangcai Chen, for their work on imaging nanoparticles within cells. I would like to thank Prof. Michelle Dawson and her postdoc, Dr. Deepraj Ghosh, for studying cancer cell migration. I would like to thank Prof. Salah Selim and Dr. Hala R. Ali, my sister, for their great collaboration during the animal studies conducted on dogs and cats.

I thank the people in LDL, especially Yue (Jane) Wu. On the first day Yue arrived to El-Sayed's group, I knew that she would be a great colleague to work with. I am very grateful to have worked with her throughout my entire Ph.D. program. I would also like to

acknowledge Dr. Hongje Jang, Dr. Sajanlal R. Panikkanvalappil, Dr. Xiongwu Kang, Mr. Brian Snyder, Dr. Steven Hayden, Adam Poncheri, Dr. Nageh K. Allam for their support. I would like to thank my good friends at Georgia Tech, Jean Guillaume Durand and Rajiv Jiani. Jean provided useful feedback for my thesis. I am blessed to have had the support of Jean and Rajiv during my time here. I would also like to thank my friends in the chemistry department including Nicholas Kovacs, Kevin Omolo, Sabiha Runa, Melony Ochieng, and Katily Ramirezmendez. Also, I would like to thank my friends, Harold Nikoue and Fang Jung (Zhengyuan). I would like to thank my undergraduate students: Savita Chapman, Kamillah Kassam, Tsion Assaye, Tessneem Belhadj Yahya, Sarah Ghalayini, Cecily Ritch, Arusha Siddiqa, Cassidy Tobin, Samuel Nelson, Sreenath Raparti, Mostafa Nasser, and Ahmed Amer. I would like to acknolwdge my friends from the National Research Center including: Dr. Ibrahim Mohamed, Mr. Karemm Elgoahry, Dr. Ahmed Nabil, and Mr. Ahmed Abdeltwab. Also, I would like to thank my advisors, Prof. Mahmoud Zawrah and Prof. Mohamed Zaid, during my Masters program.

I would like to especially thank Dr. Kenyetta Johnson for her great support during my Ph.D. program.

Finally, I would like to thank my family, including my mom, dad, sisters, brother, nieces, and nephews. Without their great support and love, I would never have accomplished this great feat. I love you all so much.

TABLE OF CONTENTS

LIST OF TABLES

LIST OF FIGURES

LIST OF SYMBOLS AND ABBREVIATIONS

3D	3 Dimensional
ACAT1	Mitochondrial Acetyl-Coa Acetyltransferase
AFM	Atomic Force Microscopey
ANOVA	Analysis of Variance
AuNPs	Gold Nanoparticles
AuNRs	Gold Nanorods
AuNSs	Gold Nanospheres
BSA	Bovine Serum Albumin
CTAB	Cetyltrimethylammo-Nium Bromide
DDA	Data Dependent Acquisition
DF	Dark-Field
DF	Dark-field Microscopy
DIC	Differential Interference Contrast Microscopy
ESI	Electrospray Ionization
FasR	Fas Receptor
FDR	False Discovery Rate
HAADF	High Angle Annular Dark Field
HADHA	Hydroxyl-Coenzyme A Dehy-Drogenase/3-Ketoacyl-Coenzyme A Thiolase/Enoyl-Coenzyme;
HEPES	4-(2-Hydroxyethyl)-1-Piperazineethanesulfonic Acid;
HSC-3	Human Oral Squamous Cell Carcinoma
HSP	Heat Shock Proteins
Huh7.5,	Human Hepatocellular Carcinoma
LAMP2	Lysosome-Associated Membrane Protein 2
LC-MS	Liquid Chromatography-Mass Spectrometry
LDA	Linear Discriminant Analysis

LSPR	Localized Surface Plasmon Resonance
Lys-C	Lysyl Endopeptidase
MCF-7	Human Squamous Carcinoma
mPEG-SH	Meth-Oxypolyethylene Glycol Thiol
NIR	Near-Infrared
NLS	Nuclear Localization Signal
NPs	Nano Particles
PBS	Phosphate Buffered Saline
PEG	Poly-Ethylene Glycol
m-PEG-SH	Methoxy Polyethylene Glycol Thiol
PPP1R12A	Myosin Phosphatase Targeting Subunit 1
PPTT	Plasmonic Photo-Thermal Therapy
RF	Rifamipicin
RGD	Arginylglycylaspartic Acid
SDC	Sodium Deoxycholate
SERS	Surface Enhanced Raman Spectroscopy
STEM	Scanning Transmission Electron Microscopy
TEM	Transmission Electron Microscopy
UPLC	Ultra-Performance Liquid Chromatography

SUMMARY

In cancer plasmonic photothermal therapy (PPTT), gold nanoparticles (AuNPs) are used to convert light energy into localized heat leading to cancer cell death. Among plasmonic nanoparticles, gold nanorods (AuNRs) have been widely used as they absorb near-infrared (NIR) laser light (safe to biological system). Detailed background information was introduced in **Chapter 1**. Herein, 1) we developed new AuNRs formulations techniques, yielding better generation of AuNRs, for enhancing PPTT (**Chapter 2**). 2) We studied PPTT in vitro (**Chapter 3**). We developed novel surface conjugations, greatly enhance the endocytosis of gold nanoparticles and the PPTT efficacy in cells. We explored its molecular mechanism. We also studied the AuNPs' effect on inhibiting cancer cells migration. 3) Moving from cells to animals (**Chapter 4**). We studied the efficacy, molecular mechanism and long-term toxicity of AuNRs in mice. Furthermore, the feasibility of PPTT has been verified on natural tumors in dogs and cats without any relapse or toxicity effects even after 1 year of treatment. In conclusion, together these data on cells, mice, cats and dogs demonstrated that our AuNR-PPTT inducing apoptosis is effective and safe for cancer therapy provides a strong framework for translation this approach to the clinics.

CHAPTER 1. INTRODUCTION

Cancer remains to be one of the leading causes of death worldwide. In the United States cancer is the second cause of death surpassed by heart disease. 1,658,370 new cancer cases and 589,430 cancer deaths are projected to occur in the United States in 2015 [1,2]. Current mainstream treatments include surgery, radiotherapy, chemotherapy, *etc*. Surgery is highly effective to access tumors but it is not successful in many cases. On the other hand, radiotherapy and chemotherapy can also cause damage to healthy tissues close to the cancer cells. Thus, the development of plasmonic photothermal therapy (PPTT) as an effective and safe approach has recently gained increasing attention. PPTT [1] offers a relatively noninvasive and gentle alternative for cancer treatment using targeted gold nanoparticles of specific shapes, that absorb NIR light and produces localized heat for tumor ablation. This photo-absorbers (gold nanoparticles) are then injected locally into the tumor to selectively increase the temperature under laser irradiation. Tumor destruction is thus achieved as sufficient temperature rise over desired period is carried out in the tumor region.

1.1 Plasmonic Photothermal Therapy of Cancer

Photothermal therapy is a minimally-invasive therapeutic strategy in which photon energy is converted into heat sufficient to destroy cancer cells, and has been used to treat cancer to some degree in the past few decades 4.2. It does not have the severe infection problems commonly encountered after surgery [3]. It also overcomes the side effects of

chemotherapy by circumventing the use of toxic drugs. Heating sources including NIR or visible light5, radiofrequency waves [4], microwaves [5], and ultrasound waves [6] are used to induce moderate temperature rise, which is clinically termed as hyperthermia, in a specific target region to destroy the cancer cells. Due to the low absorption efficiency of the natural tissue absorbents, synthetic organic dye molecules (photo sensitizers) such as indocyanine green and porphyrins coordinated with transition metals [7-8] are externally injected into the tumor sites to enhance the photothermal effects when NIR light is used. However, the dye molecules photobleach quickly, rendering insufficient therapeutic outcomes.

Nanotechnology is expected to bring about breakthroughs in medicine by generating new diagnostic and therapeutic technologies. By their reduced size, nanoscale materials (generally 1-100 nm) exhibit new properties that make them very useful in cellular imaging, molecular diagnosis and targeted therapy depending on their structure, composition and shape9. Plasmonic gold nanoparticles (Au NPs) are very useful in biomedical applications because of their strongly enhanced radiative (scattering) and nonradiative (absorption) and photothermal properties due to the surface plasmon resonance (SPR) properties. SPR is the coherent collective oscillation of the free electrons in the plasmonic metals upon their excitation with resonant incident light [9-17]. While the radiative properties can be utilized for cancer imaging [1, 10-11] and molecular diagnosis [12-13], the non-radiative properties have shown to have great potential in photothermal cancer therapy [14-17]. The rationale is that nanoparticles absorb light 105-106 times stronger than most strongly light-absorbing dye molecules [25]. The absorbed light by certain size and shape nanoparticles is converted into heat rapidly (on the picosecond time

scale) and highly efficiently converted (nearly 100%) into non-radiative processes including electron-electron and electron-photon interactions [17-18]. Thus, if Au NPs are bound to cancer cells, and exposed to resonant electromagnetic radiation of an optical laser, intense heat capable of destroying cells are produced. Compared to conventional strategies of using dye molecules, Au NPs enabled PPTT is envisaged to be much more effective. In addition, Au NPs overcomes the photobleaching problems of dye molecules and thus make the photo-thermal method using gold nanorods is more robust in photo-thermal clinical applications.

For in vivo applications, Au NPs have to be active in the NIR region, where optical penetration of electromagnetic radiation through tissue is optimal, and thus cylinder-shaped gold nanorods (Au NRs) [1, 19], silica/gold nanoshells [14] and nanocages [20] are generally preferred because of their tunable NIR absorption properties. Au NRs exhibit two absorption bands a strong band in the NIR region corresponding to electron oscillations along the long axis of the rod, referred to as the longitudinal band, and a weak band in the visible region corresponding to electron oscillations along the short axis of the nanorod, referred to as the transverse band (see Figure 1.1C and 1.1D below).[14] The longitudinal absorption band wavelength can be precisely tuned to any desired wavelength in the NIR region by changing the aspect ratio of the nanorod used.

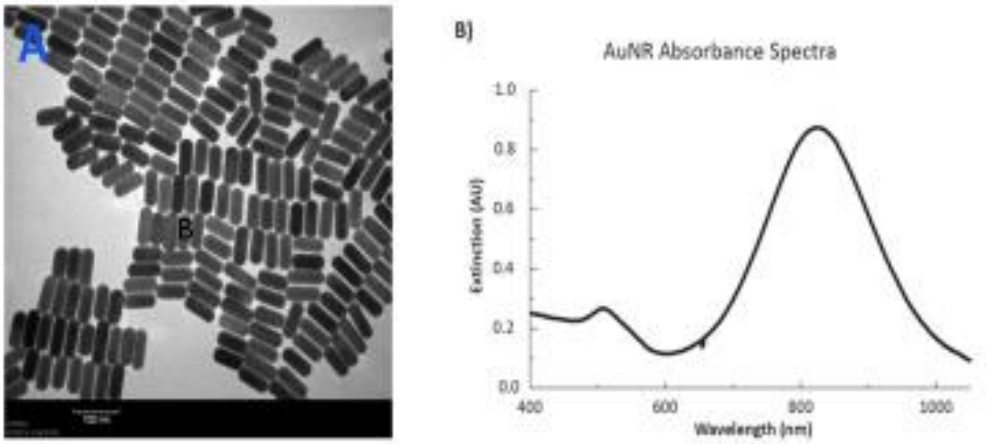

Figure 1-1: Characterization of Gold nanorods:

(A) TEM images with dimensions of 50×12 nm. (B) are UV-Vis spectrum for AuNRs [21]

1.2 The Previous Work of Gold Nanorods (AuNRs)-Assisted Plasmonic Photothermal Therapy (PPTT)

In 2006, our group (El-Sayed's group) demonstrated for the first time highly effective and selective photothermal cancer therapy using Au NRs through in vitro studies [3]. Results showed that Au NRs functionalized with the epidermal growth factor receptor (EGFR) antibodies specifically target EGFR-positive human oral cancer cells, as detected by dark field light scattering imaging (**Fig. 2A and B**). After exposure to a beam of focused NIR light (Ti: Sapphire laser, 800 nm, 10 W/cm^2, 4 mins), the two types of cancer cells were destroyed (dead cells are shown in blue color) without affecting the normal cells (**Figure 1-2C**). Cells displayed no loss of viability in the absence of Au NRs at laser intensities as high as 100 W/cm^2. The success of Au NR-assisted PPTT has later been

reported on other cell lines. Compared to gold nanoshells [14], the energy threshold for effective treatments using Au NRs is lowered by three times.

It has been shown that the tumor uptake of EGFR-targeted Au NPs is 10-fold greater than that of non-targeted particles after systemic delivery [20]. In addition, the targeted particles are internalized into the EGFR-positive tumor cells while the non-targeted particles remain in the tumor interstice. These facts strongly suggest that targeted AuNR would offer greater success in PPTT of cancer compared to non-targeted ones.

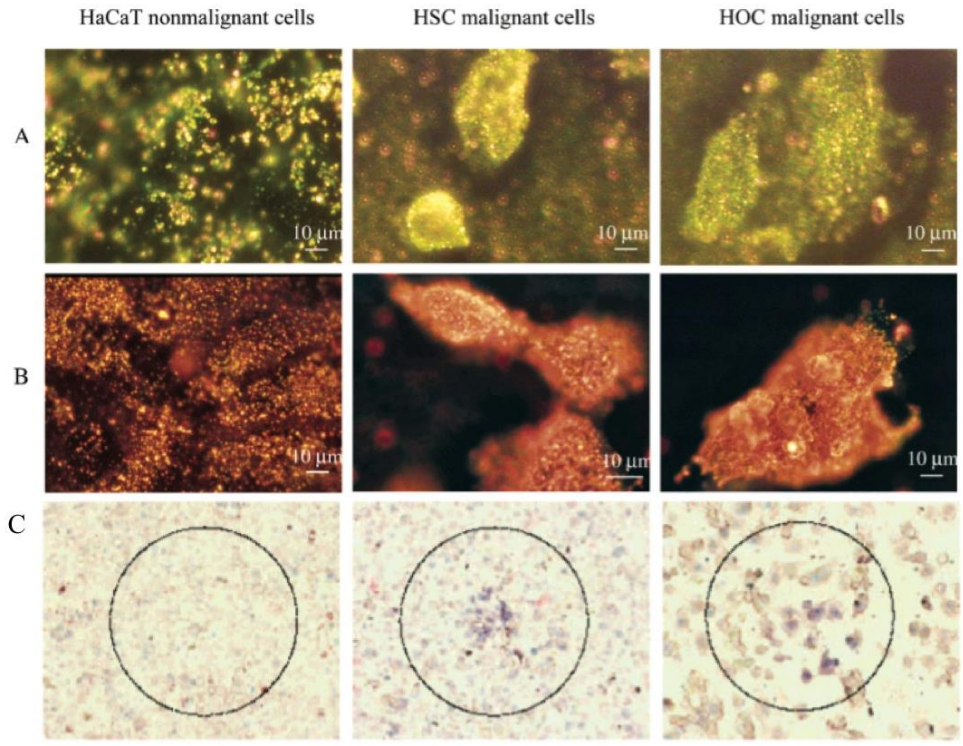

Figure 1-2: Gold nanoparticles differentiate between the cancer and healthy cells

(A) Dark field light scattering images of anti EGFR/Au nanospheres after incubation with normal and two types of head and neck cancer cells for 30 min at room temperature. (B) Light scattering images of anti-EGFR/Au nanorods after incubation with cells for 30 min at room temperature. (C) Selective photothermal therapy of cancer cells with anti-EGFR/Au nanorods incubated. The circles show the laser spots

on the samples. At 10 W/cm2, the HSC and HOC malignant cells are obviously injured while the HaCat normal cells are not affected [3].

In 2008, our group showed the feasibility of the treatment of cancer tumor in mice using a cancer xenograft mouse model [51]. Therapeutic efficiencies were examined for both intratumoral and intravenous (i.v.) injections. Following i.v. injection, Au NRs accumulate in tumors from the bloodstream by the enhanced permeability and retention (EPR) effect, which results from the leaky, defective architecture and impaired lymphatic drainage of the tumor tissue. The existence of the nanorods in the tumor was confirmed by NIR imaging. Tumor growth was significantly inhibited (

Figure 1-3) after exposure to low dose of NIR light (diode laser, 808 nm, 1-2 W/cm^2, 10-15 mins), with higher efficiency by direct injection because of the higher concentration of Au NRs that can be deposited in the tumor volume. Thermal transient measurements showed that the temperature increased by over 20 ^{o}C, and was thereby capable of inducing efficient tumor destruction. Recently, Bhatia and co-workers conducted similar studies on a melanoma cancer (MDA-MB-435) xenograft [51]. The results show that single i.v. injection of PEGylated AuNRs enables complete eradication of all irradiated tumors in mice without regrowth over 50 days of study time.

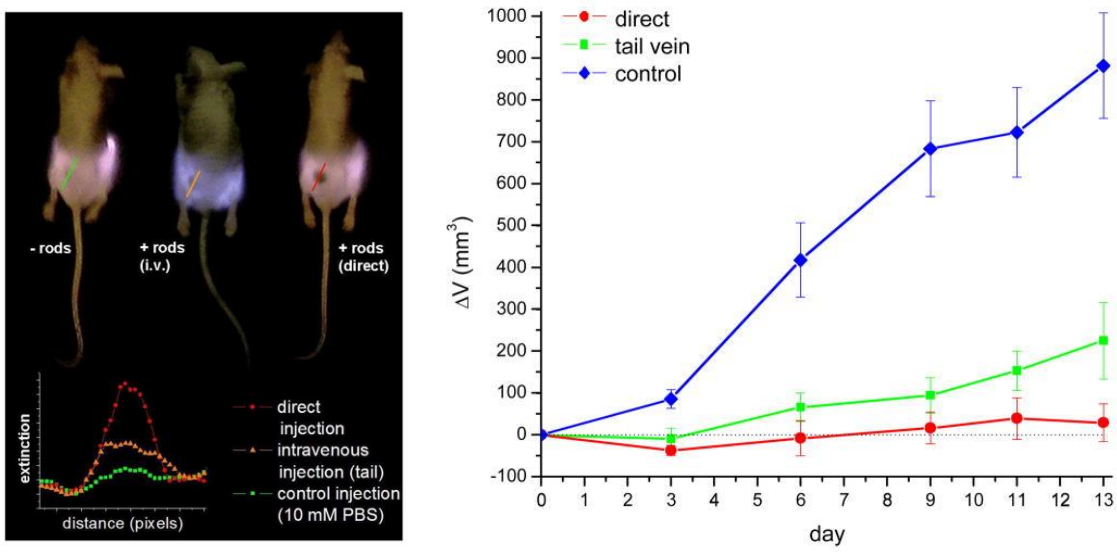

(A) **(B)**

Figure 1-3: Efficacy of PPTT on mice

(A) NIR transmission images of mice prior to PPTT treatments. Inset shows intensity line-scans of NIR extinction at tumor sites for control, intravenous, and direct administration of pegylated gold nanorods. Control mice were interstitially injected with 15 lL 10 mM PBS alone, while directly administered mice received interstitial injections of 15 lL pegy- lated gold nanorods (ODk=800 = 40, 2 min accumulation), and intravenously administered mice received 100 lL pegylated gold nanorod (ODk=800 = 120, 24 h accumulation) injections.22 (B) Average change in tumor volume for HSC-3 xenografts following near-infrared PPTT treatment by control, intravenous and direct injection of PEGylated gold nanorods.

1.3 Motivation for The Thesis/Challenges of Current PPTT

Since the PPTT could be a good alternative for treating cancer, it is very promising to improve the PPTT, to recognize the challenges and overcome them.

1.3.1 Designing new AuNRs synthesis methods for producing a new AuNRs size with homogenous yield, then optimize the best dimensions of the AuNRs that can increase the PPTT efficacy

Of all the plasmonic AuNPs developed, gold AuNRs exhibit the most ideal NIR absorption cross section [23] the need demonstrates extremely efficient AuNRs to be the best for NIR photothermal heat conversion [19]. The size and shape are the primary factors that determine their catalytic, optical and surface activity, and photo-thermal properties of the gold nanoparticles [14]. This is especially important when the nanoparticles are rod shaped with different aspect ratios (length/width) [24]. When comparing the different AuNRs structures in terms of their application in PPTT, the most important plasmonic properties to consider are the absorption cross section, absorption efficiency, and thermal transduction per particle.

The most common size of AuNR utilized for use in successful PPTT now is over 40 nm in length and 10 nm in diameter, with a longitudinal plasmon resonance around 800 nm, synthesized by seed-mediated method. Since the accumulation and toxicity of smaller AuNRs （diameter lower than 10nm） in the tumor interstitial and the organs of the reticuloendothelial system (RES) could be more ideal than that of the larger AuNRs. Also,

as previously shown theoretically by Jain et.al., plasmonic absorption becomes dominant as the nanoparticle size is decreased [25]. In the in-vivo studies in animal models, complete clearance of these nanoparticles was not accomplished and was retained especially in the liver and spleen [26]. That gives more evidence that the smaller AuNRs might enhance nanoparticle clearance. Therefore, the smaller size AuNRs could be more favorable to use in PPTT.

More specifically, the extinction of the AuNRs increases with the size of the AuNRs, while the contribution of scattering also increases, essentially decreasing the absorbance: scattering ratio as the AuNR size increases. This ultimately suggests that as the particle size decreases, the absorbance: scattering ratio increases, allowing for greater photothermal heat conversion and therefore potentially enhancing PPTT efficacy with decreased particle size. Another plasmonic property associated with photothermal heat conversion is the electric field around the AuNRs. It has previously been shown that excitation at the plasmon wavelength creates very strong electromagnetic fields, [27] and the field strength trends with absorbance, not scattering or extinction [28]. Since the field strength is derived from absorbance, not scattering, greater absorbance with smaller AuNRs would indicate a stronger field, which in turn would result in greater photothermal heat conversion and, again, enhanced PPTT efficacy.

In the synthesis of AuNRs, control over these properties has been one of the most important and challenging tasks. Different methods are utilized to synthesize different shapes of gold nanoparticles. In general, for the synthesis of gold nanorods using surfactants, three approaches are used: electrochemical, ultraviolet irradiation photoreduction,[29] and the seed mediated growth methods [30]. In the latter method,

cetyltrimethylammonium bromide (CTAB) has proven to be an effective surfactant in gold nanoparticle preparation [43]. Gold nanorods have been produced with a width greater than 10 nm, and lengths of about 50 nm depending on the silver ion content [41]. A seedless growth technique was previously published which described the purpose in using their synthetic scheme to produce gold nanorods in a gram scale. Jana's method produced gold nanorods that ranged in size from 4-50 nm [31]. The limitation of Jana's method was the low monodispersity of gold nanorods and formation of a large concentration of spherical nanoparticles. This makes the use of the resulting small gold nanorods useless for biological work.

Ali *et al* [21] have developed a new a synthetic seedless technique, previous limitations have been overcome by adjusting the pH of the growth solution while utilizing $NaBH_4$ as the reducing agent to produce small monodisperse widths lower than 10 nm [21].

The need to study a theoretical, and experimental comparison between different sizes of AuNRs to find which size could be the most effective size to be used for the PPTT applications. In Chapter 3.1 we studied deeply which is the most effective size the AuNRs that could effectively increase the heat generation, which is more favorable in PPTT [32]. Furthermore, in chapter 3.2, 3.3 we synthesized a new dimension of the AuNRs also a new shape we called gold nanobones (AuNBs), which have edges by the end, showed a novel plasmonic properties for PPTT or surface enhanced raman spectroscopy (SERS) applications.

1.3.2 Improving the PPTT mainly depends on enhancing the AuNRs selectivity to the cancer cells compared to the healthy ones. Thus, increasing the efficacy of PPTT by increase cellular uptake of AuNRs

Effective internalization of AuNRs in tumor tissue is another significant challenge [33-36]. In PPTT, two selective targeting methods can be applied: 1) active targeting and 2) passive targeting. In active targeting, specific surface modifications (ligands) of NPs can recognize and bind to the receptors on the surface of cancer cells. On the other hand, in passive targeting, NPs are usually injected directly to solid tumor and accumulate inside the tumor mainly via the enhanced permeability and retention effect. The enhanced permeability and retention effect has been regarded as a primary rationale for the delivery of NPs due to the leaky tumor blood vasculature. To increase the uptake of AuNRs, surface modification with ligands that assist endocytosis or block exocytosis has been used. Chapter 4, we aim at new surface modifications on AuNRs for greater nanoparticle retention inside cancer cells .

1.3.3 To optimize the PPTT conditions, all the drawbacks of the PPTT need to be understood, moleculare mechanisms of the PPTT are needed

Despite the operational success of PPTT, the molecular mechanisms associated with PPTT-induced apoptosis remain largely unknown or under dispute. We observed PPTT induce apoptosis initiate through heat shock proteins while several reports indicate it is mediated by the mitochondrial apoptotic pathway via Bid activation and caspase 3 activity. [18-19]. Although the surface enhanced Raman spectroscopy (SERS) reports on the real-

time, biomolecular dynamics in the microenvironment associated with the PPTT process, SERS spectra from cells are incredibly complex, reflecting overlapping signals from a variety of proteins and metabolites that are difficult to assign to individual species. It has been reported, for example, that the 1000 and 1580 cm^{-1} peaks showed significant increase during cell apoptosis [8, 20] with great debate in their assignment [21]. Per published literature, the 1000 cm^{-1} signal has been assigned to phenylalanine,[22] while a different report assigned it to tryptophan [21]. Furthermore, it has been argued[8] that these SERS signals reflect changes in protein structure, a topic still being intensively debated. One hypothesis states that the 1000 cm^{-1} signal is indicative of the exposure of protein hydrophobic rings following conformational changes, [8] while others report that the protein conformation change induced by adding methanol or SDS [23] or increasing temperature [9] does not alter the intensity of the 1000 cm^{-1} peak, therefore contradicting the hypothesis that this signal is associated with alterations in protein conformation.

Herein, we monitored the SERS spectral signature *in vitro* during apoptosis as a function of PPTT exposure time. We also performed metabolomics and proteomic studies on cell lysates under the same exact PPTT conditions. Integrative multi-omics network analysis revealed specific alterations that explain the underlying changes in SERS spectral data, demonstrating the power of combining SERS with MS for studying cellular processes following PPTT.

To better understand the cellular responses to PPTT, more systematic studies *in vivo* are required. Most previous reports concerning the mechanism of PPTT were only conducted *in vitro* [60] and focus on a single protein or pathway. Several mechanisms have been proposed *in vitro*. Pérez-Hernández et al reported that apoptosis during PTT using gold

nanoprisms is mediated by proteins Bak and Bax, through the activation of protein Bid [60]. To better understand the mechanisms involved, in Chapter 4.3 systematic analysis such as mass spectrometry (MS)-based proteomics is necessary SERS has explored the dynamic events that report in the cells [61].

1.3.4 The nano-bio interaction is still not clearly addressed. As an example, how the AuNPs could impact the mechanical properties of the cancer cell, can the AuNPs inhibit cancer cell migration?

Metastasis, a process in which cancer cells migrate to other locations of the human body, is responsible for most cancer-related mortality. It usually begins with local invasion to the surrounding tissues, followed by intravasation into the lymph and blood microvasculature before the cancer cells finally colonize within the microenvironment of other locations in the patient's body [39, 62]. Many treatments for inhibiting metastasis are based on drugs that target specific proteins that promote the cell migration process; however, past attempts to develop anti-metastasis drugs have not been efficacious in clinical trials [63]. Moreover, in many cases, the anti-cancer drugs that target specific proteins might lose their efficacy after several months of treatment due to protein mutations, thus conferring drug resistance to cancer cells,[64] and could also cause side effects on healthy tissues [65].

Recent advances in nanomedicine provide us with a great opportunity to avoid the drawbacks of current drugs [14, 64, 66, 67, 42, 68]. Nanoparticles have been widely used in cancer diagnosis and cancer therapy thanks to their intrinsic chemical, physical and optical properties [42, 69-71]. Nanoparticles with proper surface modifications can target tumors selectively, [14, 72-75]. and their effects on cancer cell migration or metastasis

have drawn attention from many researchers [76, 77-78, 79]. In 2013, Murphy *et al.* reported that gold nanoparticles (AuNPs) with different surface charges and sizes can affect cancer cell migration [76]. In 2014, Chor Yong Tay *et al* [78]. found that after incubation with nano-ceramics, such as titania, silica and hydroxyapatite, cells showed significantly impaired wound healing capability by disruption of the intracellular microtubule assembly. In the same year, Zhou *et al* [79]. showed that gold nanorods (AuNRs) coated with bovine serum albumin (BSA) exhibited reduced cell migration and invasion by impairing ATP synthesis, which subsequently inhibits the F-actin cytoskeletal assembly and decreases cancer cell migration [79]. Arvizo *et al.* used non-specific targeted gold nanospheres (AuNSs) to inhibit cancer cell migration by abrogating MAPK signaling and reversing the epithelial-mesenchymal transition [16] For most of the related works, non-specific targeted nanoparticles have been used, for instance, Zhou *et al* [79] used BSA coated AuNRs that showed inhibitory effects on cancer cell migration, but the high concentration of AuNRs (50-200 μM) that they used might be an obstacle for clinical usage. To maintain the nanoparticle effect on slowing the cancer cell migration with a minimized amount of nanoparticles, the intracellular locations of nanoparticles could be an important factor to consider. It is thus promising to design nanoparticles that can target specific intracellular regions to enhance the inhibition of cancer cell migration.

Mechanical stiffness of cancer cells has been shown to grade metastatic potential in patient tumor cells,[80] as well as in cultured cancer cell lines [81-82] Lower stiffness is related to more invasive cells [83] In eukaryotic cells, the nucleus contains most of the cell's genetic material and controls cell activities by transcriptional regulation. It is the

largest and stiffest organelle in most cells and largely determines the cell migration ability [84-86] Lamin A/C (LMNA) proteins are an important factor in nuclear stiffness. They form a dense protein network that connects the nuclear membrane and chromatin structures on the interior of the nuclear membrane. Recent studies have shown that nuclear lamin A protein scales with tissue stiffness [87] and generate a barrier to cells migrate through three-dimensional (3D) environments.88 It is shown that lamin A/C deficiency hampers cell mechanics, polarization, and migration [89-90].

In chapter 4.4 and 4.5, targeted AuNPs were used to locate the AuNPs to the cells, because of their specific physical and chemical properties and better biocompatibility than other nanomaterials such as nano-ceramics or silver nanoparticles. By targeting and locating the AuNPs to the cell in a manner to modulate the stiffness of its nucleus, we could improve the inhibition effect on cell migration. In our experiment, we used three ligands, methoxy-polyethylene glycol thiol (PEG) for

1.3.5 Toxicity of gold nanoparticles to the biosystem is a major concern, there is still a lack of systematic long term studies. This will decide whether the AuNRs can go for clinical trials or not

The safety profile of AuNRs remains largely undefined [91]. Gold is a chemically inert material. Therefore, it is generally considered biocompatible and has been used in some routine clinical practices for many years, e.g. in treating rheumatoid arthritis. Several studies have reported no significant short term toxicity of AuNPs (1 day to 3 months) [92-94] . You *et al* [95] have reported a lack of both acute and chronic toxicity over 3 months

following multiple injections of PEGylated hollow gold nanospheres in mice. However, other studies have contradictorily reported that the presence of nanoparticles causes cytotoxicity such as actin stress [96], induces apoptosis, or causes inflammation in mouse livers [97]. Some studies have explored how gold nanoparticle exposure (aside from any heat-induced effects) impacts cells at the molecular level, affects pathways such as mitochondrial oxidative phosphorylation, and causes oxidative stress [98]. The dose-dependent effects of gold nanoparticles on biological systems have been widely recognized99. A high dose of NPs or the desorbed surfactants from their surface could result in "toxic" behavior [100] Of concern for AuNRs is the incomplete purification of surfactant CTAB, which may cause cytotoxicity [101]. Therefore, the optimal dose and purification of AuNRs is of great importance in minimizing toxic effects. The preservation of spherical AuNPs without complete clearance over six months has been reported [102]. You *et al*. [95] also reported slow clearance of gold nanoparticles from the body during the 3-month period. Such body deposition of metallic NPs over a long-time period raises significant concerns regarding their long-term safety. Therefore, a comprehensive investigation of the organ uptake, biodistribution, longer-term fate and toxicity of AuNRs is essential to fundamentally understand their *in vivo* biological interactions and to use this knowledge to minimize their toxicity [93]. In chapter 5.1 we reported a long term for (15 months) toxicity on xenograft mice. Our data shown that the AuNRs remains in the liver and spleen but with no any toxicity.

1.3.6 Most of PPTT studies have been performed in vitro or in induced tumors, which do not exactly represent their human equivalents. There is a need to apply PPTT in natural tumors in animals, this might give us better application of PPTT to humans:

One of the novelty points of this study was the extension of AuNRs-assisted PPTT to natural tumors in animals larger than ones used in any previous study. Mammary gland tumors of epithelial origin are very common neoplasms of canines and felines. The similarity of molecular and biological machinery of canines/felines and that of humans suggests the suitability of using mammary tumors of these animals as a model for the study of human mammary tumors. (23-25) In chapter 5.3 We tested PPTT on canine and feline natural mammary gland tumors. To minimize side effects, we optimized PPTT dosages to enable a slow cancer cell apoptosis. Using our optimized protocol, adjusting the photothermic temperature to 44°C, we were able to ablate 100% of tumors in seven animals without any relapse or toxicity effect after 1 year from the tumor treatment.(103)

1.3.1 Furthermore, modulating PPTT conditions to generate cancer cell apoptosis (a favorable death pathway)

PPTT can induce cell death mainly via two pathways: necrosis and apoptosis [37]. During necrosis, the heat induced by PPTT (if above 50 ^{o}C) could disrupt the plasma membrane, causing the cellular components to leak out and cause inflammation, metastasis [38], and harm to surrounding normal tissues. Apoptosis is a programmed cell death

pathway that triggers cancer cell death [39-40], attenuates inflammatory activities, and is regarded as a “cleaner” process of cell elimination.

Skewing the response toward apoptotic cell death rather than necrotic death will minimize inflammatory responses that may promote the damage or destruction of healthy tissues. Therefore, modulating PPTT to trigger apoptosis would be more favorable in clinical settings [41-42].

It has been reported that different intracellular locations of AuNRs or laser strength regulate the switch between necrosis and apoptosis in PPTT [43-44]. However, lower heating would decrease the efficacy of PPTT, and might not be very effective for cells that exhibit thermo-resistance. Therefore, it is important to know the major players that contribute to thermo-resistance. Based on this, we can develop new PPTT strategies that prevent the thermo-resistance and enhance apoptosis. Heat induced apoptosis can also be resisted by a class of proteins called Heat Shock Proteins (HSPs) [45-48]. When binding to denatured proteins or partially unfolded intermediates, HSPs prevent their aggregation and initiate protein refolding [49-50]. Interestingly, PPTT induces the expression of most HSPs [51-53], and multiple studies have shown the importance of the HSP in enabling cancer cells to resist heat-induced apoptosis [54-59]. In chapter 4.2 We fabricated novel HSP70 inhibitor (Quercetin) conjugated AuNRs and compared to non-conjugated AuNRs, the new conjugate displayed a superior ability to combat thermo-resistance, causing a higher percentage of cells to undergo apoptosis. Therefore, AuNRs act as integrally in delivering of Quercetin to cancer cells as well as acting as an inducer of apoptosis-associated PPTT.

1.3.2 References

1. Huang XH, El-Sayed IH, Qian W, & El-Sayed MA (2006) Cancer cell imaging and photothermal therapy in the near-infrared region by using gold nanorods. *Journal of the American Chemical Society* 128(6):2115-2120.

2. Brunetaud JM, Mordon S, Maunoury V, & Beacco C (1995) Non-PDT Uses of lasers in oncology. *Laser Med Sci* 10(1):3-8.

3. Torpy JM, Burke AE, & Glass RM (2010) Postoperative infections. *JAMA* 303(24):2544-2544.

4. Gazelle GS, Goldberg SN, Solbiati L, & Livraghi T (2000) Tumor ablation with radio-frequency energy. *Radiology* 217(3):633-646.

5. M. H. Falk RDI (2001) Hyperthermia in oncology. *International Journal of Hyperthermia* 17(1):1-18.

6. Kremkau FW (1979) Cancer therapy with ultrasound: A historical review. *Journal of Clinical Ultrasound* 7(4):287-300.

7. Chen WR, Adams RL, Bartels KE, & Nordquist RE (1995) Chromophore-enhanced in vivo tumor cell destruction using an 808-nm diode laser. *Cancer Letters* 94(2):125-131.

8. Jori G & Spikes JD (1990) Photothermal sensitizers: Possible use in tumor therapy. *Journal of Photochemistry and Photobiology B: Biology* 6(1–2):93-101.

9. Nie SM, Xing Y, Kim GJ, & Simons JW (2007) Nanotechnology applications in cancer. *Annual Review of Biomedical Engineering,* Annual Review of Biomedical Engineering, (Annual Reviews, Palo Alto), Vol 9, pp 257-288.

10. Sokolov K, *et al.* (2003) Real-time vital optical imaging of precancer using anti-epidermal growth factor receptor antibodies conjugated to gold nanoparticles. *Cancer Research* 63(9):1999-2004.

11. El-Sayed IH, Huang XH, & El-Sayed MA (2005) Surface plasmon resonance scattering and absorption of anti-EGFR antibody conjugated gold nanoparticles in cancer diagnostics: Applications in oral cancer. *Nano Letters* 5(5):829-834.

12. Huang XH, El-Sayed IH, Qian W, & El-Sayed MA (2007) Cancer cells assemble and align gold nanorods conjugated to antibodies to produce highly enhanced, sharp, and polarized surface Raman spectra: A potential cancer diagnostic marker. *Nano Letters* 7(6):1591-1597.

13. Qian XM, *et al.* (2008) In vivo tumor targeting and spectroscopic detection with surface-enhanced Raman nanoparticle tags. *Nature Biotechnology* 26(1):83-90.

14. Hirsch LR, *et al.* (2003) Nanoshell-mediated near-infrared thermal therapy of tumors under magnetic resonance guidance. *Proceedings of the National Academy of Sciences* 100(23):13549-13554.

15. Huang X, Jain PK, El-Sayed IH, & El-Sayed MA (2007) Gold nanoparticles: interesting optical properties and recent applications in cancer diagnostics and therapy. *Nanomedicine* 2(5):681-693.

16. Zharov VP, Galitovskaya EN, Johnson C, & Kelly T (2005) Synergistic enhancement of selective nanophotothermolysis with gold nanoclusters: potential for cancer therapy. *Lasers Surg Med* 37(3):219-226.

17. El-Sayed IH, Huang X, & El-Sayed MA (2006) Selective laser photo-thermal therapy of epithelial carcinoma using anti-EGFR antibody conjugated gold nanoparticles. *Cancer Letters* 239(1):129-135.

18. Huang X, Qian W, El-Sayed IH, & El-Sayed MA (2007) The potential use of the enhanced nonlinear properties of gold nanospheres in photothermal cancer therapy. *Lasers Surg Med* 39(9):747-753.

19. von Maltzahn G, *et al.* (2009) Computationally Guided Photothermal Tumor Therapy Using Long-Circulating Gold Nanorod Antennas. *Cancer Research* 69(9):3892-3900.

20. Au L, Cobley CM, Chen JY, & Xia YN (2011) *Gold Nanocages: A Multifunctional Platform for Molecular Optical Imaging and Photothermal Treatment* (Blackwell Science Publ, Oxford) pp 615-638.

21. Ali MRK, Snyder B, & El-Sayed MA (2012) Synthesis and Optical Properties of Small Au Nanorods Using a Seedless Growth Technique. *Langmuir* 28(25):9807-9815.

22. Hu M, *et al.* (2006) Gold nanostructures: engineering their plasmonic properties for biomedical applications. *Chemical Society Reviews* 35(11):1084-1094.

23. Sau TK & Murphy CJ (2004) Room temperature, high-yield synthesis of multiple shapes of gold nanoparticles in aqueous solution. *Journal of the American Chemical Society* 126(28):8648-8649.

24. Jain PK, Lee KS, El-Sayed IH, & El-Sayed MA (2006) Calculated absorption and scattering properties of gold nanoparticles of different size, shape, and composition: Applications in biological imaging and biomedicine. *Journal of Physical Chemistry B* 110(14):7238-7248.

25. Tong L, He W, Zhang YS, Zheng W, & Cheng JX (2009) Visualizing Systemic Clearance and Cellular Level Biodistribution of Gold Nanorods by Intrinsic Two-Photon Luminescence. *Langmuir* 25(21):12454-12459.

26. Kelly KL, Coronado E, Zhao LL, & Schatz GC (2003) The optical properties of metal nanoparticles: The influence of size, shape, and dielectric environment. *Journal of Physical Chemistry B* 107(3):668-677.

27. Near R, Hayden S, & El-Sayed M (2012) Extinction vs Absorption: Which Is the Indicator of Plasmonic Field Strength for Silver Nanocubes? *Journal of Physical Chemistry C* 116(43):23019-23026.

28. Kameo A, Suzuki A, Torigoe K, & Esumi K (2001) Fiber-like gold particles prepared in cationic micelles by UV irradiation: Effect of alkyl chain length of cationic surfactant on particle size. *Journal of Colloid and Interface Science* 241(1):289-292.

29. Nikoobakht B & El-Sayed MA (2003) Surface-enhanced Raman scattering studies on aggregated gold nanorods. *J. Phys. Chem. A* 107(18):3372-3378.

30. Jana NR, Gearheart L, & Murphy CJ (2001) Wet chemical synthesis of high aspect ratio cylindrical gold nanorods. *Journal of Physical Chemistry B* 105(19):4065-4067.

31. Mackey MA, Ali MR, Austin LA, Near RD, & El-Sayed MA (2014) The most effective gold nanorod size for plasmonic photothermal therapy: theory and in vitro experiments. *The Journal of Physical Chemistry B* 118(5):1319-1326.

32. Oh N & Park JH (2014) Endocytosis and exocytosis of nanoparticles in mammalian cells. *International Journal of Nanomedicine* 9:51-63.

33. Iyer AK, Khaled G, Fang J, & Maeda H (2006) Exploiting the enhanced permeability and retention effect for tumor targeting. *Drug Discovery Today* 11(17–18):812-818.

34. Maeda H, Wu J, Sawa T, Matsumura Y, & Hori K (2000) Tumor vascular permeability and the EPR effect in macromolecular therapeutics: a review. *Journal of controlled release : official journal of the Controlled Release Society* 65(1-2):271-284.

35. Liu X, *et al.* (2013) Enhanced retention and cellular uptake of nanoparticles in tumors by controlling their aggregation behavior. *ACS nano* 7(7):6244-6257.

36. Pattani VP, Shah J, Atalis A, Sharma A, & Tunnell JW (2015) Role of apoptosis and necrosis in cell death induced by nanoparticle-mediated photothermal therapy. *Journal of Nanoparticle Research* 17(1):1-11.

37. Bonfil RD, Bustuoabad OD, Ruggiero RA, Meiss RP, & Pasqualini CD (1988) TUMOR NECROSIS CAN FACILITATE THE APPEARANCE OF METASTASES. *Clinical & Experimental Metastasis* 6(2):121-129.

38. Hanahan D & Weinberg RA (2011) Hallmarks of Cancer: The Next Generation. *Cell* 144(5):646-674.

39. Danial NN & Korsmeyer SJ (2004) Cell death: critical control points. *Cell* 116(2):205-219.

40. Ali MR, Ali HR, Rankin CR, & El-Sayed MA (2016) Targeting heat shock protein 70 using gold nanorods enhances cancer cell apoptosis in low dose plasmonic photothermal therapy. *Biomaterials* 102:1-8.

41. Ali MR, Ibrahim IM, Ali HR, Selim SA, & El-Sayed MA (2016) Treatment of natural mammary gland tumors in canines and felines using gold nanorods-assisted plasmonic photothermal therapy to induce tumor apoptosis. *International Journal of Nanomedicine* 11:4849.

42. Huang XH, *et al.* (2010) Comparative study of photothermolysis of cancer cells with nuclear-targeted or cytoplasm-targeted gold nanospheres: continuous wave or pulsed lasers. *J. Biomed. Opt.* 15(5):7.

43. Li JL & Gu M (2010) Surface plasmonic gold nanorods for enhanced two-photon microscopic imaging and apoptosis induction of cancer cells. *Biomaterials* 31(36):9492-9498.

44. Hendrick JP & Hartl FU (1995) The role of molecular chaperones in protein folding. *Faseb J.* 9(15):1559-1569.

45. Bakthisaran R, Tangirala R, & Rao CM (2015) Small heat shock proteins: Role in cellular functions and pathology. *BBA-Proteins Proteomics* 1854(4):291-319.

46. Bharti S, Rani N, Bhatia J, & Arya DS (2015) 5-HT2B receptor blockade attenuates beta-adrenergic receptor-stimulated myocardial remodeling in rats via inhibiting apoptosis: role of MAPKs and HSPs. *Apoptosis* 20(4):455-465.

47. Ciocca DR & Calderwood SK (2005) Heat shock proteins in cancer: diagnostic, prognostic, predictive, and treatment implications. *Cell Stress & Chaperones* 10(2):86-103.

48. Kregel KC (2002) Heat shock proteins: modifying factors in physiological stress responses and acquired thermotolerance. *Journal of Applied Physiology* 92(5):2177-2186.

49. Bukau B & Horwich AL (1998) The Hsp70 and Hsp60 chaperone machines. *Cell* 92(3):351-366.

50. Miyako E, *et al.* (2012) Photothermic regulation of gene expression triggered by laser-induced carbon nanohorns. *Proceedings of the National Academy of Sciences of the United States of America* 109(19):7523-7528.

51. Burke A, *et al.* (2009) Long-term survival following a single treatment of kidney tumors with multiwalled carbon nanotubes and near-infrared radiation. *Proceedings of the National Academy of Sciences of the United States of America* 106(31):12897-12902.

52. Fisher JW, *et al.* (2010) Photothermal Response of Human and Murine Cancer Cells to Multiwalled Carbon Nanotubes after Laser Irradiation. *Cancer Research* 70(23):9855-9864.

53. Rylander MN, Stafford RJ, Hazle J, Whitney J, & Diller KR (2011) Heat shock protein expression and temperature distribution in prostate tumours treated with laser irradiation and nanoshells. *International Journal of Hyperthermia* 27(8):791-801.

54. Larson N, Gormley A, Frazier N, & Ghandehari H (2013) Synergistic enhancement of cancer therapy using a combination of heat shock protein targeted HPMA copolymer-drug conjugates and gold nanorod induced hyperthermia. *Journal of Controlled Release* 170(1):41-50.

55. Wong S, Luna M, Ferrario A, & Gomer CJ (2004) CHOP activation by photodynamic therapy increases treatment induced photosensitization. *Lasers in Surgery and Medicine* 35(5):336-341.

56. Ito A, *et al.* (2009) Inhibition of heat shock protein 90 sensitizes melanoma cells to thermosensitive ferromagnetic particle-mediated hyperthermia with low Curie temperature. *Cancer Science* 100(3):558-564.

57. Yang LY, *et al.* (2015) Photothermal Therapeutic Response of Cancer Cells to Aptamer-Gold Nanoparticle-Hybridized Graphene Oxide under NIR Illumination. *Acs Applied Materials & Interfaces* 7(9):5097-5106.

58. Milanovic D, Firat E, Grosu AL, & Niedermann G (2013) Increased radiosensitivity and radiothermosensitivity of human pancreatic MIA PaCa-2 and U251 glioblastoma cell lines treated with the novel Hsp90 inhibitor NVP-HSP990. *Radiation Oncology* 8.

59. Pérez-Hernández M, *et al.* (2015) Dissecting the Molecular Mechanism of Apoptosis during Photothermal Therapy Using Gold Nanoprisms. *ACS nano* 9(1):52-61.

60. Ali MRK, *et al.* (2016) Simultaneous Time-dependent Surface Enhanced Raman Spectroscopy, Metabolomics and Proteomics Reveal Cancer Cell Death Mechanisms Associated with Au-Nanorod Photo-thermal Therapy. *Journal of the American Chemical Society*.

61. Fidler IJ (2003) The pathogenesis of cancer metastasis: the 'seed and soil' hypothesis revisited. *Nature reviews. Cancer* 3(6):453-458.

62. Weber GF (2013) Why does cancer therapy lack effective anti-metastasis drugs? *Cancer Lett* 328(2):207-211.

63. Morgillo F & Lee HY (2005) Resistance to epidermal growth factor receptor-targeted therapy. *Drug resistance updates : reviews and commentaries in antimicrobial and anticancer chemotherapy* 8(5):298-310.

64. Anonymous (2005) Effects of chemotherapy and hormonal therapy for early breast cancer on recurrence and 15-year survival: an overview of the randomised trials. *Lancet (London, England)* 365(9472):1687-1717.

65. Murphy CJ, *et al.* (2008) Gold Nanoparticles in Biology: Beyond Toxicity to Cellular Imaging. *Accounts Chem Res* 41(12):1721-1730.

66. Peer D, *et al.* (2007) Nanocarriers as an emerging platform for cancer therapy. *Nature nanotechnology* 2(12):751-760.

67. Ali HR, *et al.* (2016) Gold Nanorods as Drug Delivery Vehicles for Rifampicin Greatly Improve the Efficacy of Combating Mycobacterium tuberculosis with Good Biocompatibility with the Host Cells. *Bioconjugate Chemistry* 27(10):2486-2492.

68. Jun Y-w, *et al.* (2005) Nanoscale Size Effect of Magnetic Nanocrystals and Their Utilization for Cancer Diagnosis via Magnetic Resonance Imaging. *Journal of the American Chemical Society* 127(16):5732-5733.

69. Jain PK, Lee KS, El-Sayed IH, & El-Sayed MA (2006) Calculated Absorption and Scattering Properties of Gold Nanoparticles of Different Size, Shape, and Composition: Applications in Biological Imaging and Biomedicine. *The Journal of Physical Chemistry B* 110(14):7238-7248.

70. Ali MR, Panikkanvalappil SR, & El-Sayed MA (2014) Enhancing the efficiency of gold nanoparticles treatment of cancer by increasing their rate of endocytosis and cell accumulation using rifampicin. *Journal of the American Chemical Society* 136(12):4464-4467.

71. Danhier F, Feron O, & Preat V (2010) To exploit the tumor microenvironment: Passive and active tumor targeting of nanocarriers for anti-cancer drug delivery. *Journal of controlled release : official journal of the Controlled Release Society* 148(2):135-146.

72. Ali MRK, Panikkanvalappil SR, & El-Sayed MA (2014) Enhancing the Efficiency of Gold Nanoparticles Treatment of Cancer by Increasing Their Rate of Endocytosis and Cell Accumulation Using Rifampicin. *Journal of the American Chemical Society* 136(12):4464-4467.

73. Dickerson EB, *et al.* (2010) Chemosensitization of cancer cells by siRNA using targeted nanogel delivery. *BMC Cancer* 10(1):10.

74. Ali MRK, Ali HR, Rankin CR, & El-Sayed MA (2016) Targeting heat shock protein 70 using gold nanorods enhances cancer cell apoptosis in low dose plasmonic photothermal therapy. *Biomaterials* 102:1-8.

75. Yang JA, Phan HT, Vaidya S, & Murphy CJ (2013) Nanovacuums: Nanoparticle Uptake and Differential Cellular Migration on a Carpet of Nanoparticles. *Nano Letters* 13(5):2295-2302.

76. Arvizo RR, *et al.* (2013) Inhibition of tumor growth and metastasis by a self-therapeutic nanoparticle. *Proceedings of the National Academy of Sciences of the United States of America* 110(17):6700-6705.

77. Tay CY, *et al.* (2014) Nanoparticles strengthen intracellular tension and retard cellular migration. *Nano Lett* 14(1):83-88.

78. Zhou T, *et al.* (2014) Inhibition of Cancer Cell Migration by Gold Nanorods: Molecular Mechanisms and Implications for Cancer Therapy. *Advanced Functional Materials* 24(44):6922-6932.

79. Swaminathan V, *et al.* (2011) Mechanical stiffness grades metastatic potential in patient tumor cells and in cancer cell lines. *Cancer research* 71(15):5075-5080.

80. Cross SE, *et al.* (2008) AFM-based analysis of human metastatic cancer cells. *Nanotechnology* 19(38):384003.

81. Wirtz D, Konstantopoulos K, & Searson PC (2011) The physics of cancer: the role of physical interactions and mechanical forces in metastasis. *Nature reviews. Cancer* 11(7):512-522.

82. Lautscham LA, *et al.* (2015) Migration in Confined 3D Environments Is Determined by a Combination of Adhesiveness, Nuclear Volume, Contractility, and Cell Stiffness. *Biophysical journal* 109(5):900-913.

83. Dahl KN, Ribeiro AJS, & Lammerding J (2008) Nuclear Shape, Mechanics, and Mechanotransduction. *Circulation Research* 102(11):1307.

84. Isermann P & Lammerding J (2013) Nuclear Mechanics and Mechanotransduction in Health and Disease. *Current Biology* 23(24):R1113-R1121.

85. McGregor AL, Hsia CR, & Lammerding J (2016) Squish and squeeze-the nucleus as a physical barrier during migration in confined environments. *Current opinion in cell biology* 40:32-40.

86. Swift J, *et al.* (2013) Nuclear lamin-A scales with tissue stiffness and enhances matrix-directed differentiation. *Science (New York, N.Y.)* 341(6149):1240104.

87. Harada T, *et al.* (2014) Nuclear lamin stiffness is a barrier to 3D migration, but softness can limit survival. *The Journal of cell biology* 204(5):669-682.

88. Lee JS, *et al.* (2007) Nuclear lamin A/C deficiency induces defects in cell mechanics, polarization, and migration. *Biophysical journal* 93(7):2542-2552.

89. Davidson PM, Denais C, Bakshi MC, & Lammerding J (2014) Nuclear deformability constitutes a rate-limiting step during cell migration in 3-D environments. *Cell Mol Bioeng* 7(3):293-306.

90. Alkilany AM & Murphy CJ (2010) Toxicity and cellular uptake of gold nanoparticles: what we have learned so far? *Journal of Nanoparticle Research* 12(7):2313-2333.

91. Connor EE, Mwamuka J, Gole A, Murphy CJ, & Wyatt MD (2005) Gold nanoparticles are taken up by human cells but do not cause acute cytotoxicity. *Small* 1(3):325-327.

92. Axiak-Bechtel AM, *et al.* (2014) Gum arabic-coated radioactive gold nanoparticles cause no short-term local or systemic toxicity in the clinically relevant canine model of prostate cancer. *International Journal of Nanomedicine* 9:5001-5011.

93. Chen H, *et al.* (2013) In Vivo Study of Spherical Gold Nanoparticles: Inflammatory Effects and Distribution in Mice. *PLoS ONE* 8(2):e58208.

94. You J, *et al.* (2014) Pharmacokinetics, clearance, and biosafety of polyethylene glycol-coated hollow gold nanospheres. *Particle and Fibre Toxicology* 11.

95. Pernodet N, *et al.* (2006) Adverse effects of citrate/gold nanoparticles on human dermal fibroblasts. *Small* 2(6):766-773.

96. Cho YS, *et al.* (2009) Phosphorylation-driven assembly of the RIP1-RIP3 complex regulates programmed necrosis and virus-induced inflammation. *Cell* 137(6):1112-1123.

97. Qu Y, Huang Y, & Lu X (2013) Proteomic analysis of molecular biocompatibility of gold nanoparticles to human dermal fibroblasts-fetal. *Journal of biomedical nanotechnology* 9(1):40-52.

98. Yildirimer L, Thanh NTK, Loizidou M, & Seifalian AM (2011) Toxicology and clinical potential of nanoparticles. *Nano Today* 6(6):585-607.

99. Boisselier E & Astruc D (2009) Gold nanoparticles in nanomedicine: preparations, imaging, diagnostics, therapies and toxicity. *Chemical Society Reviews* 38(6):1759-1782.

100. Niidome T, *et al.* (2006) PEG-modified gold nanorods with a stealth character for in vivo applications. *Journal of Controlled Release* 114(3):343-347.

101. Sadauskas E, *et al.* (2009) Protracted elimination of gold nanoparticles from mouse liver. *Nanomedicine* 5(2):162-169.

102. Ali MRK, Ibrahim IM, Ali HR, Selim SA, & El-Sayed MA (2016) Treatment of natural mammary gland tumors in canines and felines using gold nanorods-assisted plasmonic photothermal therapy to induce tumor apoptosis. *International Journal of Nanomedicine* 11:4849-4863.

103. Ali MRK, Rahman MA, Wu Y, *et al*. (2017) Efficacy, long-term toxicity, and mechanistic studies of gold nanorods photothermal therapy of cancer in xenograft mice. *Proceedings of the National Academy of Sciences*. 201619302.

CHAPTER 2. IMPROVING AND UNDERSTANDING THE PLASMONIC PHOTOTHERMAL THERAPY *IN VITRO*

2.1 Fabrication and Optical Properties of Different Sizes of Gold nanorods [1-3]

Anisotropic nanoparticles, such as rods, are an evolution of the nanocrystal system as new properties may emerge due to unexpected thermodynamic geometries. The unique catalytic performance of anisotropic nanoparticles. Great studies in the field of nanotechnology have made the synthesizing of gold nanorods with a desired aspect ratio possible. Controlling the precision of gold nanorods' (AuNRs) size and shape remains challenging as it adds more optical, catalytic and mechanical character to the AuNRs. The synthesis of variant sizes or shapes of AuNRs has shown more interesting results, which was often not easy to achieve. Herein, we developed a new synthesitic technique, named seedless growth technique. In this method, the pH was found to play a crucial role in the monodispersity of the nanorods. Instead of seeds, the concentration of $NaBH_4$ in the growth solution was adjusted to control the reduction rate of the gold ions, smaller gold nanorods were produced. In addition, we used anionic surfactant, 5-bromosalicylic acid as a unique co-surface capping competitor with cetyltrimethylammonium bromide (CTAB) to guide the particle geometry evolution during nanorod overgrowth. The 5-bromosalicylic acid plays a role as a co-surfactant in a highly controllable and selective manner. The concentration of the 5-bromosalicylic acid played a key role in the development of the bone shape. In conclusion, the preparation of gold nanorods with different sizes and shapes using the the optimizied seedless method was found to be dependent on the $NaBH_4$ concentration used in the growth solution. Based on the results, the size and shape of the formed AuNPs

are dependent on the reduction rate of the gold ions in the solution. By using the seedless growth method, we have succeeded in the preparation of monodisperse AuNRs and AuNBs with low dimensions and aspect ratios, which enables the AuNRs and AuNBs to absorb in the nearinfrared radiation for we found to be useful for many catalytic activities: such as surface-enhanced Raman spectroscopy as an ultrasensitive spectroscopic tool with unique time-resolving and molecular finger-printing capabilities, for studying the cellular changes. In addition, potential use in in vivo photothermal therapeutic applications.

2.1.1 Introduction:

In recent years, gold nanoparticles (AuNPs) have been utilized in various fields. The interaction of light with the conduction band electrons gives rise to their collective oscillation which is known as localized surface plasmon resonance (LSPR) [3-4]. Within the realm of AuNPs, gold nanorods (AuNRs) show distinct physicochemical properties. AuNRs have two peaks, the transverse and longitudinal peaks. The latter could absorb near infrared light and convert it into heat rapidly and efficiently by non-radioactive processes such as electron-electron interactions and electron-photon interactions [3, 5-10]. The seed mediated method of synthesis is preferred to optimize the aspect ratios of AuNRs. In the seed mediated method, gold ions (Au+) are guided by silver ions (Ag+) in the presence of cetyltrimethylammonium bromide (CTAB), a surfactant template used to produce longitudinal and transverse dimensions of cylindrical AuNRs. Constricted control over the AuNRs' aspect ratios allows one to fine-tune the plasmon resonances over a broad spectral

range that spans the entire visible and near-infrared regions through either the first (650-900 nm) or (900-1200 nm) second window [5]. The AuNRs' tunability and their interactions with light yield unique absorption and scattering properties, which combined with the surface modification, endows AuNRs with significant potential for broad applications. In the synthesis of AuNPs, controling over these properties has been one of the most interesting and challenging tasks. The ability to control the surface structure of the AuNR with atomic precision while specifying the AuNR aspect ratio is crucial. The crystal facets exposed on the AuNRs determine the dynamic interaction between AuNRs as well as the interaction between the AuNR and the surface ligands. Furthermore, precise facet control allows for the opportunity to functionalize the nanorod surfaces with a desired geometry in a site-selective manner, enabling the molecularly guided assembly of AuNRs for spectroscopic applications [11]. This is especially important when the nanoparticles are rod shaped with overgrowth at their edges, which creates a hot spot for electrons. A nanoparticle with this feature is beneficial for generating a strong surface-enhanced raman spectroscopy (SERS) signal, which is sensitive to the shape (edges), size of the particles, and the nanoparticle assembly. A recent synthesis method that obtained AuNRs with variant atomic distribution at the edges was shown to be helpful for enhancing the SERS peaks [12]. However, this method involved cupper in the synthesized particles, which could be toxic for the bio-system. In addition, fabrication of small AuNRs that lower than 8 nm is not easy to achieve. Herein, we show our new seedless growth technique and include 5-bromosalicylic acid as an anionic surfactant can obtain different sizes, shapes of AuNRs with narrow distribution.

2.1.2 Experimental methods

2.1.2.1 Materials and equipments

$HAuCl_4$, $NaBH_4$, $AgNO_3$, ascorbic acid, CTAB, 5-bromosalicylic acid, were purchased from Sigma-Aldrich. Hydrochloric acid was purchased from the VWR Company. Characterization was carried out using a Cary 500 UV-Vis spectrometer and a JEOL 100 CX transmission electron microscope. An axial inductively coupled plasma (ICP) atomic emission spectrometer machine was used to determine the concentration of AuNPs in the solutions. A minimum of three ICP measurements were made for each sample.

2.1.2.2 Synthesis of Gold Nanorods using seed-mediated growth [1]

The seed solution was created with $HAuCl_4$ (0.025 mL, 0.1 M) in an aqueous solution of CTAB (10 mL, 0.1 M). A freshly prepared, ice-cold $NaBH_4$ solution (0.6 mL, 0.01 M) was then added into the mixture under vigorous stirring conditions for 2 minutes. The solution was left to age for 2 hours. The growth solution was prepared using the seed mediated method. Briefly, $HAuCl_4$ (100 μL, 0.1 M) was added to CTAB (20 mL, 0.1 M) and 80 μL of 5-bromosalicylic acid (0, 0.001 μL, 0.01 M). Then, 550 μL ascorbic acid (0.1M) was added, followed by gentle mixing to form the growth solution. Varied volume of seed solution (8-80 μL) was then added to the growth solution and allowed to react for 6 h.

2.1.2.3 Synthesis of gold nanobones by seed-mediated growth [1]

Gold nanobones with variant lengths and widths were synthesized by following the seed-mediated protocol. In the first step, the seed nanoparticles were synthesized by adding 5.0 mL of $HAuCl_4$ (1.0 mM) to 5.0 mL of CTAB (0.2 M) followed by the addition of ice-cold $NaBH_4$ (0.6 mL, 10.0 mM). The solution was then stirred for 2 min. In the second step, (80-240 µL) of seed solution was added to the growth solution containing 1 mL of 5-Bromosalysilice acid (4.6 mM), 100 mL of $HAuCl_4$ (1.0 mM), 100 mL of CTAB (0.2 M), 5 mL of $AgNO_3$ (4.0 mM), HCl (160 µL, 37%) and 1.4 mL of ascorbic acid (78.8 mM). After the injection of seed solution, the growth solution kept undisturbed for 6 h. The resultant CTAB stabilized AuNRs were purified by centrifugation and redispersion in deionized (DI) water.

2.1.2.4 Synthesis of gold nanorods/ nanbones by seedless mediated growth [1-3]

We followed our early reported procedure [1-3]. Briefly1 mL of 5-Bromosalysilice acid (4.6 mM) and 50 mL of $HAuCl_4$ (1.0 mM) were added to 100 mL of CTAB (0.2 M), 5 mL of $AgNO_3$ (4.0 mM) and HCl (160 µL, 37%). Then, 700 µL of ascorbic acid (78.8 mM) was added, followed by immediate injection of ice-cold $NaBH_4$ (15-150 µL, 10.0 mM), the higher concentration is the lower sizes were obtained. The solution left undisturbed for 6 h.

2.1.2.5 Using centrifugation to concentrate and prepare monodisperse nanoparticles.

The solution was centrifuged for 15 min at 14,500 rpm. The supernatant was removed, and the solution was then spun down again. The precipitate was dispersed in deionized water and centrifuged again at the same speed and time.

2.1.3 Results and discussion

The seed solution is usually prepared under chemical supersaturation, as required for the rapid nucleation of particles in the growth solution. The growth solution is used in a two-step reduction process. The first reduction occurs by the reaction with ascorbic acid ($Au^{3+} \rightarrow Au^{+}$). The second reduction ($Au^{+} \rightarrow Au^{0}$) requires a seed to act as a catalyst. This results in gold nanorods in the presence of the Ag^{+} ions. To achieve gold nanobones (AuNBs), the 5-bromosalicylic acid is required to facilitate particle overgrowth while $NaBH_4$ is used as a reducing agent in the growth solution to enhance the reduction of $Au^{+} \rightarrow Au^{0}$. The resulting gold nanorods have an average width of 25 to 2.5 nm in another setting.

2.1.3.1 The influence of 5-bromosalicylic acid concentration on the bone shape distribution:

Different molar ratios of 5-bromosalicylic acid to $HAuCl_4$ were used in the growth solution. After the first reduction where ascorbic acid was utilized in the seed mediated method, 5-bromosalicylic acid was added, which plays an essential role in growth. The nucleation of the nuclei and the growth of these nuclei happen under high chemical supersaturation. These conditions ensure the generation and immediate growth of the gold nuclei and rapid overgrowth at the edges. A UV-Vis spectrometer and a transmission electron microscope were used to track the rod to bone evolution in shape and size. Separate growth solutions with different molar ratios of 5-bromosalicylic acid to $HAuCl_4$, as shown in (**Figure 2-1A &Figure A2**), has two plasmon bands. The transverse plasmon band has an absorption peak of around 525 nm and is nearly identical for each solution. However, the longitudinal plasmon band, which is attributed to the rod or bone shape of the particle, appears at a longer wavelength in each solution. Increasing the concentration of 5-

bromosalicylic acid in the separate growth solutions prompted the longitudinal peaks to red shift.

2.1.3.2 The influence sodium borohydride and seed concentrations on producing different rods with the same length but different widths:

The synthesis of three different sizes of AuNRs with the same length but variant widths comparing the absorbance spectra in sample (**Figure 1-2**) revealed that they have the different absorption. It has been observed that by increasing the concentration of 5-bromosalicylic acid in the growth solution, the length of the rod increased, which is evident from the increasing longitudinal surface plasmon (LSP) intensity in comparison to the transverse surface plasmon (TSP) intensity. (**Figure 2-2B** & **Figure A.1**)

2.1.3.3 The influence of 5-bromosalicylic acid, sodium borohydride and seed concentrations on producing different rods with the same length but different widths:

By repeating the above experiment in the presenece 5-bromosalicylic acid with increasing seed solution concentrations, the effect of seed size on the growth solution was studied. Three separate growth solutions with different molar ratios of 5-bromosalicylic acid ($HAuCl_4$) were used in the growth solution, as described above. Figure 2-3A shows the UV-Vis-NIR absorption spectra with different molar ratios. We determined the FWHM for the longitudinal band of the samples prepared at the variant addition of the 5-bromosalicylic acid, all the samples showed very small FWHM (**Figure 2-3)** was found for the sample prepared by adding 0.001 M of 5-Bromosalicylic acid. The 5-

bromosalicylic acid in the solution plays a crucial role in both the reduction of $Au^{3+} \rightarrow Au^{+}$ as well as $Au^{+} \rightarrow Au^{0}$. The homogeneity of the bones increased also increased alongside the increasing concentration of 5-bromosalicylic acid. The resulting AuNBs were small and the sample was monodisperse as shown in the TEM (**Figure 2-3B-D**). The homogeneity for the produced nanorods increased.

2.1.3.4 Assembling Pattern Comparing the AuNBs with the AuNRs:

Recently, electrostatic-force-based assembly of nanoparticles has been proposed as a general, precise, and reliable methodology. In the most direct type of electrostatic-force-based assembly, charge patterns are created by scanning-probe or micro contact charging techniques onto electret materials via electron- or hole-tunneling processes. As the electret materials, can retain electric charge or polarization for a long time, these charge patterns can be used as templates for assembling charged or polarizable nanoparticles. As shown in **figure 2-4**, the AuNBs shows great assembling from edges when diluted in water. We have observed the from the UV-vis in **figure 2-4**, that a new longitudinal plasmon peak appears in the second window near IR after an hour of assembling in water. This introduce new catalytic properties of the AuNBs.

2.1.3.5 Comparison between Gold Nanorods of the Same Aspect Ratio Prepared by Seedless and Seeded Methods:

Different parameters can influence small gold nanorods growth such as silver ions content on the growth solution. By adding 270 μL of 4.0 mM $AgNO_3$ to the seeded and seedless

growth solutions nanorods with the same aspect ratios, but with different sizes, were obtained. The longitudinal surface plasmon absorbance of the nanorods that was prepared from the two methods is nearly 800 nm (**Figure 2-5**). As shown in the TEM images, the gold nanorods obtained using the seeded method showed average particle dimensions of 54.0 × 11.2 nm. The gold nanorods prepared by seedless method have average particle dimensions of 25.0 × 5.2 nm (**Figure 2-5**). The aspect ratio for both sets of nanorods is 4.8 ± 0.6. Table 2 shows a comparison between the extinction coefficients for the two gold nanorods. The extinction coefficient is smaller for the gold nanorods prepared using the seedless method than those prepared using the seeded technique. The ratio of the extinction coefficients (seeded/seedless) having the same aspect ratio (4.8) is ~26 and a volume ratio of ~10. Obviously, the two ratios are not the same. It is possible that as the nanoparticle gets smaller, its surface is more defective giving rise to surface scattering of the coherent motion of the conduction band electrons. This leads to weaker plasmonic fields and thus smaller extinction coefficient (the seedless particles).

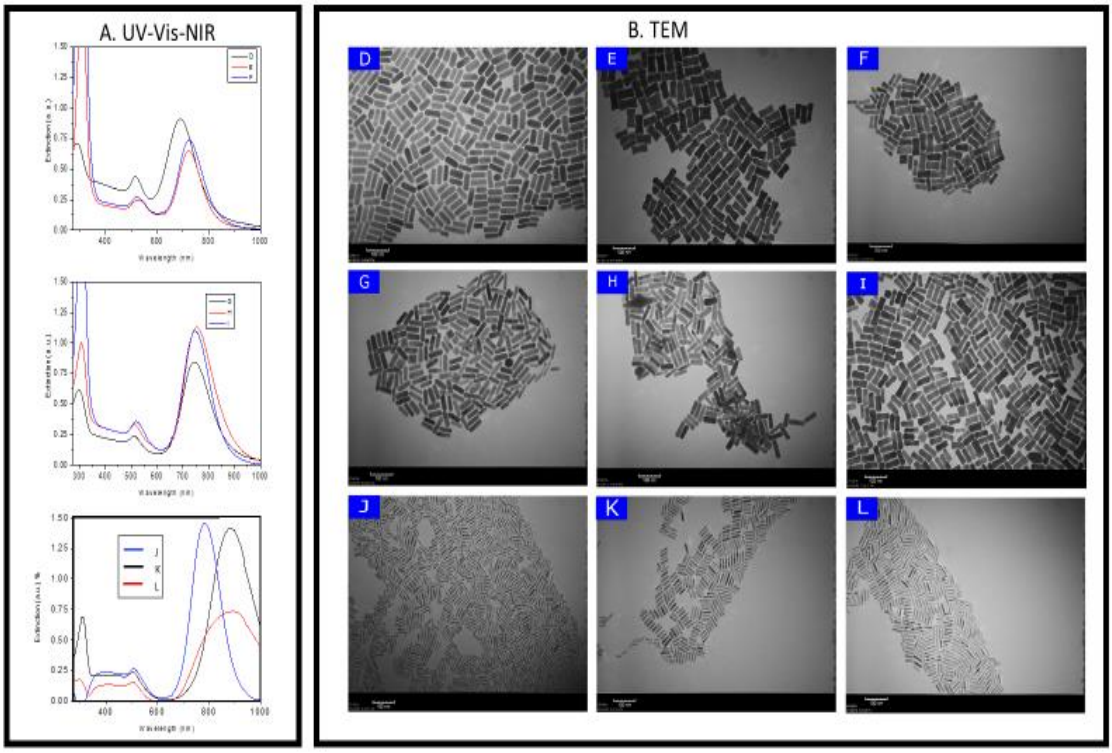

Figure 2-1: The UV-Vis-NIR absorption spectra with different additions of 5-bromo salicylic acid.

The synthesis media was maintained at a constant of 8 µL of seed solution D) Rod shaped E) Bone shaped, F) Semi-bone shape. Samples from (G-I) synthesis media was maintained at 12 µL of seed G) Rod shaped, H) Semi-bone shape, I) Bone shape. Samples (J-K) maintained at 80 µL of seed., J) Rod shaped, K) Rod shaped, L) Rod shaped. The three additions of 80 µL of 5 bromosalicylic acids at different concentrations 0 (A), 0.0001 µL (B), and 0.001 µL (C). Gold nanoparticles TEM images showing the effect 5 bromosalicylic acid on the AuNRs/AuNBs distributions. The three sample (D-F) are prepared at the molar ratios of the effect 5 bromosalicylic acid: Au. While the synthesis media was maintained at a constant of 8 µL of seed solution D) Rod shaped with dimensions of 64 x 24 nm, E) Bone shaped with dimensions of 65 x 31 nm, F) Semibone shape with dimensions of 60 x 24 nm. Samples from (G-I) synthesis media was maintained at 12 µL of seed G) Rod shaped with dimensions of 59 x 18 nm, H) Semi-bone shape with dimensions of 57 x 16 nm, I) Bone shaped with dimensions of 58 x 21 nm. Samples (J-K) maintained at 80 µL of seed., J) Rod shaped with dimensions of 36 x 6 nm, K) Rod shaped with dimensions of 36 x 6 nm, L) Rod shaped with dimensions of 36 x 6 nm.

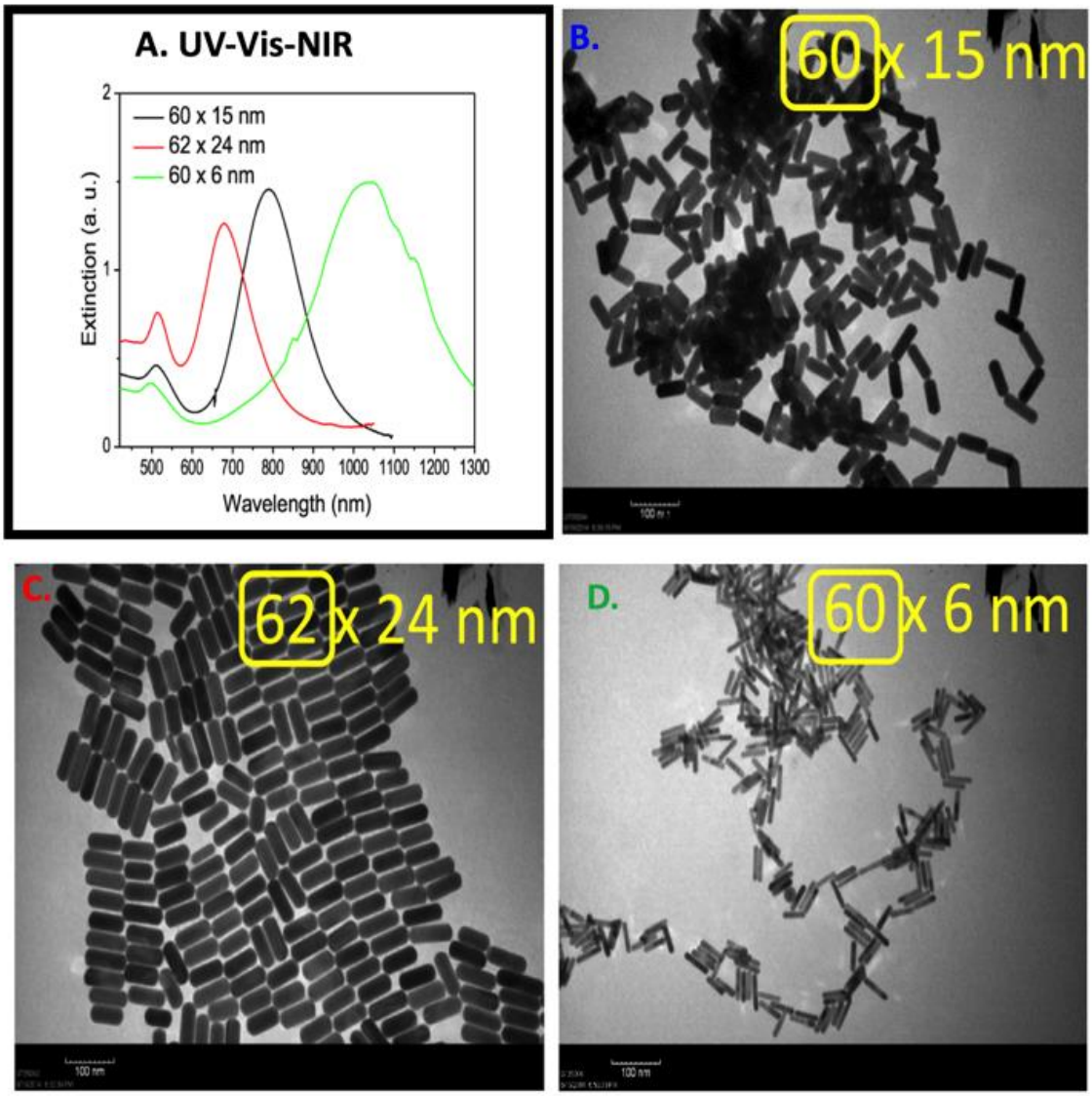

Figure 2-2 AuNRs with the same length but variant widths:

A) UV-Vis absorbance spectra of three different sizes of AuNBs. B) TEM of small bones (Length 60±2 x Width 15±0.5 nm)., black). C (Length 62±4 x Width 24±2 nm., red). and D) (Length 60±6 x Width 6±1 nm). CTAB- stabilized AuNBs, The SPR peaks of the three AuNBs were about 770 nm.

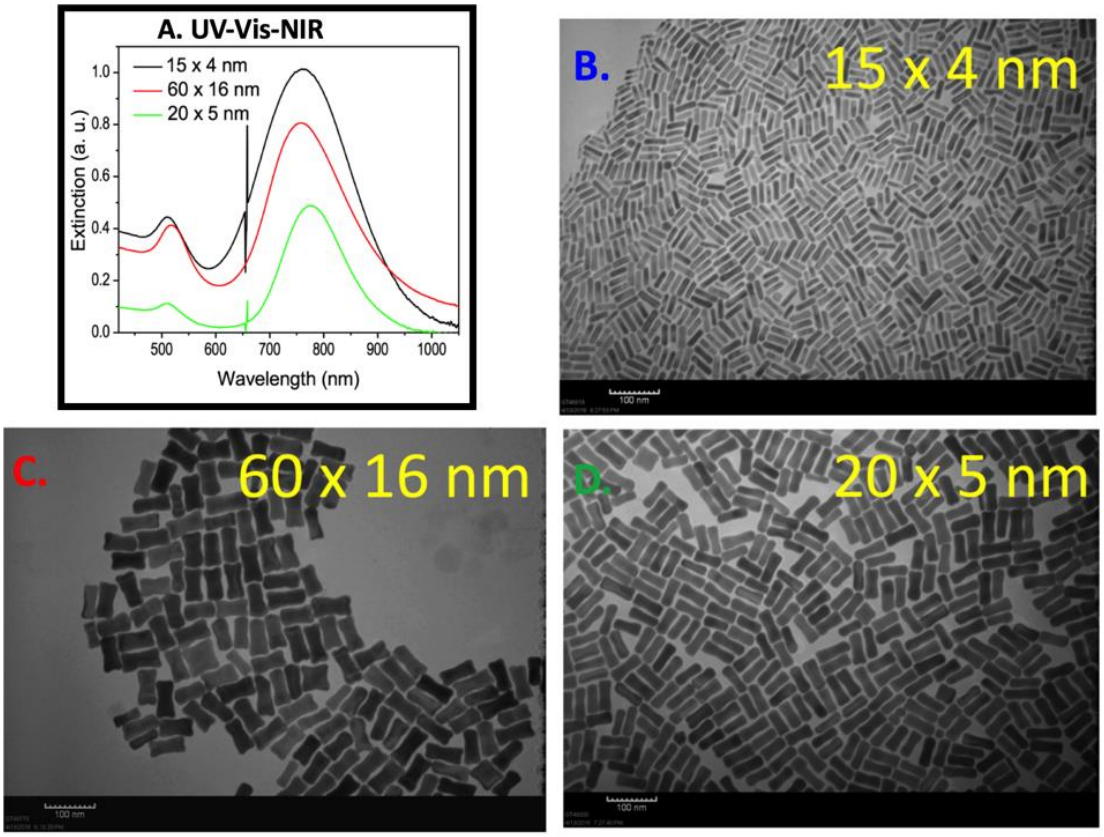

Figure 2-3 AuNBs with the same aspect ratio:

A) UV-Vis absorbance spectra of three different sizes of AuNBs. B) TEM of small bones (Length 15±2 x Width 4±0.5 nm)., black). C (Length 60±4 x Width 16±2 nm., red). and D) (Length 20±2.5 x Width 5±1 nm). CTAB- and 5-bromosalusilic acid stabilized AuNBs, The SPR peaks of the three AuNBs were about 770 nm.

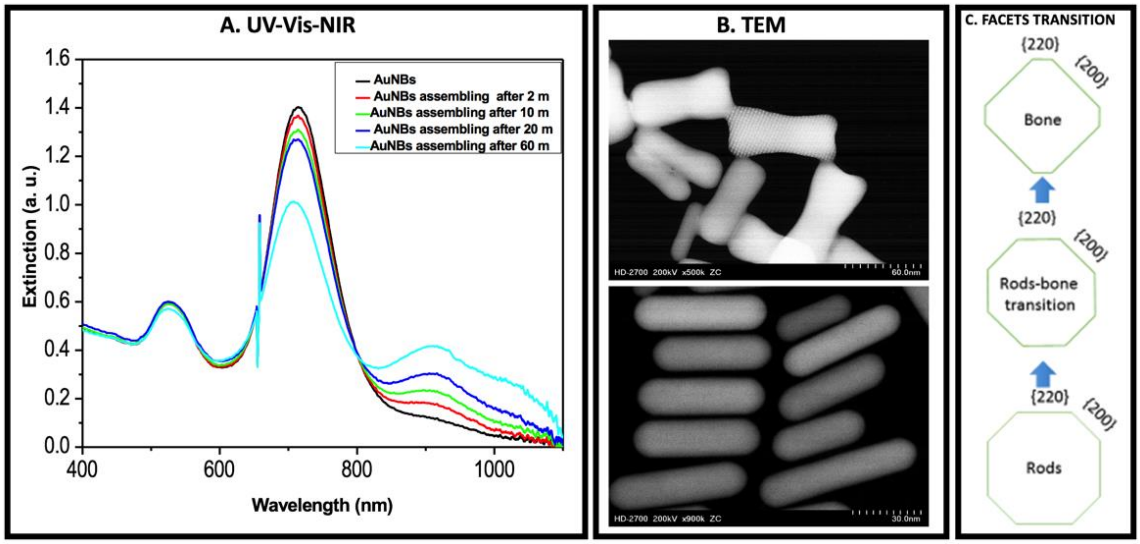

Figure 2-4. Comparison between Au nanorods and Au nanobones grown:

A) UV-Vis-NIR absorption spectra of AuNBs showing self-assembling in water with time. The spectra clearly show that the transverses peak at 760nm decreases and a new peak at 950 nm develops with time. B) top, TEM images shown above are fromor the AuNBs after they were left in deionized water with respect to time: 2,10,20, and 60 minutes. B) bottom TEM of AuNRs showing different assemebly in water. C) High-resolution STEM projections model of the facet transition from rods to bones shape, oriented along the [220] direction

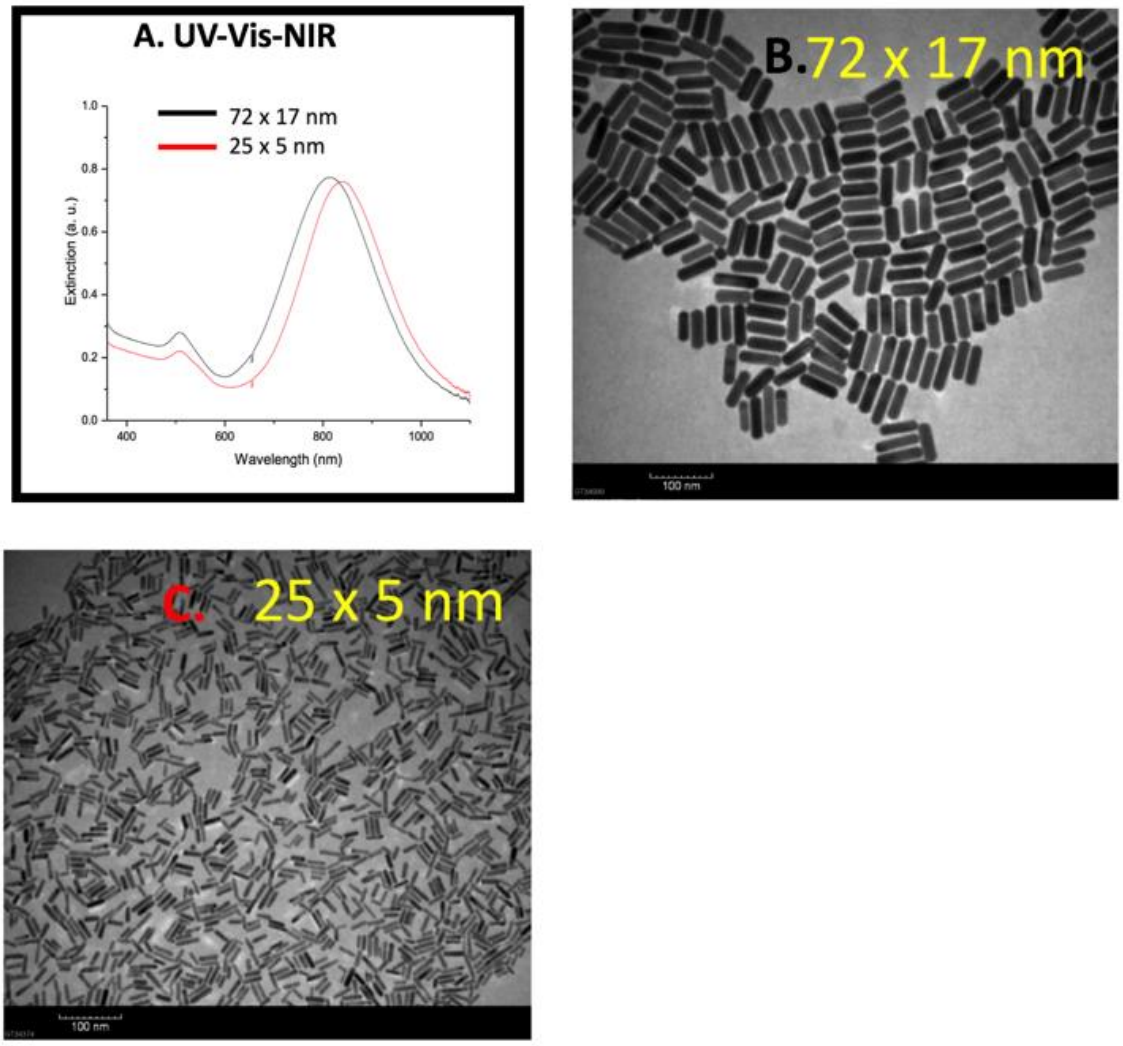

Figure 2-5: Two different sizes of AuNRs with the same aspect ratio:

A) UV-Vis absorbance spectra of the large (Length 72 nm, black) small (Length 25 nm, black) CTAB-stabilized AuNRs, (B) TEM of large rods (Length 72±7 x Width 19±4 nm) small rods Length 25±2 x Width 5±1 nm). The SPR peaks of the large and small AuNRs were about 767 nm.

2.1.4 Conclusion and Future Outlook

Relatively small gold nanorods or nanobones with widths lower than 10 nm: ranging from 2.5 in one setting and 5.5 nm in another setting with different aspect ratios were synthesized using a one-step seedless growth procedure. Seeds are necessary for large gold nanorods, but $NaBH_4$ was used as a substitute in the seedless growth process. The pH of the solution also plays an important role in the synthesis of nanorods. Decreasing the pH results to the decreases the rate of the reduction, which increases the growth time (if the concentration of $NaBH_4$ has been optimized in the growth solution) and gives a more monodisperse solution. CTAB is an important contributor in controlling the gold nanorods dimension in seedless growth technique. Increasing the CTAB concentration produces rods with smaller size. The growth kinetics of the length and the width of gold nanorods can be controlled by changing the CTAB as well as the silver ion concentrations in the reaction mixture. By increasing the amount of $NaBH_4$ added to the solution in the absence of silver ions, smaller gold nanospheres were synthesized. While the extinction coefficient is found to depend linearly on either the aspect ratio or the wavelength of the longitudinal plasmonic band for the large nanorods, it is found to be independent for the small nanorods. This was explained by the fact that the extinction band of the plasmonic nanoparticle is dominated by scattering processes, while for small nanoparticles they are determined by absorption processes. Each of these properties has different dependences on the size of the nanoparticle. From conclusion and the fact that the extinction coefficient of the large rods are more sensitive to size than the small rods, that the scattering processes are more sensitive to size changes than absorption, as one expects. We have optimized a new gold

nanoparticles synthesis technique, obtained variant sizes and shapes of AuNRs, and showed variend plasmonic properties for several potential applications.

2.1.5 References

1. Ali MRK, Ali, M. R. K.; Chapman S.; Wu, Y.; El-Sayed MA (2012); The Synthesis and Optical Properties of Different Sizes of Gold nanobones (AuNBs) and their self-assembly in water. *Under preparation.*

2. Ali MRK, Ali.; Kassam K.; Wu, Y.; El-Sayed MA (2012); Fabrication and Charactrization of Gold Nanorods, Especially Second Window Near IR. *Under preparation.*

3. Ali MRK, Snyder B, & El-Sayed MA (2012) Synthesis and Optical Properties of Small Au Nanorods Using a Seedless Growth Technique. *Langmuir* 28(25):9807-9815.

4. Alkilany AM, Thompson LB, Boulos SP, Sisco PN, & Murphy CJ (2012) Gold nanorods: Their potential for photothermal therapeutics and drug delivery, tempered by the complexity of their biological interactions. *Adv. Drug Deliv. Rev.* 64(2):190-199.

5. Dickerson EB, et al. (2008) Gold nanorod assisted near-infrared plasmonic photothermal therapy (PPTT) of squamous cell carcinoma in mice. *Cancer Lett*. 269(1):57-66.

6. Shen JL, et al. (2014) Multifunctional Gold Nanorods for siRNA Gene Silencing and Photothermal Therapy. *Adv. Healthc. Mater.* 3(10):1629-1637.

7. Huang XH, et al. (2010) Comparative study of photothermolysis of cancer cells with nuclear-targeted or cytoplasm-targeted gold nanospheres: continuous wave or pulsed lasers. *Journal of Biomedical Optics* 15(5).

8. Yang XJ, et al. (2012) Near-Infrared Light-Triggered, Targeted Drug Delivery to Cancer Cells by Aptamer Gated Nanovehicles. *Advanced Materials* 24(21):2890-2895.

9. Zhu ZF, et al. (2016) Near-Infrared Plasmonic 2D Semimetals for Applications in Communication and Biology. *Adv. Funct. Mater.* 26(11):1793-1802.

10. Shao JX, et al. (2015) Near-Infrared-Activated Nanocalorifiers in Microcapsules: Vapor Bubble Generation for In Vivo Enhanced Cancer Therapy. *Angew. Chem.-Int. Edit.* 54(43):12782-12787.

11. Ali MRK, et al. (2016) Simultaneous Time-dependent Surface Enhanced Raman Spectroscopy, Metabolomics and Proteomics Reveal Cancer Cell Death Mechanisms Associated with Au-Nanorod Photo-thermal Therapy. *Journal of the American Chemical Society.* 138(47): 15434-15442.

12. Zhang Q, et al. (2016) Facet Control of Gold Nanorods. *ACS Nano* 10(2):2960-2974.

13. Ali MRK, Snyder B, & El-Sayed MA (2012) Synthesis and Optical Properties of Small Au Nanorods Using a Seedless Growth Technique. *Langmuir* 28(25):9807-9815.

14. Chen PS, et al. (2007) CTGF enhances the motility of breast cancer cells via an integrin-alpha v beta 3-ERK1/2-dependent S100A4-upregulated pathway. *Journal of Cell Science* 120(12):2053-2065.

15. Ali MR, Snyder B, & El-Sayed MA (2012) Synthesis and optical properties of small Au nanorods using a seedless growth technique. *Langmui*r 28(25):9807-9815.

2.2 Enhancing the Efficiency of Gold Nanoparticles Treatment of Cancer by Increasing Their Rate of Endocytosis and Cell Accumulation by Using Rifampicin [1]

To minimize the toxicity of gold nanoparticles (AuNPs) in cancer treatment, we have developed a technique, which uses less amount gold NPs but increases the treatment efficiency. Rifampicin (RF) is known to enhance the multidrug resistance (MDR) by imprisoning higher concentrations of the drug inside the cancer cell. In this work, we have shown that RF-conjugated Au NPs can greatly enhances the rate as well as efficiency of endocytosis of nanoparticle hence their concentration inside the cancer cell. This is expected to decrease the demand on the overall amount of Au NPs needed for treating cancer and thus decreasing its toxicity.

2.2.1 Introduction

Cancer, often described as one of the most dreadful disease, remains as an important challenge across the world. Enhancing the efficiency of delivering anticancer drugs precisely to the cancer sites is critical for its successful treatment. [2, 3] Hence, ongoing cancer researchers are keenly focused on identifying innovative ways to enhance the targeting efficiency of targeting nanoparticles to elevate the rate of endocytosis hence to decrease the toxicity. Though nanotechnology-based methods have showed promising results in view of screening cancer cells [4-6] and targeted drug delivery, [7-9] it is still challenging to bypass the efflux of drug carrying nanoparticles through multidrug

resistance (MDR) mechanism [10-12] in cancer cells. In view of minimizing the toxicity during the gold NPs-based plasmonic chemotherapy, it is highly desirable to develop novel functionalized nanomaterials, which could effectively deliver the drug carrying nanoparticles into the cancer cells, without being accumulated outside the cells.

Among the nanoparticles, gold nanorods (AuNRs) have been considered as an efficient drug delivery platform owing to their unique optical and photothermal properties. [7, 13] Though many molecules such as PEG PNIPAM, SiO_2, etc. are well-known [2, 7, 14, 15] for passivation of AuNRs against its toxic effect and carrying the drug to the target cells, proteins are more convenient and efficient carrier system as they can accommodate more drug molecules per molecules and their biocompatible nature. [16, 17] The concept of plasmonic chemotherapy [18-21] using near-infrared (NIR) absorbing AuNRs carrying anticancer drug molecules as an efficient drug delivery vehicle has greater relevance in this regards as it can reduce the side effects of chemotherapy. Here, we introduce a novel multifunctional AuNR-based plasmonic chemotherapy platform, carrying rifampicin (RF) (an antibiotic used to treat infections, including tuberculosis), for efficient delivery of paclitaxel (Ptxl) carrying bovine serum albumin (BSA)-conjugated AuNRs into the cancer cells. Our study confirms that RF can act as a chemosensitizer to bypass the multidrug resistance [22, 23] in cancer cells and enhancing the efficiency of endocytosis of drug carrying nanoparticles into the cancer cells. Moreover, the fast endocytosis of the nanoparticels could be an attractive treatment modality, which could decrease the possibility of targeted nanoparticles being excreted through extracellular fluids during their intravenous administration.

As a drug carrier system, BSA has been used to conjugate AuNRs due to their excellent biocompatibility, low cost and presence of two primary drug-binding sites. [17, 24, 25] The conjugation of BSA with the AuNRs has been confirmed using various spectroscopic techniques (experimental details are given in the supporting information (SI) 1). For this study, we used three different nanoparticle systems such as spherical Au@Citrate nanoparticles (AuNSs) (~20 nm), small Au nanorods (sAuNRs) [26] (17 nm length, and 3.5 nm diameter), and bigger Au nanorods (bAuNRs) (47 nm length and 10 nm diameter). Conjugations of BSA with these nanoparticles were obvious from their extinction spectra, as all the nanoparticles showed a distinct red shift in their absorption maxima after binding with BSA (Figure 2-6A-C). TEM images of each nanoparticle used in this study are also given in Figure 1 D-F.

2.2.2 Methods and Experimental Methods

2.2.2.1 Synthesis of Gold Nanorods (47 Nm Length and 10 Nm Width) by Seed-Mediated Growth

Gold nanorods (AuNRs) were synthesized by following the modified seed-mediated protocol of Nikoobakhat *et al* [27]. and Ali *et al* [26]. In the first step, the seed nanoparticles were synthesized by adding 5.0 mL of $HAuCl_4$ (1.0 mM) to 5.0mL of CTAB (0.2 M) followed by the addition of ice-cold $NaBH_4$ (0.6 mL, 10.0 mM). The solution was then stirred for 2 min. In the second step, 240 µL of seed solution was added to the growth solution containing 100 mL of $HAuCl_4$ (1.0 mM), 100 mL of CTAB (0.2 M), 5 mL of

$AgNO_3$ (4.0 mM), HCl (160 µL, 37%) and 1.4 mL of ascorbic acid (78.8 mM). After the injection of seed solution, the growth solution kept undisturbed for 12 h. The resultant CTAB stabilized AuNRs were purified by centrifugation and redispersion in deionized (DI) water.

2.2.2.2 Synthesis of Gold Nanorods (17 Nm Length and 3.5 Nm Width) by Seedless Growth Technique

For making smaller AuNRs we followed our early reported procedure in Ali *et al*. [26] Briefly, 50 mL of $HAuCl_4$ (1.0 mM) was added to 100 mL of CTAB (0.2 M), 5 mL of $AgNO_3$ (4.0 mM) and HCl (160 µL, 37%). Then, 700 µL of ascorbic acid (78.8 mM) was added, followed by immediate injection of ice-cold $NaBH_4$ (150 µL, 10.0 mM). The solution left undisturbed for 12 h, which was then centrifuged at 16000 rpm for 20 min and redispersed in DI water.

2.2.2.3 Synthesis of Au@Citrate Nanoparticles

Citrate-capped gold nanospheres (AuNSs) with an average diameter of 15–20 nm was synthesized by the reduction of $HAuCl_4.3H_2O$ (Sigma Aldrich) with trisodium citrate (Sigma Aldrich). [28] In this method, 5 mL of 5 mM $HAuCl_4.3H_2O$ was diluted with 90 mL of deionized (DI) water and heated until it begins to boil. An amount measuring 5 mL of 0.5% trisodium citrate solution was added and continued heating until the solution turned wine red. It was cooled under ambient conditions and used for further studies.

2.2.2.4 Preparation of Drug-Loaded, BSA-Conjugated Nanorods (Aunrs@BSA-Drug@RGD)

Conjugation of BSA with various gold nanoparticles were carried out by adding 50 ml of 0.5 mM bovine serum albumin (BSA) (Sigma-Aldrich, USA) into the nanoparticles solution (AuNRs or spheres) (1 nM), which was then incubated for 10 h at room temperature. The excess BSA was removed from the nanoparticle solution by centrifugation. For making multifunctional drug (RF or Ptxl)-loaded AuNRs@BSA, 5 mL of 5 mM drug solution was added to the 50 mL of Au@BSA nanoparticles (1 nM). The solution was gently shaken and kept for 5 h. To this solution, 1 mL of 5 mM RGD (CGPDGRDGRDGRDGR) solution was added. The resultant AuNRs@BSA-drug-RGD nanoparticles were centrifuged to remove unbound drug molecule as well as RGD molecules. Similar procedure was used to make AuNSs@BSA-drug-RGD.

The number of RF molecules per AuNR has been calculated from the absorption spectra of RF solution before and after treating them with AuNRs@BSA. The value was obtained by subtracting the concentration of RF in the supernatant solution from their original concentration. The extinction coefficient of RF at 334 nm was 28000 $M^{-1}cm^{-1}$. [29]

2.2.2.5 Photothermal Studies

For the photothermal studies, RF-functionalized nanoparticles (1 mL, 1 OD) were exposed for to CW laser of 808 nm (5.8 W/cm^2) for various time intervals. Afterwards, each sample

were centrifuged and the UV-vis absorption spectra of the supernatant solutions were measured.

2.2.2.6 Cell Culture

Human oral squamous cell carcinoma (HSC) cells were cultured in Dulbecco's modified Eagles' medium (DMEM, Mediatech), without phenol red, supplemented with 10% v/v fetal bovine serum (FBS, Mediatech) and 1% antimycotic solution (Mediatech) in a 37 ºC, 5% CO_2 humidified incubator.

2.2.2.7 Cell Viability Assay

HSC cells were plated in a 96-well tissue culture plate and incubated for 24 h. The culture medium was then removed and replaced with culture medium containing the various nanoparticles (details about the nanoparticles are given in the manuscript). Cells were incubated for 24 h. Afterwards the cells were washed with PBS and the XTT solution and incubated for 6 h. A Biotek Synergabsoy H4 multi-mode plate reader was used for reading the cell viability results. The error bar is expressed as +/- the percent relative standard deviation (% rsd).

Experiments were also conducted by exposing the similar set of cell samples by exposing them to the laser (808 nm) for 2 min. The cell viability was measured after 6 h by following the method described earlier.

For the cell uptake studies, the cells were grown on sterilized round coverslips that were placed in 12-well dish and treated with different conjugated nanoparticles (details of nanoparticles are given in the manuscript) for 0.5, 2, and 24 h. Then the rounded cover slips incubated with 1 mL of 4% paraformaldehyde for 30 minutes, which were washed with DI water and analyzed under dark field microscope.

Statistical analysis: Statistical significance (*p*-value), which is indicated by *, was calculated by a *t-test calculator* (GraphPad Software, Inc.). Data is considered statistically significant when $p < 0.05$.

2.2.3 Results and Discussion

Loading of drug molecules (RF and Ptxl) with BSA has been performed in aqueous solution under physiological conditions and their binding with BSA was confirmed fluorometrically, which showed a distinct reduction in the fluorescence emission (~350 nm) intensity of BSA (excitation at 294 nm) as well as slight shift in their emission after the addition of 5 mM of drug into 1 mM BSA solution.

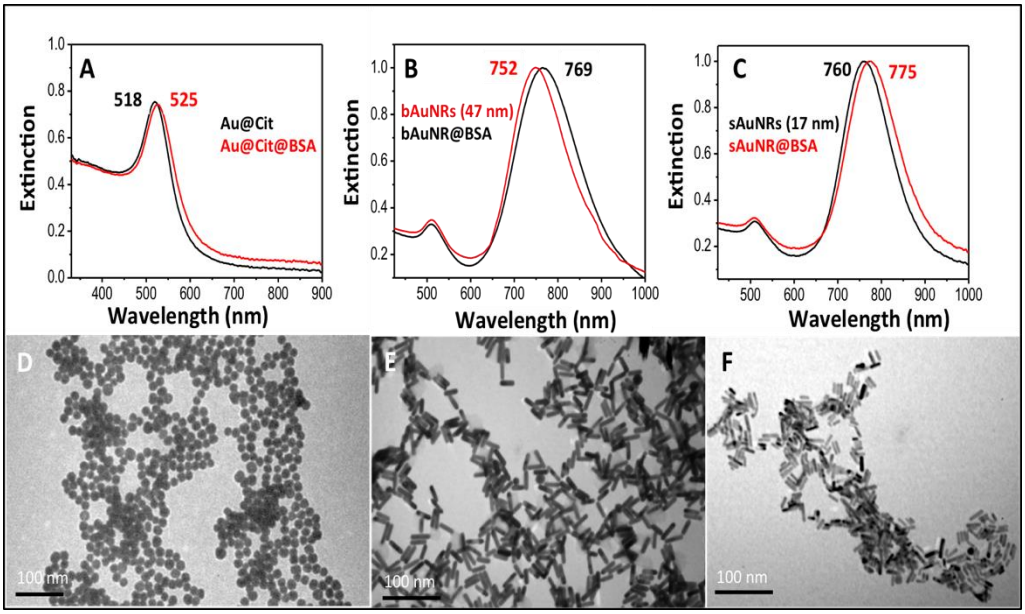

Figure 2-6 Conjugated of gold nanoparticles with BSA

(A, D), (B, E), and (C, F) are UV-vis absorption spectra and respective TEM image of AuNSs, bAuNRs, and sAuNRs, respectively

Similar result was also found when BSA-conjugated AuNRs were treated with 5 mM RF (see SI 3). The observed red shift in fluorescence emission of BSA after drug binding can be attributed to an increased polarity of the region surrounding the tryptophan site. [30] Whereas, quenching of fluorescence is mainly due to the process of energy transfer by the intermolecular interaction of drug molecules with tryptophan moiety present in the proximity of drug binding site in BSA. [31, 32] Interestingly, we also found that the solubility of Ptxl considerably increased when it is conjugated with BSA the amount of RF bound to BSA-conjugated nanoparticles was calculated from their absorption spectra, before and after addition to the nanoparticles. RF shows characteristic absorption bands at 256 and 334 nm corresponds to the π-π* transitions of the chromophore. The band at 474 nm is assigned to a π-π* CT (electron charge transfer) transition between the electron donating group (CO) and the substituent (OH) of the naphthohydroquinone chromophore

in RF. (33) Further, the conjugation of RF and Ptxl was confirmed by surface enhanced Raman spectroscopic (SERS) studies (SI 5 and SI 6). All the SERS spectra were measured in the solution state. The RF-loaded BSA-conjugated AuNRs (AuNRs@BSA-RF) showed clear Raman features 0f RF, which was in concordance with the Raman features of pure RF [33] (see SI 5). Absence of any prominent Raman features of CTAB or BSA can be due to their low Raman cross-section compared to the RF.

To study the efficiency of drug release for each nanorods (sAuNRs and bAuNRs), we used their RF-loaded analogue as they showed distinct features of RF in the absorption spectra (Figure 2-7A). The charge transfer band of RF found at 474 nm slightly red shifted to 482 nm after addition into BSA-conjugated AuNRs, which clearly suggests the binding of RF with BSA. The triggering of drug release was achieved by irradiating the AuNRs solution with a CW laser source with excitation wavelength of 808 nm, which overlaps with the longitudinal surface plasmon resonance (LSPR) band of AuNRs. Exact concentrations of liberated RF after laser irradiation was calculated using the extinction coefficient of RF and the absorption at 334 nm (**Figure 2-7B**). Photothermal studies suggest an enhancement in the drug release for sAuNRs compared to bAuNRs, when RF-loaded nanorod solutions of same optical density were used. Due to the higher absorption and lower scattering properties, sAuNRs are a good candidate in plasmonic chemotherapy. Enhanced drug release capability of sAuNRs is attributed to their higher efficiency in generating heat upon laser irradiation compared to the bAuNRs of same optical density.

We found that laser irradiation of sAuNRs (OD=1) for 2 min can increase the solution temperature from 27 ^{0}C to 82±0.5 ^{0}C. Whereas, laser irradiation of bAuNRs (OD=1) for 2 min resulted in the enhancement of the temperature from 27 ^{0}C to 65±0.5 ^{0}C, suggests the

higher photothermal ability of sAuNRs. A plot of laser irradiation time *versus* amount of RF released at different irradiation time is depicted in **Figure 2-2B**. There was no significant enhancement in the temperature observed in the case of AuNSs, owing to their mismatch between the laser excitation source (808 nm) and surface plasmon resonance band (525 nm).

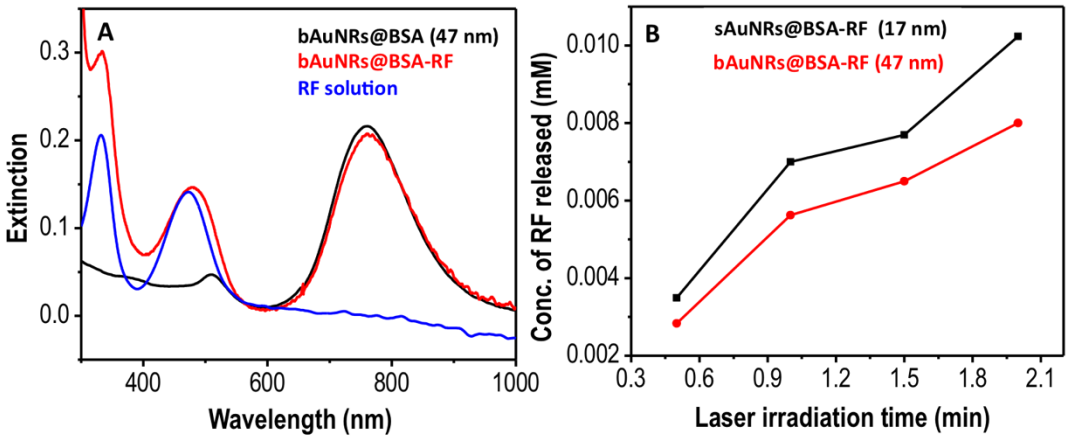

Figure 2-7 Conjugation gold nanoparticles with RF

(A) Absorption spectra of BSA-conjugated bAuNR after binding with RF (red trace). Spectra correspond to bare bAuNR (black trace) and RF (blue trace) is also given. (B) Plots showing the release of RF (function of laser exposure time) from bAuNRs@BSA-RF (red trace) and sAuNRs@BSA-RF (black trace).

Cellular uptake of bAuNRs was monitored using dark field microscopy as function of time. Interestingly, we found that the amount as well as the rate of endocytosis of nanoparticles was substantially high, when it was introduced along with the RF-loaded nanoparticles. The schematic showing the enhanced uptake of nanorods in presence of RF-loaded nanorods is shown in **Figure 2-8A**. Here, the human squamous carcinoma (HSC) cells were incubated with a 19:1 solution of 0.1 nM of bAuNRs@BSA@RGD solution and 0.1 nM of RF-loaded Au nanorods (bAuNRs@BSA-RF@RGD). Figure 3B-D shows the

dark-field images of the HSC cells, treated with only 0.1 nM bAuNRs@BSA@RGD, collected at 0.5, 2, and 24 h, respectively. Similarly, the dark-field images of the HSC cells, treated with 19:1 solution of 0.1 nM bAuNRs@BSA@RGD and bAuNRs@BSA-RF@RGD (0.1 nM) collected at 0.5, 2, and 24 h is shown in Fig. 3E-G, respectively. The experiment was conducted by keeping the amount of AuNRs constant in each experiment. We did not use sAuNRs for this study as the scattering due to the sAuNRs were very negligible, hence we could not image under the dark field microscope, effectively. Even after 30 min of cell uptake study, the cells exposed with bAuNRs in presence of 5% of RF-loaded bAuNRs showed remarkably high uptake compared to the experiment conducted in the absence of RF-loaded bAuNRs. This was very clear from the dark field images (Figure 2-8). The enhancement in the efficiency of plasmonic chemotherapy by using RF-loaded AuNRs was further confirmed by conducting various cell viability experiments (see later). The capability of RF in enhancing the endocytosis of nanoparticles can be attributed to the chemo-sensitizing activity [23, 34, 35] of RF by down regulating the activity of multi-drug resistant plasma membrane protein (P-glycoprotein).

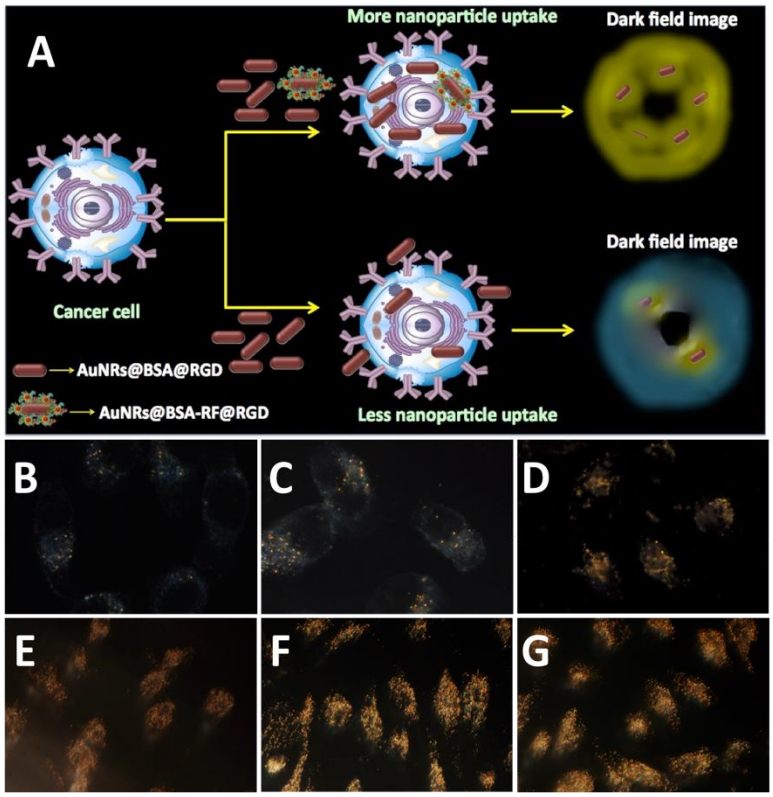

Figure 2-8: Endocytosis of AuNRs

(A) Schematic showing higher uptake of conjugated AuNRs in presence of RF conjugated nanorods (B-D) Dark field images of HSC cells collected at 0.5, 2, and 24 h, respectively during the uptake of AuNRs@BSA@RGD. (E-G) Dark field images of HSC cells collected at 0.5, 2, and 24 h, respectively during uptake of AuNRs@BSA@RGD (0.1 nM) along with 5% of AuNRs@BSA-RF@RGD (0.1 nM).

The cell viability studies clearly showed a distinct decrease in the percentage of viability (~30%) for the HSC cells exposed to laser (808 nm) for 2 min in presence of 19:1 solution of bAuNRs@BSA@RGD (0.1 nM) and bAuNRs@BSA-RF@RGD (0.1 nM). At the same time, the viability was around 80% during the laser exposure in the absence of RF-loaded bAuNRs (**Figure 2-9A**). The higher killing efficiency in the former case is attributed to the higher internalization of AuNRs to the cancer cells by the influence of RF-loaded nanorods and subsequent enhancement in the resultant heat generated inside the medium during the laser exposure. Among the nanorods, sAuNRs exhibited higher efficiency in killing the

cancer cells (viability~20%), when exposed to laser in presence of RF-loaded nanorods (Figure 2-4B).

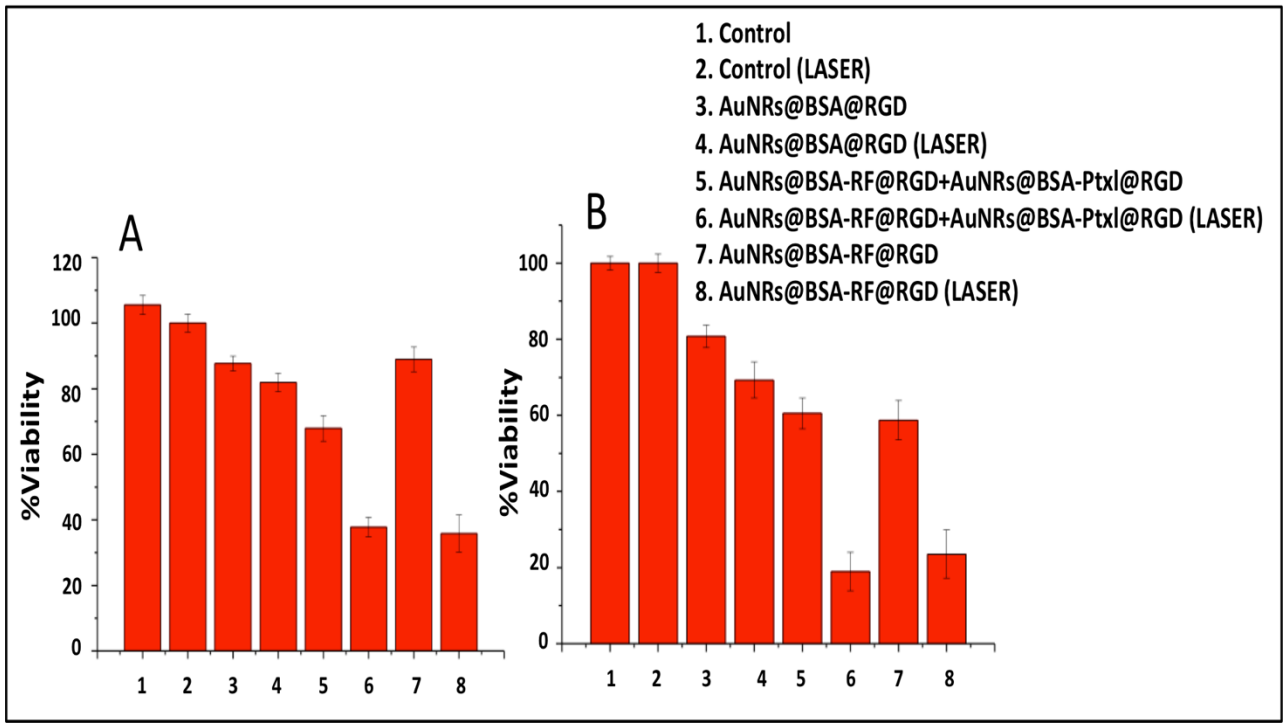

Figure 2-9 Cell viability results for exposure of HSC cells to 0.1 nM of AuNRs solutions of different sizes and functionalities

(A) For bAuNRs and (B) for sAuNRs. The amount of AuNRs in each case was made constant. Different AuNRs solutions used for the experiments are also given in panel B.

In absence of RF-loaded nanorods, the viability was nearly 70%. In AuNRs, due to the higher absorbance, the generation of net heat was very high (from 27 ^{0}C to 82±0.5 ^{0}C) compared to bAuNRs (from 27 ^{0}C to 65±0.5 ^{0}C). Similarly, the viability was very low (28%) when the Ptxl-loaded nanorods (AuNRs@BSA-Ptxl@RGD) were used. This reduction in the viability has been attributed to the photothermal effect as well as the chemotherapeutic nature of Ptxl-loaded nanorods. The viability was very low in sAuNRs

(18%) compared to bAuNRs (30%) (**Figure 2-9B**), which further confirms the higher photothermal efficiency of sAuNRs.

2.2.4 Conclusion and Future Outlook

We developed a novel multifunctional gold nanoparticle-based drug delivery platform capable of enhancing the internalization of drug-loaded nanoparticles more effectively into the cancer cells. This was achieved by introducing trace amount of rifampicin-loaded Au nanoparticles into the cancer cells along with the drug-loaded nanoparticles. Fast and enhanced internalization of nanoparticles inside the cells during this approach was probed by using darkfield microscopy. A range of cell viability studies has demonstrated the advantages of this approach over conventional plasmonic chemotherapy. The current method has greater impact in prospect of conquering new avenues in bypassing multidrug resistance in various cancer cells thereby to decrease the demand on the overall concentration gold NPs needed for plasmonic chemotherapy.

2.2.5 References

1. Ali, M. R. K., Panikkanvalappil, S.R., El-Sayed, M. A. (2014) Enhancing the Efficiency of Gold Nanoparticles Treatment of Cancer by Increasing Their Rate of Endocytosis and Cell Accumulation Using Rifampicin. *Journal of the American Chemical Society* 136, 4464-4467.
2. Wang, A. Z., Langer, R., Farokhzad, O. C. (2012) Nanoparticle Delivery of Cancer Drugs. *Annual Review of Medicine* 63,185-198.

3. Chow, E. K., *et al.* (2011) Nanodiamond Therapeutic Delivery Agents Mediate Enhanced Chemoresistant Tumor Treatment. *Science Translational Medicine* 3, 73ra21.

4. Dreaden, E. C., El-Sayed, M. A. (2012) Detecting and Destroying Cancer Cells in More than One Way with Noble Metals and Different Confinement Properties on the Nanoscale. *Accounts Chem Res* 45,1854-1865.

5. Panikkanvalappil, S. R., Mackey, M. A., El-Sayed, M. A. (2013) Probing the Unique Dehydration-Induced Structural Modifications in Cancer Cell DNA Using Surface Enhanced Raman Spectroscopy. *Journal of the American Chemical Society* 135(12):4815-4821.

6. Panikkanvalappil, S. R., Mahmoud, M. A., Mackey, M. A., El-Sayed, M. A. (2013) Surface-Enhanced Raman Spectroscopy for Real-Time Monitoring of Reactive Oxygen Species-Induced DNA Damage and Its Prevention by Platinum Nanoparticles. *ACS Nano*.

7. Dreaden, E. C., Mackey, M. A., Huang, X., Kang, B., El-Sayed, M. A. (2011) Beating cancer in multiple ways using nanogold. *Chemical Society Reviews* 40(7):3391-3404.

8. Davis, M. E., Chen, Z., Shin, D. M. (2008) Nanoparticle therapeutics: an emerging treatment modality for cancer. *Nat Rev Drug Discov* 7, 771-782.

9. Dykman, L., Khlebtsov, N. (2012) Gold nanoparticles in biomedical applications: recent advances and perspectives. *Chemical Society Reviews* 41, 2256-2282.

10. Szakacs, G., Paterson, J. K., Ludwig, J. A., Booth-Genthe, C., Gottesman, M. M. (2006) Targeting multidrug resistance in cancer. *Nat Rev Drug Discov* 5, 219-234.

11. Persidis, A. (1999) Cancer multidrug resistance. *Nat Biotechnol* 17, 94-95.

12. Wang, F., *et al.* (2011) Doxorubicin-Tethered Responsive Gold Nanoparticles Facilitate Intracellular Drug Delivery for Overcoming Multidrug Resistance in Cancer Cells. *ACS Nano* 5, 3679-3692.

13. Dreaden, E. C., Austin, L. A., Mackey, M. A., El-Sayed, M. A. (2012) Size matters: gold nanoparticles in targeted cancer drug delivery. *Therapeutic Delivery* 3, 457-478.

14. Mackowiak, S. A., *et al.* (2013) Targeted Drug Delivery in Cancer Cells with Red-Light Photoactivated Mesoporous Silica Nanoparticles. *Nano Letters* 13, 2576-2583.

15. Shen, Y., *et al.* (2010) Prodrugs Forming High Drug Loading Multifunctional Nanocapsules for Intracellular Cancer Drug Delivery. *Journal of the American Chemical Society* 132, 4259-4265.

16. MaHam, A., Tang, Z., Wu, H., Wang, J., Lin, Y. (2009) Protein-Based Nanomedicine Platforms for Drug Delivery. *Small* 5, 1706-1721.

17. Au, K. M., Armes, S. P. (2012) Heterocoagulation as a Facile Route To Prepare Stable Serum Albumin-Nanoparticle Conjugates for Biomedical Applications: Synthetic Protocols and Mechanistic Insights. *ACS Nano* 6, 8261-8279.

18. Lukianova-Hleb, E. Y., Ren, X., Zasadzinski, J. A., Wu, X., Lapotko, D. O. (2012) Plasmonic Nanobubbles Enhance Efficacy and Selectivity of Chemotherapy Against Drug-Resistant Cancer Cells. *Advanced Materials* 24, 3831-3837.

19. Ren, F., *et al.* (2013) Gold Nanorods Carrying Paclitaxel for Photothermal-Chemotherapy of Cancer. *Bioconjugate Chemistry* 24, 376-386.

20. Zheng, M., *et al.* (2013) Single-Step Assembly of DOX/ICG Loaded Lipid–Polymer Nanoparticles for Highly Effective Chemo-photothermal Combination Therapy. *ACS Nano* 7, 2056-2067.

21. Dickerson, E. B., *et al.* (2008) Gold nanorod assisted near-infrared plasmonic photothermal therapy (PPTT) of squamous cell carcinoma in mice. *Cancer Letters* 269, 57-66.

22. Kim, H. S, Min, Y. D, Choi, C. H. (2001) Double-Edged Sword of Chemosensitizer: Increase of Multidrug Resistance Protein (MRP) in Leukemic Cells by an MRP Inhibitor Probenecid. *Biochemical and Biophysical Research Communications* 283, 64-71.

23. Courtois, A., *et al.* (1999) Inhibition of multidrug resistance-associated protein (MRP) activity by rifampicin in human multidrug-resistant lung tumor cells. *Cancer Letters* 139, 97-104.

24. Khullar, P., *et al.* (2012) Bovine Serum Albumin Bioconjugated Gold Nanoparticles: Synthesis, Hemolysis, and Cytotoxicity toward Cancer Cell Lines. *The Journal of Physical Chemistry C* 116, 8834-8843.

25. Dominguez-Medina, S., Blankenburg, J., Olson, J., Landes, C. F., Link, S. (2013) Adsorption of a Protein Monolayer via Hydrophobic Interactions Prevents Nanoparticle Aggregation under Harsh Environmental Conditions. *ACS Sustainable Chemistry & Engineering*.

26. Ali, M. R. K., Snyder, B., El-Sayed, M. A. (2012) Synthesis and Optical Properties of Small Au Nanorods Using a Seedless Growth Technique. *Langmuir* 28, 9807-9815.

27. Nikoobakht, B., El-Sayed, M. A. (2003) Preparation and Growth Mechanism of Gold Nanorods (NRs) Using Seed-Mediated Growth Method. *Chemistry of Materials* 15, 1957-1962.

28. Turkevich J, Stevenson PC, & Hillier J (1951) A study of the nucleation and growth processes in the synthesis of colloidal gold. *Discussions of the Faraday Society* 11, 55-75.

29. Kumar KP & Chatterji D (1990) Resonance energy transfer study on the proximity relationship between the GTP binding site and the rifampicin binding site of Escherichia coli RNA polymerase. *Biochemistry* 29, 317-322.

30. Yu O-Y, Cheng Y-F, Huang S-Y, Bai A-M, & Hu Y-J (2011) Probing the Binding of Rifampicin to Bovine Serum Albumin in Aqueous Solution. *J Solution Chem* 40, 1711-1723.

31. Kamat, B., Seetharamappa, J. (2005) Mechanism of interaction of vincristine sulphate and rifampicin with bovine serum albumin: A spectroscopic study. *J Chem Sci* 117, 649-655.

32. Agudelo, D., *et al.* (2012) Probing the Binding Sites of Antibiotic Drugs Doxorubicin and <italic>N</italic>-(trifluoroacetyl) Doxorubicin with Human and Bovine Serum Albumins. *PLoS ONE* 7, e43814.

33. Howes, B. D., *et al.* (2007) The influence of pH and anions on the adsorption mechanism of rifampicin on silver colloids. *Journal of Raman Spectroscopy* 38, 859-864.

34. Fardel, O., Lecureur, V., Loyer, P., Guillouzo, A. (1995) Rifampicin enhances anti-cancer drug accumulation and activity in multidrug-resistant cells. *Biochemical Pharmacology* 49, 1255-1260.

35. Shichiri, M., Fukai, N., Kono, Y., Tanaka, Y. (2009) Rifampicin as an Oral Angiogenesis Inhibitor Targeting Hepatic Cancers. *Cancer Research* 69, 4760-4768.

2.3 Targeting Heat Shock Protein 70 using Gold Nanorods Enhances Cancer Cell Apoptosis in Low Dose Plasmonic Photothermal Therapy [1]

Plasmonic photothermal therapy (PPTT) is a promising cancer treatment where plasmonic nanoparticles are used to convert near infrared light to localized heat to cause cell death, mainly via apoptosis and necrosis. Modulating PPTT to induce cell apoptosis is more favorable than necrosis. Herein, we used a mild treatment condition using gold nanorods (AuNRs) to trigger apoptosis and tested how different cell lines responded to it. Three different cancer cell lines of epithelial origin: HSC (oral), MCF-7 (breast) and Huh7.5 (liver) had comparable AuNRs uptake and were heated to same environmental temperature (under 50^{o}C). However, Huh7.5 cells displayed a significant increase in cell apoptosis after PPTT as compared to the other two cell lines. As HSP70 is known to increase cellular resistance to heat, we determined relative HSP70 levels in these cells and results indicated that Huh7.5 cells had ten-fold decreased levels of HSP70 as compared with HSC and MCF-7 cells. We then down-regulated HSP70 with a siRNA and observed that all three cell lines displayed significant reduction in viability and an increase in apoptosis after PPTT. As an enhancement to PPTT, we conjugated AuNRs with Quercetin, an inhibitor of HSP70 which displayed anti-cancer effects via apoptosis.

2.3.1 Introduction

In the last decade, many publications associated with the use of gold nanorods (AuNRs) in plasmonic photothermal therapy (PPTT) have shown great promise for combating cancer [2-4]. PPTT relies on the principle that AuNRs show distinct physicochemical properties

compared to other gold nanoparticles [5-7]. AuNRs absorb near infrared light and convert it into heat rapidly and efficiently by non-radioactive processes, including electron-electron and electron-photon interactions [8-11]. Thus, when AuNRs are targeted to cancer cells, electromagnetic irradiation with an optical laser induces enough heat to selectively destroy cancerous cells [12-16].

PPTT causes cancer cell death mainly via necrosis and apoptosis [17, 18]. One of the main challenges in PPTT is the overheating caused by large dose of nanoparticles or laser exposure, which can easily cause necrosis. During necrosis the plasma membrane is broken causing cytoplasmic components to leak out and inflammation which is known to induce metastasis and cancer growth [19-21]. Additionally, the overheating could hurt the neighboring healthy cells. On the other hand, PPTT induced apoptosis occurs through a programming cell death, which does not cause inflammation [22]. Therefore, developing a new strategy targeting cancer cell apoptosis and avoiding necrosis would be of great importance for the next generation of PPTT.

It has been reported that different intracellular locations of AuNRs or laser strength regulate the switch between necrosis and apoptosis in PPTT [13, 23]. However, lower heating would decrease the efficacy of PPTT, and might not be very effective for cells that exhibit thermo-resistance. Therefore, it is important to know the major players that contribute to thermo-resistance. Based on this, we can develop new PPTT strategies that prevent the thermo-resistance and enhance apoptosis. Many factors could contribute to thermo-resistance such as: the inhibition of cell death signals, inhibition of endocytosis or increased exocytosis of nanoparticles [17, 18]. Heat induced apoptosis can also be resisted by a class of proteins called Heat Shock Proteins (HSPs) [24-27]. When binding to

denatured proteins or partially unfolded intermediates, HSPs prevent their aggregation and initiate protein refolding [28, 29]. Interestingly, PPTT induces the expression of most HSPs [30-32], and multiple studies have shown the importance of the HSP in enabling cancer cells to resist heat-induced apoptosis [33-38]. However, the specificity of these inhibitors to individual heat shock proteins has not been tested [36].

As HSP70 inhibits cell apoptosis directly by preventing the cytochrome c/dATP-mediated caspase activation [39] and binds with multiple other HSPs to mediate protein refolding [30], we conducted PPTT on multiple cell lines and positively correlated HSP70 levels with PPTT response. We then used siRNA to remove HSP70 and observed an enhancement in PPTT. These results led us to fabricate novel HSP70 inhibitor (Quercetin) conjugated AuNRs and compared to non-conjugated AuNRs, the new conjugate displayed a superior ability to combat thermo-resistance, causing a higher percentage of cells to undergo apoptosis. Therefore, AuNRs act as integrally in delivering of Quercetin to cancer cells as well as acting as an inducer of apoptosis-associated PPTT.

2.3.2 Experimental Methods

2.3.2.1 Cell Culture and Transfections

HSC (human squamous carcinoma), MCF-7 (human breast cancer) and Huh7.5 (human hepatocellular carcinoma) cells were cultured in Dulbecco's modified Eagles' medium (Mediatech) supplemented with 10% fetal bovine serum (Mediatech) and 1% antibiotic

antimycotic solution (Mediatech). Lipofectamine 2000 (Invitrogen) was used for siRNA transfections per the manufacturer's protocol. The following siRNAs (Sigma-Aldrich) were used: control (SASI_HS SIC001) and HSP70 (GCCUUUCCAAGAUUGCUGU). The siRNA control was a sequence that had no homology to any human gene. Cells were incubated with the siRNA for two days before incubating cells with AuNRs.

2.3.2.2 Preparation of AuNRs and Conjugation with different surface modifications

AuNRs were prepared similarly as previously described. [7, 37] Specifically, AuNRs were synthesized by a seedless growth technique where the growth solution was prepared at 25-30°C. Briefly, 5 mL of 1.0 mM $HAuCl_4$ was added to 5 mL 0.20M cetyltrimethylammonium bromide. Then 250 μL of 4.0 mM AgNO3 250 μL was added and the solution was gently shaken. 8 μL of 37% HCl was then added to obtain a pH of 1-1.15. Next, 70 μL of 78.8 mM ascorbic acid was added to the solution with gentle shaking until the solution was clear. 15 μL of 0.01M ice-cold NaBH4 was injected immediately to the unstirred growth solution and allowed to react for six hours. The resulting gold AuNRs had dimensions of 25 × 5.5 nm, aspect ratio of approximately 4.5, and longitudinal plasmon absorption ~ 800 nm [7]. The solution was centrifuged for 15 min at 14 500 RPM and the supernatant was removed. The resulting precipitate was suspended in water and centrifuged at the same speed and time. To conjugate the AuNRs with BSA, 50 mL of 0.5 mM bovine serum albumin (Sigma-Aldrich, USA) into a 1 nM nanoparticles solution and then incubated for 10 hours at room temperature. The excess BSA was removed from the nanoparticle solution by centrifugation. To this solution, 1 mL of 5 mM RGD

(CGPDGRDGRDGRDGR) (Genscript) solution was added. To conjugate rifampicin (RF) to AuNRs, 5 mL of 5 mM RF (Sigma-Aldrich) was added to the solution containing 50 mL of 1 nM AuNRs. The resulting solution was gently shaken and incubated for 5 hours. The resultant BSA+RF-RGD conjugated nanoparticles (AuNRs) were centrifuged to remove unbound RF molecule. [37] To conjugate Quercetin (QE) to AuNRs, 5 mL of 5 mM QE (Sigma-Aldrich) was added to the solution containing 50 mL of 1 nM AuNRs. The resulting solution was gently shaken and incubated for 5 hours. The resultant BSA-QE-RGD conjugated AuNRs were centrifuged to remove unbound QE molecule. To determine if the QE release from the surface of the AuNRs after laser irradiation or not; 1 nM of the AuNRs@ QE in solution has been irradiates exposed to a near Infra-red (NIR) CW laser (808 nm, M2W dragon laser) at 5.8 W / cm^2 for 2 minutes with a spot size of approximately 5.6 mm. Then we separated the AuNRs from the supernatant using centrifugation (15 min at 14 500 RPM). Both the supernatant and the pellet were examined using UV-Vis spectrometer.

2.3.2.3 TEM, Fluorimetry and UV-vis and zeta potential Measurements

UV-vis absorption measurements were carried out using a Cary 500 UV−vis spectrometer, while the transmission electron microscopic (TEM) images were taken on a JEOL 100CX-2 microscope and the average diameter was determined using Image J software. Excitation and emission measurements were carried out using a Quanta Master™ 300 — Phosphorescence/Fluorescence Spectrofluorometer. For quenching experiments

BSA was used at the concentration of 10^{-4} M). Zeta potentials were measured by a ZetaSizer 3000 (Malvern Instruments).

2.3.2.4 Measurement of AuNRs Endocytosis

Cell lines were grown until 60-70% confluence in 12-well dishes and then treated with AuNRs for 24 hours. The supernatant was then removed and the intensity of the AuNRs for the three cell lines was measured using Cary 500 UV−vis spectrometer, the calculations established by subtracting the intensity of the supernatant from the AuNRs before endocytosis.

2.3.2.5 Plasmonic Photothermal Therapy (PPTT)

Cells were plated on either 96 or 12 well tissue culture plates and incubated for 24 hours [48]. The culture medium was then removed and replaced with culture medium containing the conjugated nanoparticles and the left in DMEM containing 2.5 nM AuNRs. Afterwards, each sample was exposed to a near Infra-red (NIR) cw laser (808 nm, M2W dragon laser) at 5.8 W / cm^2, for 2 minutes with a spot size of approximately 5.6 mm.

2.3.2.6 Apoptosis/Necrosis Assay

Cells were washed with PBS and then trypsinized (Clonetech). [39] After trypsinization cells were subsequently centrifuged and washed with PBS. Cells were then resuspended in

493 µL 1x Annexin binding buffer (Invitrogen) with 2 µL working Propidium Iodine PI (BioLegend) and 5 µL Annexin-V-FITC (BioLegend) before being incubated at room temperature for 15 minutes. Cells were then filtered and subjected to flow cytometry using a BSR LSR II flow cytometer (BD Biosciences). Samples were excited with a 488-nm laser, and FITC was detected in FL-1 by a 525/30 BP filter while PI was detected in FL-2 by a 575/30 BP filter. FlowJo software (Tree Star Inc.) was used to count Annexin V+ cells from at least 10000 events.

2.3.2.7 Cell Viability Assay:

Cells were washed with PBS and then an XTT assay was performed per the manufacturer's protocol (Biotium). A Biotek Synergabsoy H4 multi-mode plate reader measured the intensity of orange formazan that viable cells produce.

2.3.2.8 Immunoblots:

Cells were lysed in RIPA (20 mM Tris pH 7.4, 150 mM NaCl, 2 mM EDTA, 2 mM EGTA, 0.1% Sodium Deoxycholate, 1% Triton X-100, 0.1% SDS) supplemented with protease inhibitors (Sigma-Aldrich). [51] Post-nuclear supernates were subjected to a BCA assay (Pierce) and equal amounts of protein were loaded on a SDS-PAGE gel. After SDS-PAGE, resulting gels were transferred to PVDF membranes (Millipore) overnight and then blocked with 5% milk in TBS (20 mM Tris 150 mM NaCl). A rat monoclonal (6B3) antibody to HSP70 was used as the primary antibody (Cell Signaling). A goat anti rat HRP

labeled antibody was used as the secondary antibody (Jackson Immuno Research Laboratories). Blots were washed 3 times in TBS after primary and secondary antibodies. Hyglo enhanced chemiluminescence (Denville) and a Konica Minolta developer were used to develop the immunoblots.

2.3.2.9 Immunofluorescence Labeling and Confocal Microscopy:

Cells were plated on 8 well chamber slides (Fisher). After siRNA and PPTT treatment cells were fixed in 4% Paraformaldehyde for 20 mins at room temperature. Cells were then permeabilized with 0.1% Triton X-100 for 5 minutes at room temperature. Cells were then blocked with 5% BSA and incubated with the same primary antibody as stated in the immunoblot method. Cells were then incubated for 1 hour with an Alexa Fluor donkey anti rat 488 secondary antibody (Invitrogen) for 1 hour before mounting with Prolong Gold (Invitrogen). Lastly images were taken with a Zeiss LSM 700-405 confocal microscope and the fluorescence intensity was quantified in Image J.

2.3.2.10 Statistics:

The statistical significance was determined by a t-test calculator (Graph Pad Software, Inc.). A z test was used for control-normalized experiments.

2.3.3 Results and Discussion

To better define which cancers might be best treated with PPTT and to determine if and how PPTT displays effectiveness against different cancer types, we created nanorods (AuNRs) using a novel technique [8, 40]. We performed transmission electron microscopy (TEM) to determine the quality and homogeneity. These AuNRs were uniformly shaped (**Figure 2-10a**) with an approximate length and width of 25 ± 3 nm × 5.5 ± 0.8 nm (**Figure A.9. a, b**). Additionally, these AuNRs displayed an excitation at 800 nm (**Figure 2-10b**). AuNRs were then conjugated with bovine serum albumin (BSA), to block nonspecific interactions, arginylglycylaspartic acid (RGD) to enable integrin-mediated endocytosis, and Rifampicin (RF), an inhibitor of drug exocytosis [40]. To confirm conjugation with RF we measured the absorption spectra of AuNRs before and after conjugation with RF. AuNRs conjugated only with BSA absorb at 530 nm and 800 nm **(Figure 2-10b)**. RF alone has two absorption wavelengths: 330 nm and 470 nm (**Figure 2-10b**). When the AuNRs were conjugated with RF two new peaks appeared at the same absorption wavelength as RF, suggesting a successful conjugation with RF [40]. The effectiveness of these AuNRs was then tested on three different cancer cell lines: HSC (human squamous carcinoma), MCF-7 (human breast cancer) and Huh7.5 (human hepatocellular carcinoma) cells. To ensure each cell line endocytosed similar amounts of AuNRs the absorbance of the AuNRs in the media before and after PPTT was measured by ultraviolet-visual spectroscopy (UV-vis). We observed a similar loss in AuNR absorbance from the media in all three cell lines before laser treatment, suggesting that all three cell lines endocytosed similar amounts of AuNRs (**Figure 2-10c**). When performing PPTT we chose an 808 nm laser with a power of 5.8 W / cm^2 for duration of 2 minutes. The duration and strength of these laser settings

have been shown not to harm cells in culture [10, 11, 39-43]. Under these laser settings we observed that the media from all three cell lines consistently reached approximately 50°C after PPTT treatment as measured by a hypodermic thermocouple.

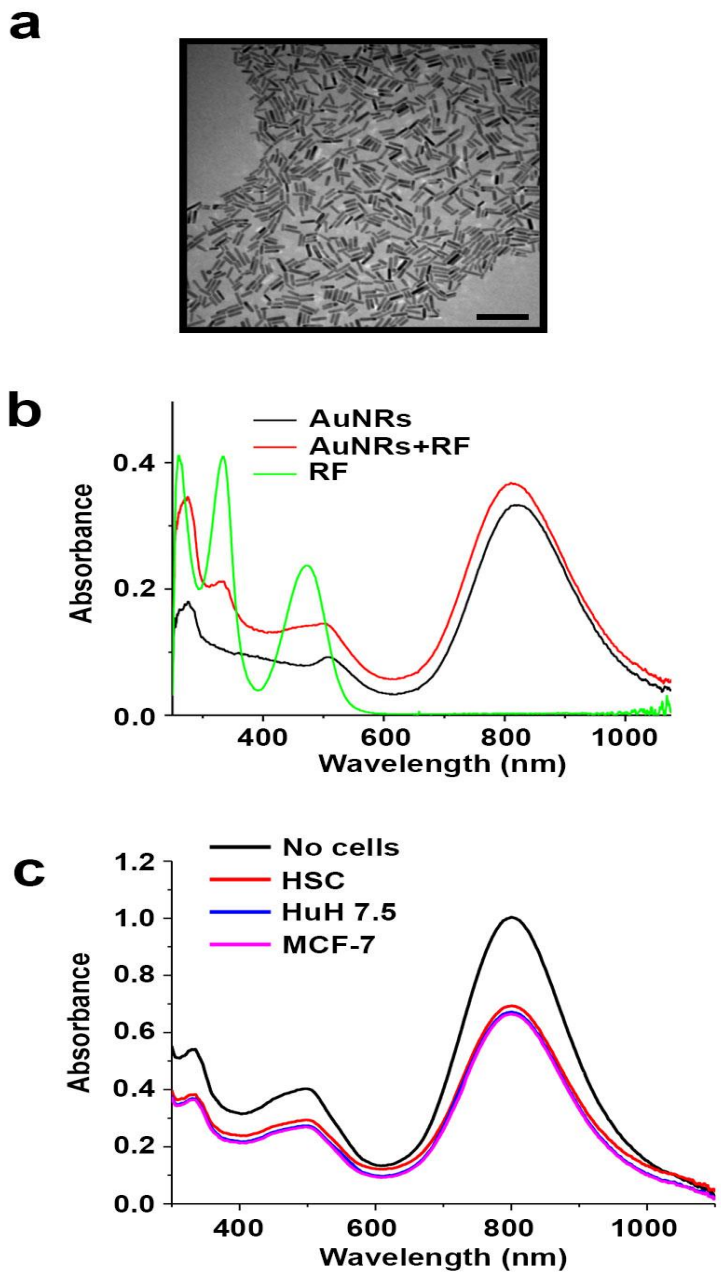

Figure 2-10 . Characterization of conjugated AuNRs and measurement AuNRs of endocytosis

(A) Transmission Electron Microscopic (TEM) image of conjugated nanorods (AuNRs). Scale bar = 100 nm. (B) UV-vis absorption spectra of the unconjugated AuNRs or the nanorods conjugated with Rifampicin (AuNRs+RF-RGD). (C) The UV-vis spectra for the AuNRs in cell culture media before and after incubation with HSC (human squamous carcinoma), MCF-7 (human breast cancer) and Huh7.5 (human hepatocellular carcinoma) cells for 24 hours.

Noticing no differences in the amount of AuNRs uptake or temperature of the media we used two different methods to measure the effectiveness of PPTT. To measure apoptosis and necrosis we labeled cells with Annexin V and propidium iodide and then performed flow cytometry. Similar percentages of apoptotic cells (AnnexinV+) were observed between AuNR treated without laser and AuNR with laser treated HSC and MCF-7 cells **(Figure 2-11a)**. However, PPTT treated Huh7.5 cells displayed a significant increase in apoptosis after PPTT as compared to HSC and MCF-7 cells. We did not observe propdidium iodide staining under any conditions suggesting necrosis was not occurring (**Figure A. 10. a**), as has been previously observed for other cell lines [44]. To measure the effectiveness of PPTT by another method we performed an XTT assay. All three cell lines displayed similar levels of cell viability without laser treatment after AuNRs treatment, indicating the AuNRs alone were not toxic to the cells. Consistent with the flow cytometry data Huh7.5 cells were significantly less viable than HSC or MCF-7 cells after PPTT **(Figure 2-11b)**.

Next we wanted to determine if the differences in cell viability and apoptosis after PPTT observed between cancer cell lines could be explained by differences in protein composition. As Heat Shock Proteins (HSPs) are known to enable cells to resist temperature-induced apoptosis [25, 45, 46], and PPTT can induce apoptosis, we hypothesized that the increased efficacy of PPTT against Huh7.5 cells could be explained

by differences in HSP levels. We first tested and chose to focus on HSP70 as HSP70 is the major heat shock protein in mammalian cells as it complexes with both HSP40 and HSP90 to refold denatured proteins [47-49]. Immunoblots of HSP70 from cells treated with AuNRs with or without laser treatment demonstrate that MCF-7 and HSC cells have similar amounts of HSP70 in relation to a loading control, actin **(Figure 2-11c)**. However, with and without laser treatment Huh7.5 cells have greater than 10-fold less HSP70 than MCF-7 and HSC cells. We also observed a 2-fold decrease in HSP70 protein levels in MCF-7 cells after PPTT treatment and a modest 10 percent decrease in HSP70 protein levels in HSC cells after PPTT. These results suggest that the level of HSP70 impacts the mechanism of cellular thermos-resistance to PPTT.

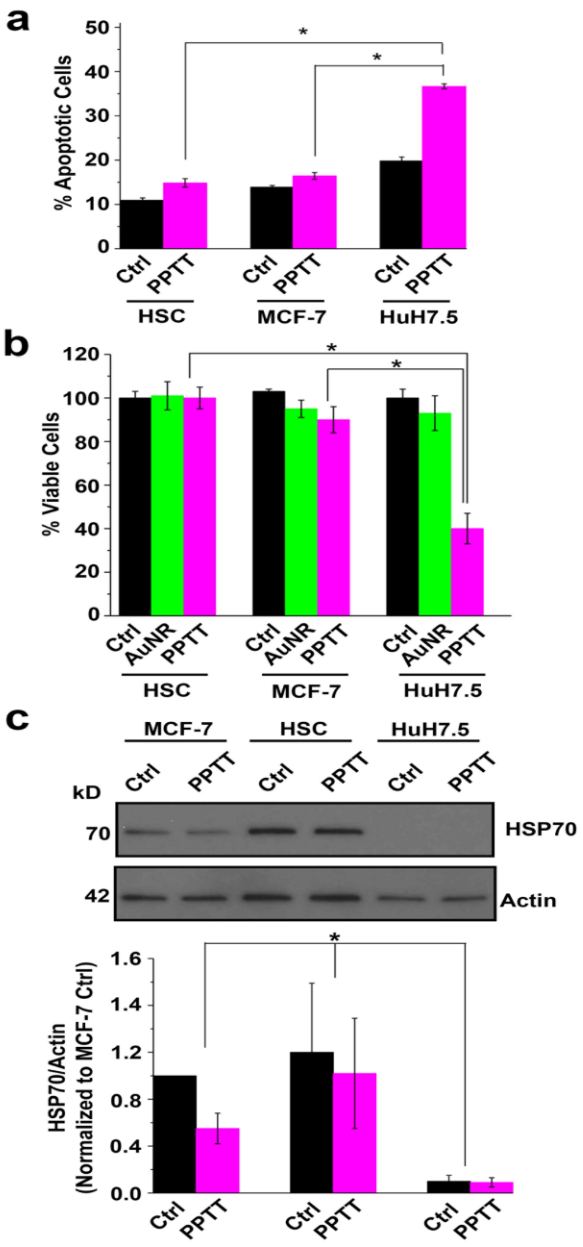

Figure 2-11. Huh7.5 cells have less HSP70 and are more susceptible to cell death following PPTT than MCF-7 or HSC cells

(A) Histograms were generated from flow cytometry data of Annexin V+ Huh7.5 (human hepatocellular carcinoma), MCF-7 (human breast cancer) or HSC (human squamous carcinoma) cells with (PPTT) and without (Ctrl) laser treatment. Mean±SEM. * p<0.05 (B) Cell viability results from an XTT assay data performed on cells treated with laser but no AuNRs (Ctrl), with AuNRs but no laser (AuNR) or with AuNRs and laser treatment (PPTT). Mean±SEM. * p<0.05 (C) The relative amounts of HSP70 in all three cell lines with and without laser treatment was determined by immunoblotting. Error bars are presented as the Mean±SEM. * p<0.05.

There are many methods to determine if HSP70 levels play a role in the efficacy of PPTT including: down-regulation, overexpression or small molecule inhibitors. Since transient overexpression experiments can lead to non-specific effects such as decreased cell viability due to sequestering of translational machinery and protein overcrowding [50], we first chose to down-regulate HSP70 with an siRNA, confirm protein loss by immunofluorescence microscopy and then determine cell viability. After siRNA treatment, HSP70 was immunolabeled and then confocal microscopy was performed. All control siRNA treated cell lines displayed a cytoplasmic distribution of HSP70 and a 89% and 93% loss of signal was seen in HSC and MCF-7 cells after siRNA treatment, respectively **(Figure 2-12a)**. Confirming immunoblot results, the relative amount of HSP70 between control siRNA treated Huh7.5 cells was decreased as compared to control siRNA treated MCF-7 and HSC cells. Again, we used flow cytometry to measure the percentage of cells undergoing apoptosis (Annexin V+). The percentage of MCF-7 cells treated with the HSP70 siRNA undergoing apoptosis increased 1.8-fold compared to the siRNA control **(Figure 2-12b)**. Huh7.5 cells treated with the HSP70 siRNA exhibited slight but significant increases in apoptosis as compared to control siRNA treated cells, however 80% of Huh7.5 control siRNA treated cells were already undergoing apoptosis after PPTT. We did not observe any differences in apoptosis between control siRNA treated cells after laser treatment and HSP70 siRNA without laser treatment. Additionally, we did not observe any increases in the percentage of cells undergoing necrosis in siRNA treated cells (**Figure A.10.b.**). We again used the XTT cell viability assay as another measurement of PPTT effectiveness. The percentage of viable cells treated with the HSP70 siRNA as compared to control siRNA treated cells decreased 25% for HSC and MCF-7 cells **(c)**. While Huh7.5

cells treated with the HSP70 siRNA were only 10% less viable, the control siRNA cells after laser treatment were only 30% viable. Similar to the apoptosis assay we did not observe any differences in cell viability between control siRNA treated cells after laser treatment and HSP70 siRNA treated cells without laser treatment. These experiments show that specific loss of HSP70 enhances the efficacy of PPTT against multiple cancer cell lines. The remaining viability after loss of HSP70 and PPTT is likely due to the expression of other HSPs.

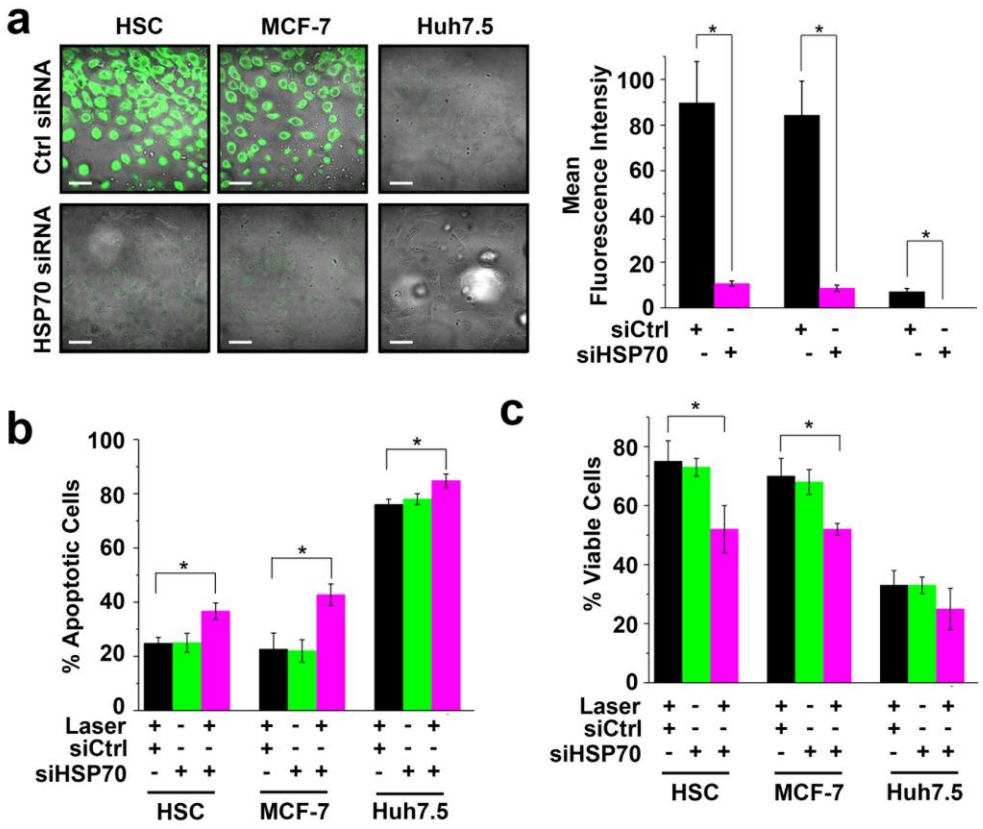

Figure 2-12. HSP70 regulates cell death in response to PPTT

(a) After immunolabeling HSP70, confocal microscopy was performed on HSC (human squamous carcinoma), MCF-7 (human breast cancer) and Huh7.5 (human hepatocellular carcinoma) cells treated with a control siRNA (Ctrl siRNA) or a HSP70 siRNA. Representative images and quantification are shown. Mean ± SD. *p < 0.05 (b) Histograms were generated from flowcytometry data of Annexin Vþcells after PPTT that werealso treated with a control siRNA (siCtrl) or a siRNA against HSP70 (siHSP70). Error bars are presented as the Mean ± SEM. *p < 0.05 (c) Cell viability results from an XTT assay performed on siCtrl or siHSP70 treated cells. Error bars are presented as the Mean ± SEM. *p < 0.05

If HSP70 is essential for the resistance of cancers to PPTT then AuNRs conjugated with inhibitors to HSP70 would make PPTT more effective. As Quercetin (QE) has been shown to be a promising inhibitor of HSP70 [51, 52], we conjugated AuNRs with QE. To ensure conjugation we measured the absorbance of AuNRs with and without QE. QE alone absorbed at 370 nm **(**

Figure 2-13a). AuNRs alone did not show a peak at 370 nm before conjugation with QE, however after conjugation with QE AuNRs display a peak at 370 nm confirming QE conjugation to the AuNRs. Fluorimetry was also used to demonstrate QE attachment to BSA. BSA alone displays an excitation peak at 300 nm and emission peak at 360 nm. However, after conjugation with QE the emission intensity of BSA is dramatically decreased **(**

Figure 2-13b) (Figure A.11.b). Furthermore, confirming the stability of the BSA surface conjugation after the QE conjugation, BSA conjugated to the surface of the AuNRs still displayed a negative zeta potential after conjugation with QE **(table A.1.)**. We then tested the efficacy of QE conjugated AuNRs on cell viability and apoptosis after PPTT. After Annexin V labeling and performing flow cytometry on HSC cells we observed a significantly increased percentage of cells undergoing apoptosis when AuNRs were conjugated with QE as compared to without (

Figure 2-13c). We did not observe any differences in cells that did not receive AuNRs that received only laser treatment or received AuNRs but no laser. An XTT assay was used to measure cell viability in cells treated with AuNRs that were conjugated with and without QE. While HSC cells treated with AuNRs without QE had a 40% decrease in cell viability as compared to controls, HSC cells treated with AuNRs conjugated with QE displayed an 80% decrease in cell viability as compared to controls **(**

Figure 2-13d). We did not observe any loss or differences in viability in control cells that did not receive AuNRs, received only laser treatment or received AuNRs but no laser. These results suggest that AuNRs conjugated with HSP70 inhibitors enhance the efficacy

of PPTT. To test if QE is released from the AuNRs after PPTT we irradiated the particles in solution, centrifuged the AuNRs and compared the UV vis spectrum of AuNRs conjugated with QE and no laser treatment to both the supernatant and AuNRs after laser treatment. Like QE alone (

Figure 2-13a) the supernatants from QE conjugated AuNRs displays peaks at 270 nm and 370 nm (**figure A.11.b**). Additionally, the UV-vis spectrum of isolated AuNRs displayed a loss in the absorption wavelengths of QE after PPTT. These results suggest that after irradiation the AuNRs + QE, the QE is released from the AuNRs enabling it to inhibit HSP70 and enhance the efficacy of PPTT.

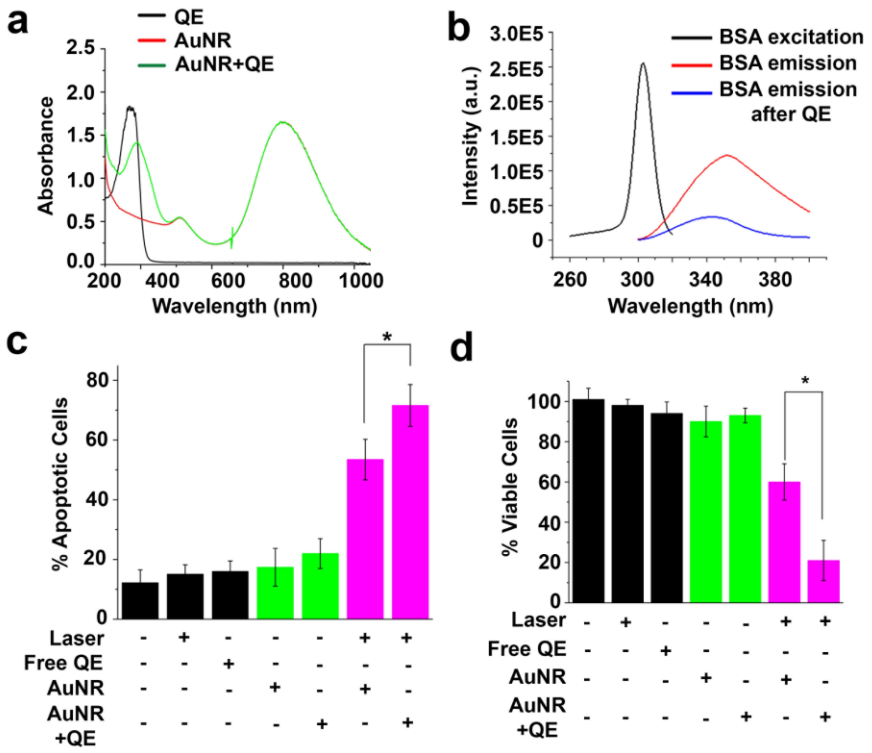

Figure 2-13. Conjugation with a HSP70 inhibitor makes AuNRs more efficient at PPTT

(A) UV-vis absorption spectra of AuNRs alone, AuNRs conjugated with Quercetin (QE), and QE only. (B) Excitation and emission spectra of BSA before and after addition of QE. (C) Histograms were generated from flow cytometry data of Annexin V+ HSC (human squamous carcinoma) cells under control conditions and with AuNRs conjugated to QE. Mean±SEM. * p<0.05 (d) Cell viability results from an XTT assay performed on HSC cells under control conditions and after treatments. Mean±SEM. * p<0.05

A better understanding of the molecular mechanisms of PPTT and optimization based on those findings represent the next steps in AuNR based cancer therapies. In PPTT AuNRs have the beneficial ability of being only active during laser treatment and have been seen to not display toxic effects otherwise (2, 39). Additionally, AuNRs are desirable as they can be easily conjugated with different molecules that could enhance their function. Previous studies from our lab have developed enhanced PPTT strategy by increasing the selectivity to target cancer cells, increasing cell uptake of nanoparticles by developing specific surface conjugation or developing new AuNRs size that has higher efficient in convert light energy into heat [39, 40, 53-55]. In this work, we sought to know more about the mechanism of thermotolerance in different cells and develop new strategy to enhance the PPTT-induced apoptosis.

PPTT either induces cell death via apoptosis or necrosis. High doses of heating (>50^{o}C) cause necrosis, which result in inflammation and is harmful to the neighboring healthy cells. On the other hand, lower temperature (<50^{o}C) mainly induces apoptosis, which is very favorable as programing cell death is a “clean” way to remove cancer cells [56]. Our main target is to only trigger apoptosis during PPTT. To accomplish apoptosis at lower temperatures, cellular mechanisms of thermo-resistance need to be bypassed.

We conducted PPTT in three different cell lines HSC, MCF-7 and Huh7.5 and correlated their response to PPTT to their HSP70 levels. HSP70 act as an upstream inhibitor to cell apoptosis by preventing cytochrome c/dATP-mediated caspase activation [37]. We observed that the less the initial HSP70 level, the higher percentage of cells underwent apoptosis after PPTT and reducing HSP70 protein levels enhanced apoptosis in all cell lines tested. We extended these results by conjugating AuNRs with a heat shock protein inhibitor that would sensitize cells to PPTT thereby promoting apoptosis as a non-inflammatory cancer cell death (**Figure 2-14)**. After demonstrating a successful AuNRs conjugation with an HSP70 inhibitor these new AuNRs were tested for their ability to enhance cancer cell apoptosis. Similar to siRNA based studies, HSP70 inhibitor conjugation enhanced the ability of AuNRs after PPTT.

Unlike adding HSP inhibitor directly onto cells, we used AuNRs as a drug delivery system. The AuNRs give an efficient delivery system to target drugs towards cancer cells as minor amounts of HSP inhibitor are present at the surface, eliminating side effects that a HSP inhibitor might cause to the non-cancerous cells. This strategy greatly enhanced the PPTT induced cell apoptosis *in vitro*. The extension of these results into *in vivo* models represents the next step to ablate cancers efficiently and with minimal side effects.

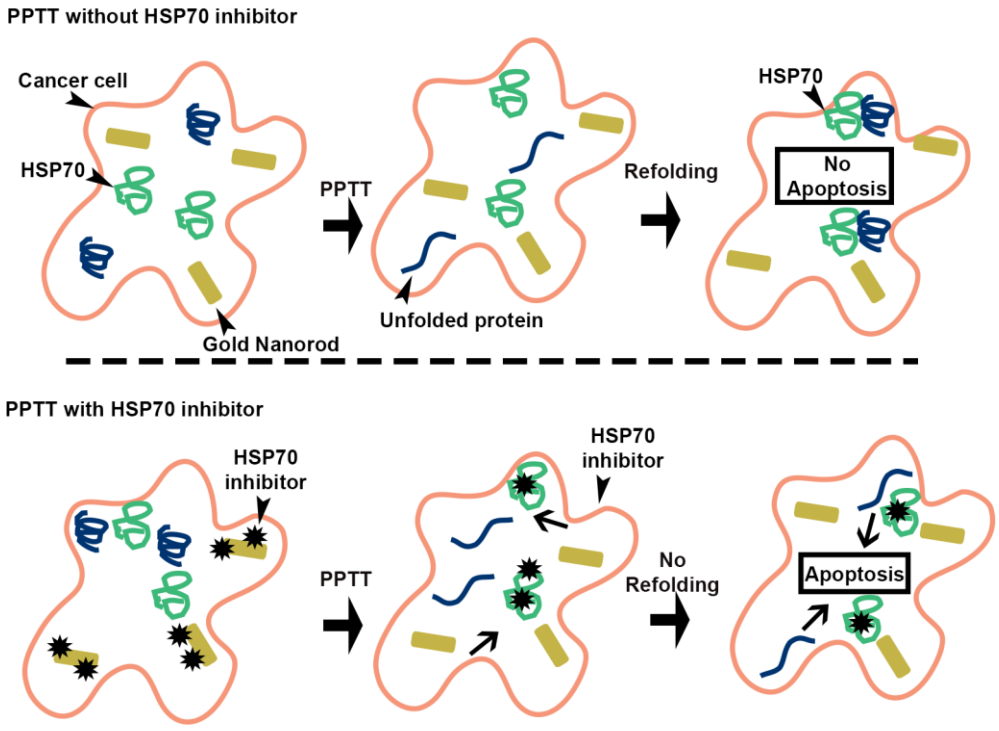

Figure 2-14. A model for HSP70 inhibitor optimized PPTT

2.3.4 Conclusion and Future Look

We undertook this work to get a deeper understanding of factors affecting photothermal therapy. We tested the efficacy of PPTT on different cancer cell lines and determined that compared to MCF7 and HSC cell lines, HuH7.5 cells were much more susceptible to PPTT. We correlated the levels of HSP70 to PPTT susceptibility and determined that reducing the amount of HSP70 in all three cancer cell lines increased the efficacy of PPTT significantly. Therefore, thermo-tolerance of cancers to PPTT through differences in HSPs represents a new area of study that might improve the efficacy of PPTT.

2.3.5 References

1. Ali, M. R. K., Ali, H. R., Rankin, C. R., El-Sayed, M. A. (2016) Targeting heat shock protein 70 using gold nanorods enhances cancer cell apoptosis in low dose plasmonic photothermal therapy. *Biomaterials 102*, 1-8.
2. Dickerson, E. B., *et al.* (2008) Gold nanorod assisted near-infrared plasmonic photothermal therapy (PPTT) of squamous cell carcinoma in mice. *Cancer Lett 269*, 57-66.
3. Li, W. Q., *et al.* (2013) Achieving a New Controllable Male Contraception by the Photothermal Effect of Gold Nanorods. *Nano Letters 13*, 2477-2484.
4. Bagley, A. F., Hill, S., Rogers, G. S., Bhatia, S. N. (2013) Plasmonic Photothermal Heating of Intraperitoneal Tumors through the Use of an Implanted Near-Infrared Source. *ACS Nano 7*, 8089-8097.
5. Zhou, T., *et al.* (2014) Inhibition of Cancer Cell Migration by Gold Nanorods: Molecular Mechanisms and Implications for Cancer Therapy. *Advanced Functional Materials 24*, 6922-6932.
6. Huang, X. H., El-Sayed, I. H., El-Sayed, M. A. (2010) Applications of Gold Nanorods for Cancer Imaging and Photothermal Therapy. *Cancer Nanotechnology: Methods and Protocols, Methods in Molecular Biology, eds Grobmyer SR & Moudgil BM (Humana Press Inc, Totowa) 624*, 343-357.
7. Alkilany, A. M., Thompson, L. B., Boulos, S. P., Sisco, P. N., Murphy, C. J. (2012) Gold nanorods: Their potential for photothermal therapeutics and drug delivery, tempered by the complexity of their biological interactions. *Advanced Drug Delivery Reviews 64*,190-199.

8. Ali, M. R. K., Snyder, B., El-Sayed, M. A. (2012) Synthesis and Optical Properties of Small Au Nanorods Using a Seedless Growth Technique. *Langmuir* 28, 9807-9815.

9. Huang XH, Neretina S, & El-Sayed MA (2009) Gold Nanorods: From Synthesis and Properties to Biological and Biomedical Applications. *Advanced Materials 21*, 4880-4910.

10. Shi, P., Li, M., Ren, J. S., Qu, X. G. (2013) Gold Nanocage-Based Dual Responsive "Caged Metal Chelator" Release System: Noninvasive Remote Control with Near Infrared for Potential Treatment of Alzheimer's Disease. *Advanced Functional Materials 23*, 5412-5419.

11. Sun, M. M., *et al.* (2016) Salt-induced aggregation of gold nanoparticles for photoacoustic imaging and photothermal therapy of cancer. *Nanoscale 8*, 4452-4457.

12. Shen, J. L., *et al.* (2014) Multifunctional Gold Nanorods for siRNA Gene Silencing and Photothermal Therapy. *Advanced Healthcare Materials 3*, 1629-1637.

13. Huang. X. H., *et al.* (2010) Comparative study of photothermolysis of cancer cells with nuclear-targeted or cytoplasm-targeted gold nanospheres: continuous wave or pulsed lasers. *Journal of Biomedical Optics 15*, 7.

14. Yang, X. J., *et al.* (2012) Near-Infrared Light-Triggered, Targeted Drug Delivery to Cancer Cells by Aptamer Gated Nanovehicles. *Advanced Materials 24*, 2890-2895.

15. Zhu, Z. F., *et al.* (2016) Near-Infrared Plasmonic 2D Semimetals for Applications in Communication and Biology. *Advanced Functional Materials 26*, 1793-1802.

16. Shao, J. X., *et al.* (2015) Near-Infrared-Activated Nanocalorifiers in Microcapsules: Vapor Bubble Generation for In Vivo Enhanced Cancer Therapy. *Angew. Chem.-Int. Edit. 54*, 12782-12787.

17. Kannadorai, R. K., Chiew, G. G. Y., Luo, K. Q., Liu, Q. (2015) Dual functions of gold nanorods as photothermal agent and autofluorescence enhancer to track cell death during plasmonic photothermal therapy. *Cancer Lett 357*, 152-159.

18. Perez-Hernandez, M., *et al.* (2015) Dissecting the Molecular Mechanism of Apoptosis during Photothermal Therapy Using Gold Nanoprisms. *ACS Nano 9*, 52-61.

19. Orosz, P., *et al.* (1993) Enhancement Of Experimental Metastasis By Tumor-Necrosis-Factor. *J. Exp. Med. 177*, 1391-1398.

20. Kudryavets, Y.I. (1998) Enhancement of tumor colony formation in lungs of mice by tumor necrosis factor. *Exp. Oncol. 20*, 114-118.

21. Bonfil, R. D., Bustuoabad, O. D., Ruggiero, R. A., Meiss, R. P., Pasqualini, C. D. (1988) Tumor Necrosis Can Facilitate The Appearance Of Metastases. *Clinical & Experimental Metastasis 6*, 121-129.

22. Davidovich, P., Kearney, C. J., Martin, S. J. (2014) Inflammatory outcomes of apoptosis, necrosis and necroptosis. *Biol Chem 395*, 1163-1171.

23. Li, J. L., Gu, M. (2010) Surface plasmonic gold nanorods for enhanced two-photon microscopic imaging and apoptosis induction of cancer cells. *Biomaterials 31*, 9492-9498.

24. Hendrick, J. P., Hartl, F. U. (1995) The role of molecular chaperones in protein folding. *Faseb J 9*, 1559-1569.

25. Bakthisaran, R., Tangirala, R., Rao, C. M. (2015) Small heat shock proteins: Role in cellular functions and pathology. *BBA-Proteins Proteomics 1854*, 291-319.

26. Bharti, S., Rani, N., Bhatia, J., Arya, D. S. (2015) 5-HT2B receptor blockade attenuates beta-adrenergic receptor-stimulated myocardial remodeling in rats via inhibiting apoptosis: role of MAPKs and HSPs. *Apoptosis 20*, 455-465.

27. Ciocca, D. R., Calderwood, S. K. (2005) Heat shock proteins in cancer: diagnostic, prognostic, predictive, and treatment implications. *Cell Stress & Chaperones 10*, 86-103.

28. Kregel, K. C. (2002) Heat shock proteins: modifying factors in physiological stress responses and acquired thermotolerance. *Journal of Applied Physiology 92*, 2177-2186.

29. Bukau, B., Horwich, A. L. (1998) The Hsp70 and Hsp60 chaperone machines. *Cell 92*, 351-366.

30. Miyako, E., *et al.* (2012) Photothermic regulation of gene expression triggered by laser-induced carbon nanohorns. *Proceedings of the National Academy of Sciences of the United States of America 109*, 7523-7528.

31. Burke, A., *et al.* (2009) Long-term survival following a single treatment of kidney tumors with multiwalled carbon nanotubes and near-infrared radiation. *Proceedings of the National Academy of Sciences of the United States of America 106*, 12897-12902.

32. Fisher, J. W., *et al.* (2010) Photothermal Response of Human and Murine Cancer Cells to Multiwalled Carbon Nanotubes after Laser Irradiation. *Cancer Research 70*, 9855-9864.

33. Rylander, M. N., Stafford, R. J., Hazle, J., Whitney, J., Diller, K. R. (2011) Heat shock protein expression and temperature distribution in prostate tumours treated with laser irradiation and nanoshells. *International Journal of Hyperthermia 27*, 791-801.

34. Larson, N., Gormley, A., Frazier, N., Ghandehari, H. (2013) Synergistic enhancement of cancer therapy using a combination of heat shock protein targeted HPMA copolymer-drug conjugates and gold nanorod induced hyperthermia. *Journal of Controlled Release 170*, 41-50.

35. Wong, S., Luna, M., Ferrario, A., Gomer, C. J. (2004) CHOP activation by photodynamic therapy increases treatment induced photosensitization. *Lasers in Surgery and Medicine 35*, 336-341.

36. Ito, A., *et al.* (2009) Inhibition of heat shock protein 90 sensitizes melanoma cells to thermosensitive ferromagnetic particle-mediated hyperthermia with low Curie temperature. *Cancer Science 100*, 558-564.

37. Yang, L. Y., *et al.* (2015) Photothermal Therapeutic Response of Cancer Cells to Aptamer-Gold Nanoparticle-Hybridized Graphene Oxide under NIR Illumination. *Acs Applied Materials & Interfaces 7*, 5097-5106.

38. Milanovic, D., Firat, E., Grosu, A. L., Niedermann, G. (2013) Increased radiosensitivity and radiothermosensitivity of human pancreatic MIA PaCa-2 and

U251 glioblastoma cell lines treated with the novel Hsp90 inhibitor NVP-HSP990. *Radiation Oncology 8*.

39. Mackey, M. A., Ali, M. R. K., Austin, L. A., Near, R. D., El-Sayed, M. A. (2014) The Most Effective Gold Nanorod Size for Plasmonic Photothermal Therapy: Theory and In Vitro Experiments. *Journal of Physical Chemistry B 118*,1319-1326.

40. Ali, M. R. K., Panikkanvalappil, S. R., El-Sayed, M. A. (2014) Enhancing the Efficiency of Gold Nanoparticles Treatment of Cancer by Increasing Their Rate of Endocytosis and Cell Accumulation Using Rifampicin. *J. Am. Chem. Soc. 136*, 4464-4467.

41. Lin, L., *et al.* (2015) Carbon nanotube-assisted optical activation of TGF-beta signalling by near-infrared light. *Nature Nanotechnology 10*, 465-471.

42. Moon, H. K., Lee, S. H., Choi, H. C. (2009) In vivo near-infrared mediated tumor destruction by photothermal effect of carbon nanotubes. *ACS Nano 3*, 3707-3713.

43. Feng, W., *et al.* (2015) Au/Polypyrrole@Fe3O4 Nanocomposites for MR/CT Dual-Modal Imaging Guided-Photothermal Therapy: An in Vitro Study. *Acs Applied Materials & Interfaces 7*, 4354-4367.

44. Kang, B., Austin, L. A., El-Sayed, M. A. (2014) Observing real-time molecular event dynamics of apoptosis in living cancer cells using nuclear-targeted plasmonically enhanced Raman nanoprobes. *ACS nano 8*, 4883-4892.

45. Wang, X. X., Chen, M. J., Zhou, J., Zhang, X. (2014) HSP27,70 and 90, anti-apoptotic proteins, in clinical cancer therapy (Review). *International Journal of Oncology 45*, 18-30.

46. Nakamoto, H., *et al.* (2014) Physical Interaction between Bacterial Heat Shock Protein (Hsp) 90 and Hsp70 Chaperones Mediates Their Cooperative Action to Refold Denatured Proteins. *Journal of Biological Chemistry 289*, 6110-6119.

47. Lepock, J. R., Frey, H. E., Heynen, M. L., Senisterra, G. A., Warters, R. L. (2001) The nuclear matrix is a thermolabile cellular structure. *Cell Stress & Chaperones 6*, 136-147.

48. Lepock, J. R. (2003) Cellular effects of hyperthermia: relevance to the minimum dose for thermal damage. *International Journal of Hyperthermia 19*, 252-266.

49. He, L. S., Fox, M. H. (1997) Variation of heat shock protein 70 through the cell cycle in HL-60 cells and its relationship to apoptosis. *Experimental Cell Research 232*, 64-71.

50. Gibson, T. J., Seiler, M., Veitia, R. A. (2013) The transience of transient overexpression. *Nature Methods 10*, 715-721.

51. Ye, B., *et al.* (2007) Induction of apoptosis by phenylisocyanate derivative of quercetin: involvement of heat shock protein. *Anti-Cancer Drugs 18*, 1165-1171.

52. Wei, Y. Q., *et al.* (1994) Induction Of Apoptosis By Quercetin - Involvement Of Heat-Shock Protein. *Cancer Research 54*, 4952-4957.

53. Shichiri, M., Tanaka, Y. (2010) Inhibition of cancer progression by rifampicin Involvement of antiangiogenic and anti-tumor effects. *Cell Cycle 9*, 64-68.

54. Fardel, O., Lecureur, V., Loyer, P., Guillouzo, A. (1995) Rifampicin Enhances Anticancer Drug Accumulation And Activity In Multidrug-Resistant Cells. *Biochem Pharmacol 49*, 1255-1260.

55. Rankin, C. R., *et al.* (2013) Annexin A2 regulates beta1 integrin internalization and intestinal epithelial cell migration. *The Journal of biological chemistry 288*, 15229-15239.

56. Huang, X. H., *et al.* (2010) Comparative study of photothermolysis of cancer cells with nuclear-targeted or cytoplasm-targeted gold nanospheres: continuous wave or pulsed lasers. *Journal of Biomedical Optics 15*.

2.4 Simultaneous Time-dependent Surface Enhanced Raman Spectroscopy, Metabolomics and Proteomics Reveal Cancer Cell Death Mechanisms Associated with Au-Nanorod Photo-thermal Therapy [1]

In cancer plasmonic photothermal therapy (PPTT), plasmonic nanoparticles are used to convert light into localized heat leading to cancer cell death. Among plasmonic nanoparticles, gold nanorods (AuNRs) with specific dimensions to absorb the near-infrared (NIR) laser light have been widely used. The detailed mechanism of PPTT therapy, however, remains poorly understood. Typically, surface enhanced Raman spectroscopy (SERS) has been used to detect time-dependent changes in the intensity of the vibration frequencies of molecules that appear or disappear during different cellular processes. A complete proven assignment of the molecular identity of these vibrations and their biological importance have not yet been accomplished. Mass spectrometry (MS) is a powerful technique that can accurately identify molecules in chemical mixtures by observing their m/z values and fragmentation patterns. Here, we complemented the study of changes in SERS spectra with MS-based metabolomics and proteomics to identify the chemical species responsible for the observed changes in SERS band intensities. Using PPTT, we observed that the bands at around 1000, 1207 and 1580 cm^{-1} increase in intensity, which were assigned in the literature to phenylalanine with dispute. Our metabolomics results showed increased levels of phenylalanine, its derivatives and phenylalanine-containing peptides, providing evidence for more confident SERS peak assignments. To better understand the mechanism of phenylalanine, increase upon PPTT, we combined metabolomics and proteomics results through network analysis, which proved that phenylalanine metabolism was perturbed. Furthermore, several apoptosis

pathways were activated, via key proteins (e.g. HADHA and ACAT1), which are consistent with the proposed role of altered phenylalanine metabolism in inducing apoptosis. In conclusion, our study shows that the integration of the SERS with MS-based metabolomics and proteomics can assist the assignment of signals in SERS spectra, and further characterize the related molecular mechanisms involved in the cellular processes involved in PPTT.

2.4.1 Introduction

Plasmonic nanoparticles offer a powerful means to follow dynamic changes associated with intracellular molecular events in real-time. [2-3] Their localized surface plasmon resonance (LSPR) confers these particles unique optical properties. For example, the electromagnetic fields on the surface of plasmonic nanoparticles are greatly increased, and exhibit exponential decay patterns following non-radiative (heat) or radiative (e. g. light scattering) processes.[4-5] Raman scattering from the molecules localized near the plasmonic nanoparticles' surface is therefore enhanced by orders of magnitude, resulting in the well-known surface enhanced resonance (SERS) phenomenon [5-6] SERS has been successfully applied to single cell analysis, where plasmonic gold nanoparticles are placed inside the cell and the resulting SERS spectrum collected in order to record the intracellular microenvironment changes occurring in time near the nanoparticles. Our group reported on the SERS spectral changes observed during the full cell cycle of a single cancer cell. The time required to kill cancer cells associated with the time taken for the SERS spectrum to stop changing when the cells were given anti-cancer drugs [7] or were heated [8] was

also determined. However, the molecular species associated with the observed SERS bands could not be confidently assigned, preventing from elucidating the molecular mechanisms involved in these critical cellular processes.

Photothermal therapy has its foundation in the targeted destruction of cancerous cells via the heat released by gold nanorods following near IR radiation absorption. The so called "water wavelength window" between 700–1200 nm is widely considered to be the optimal spectral region for conducting PPTT [9-10], as tissue and water absorption are minimized in this range. Gold nanorods (AuNRs), on the other hand, readily absorb near-infrared laser light, resulting in effective photothermal generators, for both *in vitro* and *in vivo* applications. AuNRs-based PPTT has been successful at inducing cancer cell apoptosis [11-12] resulting in *in vivo* tumor removal. [12-14]

Despite the operational success of PPTT, the molecular mechanisms associated with PPTT-induced apoptosis remain largely unknown or under dispute. We observed PPTT induce apoptosis initiate through heat shock proteins previously, [15] while several reports indicate it is mediated by the mitochondrial apoptotic pathway via Bid activation and caspase 3 activity. Although SERS reports on the real-time biomolecular dynamics in the microenvironment associated with the PPTT process, [16-17] SERS spectra from cells are incredibly complex, reflecting overlapping signals from a variety of proteins and metabolites that are difficult to assign to individual species. It has been reported, for example, that the 1000 and 1580 cm^{-1} peaks showed significant increase during cell apoptosis [18] with great debate in their assignment. [19] According to published literature, the 1000 cm^{-1} signal has been assigned to phenylalanine, [20] while a different report assigned it to tryptophan. [21] Furthermore, it has been argued [7] that these SERS signals

reflect changes in protein structure, a topic still being intensively debated. One hypothesis states that the 1000 cm^{-1} signal is indicative of the exposure of protein hydrophobic rings following conformational changes, [7] while others report that the protein conformation change induced by adding methanol or SDS [21] or increasing temperature [8] does not alter the intensity of the 1000 cm^{-1} peak, therefore contradicting the hypothesis that this signal is associated with alterations in protein conformation.

Herein, we monitored the SERS spectral signature *in vitro* during apoptosis as a function of PPTT exposure time. We also performed metabolomics and proteomic studies on cell lysates under the same exact PPTT conditions. Integrative multi-omics network analysis revealed specific alterations that explain the underlying changes in SERS spectral data, demonstrating the power of combining SERS with MS for studying cellular processes following PPTT.

2.4.2 Experimental Methods

Materials. Tetrachloroauric acid trihydrate ($HAuCl_4.3H_2O$), trisodium citrate, $NaBH_4$, ascorbic acid, cetyltrimethylammonium bromide (CTAB), $AgNO_3$, 4-(2-hydroxyethyl)-1-piperazineethanesulfonic acid (HEPES), NaCl, sodium deoxycholate

SDC) were purchased from Sigma-Aldrich (USA). Methoxypolyethylene glycol)-thiol (mPEG-SH, MW 5000) was purchased from Laysan Bio, Inc. Cell penetrating peptide RGD (RGDRGDRGDRGDPGC) and nuclear localization signal NLS (CGGGPKKKRKVGG) peptides were obtained from GenScript, Inc. Dulbecco's phosphate buffered saline (PBS), Dulbecco's modified Eagle's medium (DMEM), fetal

bovine serum (FBS), antibiotic solution, 0.25% trypsin/2.2 mM EDTA solution were purchased from VWR. Mammalian cell protease inhibitors were purchased from Roche Applied Sciences, sequencing grade trypsin was purchased from Promega, and Lysyl endopeptidase (Lys-C) was from Wako.

Instrumentation. Gold nanoparticles were imaged using a JEOL 100CX-2 transmission electron microscope (TEM) microscope and their average size was then measured by ImageJ software. UV−vis spectra were obtained using an Ocean Optics HR4000CG UV-NIR spectrometer. SERS spectra were collected using a Renishaw InVia Raman microscope equipped with a 785-nm diode Raman excitation laser and a Leica optical microscope. Comprehensive metabolomics analyses were performed with ultra-performance liquid chromatography-mass spectrometry (UPLC-MS), using a Waters ACQUITY UPLC H Class system fitted with a Waters ACQUITY UPLC BEH C18 column (2.1×50 mm, 1.7 μm particle size, Waters Corporation, Milford, MA, USA), coupled to a Xevo G2 QTOF mass spectrometer (Waters Corporation, Manchester, UK) with an electrospray ionization (ESI) source. The typical resolving power and mass accuracy of the Xevo G2 QTOF mass spectrometer were 25,000 (FWHM) and 1.8 ppm at m/z 554.2615, respectively. Proteomics analysis was done on a hybrid dual-cell quadrupole linear ion trap - Orbitrap mass spectrometer (LTQ Orbitrap Elite, Thermo Fisher) with Xcalibur 3.0.63 software. Flow cytometry experiments were conducted on a BD LSR II Flow Cytometer (BD Biosciences).

Synthesis, Conjugation and Characterization of AuNSs and AuNRs. Gold nanospheres (AuNSs) with an average diameter of 30-40 nm were synthesized using the citrate reduction method.[22] Briefly 200 mL of 0.254 mM $HAuCl_4.3H_2O$ solution was heated until

boiling, then reduced by adding 5 mL of 0.35% of trisodium citrate. The solution was then left heating until it turned wine red, followed by cooling under water flow. The citrate stabilized AuNSs were first centrifuged at 5000 g for 10 min and re-dispersed in deionized (DI) water to remove extra citrate for the next step of conjugation. Gold nanorods (AuNRs) with an average size of 25 x 6 nm (length x width) were synthesized using a seedless growth method [23]. Briefly, 5 ml of 1.0 mM $HAuCl_4$ was added to a mixture of 5 mL of 0.20 M CTAB, 250 μL of 4.0 mM $AgNO_3$ and 8 μL of 37% HCl. 70 μL of 78.8 mM ascorbic acid was added, then, 15 μL of 0.01M of ice-cold $NaBH_4$ was immediate injected. The solution was left undisturbed for 12 h, followed by centrifugation at 21000 g for 50 min and re-dispersed in DI water and a second centrifugation at 19000 g for 40 min to remove the extra CTAB. TEM was used to measure the sizes and homogeneity of the nanoparticles. AuNSs and AuNRs were then conjugated according to previous work. 8 First, mPEG-SH (1 mM) was added to the nanoparticles for overnight to achieve about 1000 ligands on each particle. Then, the PEGylated nanoparticles (1 nM) were treated with RGD (1 mM) and NLS (1 mM) to achieve 10^4 and 10^5 molar excess, respectively. The number of the bounded ligands to the AuNPs, were about 25% of the added ligands. evaluated based on Ellman's protocol. [24] The solution was then allowed to shake overnight at room temperature. Excess of ligands were removed by centrifugation. UV-vis spectrometer and zetasizer was used to test the conjugation. Surface modification causes red shift of UV-vis spectra due to the change in the dielectric constant of the surrounding environment of AuNSs.

Cell culture, AuNPs incubation and Plasmonic photothermal therapy. Human oral squamous cell carcinoma (HSC-3) cells were grown in DMEM medium containing 10% (v/v) fetal bovine serum and 1% (v/v) antibiotic solution. Cells were kept at 37 ^oC in a

humidified incubator under 5% CO_2. HSC-3 Cells were left under overnight incubation with 2.5 nM AuNRs in complete media, and then were exposed to a CW laser (808 nm 5.8 W/cm^2) for different time course. The concentration of nanoparticles was carefully chosen to avoid cytotoxicity or perturbation to the cell cycle.

In vitro SERS measurement. Time dependent SERS spectra were collected throughout the NIR laser exposure period to monitor molecular changes in the plasmonic nanoparticle microenvironment during photothermal heating of the AuNRs. The Raman laser was directed into a microscope, after focusing on the sample by a 50×/0.75 N.A. objective, forms a 1-2 μm spot size. Spectra of molecules in the single cell were measured with a 1200 lines/mm grating and collected by a CCD detector in the range of 400−1800 cm^{-1} using a Renishaw InVia Raman spectrometer. Spectrum baseline was removed using R Package Baseline (version 1.2-1). Dark field images were taken by a Lumenera Infinity2 CCD camera. For SERS studies, the cells were seeded on glass coverslips in complete growth medium for 24 h to achieve a 40 % final confluence before SERS study. Then, the cells were incubated with 0.05 nM PEG/RGD/NLS-functionalized AuNSs in supplemented DMEM cell culture medium for 24 h. [25] Six hours before the SERS examination, the cell media (with AuNSs) were removed and 2.5 nM of AuNRs suspended in supplemented medium was added to the cells to perform PPTT.

Apoptosis/necrosis assay. HSC-3 cells were cultured in 12-well plates for 24 h and then treated with 2.5 nM of AuNRs@NLS for 24 h. After AuNRs incubation, PPTT was applied for different time periods. Before the apoptosis/necrosis assay, the cell culture media was removed and cells were collected after trypsinization, followed by washing with cold PBS twice. Then, cells were dispersed in 493 ml of Annexin V binding buffer, and 5 μL of

Annexin V FITC (BioLegend) and 2 μL of propidium iodide PI (BioLegend, 100 μg / mL) were added to the cell suspension and incubated for 15 min at room temperature. [26] The cells were then filtered and subjected to flow cytometry analysis using a BSR LSR II flow cytometer (BD Biosciences). A 488-nm laser was applied for excitation, and FITC was detected in FL-1 using a 525/30 BP filter while PI was detected in FL- 2 using a 575/30 BP filter. Standard compensation using unstained and single-stained cells was done before performing actual experiments. FlowJo software (Tree Star Inc.) was used for analysis of the viable, apoptotic and necrotic cells from at least 10000 events.

Sample preparation for metabolomics experiments. Cells were cultured in 60 mm petri dishes. The culture media was removed and cells were washed 3 times with PBS, followed by a wash with deionized water for 2 s and immediate removal of the wash solution. Seven mL of metabolite extraction solvents (HPLC grade methanol: acetonitrile: 0.5 M formic acid, 2:2:1 v/v, -20 ^{o}C) was added immediately for quenching and lysing the cells. [26] Cells were then scraped down, and the cell suspension was transferred to centrifuge tubes, followed by vortexing and sonication in ice water bath and incubation on ice for 15 min for metabolite extraction. The cell suspension was then centrifuged at 20,400 g at 4 ^{o}C for 15 min. Solvent in the sample was evaporated using a CentriVap Vacuum Concentrator until dryness. The dried samples were kept at -80 °C until analysis. [26]

Sample preparation for proteomics experiments. Cells were cultured in 60 mm Petri dishes. Ice-cold lysis buffer (50 mM HEPES, pH 7.8, 150 mM NaCl 0.1% SDS (optional) 0.5% sodium deoxycholate 1% Triton X 100 or NP-40, phosphatase inhibitors) was added directly to the cells after washing with PBS twice. The cells were then scraped down and the obtained mixtures homogenized with sonication and vortexing. Cell debris was then

removed by centrifugation at 18,000 g for 20 min at 4 °C. Four volumes of ice-cold acetone/ethanol/acetic acid (v/v/v = 50/50/0.1) was added to the supernatant to precipitate the proteins at -20 °C overnight. After centrifugation, the protein pellet was re-dissolved in denaturing buffer (pH 8.0) containing 8 M urea and 50 mM HEPES, and the protein concentration was tested using a Bradford assay. The disulfide bonds in the protein solution were reduced by 2 mM dithiothreitol (DTT) at 37 °C for 2 h and subsequently alkylated by adding 6 mM iodoacetamide (IAA) and kept in darkness at room temperature for 40 min. [27]

Ultra-Performance Liquid Chromatography (UPLC)-MS Metabolomics Analysis. Before analysis, ultrapure water was added to each dried sample to obtain a final biomass concentration of ~50,000 cells/ μL. Samples were further vortexed and then centrifuged at 15,000 rpm for 10 min at 4 °C. The supernatant of each biological sample was transferred to autosampler vials for UPLC-MS analysis. Gradient elution was employed in the chromatographic separation method using 0.1% acetic acid in water (mobile phase A) and acetonitrile (mobile phase B), with the following program: 0-1 min, 98% A, 1-3 min 98%-70% A, 3-8 min 70%-50% A, 8-10 min 50%-5% A, 10-15 min 5% A. The flow rate was constant at 0.3 mL min-1. After each sample run, the column was re-equilibrated to the initial conditions in 6 min. The injection volume was 5 μL. The column and auto sampler tray temperatures were set at 35 and 5 °C, respectively. The mass spectrometer was operated in negative ion mode with a probe capillary voltage of 2.2 kV and a sampling cone voltage of 45.0 V. The source and desolvation gas temperatures were set to 120 and 350 °C, respectively. The nitrogen gas desolvation flow rate was 650 L/h. The mass spectrometer was calibrated across the range of m/z 50-1200 using a 0.5 mM sodium

formate solution prepared in 2-propanol/water (90:10 v/v). Data were drift corrected during acquisition using a leucine encephalin (m/z 554.2615) reference spray (Lock Spray) infused at 3 μL min-1. Data were acquired in the range of m/z 50-1200, and the scan time was set to 1 s. Technical duplicates were acquired in all cases. Tandem MS experiments were carried out by fast data dependent acquisition (fast DDA) or MS/MS in negative polarity and resolution mode. Targeted ions for MS/MS were entered in an include list. A 0.2 s continuum MS survey scan was collected from 50 to 650 Da until the intensity of an individual precursor ion raised above 5000, then switched to MS/MS acquisition, in which a 0.1s continuum scan was collected from 30 to 650 Da. The MS/MS scan switched off once the accumulated total ion current reached 100,000 or after 0.25 s. A collision energy profile of 15, 25 and 35 V was applied to the trap cell for ion fragmentation. For the MS/MS method, a scan time was 1s and collision voltages between 8 to 30 V were applied to the trap cell. Data acquisition and processing were performed with Masslynx v4.1.

LC-MS/MS Analysis for proteomic experiments. Purified and dried peptide samples were dissolved in a 10 μL solution containing 5% ACN and 4% formic acid (FA), and 3 μL was loaded onto a micro capillary column packed with C18 beads (Magic C18AQ, 3 μm, 200 Å, 100 μm x 16 cm, Michrom Bioresources) by a Dionex WPS-3000T PLUS auto sampler (UltiMate 3000 thermostatted Rapid Separation Pulled Loop Well Plate Sampler). Peptides were separated by reverse-phase chromatography using an UltraMate 3000 binary pump with a 110-min gradient of 8-38% ACN (with 0.125% FA) for the triplicates. Peptides were detected with a data-dependent Top 20 method (the 20 most abundant ions were selected for MS2), [28] in a hybrid dual-cell quadrupole linear ion trap – Orbitrap mass spectrometer (LTQ Orbitrap Elite, Thermo Fisher, with Xcalibur 3.0.63 software).

For each cycle, each full MS scan (resolution: 60,000) in the Orbitrap at 10^6 AGC target was followed by up to 20 MS/MS for the most intense ions in the LTQ. The selected ions were excluded from further analysis for 90 seconds. Ions with singly or unassigned charge were not sequenced. For each full MS scan, the maximum ion accumulation time was 1000 ms and the one for MS/MS scans was 50 ms. Mass spectra Raw files were converted into mzXML format, then searched using the SEQUEST algorithm (version 28). [29] Spectra were matched against a database containing sequences of all proteins in the UniProt Human (Homo sapiens) database (downloaded in February 2014). The search was performed using following parameters: fully digested with trypsin; up to 3 missed cleavages; fixed modifcations: carbamidomethylation of cysteine (+57.0214); variable modifcations: oxidation of methionine (+15.9949). False discovery rates(FDR) of peptide and protein identifications were controlled by the target-decoy method. [30] Linear discriminant analysis (LDA) was used to control the quality of peptide identifcations using parameters such as Xcorr, precursor mass error, and charge state. [31] Peptides fewer than seven amino acid residues in length were deleted. Furthermore, peptide spectral matches were filtered to <1% FDR.

Data analysis. For metabolomics, spectral features (retention time (Rt), m/z pairs) were extracted from UPLC-MS data using Progenesis QI version 2.0 (Nonlinear Dynamics, Waters Corp.). The data preprocessing procedures included retention time alignment, peak picking, integration, and de-convolution to group the adducts derived from the same compound.

Raw data from metabolomics were normalized using supervised normalization of microarray. [32] In the SNM procedure, variances due to biological and technical replicates

were adjusted by setting them as variables in the model. Variance explained by different experimental treatments (control, AuNRs@NLS, and AuNRs@NLS/PPTT) was fitted as a biological variable in the model. Clustering analysis on similarity matrix of metabolomics data was carried out to verify the reproducibility of metabolomics experiments. Hierarchical clustering was done with JMP software (JMP®, Version 9. SAS Institute Inc., Cary, NC.). Metabolomics data were log2 transformed before analysis of variance (ANOVA) which was used to detect differential levels of metabolites between control and treatment groups. We fitted models with treatment conditions as fixed effects. A Benjamini-Hochberg 5% false discovery rate (FDR) correction was used to select differential metabolites. For identified differential metabolites perturbed by PPTT, we used the Mummichog program for network-level metabolites annotation. [33] The MS mode considered in Mummichog was negative ion in order to compute isotopic and adduct species. The metabolites identified as being affected by PPTT were subjected to pathway analysis using the MetaCore pathway analysis software ("MetaCore from Thomson Reuters").

For proteomics, raw data were also normalized using SNM. Clustering analysis on the similarity matrix of data was also carried out to show the reproducibility of the experiments. Hierarchical clustering was done with JMP software (JMP®, Version 9. SAS Institute Inc., Cary, NC). The identified proteins were subjected to pathway analysis using the MetaCore pathway analysis software ("MetaCore from Thomson Reuters") to study the effect of PPTT.

2.4.3 Results and Discussion

Formulation of AuNRs and cell uptake

To perform PPTT inside human oral squamous cell carcinoma (HSC-3) cells, AuNRs were used to efficiently convert NIR light into heat. The AuNRs were synthesized using a seedless method [34] with an average size of 25 x 6 nm as shown in Figure 2-15b (TEM figure) which has an absorption maximum at about 800 nm (as shown in the UV-Vis spectrum in Figure 2-15c). This particle size is favorable in conducting PPTT as it has better conversion of light into heat efficiency. [35]

For formulation of AuNRs@NLS, we first used methoxypolyethylene glycol thiol (mPEG-SH) to modify the surface of AuNRs to gain better biocompatibility. [36] The PEGylated particles were then functionalized with Arg-Gly-Asp (RGD) peptides (known to bind to Rvβ6 integrin on the surface of cancer cells to enhance the receptor-mediated endocytosis of the nanoparticles) [37] and nuclear localization signal (NLS) peptides (peptide sequences that are recognized by importin and translocate near the nucleus [38]) , as shown in Figure 1a. Successful surface modification of AuNRs@NLS is evident in the red-shift of the plasmon peak of AuNRs to longer wavelengths, from 800 nm for the as-synthesized AuNRs to 825 nm AuNRs@NLS (Figure 2-15c). The zeta potentials of the AuNRs at different stages were measured (Table A.2.) to confirm surface modifications. The as-synthesized CTAB-coated AuNRs had highly positive surface charges as imparted by the CTAB cationic surfactant. Following PEG modification, the AuNRs became negatively charged (-10.2 ± 6.73 mV). The zeta potential of the AuNRs became positive again after further modification of the RGD and the NLS peptides.

The uptake of AuNRs was first monitored by dark-field (DF) microscopy. The HSC cells were incubated with 2.5 nM of AuNRs for 24 h. For AuNRs@NLS, as shown in the DF image (Figure 2-10d), clear internalization of AuNRs@NLS was observed compared with cells not exposed to AuNRs and cells exposed to AuNRs without targeting agents. The DF image shows AuNRs@NLS accumulated in nuclear regions. In addition, the UV-Vis spectra of culture media with AuNRs before and after incubation with cells were also collected (Figure 2-10e), which showed the decrease of the peak intensity that, gives the portion of AuNRs being uptaken by the cells. Differential interference contrast (DIC) microscopy image also confirmed the cellular internalization of AuNRs@NLS (Supporting Figure A.12.). In summary, AuNRs were successfully formulated and then introduced into cells with good cell uptake. The cell viability and apoptosis were tested under different concentrations of AuNRs. The results indicate that the concentration of the AuNRs utilized in this study is much lower than that affecting cell viability or inducing apoptosis (Appendix Figure A.13.).

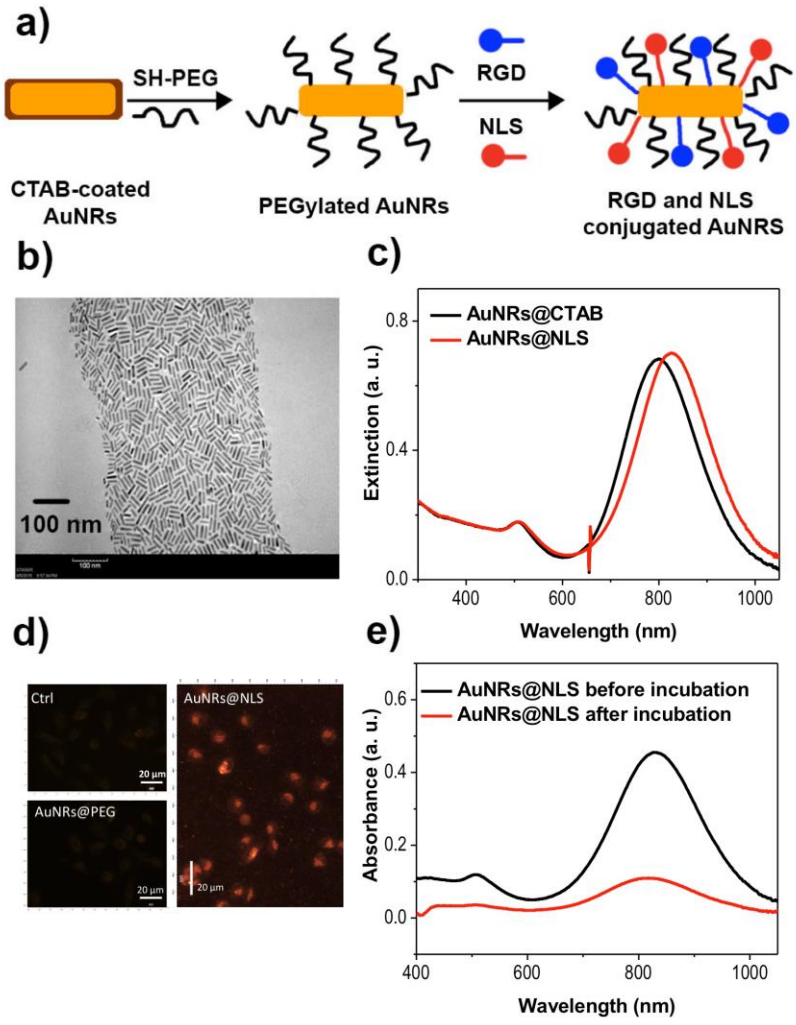

Figure 2-15. Characterization of conjugated AuNRs and measurement of HSC-3 (human squamous carcinoma) cell endocytosis with AuNRs:

(A) Schematic showing the surface conjugation of the AuNRs with PEG, followed by RGD and NLS. (B) Transmission Electron Microscope (TEM) image of conjugated nanorods (AuNRs). Scale bar = 100 nm. (C) UV-Vis absorption spectra of the unconjugated AuNRs (black spectrum), AuNRs conjugated with NLS (red spectrum). (d) The dark field images of control HSC-3 cells (not exposed to AuNRs), cells exposed toAuNRs@PEG and cells exposed to AuNRs@NLS for 24 h. Scale bar = 20 nm. (e) UV-Vis absorption spectra of the AuNRs@NLS dispersed in culture media before (black spectrum) and after (red spectrum) incubation with cells.

SERS of cancer cells undergoing AuNRs-based photothermal therapy

The AuNRs with dimensions (25×6 nm) [24] and concentration (2.5 nM) was selected for use of heat generation. After incubation with AuNRs for 24 h, a CW 808 nm NIR laser with power of 5.8 W/cm^2, [1, 39-40] was used for irradiation of the cells for different time intervals. The laser wavelength overlapped with the longitudinal SPR peaks of the AuNRs. The temperature rose to 45 °C after 2 min of laser exposure. The effect of PPTT was confirmed using a cell viability assay and apoptosis/necrosis assay. The cell viability results showed a significant decrease in the percentage of viability (~40%) for the HSC cells incubated with AuNRs (2.5 nM) after exposure to the 808 nm NIR laser for 3 min (Appendix Figure A.14.). In the apoptosis/necrosis assay, cells were labeled with Annexin V and propidium iodide (PI), and the fluorescent signals were examined by flow cytometry. As shown in Figure A.14, the number of apoptotic cells significantly increased after applying PPTT. The decrease of cell viability and increase of apoptosis indicated the efficacy of PPTT.

For real-time SERS measurement, spectra were collected at a single spot of cells to avoid the variation due to changing location. A 785 nm laser was focused on a single cell and spectra were recorded. As our AuNRs have weak SERS signals (due to their small size), to enhance the signals, 40 nm gold nanosphers (AuNSs) with the same surface modification as AuNRs were used to assist the detection. [37] The detailed information of AuNSs@NLS characterization and cellular uptake was in Appendix Figure A.15. The introduction of AuNSs does not affect AuNRs uptake or SERS spectra shapes during PPTT process due to their small amount and not absorbing NIR light (Appendix Figure A.16. and A.17.a). SERS

spectra of HSC cells without PPTT were comparable with our previous publications [41-42] with the possible assignment of each peak in Appendix Table A.3. Upon NIR laser exposure, the band around 1000 cm^{-1} increased in intensity due mainly to the benzene ring breathing of phenylalanine as mentioned before. [7] Though most of the publications assign this band to phenylalanine, some debate is still going on regarding its assignment [21]Further, we observed that the enhancement of the 1000 cm^{-1} peak was accompanied by the enhancement of the 1207 and 1580 cm^{-1} bands (Figure 2-16a), which are attributed to the in-plane CH stretching vibrations and side chain vibration coupled with the in-phase motion corresponding to phenylalanine.[43-44] The same experiment was repeated 3 times and the same trend of peak intensity changes of 1000, 1207 and 1580 cm^{-1} was obtained (Figure 2-16b and Appendix Figure A.18.). SERS data of cells 12 hours after PPTT has also been performed to confirm that the signal remains altered (Figure A.19.). On the other hand, a control experiment was conducted on cells without laser exposure. No obvious SERS spectral change was observed during the NIR laser control. (Appendix Figure A.17.b). This gave us more evidence of the phenylalanine increase after the PPTT process.

Generally, we can rule out the possibility of tryptophan contributing to the 1000 cm^{-1} signal since side-chain vibrations in its SERS spectrum appear at 758, 869, 1011, 1357, 1410, 1546 and 1602 cm^{-1}, corresponding to the counterparts at 756, 874, 1009, 1358, 1423,1558 and 1619 cm^{-1} in the solid Raman spectrum.[45] However, our SERS data didn't show obvious increase of these above peaks. Therefore, our SERS results support the conclusion that the phenylalanine increases in the microenvironment around nanoparticles during PPTT.

In addition to the phenylalanine bands we also observed a 750 cm^{-1} band whose intensity increases during PPTT (Figure 2-16), which has been assigned to the pyrrole breathing mode ν_{15} in cytochrome c. [46-47] This result suggested the increase of apoptotic cells during thermal heating through cytochrome c-mediated apoptosis. This result is in agreement with our flow cytometry data (Appendix Figure A.14.) indicating that PPTT triggered apoptosis.

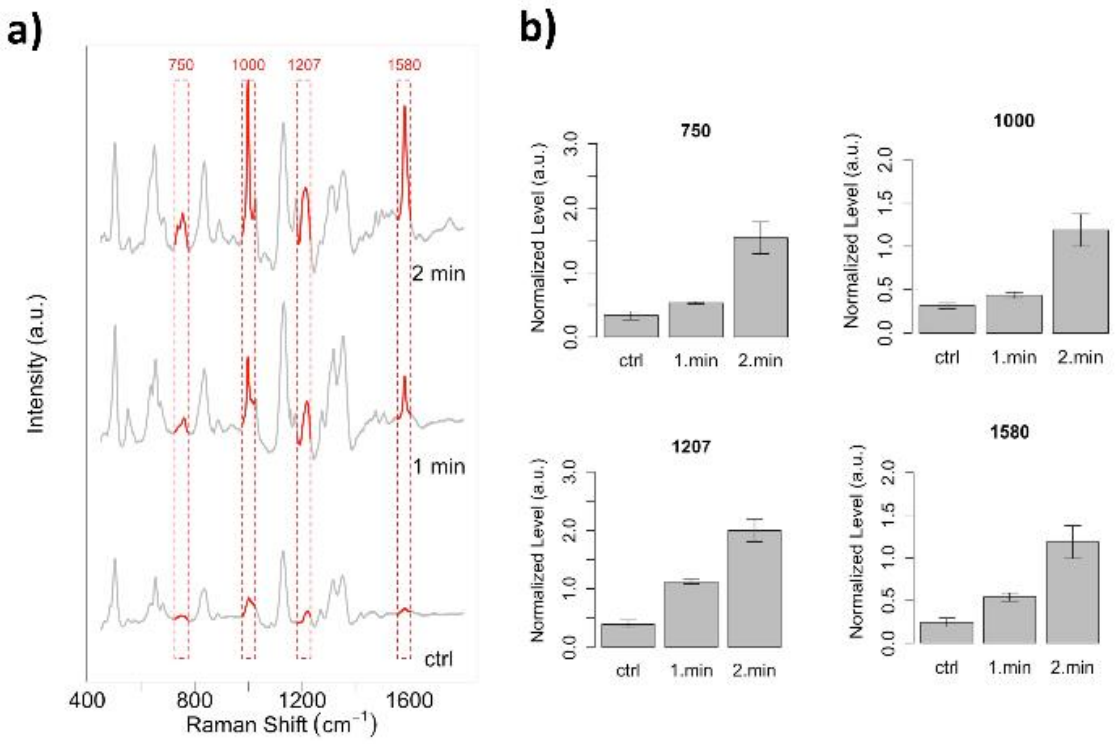

Figure 2-16. SERS spectra:

(A) collected from single HSC-3 cell under NIR laser exposure of (808 nm diode laser 5.8 W/cm^2) at 1 and 2 minutes' delays. The 750, 1000, 1207, and 1580 cm^{-1} bands are shown in red and placed in red boxes in (A) and shown in the bar graphs in (B) Raman bands associated with bio-molecules located within the AuNP plasmonic field.

Metabolomics and proteomics experiments confirming perturbation of phenylalanine metabolism during AuNRs-PPTT

For metabolomics experiments, we analyzed the metabolites of cells using liquid chromatography-mass spectrometry (LC-MS). Two biological replicates and two technical replicates were conducted. A total of 1122 tentative features (retention time, m/z pairs)

were detected in metabolite extracts, corresponding to 152 metabolites with detectable ($[M-H]^-$) primary ion. Hierarchical clustering analysis on the similarity matrix of metabolomics data was carried out to verify the reproducibility of the experiments (Appendix Figure A.20.b). Among these, 238 metabolomics features were differentially expressed in the AuNR@NLS-treated group when compared to the control group (FDR=0.05, corresponding to p=0.015) (**Appendix Figure A.20.e**); 483 metabolomics features were differentially expressed in the AuNR@NLS/PPTT group in contrast to the control group (FDR=0.05, corresponding to p=0.015) (Appendix Figure A.20.f). Specifically, many of these features corresponded to an increase in the relative amount of phenylalanine (**Figure 2-17a**) and related species after PPTT (**Figure 2-17b-d, Appendix Figure A.21.**). Phenylalanine derivatives and phenylalanine-containing short peptides, such as glutamylphenylalanine (**Figure 2-17b**), asparaginyl-phenylalanine (**Figure 2-17c**), histidinyl-phenylalanine (**Figure 2-17d**) were amongst those altered, explaining the trends observed in the SERS data. Tandem MS experiments confirmed the identity of the species detected by MS with excellent accuracy (**Figure 2-17e**).

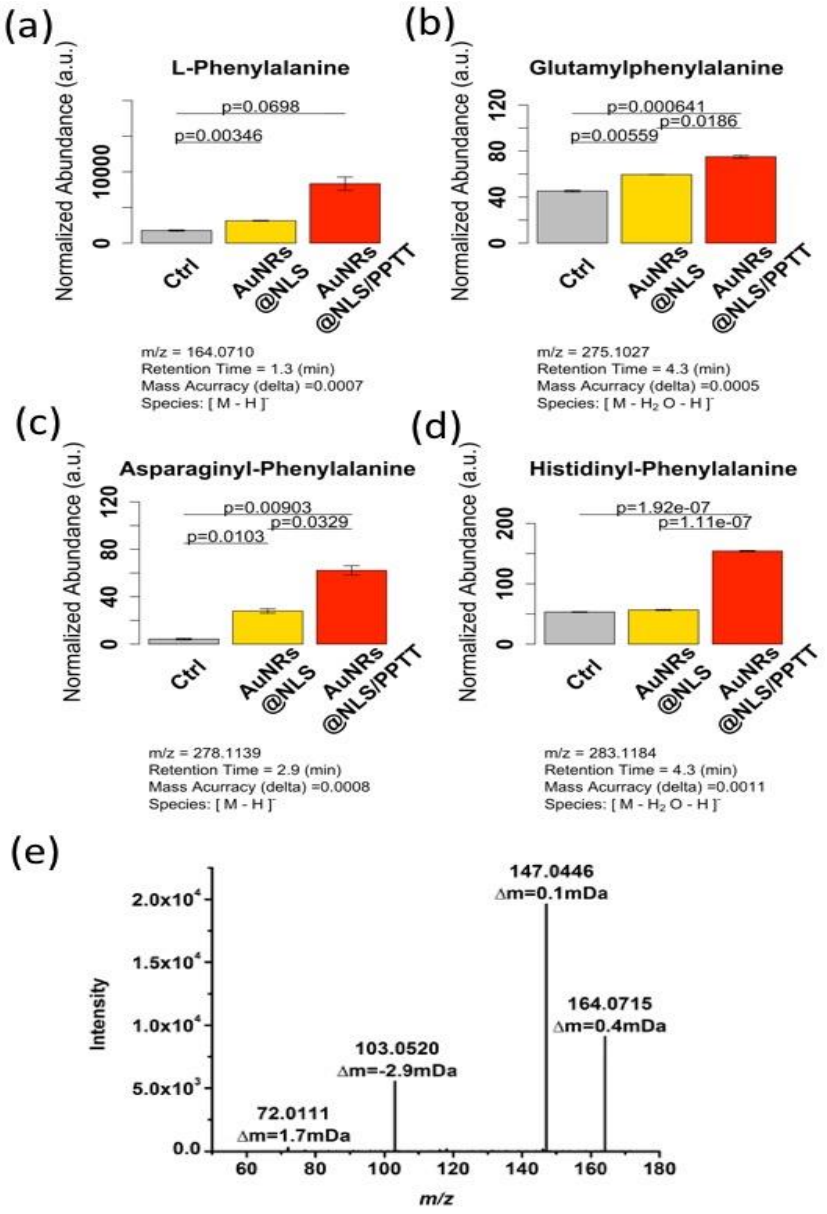

Figure 2-17. Metabolite perturbations observed in HSC-3 cells treated with AuNRs-PPTT (NLS conjugated particles):

(A-D) Bar graphs showing the normalized abundance of phenylalanine-related metabolites altered following PPTT. Normalized abundances of metabolites following AuNRs@NLS without PPTT are also given for comparison. (A) L-Phenylalanine. The result was confirmed by MS/MS (shown in figure 3e). (B) Glutamylphenylalanine. (C) Asparaginyl-Phenylalanine. (D) Histidinyl-Phenylalanine. (E) Product ion spectrum obtained under data dependent acquisition (DDA) conditions for the precursor ion at m/z 164.0710. Matching of this mass spectrum to the Metlin database MS/MS reference spectrum of phenylalanine (10 V collision energy) is shown with mass accuracies indicated for each ionic species detected.

Furthermore, we also conducted a label-free quantitative proteomics experiment for studying alterations in protein abundances and seeking possible evidence for, and understanding of the mechanisms responsible for the phenylalanine concentration increase. A test experiment was done to measure the accuracy of our proteomics workflow using the reported method, [27] where 99% of the proteins have shown accurate quantification (**Appendix Figure A.22.**). In our proteomics experiment, two biological replicates and three technical replicates were conducted. Clustering analysis (**Appendix Figure A.20.a**) indicated good reproducibility for the proteomics experiments. In total, 1341 proteins were identified. Among these, 326 proteins were differentially expressed in the AuNR@NLS-treated group compared to the trol group (Appendix Figure A.20.c); 278 proteins were differentially expressed in the AuNR@NLS/PPTT-treated group in contrast to the control group (**Appendix Figure A.20.d)**.

Proteomics results were integrated with metabolomics for a more holistic understanding of the biological processes involved. Integrated pathway analysis showed that the phenylalanine metabolism pathway was significantly perturbed by PPTT (**Appendix Figure A.23. and A.24**.). Approximately half of the metabolites in the phenylalanine metabolism pathway were identified as changes, including 2-phenyl-acetamide (increase), phenylpiruvate (decrease), 2-hydroxy-3-phenyl-acrylic acid (decrease), 3-oxobutanoate (increase), fumarate (increase), phenylacetaldehyde (increase), L-tyrosine (decrease), 4-fumarylacetoacetate (decrease) and 4-maleylacetoacetate (decrease). These alterations were accompanied by perturbations in several key proteins in the phenylalanine metabolism pathway.

Elevated levels of phenylalanine are known to induce apoptosis, [44-45] which is consistent with the apoptotic phenotype observed in PPTT-treated cells. An overview of pathways identified as being related to phenylalanine-induced apoptosis is schematically shown in **Figure 2-13A**. Two proteins in the phenylalanine metabolism pathway have been previously associated with apoptosis. Mitochondrial acetyl-CoA acetyltransferase (ACAT1) has been shown to be involved in the development of doxorubicin resistance to decrease cell apoptosis.[48] Another mitochondrial protein, hydroxyl-coenzyme A dehydrogenase/3-ketoacyl-coenzyme A thiolase/enoyl-coenzyme (HADHA), has been shown to prevent chemically-induced apoptosis in cancer treatment. [49] In our experiments, both proteins were observed to be down-regulated following PPTT treatment, suggesting that the anti-apoptotic protection was turned off resulting in enhanced vulnerability to apoptosis (**Figure 2-18b, c**).

In addition to the phenylalanine metabolism pathway, three possible mechanisms of phenylalanine-induced apoptosis were suggested by the results. Firstly, increased phenylalanine was shown to induce apoptosis by involvement of the Fas receptor (FasR)-mediated cell death receptor pathway.[50] In this study, two proteins (Lamin B1 and PAK1) in the Fas/Fas ligand death receptor pathway were identified. These two proteins have been previously demonstrated to be associated with apoptosis. Lamin B1, as the major component of the nuclear lamina underlying the nuclear membrane, plays an important role in maintaining nuclear membrane integrity. Destruction of nuclear membrane integrity being a hallmark of apoptosis. During apoptosis, Lamin B1 mRNA level have been shown to decrease, [51] which could result from induction of either p53 or pRB tumor suppressor pathways. [52-53] Literature results also show that the Fas/Fas ligand complex downstream

effector PAK1 is required to prevent apoptosis by limiting the expression of pro-apoptotic proteins or modulating post-translational modifications on effectors. [54-56] In this study, both proteins were down-regulated, suggesting a cellular shift towards apoptosis, and reduced anti-apoptotic protection (**Figure 2-18d,Figure 2-18e**).

Phenylalanine has also been shown to activate mitochondria-mediated apoptosis through the Rho/ROCK pathway. [56] In this study, we identified down-regulation of the myosin phosphatase targeting subunit 1 (PPP1R12A) in PPTT-treated cells, this being a downstream effector of ROCK (Figure 4f) that would contribute to the apoptotic phenotype following PPTT. In apoptotic cells, PPP1R12A is cleaved, with the cleaved PPP1R12A inhibiting myosin II binding, which results in membrane blebbing and apoptosis. [57]

A third mechanism of phenylalanine-induced cell death involves a component in Granzyme B signaling-mediated apoptosis, known as lysosome-associated membrane protein 2 (LAMP2). This protein was down-regulated following PPTT treatment (**Figure 2-18g**). LAMP2 is critical to maintain lysosome integrity and normal cellular function, and lower levels of LAMP proteins have been positively associated with apoptosis. [55] It is not yet conclusively established, however, whether decreased LAMP2 levels are also directly associated with phenylalanine-induced apoptosis.

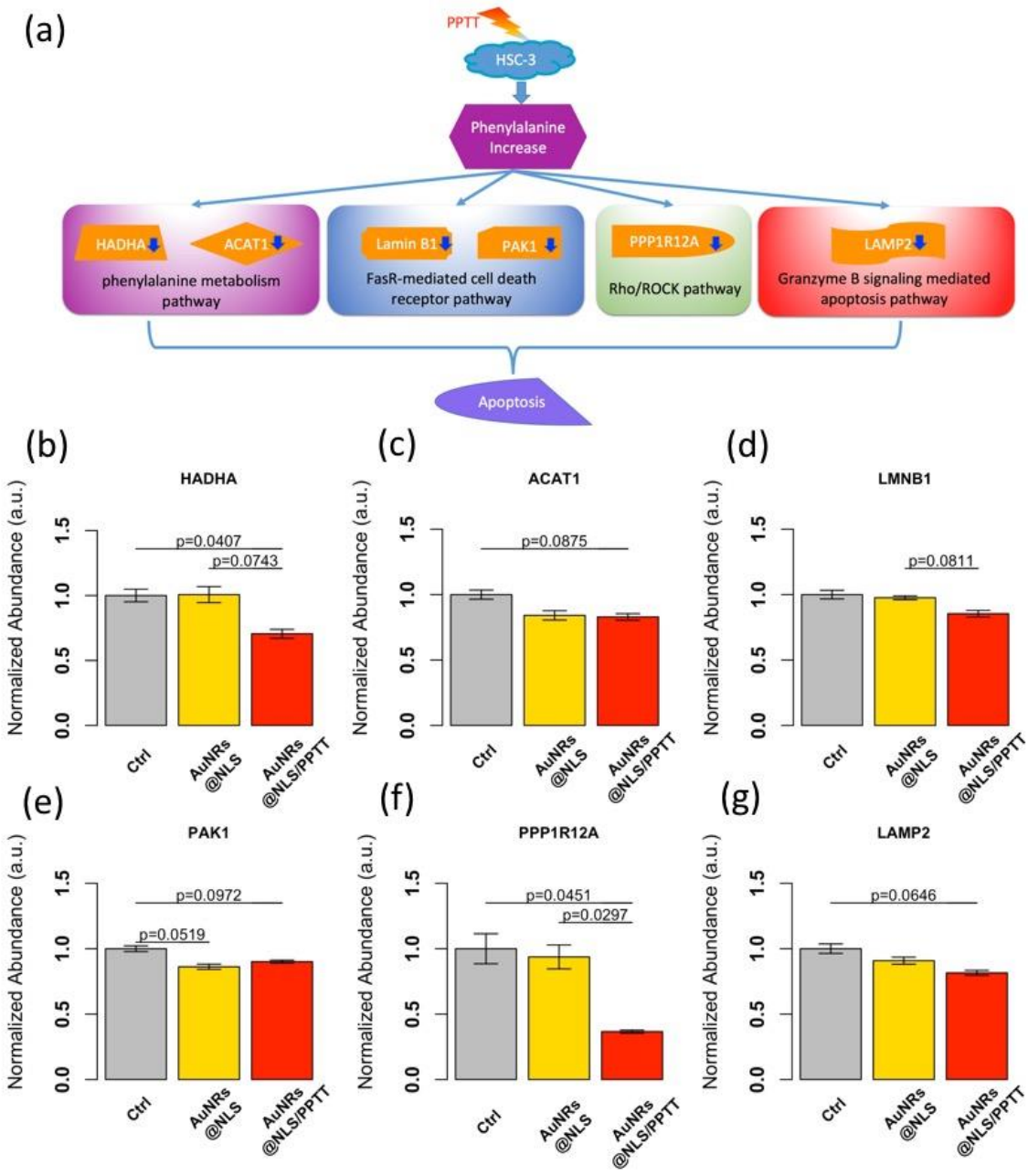

Figure 2-18. (A) Schematic diagram explaining the molecular apoptosis mechanisms involved in altering phenylalanine metabolism as induced by PPTT

(B-G) Bar graphs showing the normalized abundance of key proteins contributing to apoptosis involved in altering phenylalanine metabolism following PPTT. Normalized abundances of key proteins following AuNRs@NLS without PPTT are also given for comparison. (B) HADHA. (C) ACAT1. (D) Lamin B1 (LMNB1). (E) PAK1. (F) PPP1R12A. (G) LAMP2.

Time-dependent SERS has recently enabled to probe molecular changes in single (cancer) cells in time during the full cell cycle, or as the cell dies from exposure to drugs or from heat treatment. SERS accurately follows changes in cellular and subcellular environments during the onset and progression of processes such as apoptosis and mitosis [7] in real-time and at a single cell level. Cells present several active molecular Raman bands associated with bio-molecules located within the AuNP plasmonic field.

Herein, we coupled SERS measurements with metabolomics and proteomics experiments performed on the same set of samples, aiming to study the change of the subcellular microenvironment around AuNRs during the PPTT process. Our SERS data showed that the 1000, 1207 and 1580 cm^{-1} bands increased during PPTT, which suggested an increase of phenylalanine and its derivatives. These findings were confirmed with whole cell metabolomics experiments using high resolution mass spectrometry. We observed an increase of free phenylalanine, together with an increase of its derivatives and phenylalanine-containing peptides. Integrative analysis of proteomics and metabolomics data also showed that the proteins and metabolites in the phenylalanine metabolism pathway related to apoptosis were perturbed in apoptosis direction. Elevated levels of phenylalanine have been implicated in mitochondria-mediated apoptosis through Rho/ROCK pathway and Fas/Fas ligand mediated apoptosis. [50,58] In this study, both pathways were changed in favor of apoptosis in PPTT where level of phenylalanine was increased. In addition, the results suggested that during phenylalanine-induced apoptosis, lysosome integrity may have been perturbed, which may further contribute to cell death. This hypothesis was further strengthened by the observation of an increasing pattern of pyrrole breathing mode ν_{15} in cytochrome c shown in the SERS spectra (750 cm^{-1}), which

suggests the increase of apoptotic cells during thermal heating through cytochrome c-mediated apoptosis, which agrees with flow cytometry data (**Appendix Figure A.14**.). Meanwhile, some other apoptosis pathways were revealed by proteomics in **Appendix Figure A.25**.

Further investigations into the mechanism of how PPTT treatment increases phenylalanine levels in cells focused on the fact that phenylalanine can be converted to L-tyrosine. [59-60] Metabolomics data indicated that after PPTT treatment, the level of L-tyrosine was decreased **(Appendix Figure A.23**.). Based on our results, the channel allowing for the conversion from phenylalanine to L-tyrosine could have contributed to the accumulation of phenylalanine, which further induced mitochondria-mediated apoptosis.

We observed in our result that several metabolites/proteins change abundance in the presence of AuNRs even without light exposure, which is possibly due to the gold nanoparticles alone could perturbed apoptosis pathways of the biological system, which is reported previously. [61] This effect, however, comparing to the effect of PPTT treatment on apoptosis pathways, is to a much smaller extend, and did not cause actual apoptosis (**Appendix Figure A.13**.).

Besides phenylalanine dependent process, we further identified significantly perturbed pathways by integrative analysis of proteomics and metabolomics (**Appendix Figure A.24.).** Other amino acids metabolism pathways are enriched, including methionine-cysteine-glutamate, and lysine metabolism, which are very essential for the basic survival of the cells. Interestingly, we also found clues on the perturbation of pathways related to lipid metabolism and ketone body metabolism. [62-63]

2.4.4 Conclusion and Future Outlook

By integrative analysis of Raman spectroscopy profiles, metabolomics and proteomics mass spectrometric data, we discovered that free phenylalanine and associated metabolites are significantly perturbed by PPTT, leading to cell apoptosis. We therefore propose that phenylalanine measurements by SERS can be developed as a sensitive and convenient readout for non-invasive direct apoptosis characterization.

2.4.5 References

1. Ali, M. R.; Wu, Y.; Han, T.; Zang, X.; Xiao, H.; Tang, Y.; Wu, R.; Fernandez, F. M.; El-Sayed, M. A., (2016) Simultaneous Time-dependent Surface Enhanced Raman Spectroscopy, Metabolomics and Proteomics Reveal Cancer Cell Death Mechanisms Associated with Au-Nanorod Photo-thermal Therapy. *Journal of the American Chemical Society*.

2. Qian, X. M.; Peng, X. H.; Ansari, D. O.; Yin-Goen, Q.; Chen, G. Z.; Shin, D. M.; Yang, L.; Young, A. N.; Wang, M. D.; Nie, S. M., (2008) In vivo tumor targeting and spectroscopic detection with surface-enhanced Raman nanoparticle tags. *Nature Biotechnology*, *26* (1), 83-90.

3. Kneipp, J.; Kneipp, H.; Kneipp, K., (2008) SERS--a single-molecule and nanoscale tool for bioanalytics. *Chem Soc Rev*, *37* (5), 1052-60.

4. Jain, P. K.; Huang, X.; El-Sayed, I. H.; El-Sayed, M. A., (2008) Noble metals on the nanoscale: optical and photothermal properties and some applications in imaging, sensing, biology, and medicine. *Acc Chem Res*, *41* (12), 1578-86.

5. Willets, K. A.; Van Duyne, R. P., (2007) Localized surface plasmon resonance spectroscopy and sensing. *Annu. Rev. Phys. Chem.*, *58*, 267-297.

6. Stiles, P. L.; Dieringer, J. A.; Shah, N. C.; Van Duyne, R. P., (2008) Surface-enhanced Raman spectroscopy. *Annual review of analytical chemistry (Palo Alto, Calif.)*, *1*, 601-26.

7. Kang, B.; Austin, L. A.; El-Sayed, M. A., (2014) Observing Real-Time Molecular Event Dynamics of Apoptosis in Living Cancer Cells using Nuclear-Targeted Plasmonically Enhanced Raman Nanoprobes. *ACS Nano*, *8* (5), 4883-4892.

8. Keskin, S.; Efeoglu, E.; Kececi, K.; Culha, M., (2013) Label-free detection of proteins in ternary mixtures using surface-enhanced Raman scattering and protein melting profiles. *J Biomed Opt*, *18* (3), 037007.

9. Huang, X.; Jain, P. K.; El-Sayed, I. H.; El-Sayed, M. A., (2008) Plasmonic photothermal therapy (PPTT) using gold nanoparticles. *Lasers in medical science*, *23* (3), 217-28.

10. Alkilany, A. M.; Thompson, L. B.; Boulos, S. P.; Sisco, P. N.; Murphy, C. J., (2012) Gold nanorods: their potential for photothermal therapeutics and drug delivery, tempered by the complexity of their biological interactions. *Adv Drug Deliv Rev*, *64* (2), 190-9.

11. Huang, X.; El-Sayed, I. H.; Qian, W.; El-Sayed, M. A., (2006) Cancer Cell Imaging and Photothermal Therapy in the Near-Infrared Region by Using Gold Nanorods. *Journal of the American Chemical Society*, *128* (6), 2115-2120.

12. Ali, M. R.; Ibrahim, I. M.; Ali, H. R.; Selim, S. A.; El-Sayed, M. A., (2016) Treatment of natural mammary gland tumors in canines and felines using gold nanorods-assisted plasmonic photothermal therapy to induce tumor apoptosis. *International Journal of Nanomedicine, 11*, 4849.

13. Niidome, T.; Yamagata, M.; Okamoto, Y.; Akiyama, Y.; Takahashi, H.; Kawano, T.; Katayama, Y.; Niidome, Y., (2006) PEG-modified gold nanorods with a stealth character for in vivo applications. *Journal of Controlled Release, 114* (3), 343-347.

14. Dickerson, E. B.; Dreaden, E. C.; Huang, X. H.; El-Sayed, I. H.; Chu, H. H.; Pushpanketh, S.; McDonald, J. F.; El-Sayed, M. A., (2008) Gold nanorod assisted near-infrared plasmonic photothermal therapy (PPTT) of squamous cell carcinoma in mice. *Cancer letters, 269* (1), 57-66.

15. Mukherjee, P.; Abate, L. E.; Seyfried, T. N., (2004) Antiangiogenic and proapoptotic effects of dietary restriction on experimental mouse and human brain tumors. *Clin Cancer Res, 10*.

16. Melamed, J. R.; Edelstein, R. S.; Day, E. S., (2015) Elucidating the Fundamental Mechanisms of Cell Death Triggered by Photothermal Therapy. *Acs Nano, 9* (1), 6-11.

17. Perez-Hernandez, M.; del Pino, P.; Mitchell, S. G.; Moros, M.; Stepien, G.; Pelaz, B.; Parak, W. J.; Galvez, E. M.; Pardo, J.; de la Fuente, J. M., (2015) Dissecting the Molecular Mechanism of Apoptosis during Photothermal Therapy Using Gold Nanoprisms. *Acs Nano, 9* (1), 52-61.

18. Narayanan, N.; Nair, L. V.; Karunakaran, V.; Joseph, M. M.; Nair, J. B.; Ramya, A. N.; Jayasree, R. S.; Maiti, K. K., (2016) Investigation of apoptotic events at molecular

level induced by SERS guided targeted theranostic nanoprobe. *Nanoscale*, *8* (22), 11392-11397.

19. Aliaga, A. E.; Osorio-Roman, I.; Leyton, P.; Garrido, C.; Carcamo, J.; Caniulef, C.; Celis, F.; Diaz, G.; Clavijo, E.; Gomez-Jeria, J. S.; Campos-Vallette, M. M., (2009) Surface-enhanced Raman scattering study of L-tryptophan. *Journal of Raman Spectroscopy*, *40* (2), 164-169.

20. Zhu, G.; Zhu, X.; Fan, Q.; Wan, X., (2011) Raman spectra of amino acids and their aqueous solutions. *Spectrochimica acta. Part A, Molecular and biomolecular spectroscopy*, *78* (3), 1187-95.

21. Maiti, N. C.; Apetri, M. M.; Zagorski, M. G.; Carey, P. R.; Anderson, V. E., (2004) Raman spectroscopic characterization of secondary structure in natively unfolded proteins: alpha-synuclein. *J Am Chem Soc*, *126* (8), 2399-408.

22. Turkevich, J.; Stevenson, P. C.; Hillier, J., (1951) A study of the nucleation and growth processes in the synthesis of colloidal gold. *Discussions of the Faraday Society*, *11* (0), 55-75.

23. Ali, M. R.; Snyder, B.; El-Sayed, M. A., (2012) Synthesis and optical properties of small Au nanorods using a seedless growth technique. *Langmuir*, *28* (25), 9807-9815.

24. Ellman, G. L., (1959) Tissue sulfhydryl groups. *Archives of Biochemistry and Biophysics*, *82* (1), 70-77.

25. Austin, L. A.; Ahmad, S.; Kang, B.; Rommel, K. R.; Mahmoud, M.; Peek, M. E.; El-Sayed, M. A., (2015) Cytotoxic effects of cytoplasmic-targeted and nuclear-targeted gold and silver nanoparticles in HSC-3 cells--a mechanistic study. *Toxicology in vitro : an international journal published in association with BIBRA*, *29* (4), 694-705.

26. Martano, G.; Delmotte, N.; Kiefer, P.; Christen, P.; Kentner, D.; Bumann, D.; Vorholt, J. A., (2015) Fast sampling method for mammalian cell metabolic analyses using liquid chromatography–mass spectrometry. *Nat. Protocols*, *10* (1), 1-11.

27. Wu, Y.; Wang, F. J.; Liu, Z. Y.; Qin, H. Q.; Song, C. X.; Huang, J. F.; Bian, Y. Y.; Wei, X. L.; Dong, J.; Zou, H. F., (2014) Five-plex isotope dimethyl labeling for quantitative proteomics. *Chemical Communications*, *50* (14), 1708-1710.

28. Xiao, H.; Tang, G. X.; Wu, R., (2016) Site-Specific Quantification of Surface N-Glycoproteins in Statin-Treated Liver Cells. *Anal Chem*, *88* (6), 3324-32.

29. Eng, J. K.; McCormack, A. L.; Yates, J. R., (1994) An approach to correlate tandem mass spectral data of peptides with amino acid sequences in a protein database. *Journal of the American Society for Mass Spectrometry*, *5* (11), 976-989.

30. Elias, J. E.; Gygi, S. P., (2007) Target-decoy search strategy for increased confidence in large-scale protein identifications by mass spectrometry. *Nat Methods*, *4* (3), 207-14.

31. Kall, L.; Canterbury, J. D.; Weston, J.; Noble, W. S.; MacCoss, M. J., (2007) Semi-supervised learning for peptide identification from shotgun proteomics datasets. *Nat Methods*, *4* (11), 923-5.

32. Mecham, B. H.; Nelson, P. S.; Storey, J. D., (2010) Supervised normalization of microarrays. *Bioinformatics*, *26* (10), 1308-15.

33. Li, S.; Park, Y.; Duraisingham, S.; Strobel, F. H.; Khan, N.; Soltow, Q. A.; Jones, D. P.; Pulendran, B., (2013) Predicting Network Activity from High Throughput Metabolomics. *PLOS Computational Biology*, *9* (7), e1003123.

34. Ali, M. R. K.; Snyder, B.; El-Sayed, M. A., (2012) Synthesis and Optical Properties of Small Au Nanorods Using a Seedless Growth Technique. *Langmuir*, *28* (25), 9807-9815.

35. Mackey, M. A.; Ali, M. R.; Austin, L. A.; Near, R. D.; El-Sayed, M. A., (2014) The most effective gold nanorod size for plasmonic photothermal therapy: theory and in vitro experiments. *The Journal of Physical Chemistry B*, *118* (5), 1319-1326.

36. Prencipe, G.; Tabakman, S. M.; Welsher, K.; Liu, Z.; Goodwin, A. P.; Zhang, L.; Henry, J.; Dai, H., (2009) PEG branched polymer for functionalization of nanomaterials with ultralong blood circulation. *J Am Chem Soc*, *131* (13), 4783-7.

37. Ruoslahti, E.; Pierschbacher, M. D., (1986) Arg-Gly-Asp: a versatile cell recognition signal. *Cell*, *44* (4), 517-8.

38. Kalderon, D.; Roberts, B. L.; Richardson, W. D.; Smith, A. E., (1984) A short amino acid sequence able to specify nuclear location. *Cell*, *39* (3 Pt 2), 499-509.

39. Ali, M. R.; Panikkanvalappil, S. R.; El-Sayed, M. A., (2014) Enhancing the efficiency of gold nanoparticles treatment of cancer by increasing their rate of endocytosis and cell accumulation using rifampicin. *Journal of the American Chemical Society*, *136* (12), 4464-4467.

40. Ali, M. R. K.; Ali, H. R.; Rankin, C. R.; El-Sayed, M. A., (2016) Targeting heat shock protein 70 using gold nanorods enhances cancer cell apoptosis in low dose plasmonic photothermal therapy. *Biomaterials*, *102*, 1-8.

41. Panikkanvalappil, S. R.; Hira, S. M.; Mahmoud, M. A.; El-Sayed, M. A., (2014) Unraveling the Biomolecular Snapshots of Mitosis in Healthy and Cancer Cells Using

Plasmonically-Enhanced Raman Spectroscopy. *Journal of the American Chemical Society*, *136* (45), 15961-15968.

42. Kang, B.; Mackey, M. A.; El-Sayed, M. A., (2010) Nuclear Targeting of Gold Nanoparticles in Cancer Cells Induces DNA Damage, Causing Cytokinesis Arrest and Apoptosis. *Journal of the American Chemical Society*, *132* (5), 1517-+.

43. Hernández, B.; Pflüger, F.; Kruglik, S. G.; Ghomi, M., (2013) Characteristic Raman lines of phenylalanine analyzed by a multiconformational approach. *Journal of Raman Spectroscopy*, *44* (6), 827-833.

44. Zhang, J.; Huang, Q.; Yao, G.; Ke, Z.; Zhang, H.; Lu, Y., (2014) SERS study of transformation of phenylalanine to tyrosine under particle irradiation. *Journal of Molecular Structure*, *1072*, 195-202.

45. Kim, S. K.; Kim, M. S.; Suh, S. W., (1987) Surface-Enhanced Raman-Scattering (Sers) Of Aromatic-Amino-Acids And Their Glycyl Dipeptides In Silver Sol. *Journal of Raman Spectroscopy*, *18* (3), 171-175.

46. Okada, M.; Smith, N. I.; Palonpon, A. F.; Endo, H.; Kawata, S.; Sodeoka, M.; Fujita, K., (2012) Label-free Raman observation of cytochrome c dynamics during apoptosis. *Proc Natl Acad Sci U S A*, *109* (1), 28-32.

47. Hamada, K.; Fujita, K.; Smith, N. I.; Kobayashi, M.; Inouye, Y.; Kawata, S., (2008) Raman microscopy for dynamic molecular imaging of living cells. *J Biomed Opt*, *13* (4), 044027.

48. Lo, Y. W.; Lin, S. T.; Chang, S. J.; Chan, C. H.; Lyu, K. W.; Chang, J. F.; May, E. W.; Lin, D. Y.; Chou, H. C.; Chan, H. L., (2015) Mitochondrial proteomics with siRNA

knockdown to reveal ACAT1 and MDH2 in the development of doxorubicin-resistant uterine cancer. *Journal of cellular and molecular medicine, 19* (4), 744-59.

49. Gonzalez, V. M.; Fuertes, M. A.; Alonso, C.; Perez, J. M., (2001) Is Cisplatin-Induced Cell Death Always Produced by Apoptosis? *Molecular Pharmacology, 59* (4), 657-663.

50. Huang, X.; Lu, Z.; Lv, Z.; Yu, T.; Yang, P.; Shen, Y.; Ding, Y.; Fu, D.; Zhang, X.; Fu, Q.; Yu, Y., (2013) The Fas/Fas ligand death receptor pathway contributes to phenylalanine-induced apoptosis in cortical neurons. *PLoS One, 8* (8), e71553.

51. Sato, A.; Hiramoto, A.; Satake, A.; Miyazaki, E.; Naito, T.; Wataya, Y.; Kim, H. S., (2008) Association of nuclear membrane protein lamin B1 with necrosis and apoptosis in cell death induced by 5-fluoro-2'-deoxyuridine. *Nucleosides, nucleotides & nucleic acids, 27* (5), 433-8.

52. Freund, A.; Laberge, R. M.; Demaria, M.; Campisi, J., (2012) Lamin B1 loss is a senescence-associated biomarker. *Mol Biol Cell, 23* (11), 2066-75.

53. Rao, L.; Perez, D.; White, E., (1996) Lamin proteolysis facilitates nuclear events during apoptosis. *The Journal of cell biology, 135* (6 Pt 1), 1441-55.

54. Zha, J.; Harada, H.; Yang, E.; Jockel, J.; Korsmeyer, S. J., (1996) Serine phosphorylation of death agonist BAD in response to survival factor results in binding to 14-3-3 not BCL-X(L). *Cell, 87* (4), 619-28.

55. Schurmann, A.; Mooney, A. F.; Sanders, L. C.; Sells, M. A.; Wang, H. G.; Reed, J. C.; Bokoch, G. M., (2000) p21-activated kinase 1 phosphorylates the death agonist bad and protects cells from apoptosis. *Mol Cell Biol, 20* (2), 453-61.

56. Jin, S.; Zhuo, Y.; Guo, W.; Field, J., (2005) p21-activated Kinase 1 (Pak1)-dependent phosphorylation of Raf-1 regulates its mitochondrial localization, phosphorylation of BAD, and Bcl-2 association. *J Biol Chem*, *280* (26), 24698-705.

57. Iwasaki, T.; Katayama, T.; Kohama, K.; Endo, Y.; Sawasaki, T., (2013) Myosin phosphatase is inactivated by caspase-3 cleavage and phosphorylation of myosin phosphatase targeting subunit 1 during apoptosis. *Mol Biol Cell*, *24* (6), 748-56.

58. Koyanagi, M.; Takahashi, J.; Arakawa, Y.; Doi, D.; Fukuda, H.; Hayashi, H.; Narumiya, S.; Hashimoto, N., (2008) Inhibition of the Rho/ROCK pathway reduces apoptosis during transplantation of embryonic stem cell-derived neural precursors. *J Neurosci Res*, *86* (2), 270-80.

59. Kaufman, S., (1993) The phenylalanine hydroxylating system. *Advances in enzymology and related areas of molecular biology*, *67*, 77-264.

60. Moller, N.; Meek, S.; Bigelow, M.; Andrews, J.; Nair, K. S., (2000) The kidney is an important site for in vivo phenylalanine-to-tyrosine conversion in adult humans: A metabolic role of the kidney. *Proc Natl Acad Sci U S A*, *97* (3), 1242-6.

61. Pan, Y.; Neuss, S.; Leifert, A.; Fischler, M.; Wen, F.; Simon, U.; Schmid, G.; Brandau, W.; Jahnen-Dechent, W., (2007) Size-dependent cytotoxicity of gold nanoparticles. *Small*, *3* (11), 1941-9.

62. Seyfried, T. N.; Mukherjee, P., (2005) Targeting energy metabolism in brain cancer: review and hypothesis. *Nutrition & Metabolism*, *2* (1), 30.

63. Mukherjee, P.; El-Abbadi, M. M.; Kasperzyk, J. L.; Ranes, M. K.; Seyfried, T. N., (2002) Dietary restriction reduces angiogenesis and growth in an orthotopic mouse brain tumour model. *Br J Cancer*, *86* (10), 1615-21.

CHAPTER 3. APPLYING THE PLASMONIC PHOTOTHERMAL THERAPY IN XENOGRAFT MICE AND NATURAL MAMMARY GLAND TUMORS

3.1 The Long-Term Effects of Gold Nanorods in a Mouse Model: Circulation, Biodistribution, and Toxicity [1]

Gold nanorods (AuNRs) have great potential in plasmonic photothermal therapy (PPTT) for the treatment of cancer. However, there is limited knowledge regarding their biodistribution, long-term fate, and systemic toxicity. Herein, we examine the long-term toxicity (15 months) of AuNRs size (72 x 19 nm), the surface coating (polyethylene glycol (PEG) in BALB/c mice. Our results demonstrate that the density of PEG on the surface of AuNRs greatly decreases, while increasing tumor accumulation of AuNRs. More importantly, we observed no organ morphology changes after exposure to AuNRs for 15 months. In conclusions: To our knowledge, this is longest duration systemic toxicity and biodistribution study of AuNRs to date and these results suggest that AuNRs are safe and viable as anti-cancer agents.

3.1.1 Introduction

Owing to their absorption in the near infrared region, gold nanorods (AuNRs) have demonstrated great potential for use in plasmonic photothermal therapy (PPTT) of cancer, [2-4] as well as diagnostic imaging and biosensing. [5,6] However, there is insufficient

knowledge of their long-term fate, systemic toxicity and biodistribution with respect to surface coating (including tumor targeting ligands) and particle size.

The use of gold nanoparticles in *in vitro* cancer diagnosis and treatment [2,3,7] has drawn considerable attention to their potential *in vivo* toxicity profile, which remains largely undefined [8]. While one study has reported that citrate-capped AuNPs do not demonstrate significant cytotoxicity [9], other studies report that their presence in dermal fibroblasts results in actin stress, thus inducing major adverse effects on cell viability. [10] Some studies have shown that PEG-coated spherical AuNPs induce apoptosis and inflammation in a mouse liver, indicating the possibility of acute toxicity induced by other types of AuNPs. [11] While several other studies have reported that there is no significant short-term toxicity of AuNPs. [20,19, 21] The preservation of AuNPs, without significant clearance from the body for over six months, has been reported for spherical AuNPs.[5] Such accumulation of metallic AuNPs within the body, over a long-time, raises significant concerns regarding their long-term safety. Toxicity is also reported to be largely dependent on the size, shape, structure, and surface properties of the AuNPs.[15, 17] A comprehensive investigation of the organ uptake, biodistribution, long-term fate, and toxicity of AuNRs, based on size and surface chemistry, is essential to the fundamental understanding of *in vivo* biological interactions of these nanoparticles.[18, 19] Polyethylene glycol (PEG) is known to safeguard against plasma protein adsorption *in vivo* and has thus been widely used as a biocompatible stabilizing agent of AuNPs, enabling passive tumor targeting via the enhanced permeability and retention (EPR).[9, 18, 22-27] However, it is not fully understood whether PEG molecular weight and additional conjugation of tumor targeting ligands affects biodistribution or toxicity *in vivo*. In the present study, we have synthesized

AuNRs with the size of 72 x 19 nm (width x length). We modified the particle surface with varying densities of PEG (500, 1000 and 10000 PEG ligands/AuNR), and further conjugated the AuNRs with a head and neck squamous cell carcinoma targeting peptide (HNSCP-1). We have determined the biodistribution and the associated toxicities of these AuNRs in a BALB/c xenograft mouse model of squamous cell carcinoma of the head and neck squamous cell carcinoma (SCCHN). In addition, the short-term and long-term fate (up to 15 months) of the different AuNRs were also investigated. Our results suggest that AuNR-based agents provide a promising approach for the treatment of head and neck cancer.

3.1.2 Experimental Methods

3.1.2.1 AuNRs (72 X 19nm) Synthesis by Seed-Mediated Growth Method [27]

AuNRs of 72 nm length were synthesized at 25°C using the seed-mediated growth method where a seed solution consisting of 0.2 M CTAB, 1.0 mM $HAuCl_4$ and 0.01 M $NaBH_4$ was prepared and added to a growth solution containing 1.0 mM $HAuCl_4$, 0.2 M CTAB, 4.0 mM silver nitrate and 78.8 mM ascorbic acid. The aspect ratio and a surface plasmon resonance (SPR) of the AuNRs were obtained by adjusting the amount of silver nitrate added to the growth solution, and the large CTAB stabilized AuNRs were purified by centrifugation and redispersed in DI H_2O.

3.1.2.2 Functionalization of AuNRs

AuNRs were conjugated with a thiol-modified PEG (M.wt 5000) at varying surface coverages; 500, 1000 and 10000 PEG/AuNR while small AuNRs were conjugated with 1000, and 10000 PEG/AuNR. The PEG bounded to the surface has been calculated by the measuring the difference between the concentration of the original PEG before addition to the AuNRs and the one that left in the supernatant (with free -SH group) using Elman's reagents by calculating the molarity of (-SH) groups in the assay find the absorbance and divide by 13600 M^{-1} cm^{-1} (the extinction coefficient of the reagent).[29] It was observed that AuNRs' stability increased with increasing surface coverage of the PEG ligands. PEG-modified AuNRs were purified with centrifugation and redispersed in DI H_2O. In order to confirm nanoparticle functionalization, the hydrodynamic diameter (HD) and the size of the AuNRs were measured via dynamic light scattering (DLS) and transmission electron microscope (TEM).

3.1.2.3 Blood Clearance Properties of AuNRs

These experiments were carried out in BALB/c mice (male), 6 weeks of age. The animals were injected via the tail vein with AuNRs. At specified time points of 5 min, 30 min, 2 h, 4 h, 6 h, 8 h, 24 h and 48 h, blood was collected from the retro-orbital sinus in pre-weighed heparinized capillary tubes. The blood samples were dissolved with 70% nitric acid and assayed for Au using ICP-MS. Blood clearance was analyzed with a two-

compartmental model using WinNonlin 5.0.1 software. In Figure 7, the blood half-lives were compared for the different AuNRs tested.

3.1.2.4 Short-term and Long-Term Uptake Fate of PEG-coated AuNRs

BALB/C mice (male), 6 weeks of age, were injected via the tail vein with 200 μl solution of AuNRs (0.18mg/kg). At specified time points of 1, 3, 7, 14, 30, 60, and 90 days and 15 months, the mice were euthanized by pressurized CO_2 asphyxiation, 3 mouse each group. Organs including the liver, spleen, kidney and lung were collected, rinsed with distilled water and dried. The dried tissues were dissolved and assayed for Au using ICP-MS, and parts of the organs (liver, spleen, kidney, lung) and muscle (under skin from mouse right flank, ~20 mg) were collected and fixed in 10% (v/v) neutral buffered formalin for further pathology tests. After AuNRs injection, mice were monitored for clinical signs of toxicities including ruffled fur, impeded movement, clear sign of abnormal constitution, aberrant behavior, obvious loss of weight, ocular or nasal discharge, and respiratory distress, the inability of the animals to walk and diarrhea. [16, 31]

3.1.2.5 Peripheral Blood Analysis

Following the treatment, the mice were sacrificed by CO_2. One ml of blood was immediately harvested in a heparinized tube. Blood hematology analyses were performed using an automatic hematology analyzer which included complete blood count (CBC),

hemoglobin (Hb), platelet (Plt), LDH (lactate dehydrogenase), and white blood cell count with differentials (neutrophil, lymphocytes and eosinophils). Serum samples were subjected to chemical analyses of glutamic pyruvate transaminase (GPT), glutamic oxaloacetic transaminase (GOT), blood urea nitrogen (BUN), and creatinine (CRE) levels using Theoretical Tests Per Kit, on the P-Modular Analytics System manufactured by Roche Diagnostics Inc. (Indianapolis, IN).

The blood clearance properties of the targeted AuNRs were examined in a healthy mouse model using the same procedure as described above. For tumor uptake studies, Tu212 cells were subcutaneously planted into the right flank of nude mice (Charles Rivers, Portage, MI), 6-7 weeks of age, 3 mice per group, and were allowed to grow to approximately 250 mm3. AuNRs and a control with saline alone in PBS buffer were injected into mice bloodstream via the tail vein. After 2 h, 8 h, 24 h, 48 h and 72 h, the mice were euthanized by pressurized CO2 asphyxiation based on IACUC guidelines, and blood, tumor, liver, spleen, kidney, lung, brain, bladder and muscle were collected and assayed for Au content using ICP as described above.

3.1.2.6 Histopathology Evaluation

As described above, the liver, spleen, kidney and lung were dissected from the mice for histopathological analysis. The tissues were embedded in paraffin and cut at a 5 μm thickness. The tissues were stained with hematoxylin and eosin (H & E) to assess

pathology. The detailed pathologic evaluation of all organs at different time points was conducted by American Board Certified Pathologist (HJCS).

3.1.2.7 Nude Mice Bearing Human HNC Xenograft Tumor Model

For the tumor uptake studies, the tumors were inoculated by injection of 1x106 HNC Tu212 cells subcutaneously into the right flank of nude mice (Charles Rivers, Portage, MI), 6-7 weeks of age, 3 mice per group, and were allowed to grow to approximately 250 mm^3 (calculated by ab2/2, with a, b representing tumor length and width respectively).

3.1.2.8 Statistical Analysis

Paired t-test was conducted to compare differences in the values of same outcome variables (Au concentration, body weight change) from the same samples at two different time points. Two sample t-test were used for different samples. One-way analysis of variance (ANOVA) was employed to test the overall significance across multiple groups. We further evaluated pair-wise differences by using Tukey's method when the overall difference was significant at a p value of 0.05. The SAS statistical package (SAS Institute, Inc.) was used for all data management and analyses.

3.1.3 Results and Discussion

AuNRs with a surface plasmon resonance at approximately 800 nm (typically prepared for use as plasmonic photothermal contrast agents) were achieved (**Figure 3-1a**). The surface of the AuNRs was modified via conjugation with PEG (see Methods section). The effect of PEG density on the AuNR surface was studied in terms of circulation half-life, as well as uptake, distribution, and clearance in the main organs. **Figure 3-1** shows that increasing the density of PEG ligands on the AuNR surface (500 ligands/AuNR versus 1000 ligands/AuNR) prolongs the circulation half-life (8.7 hr versus 14.7 hrs, respectively). In addition to circulation half-life, we also compared the uptake, distribution, and clearance of AuNRs in the main organs, including the liver, spleen, lungs, and kidney for up to 15 months after intravenous administration of PEG-conjugated AuNRs at 0.18 mg Au/kg (dose comparable to that reported previously).[32] The concentration of Au remaining in organ tissue was also quantified via ICP-MS. Figure 3a and b displays the concentration of Au (ng/mg dry tissue) in the RES organs (i.e. liver and spleen, respectively). PEG-conjugated AuNRs (500 and 1000 PEG ligands/AuNR) accumulate in the RES organs with no significant differences observed with increasing or decreasing PEG density on the AuNR surface. The majority of injected PEG-AuNRs were still localized in the liver and spleen after 15 months without any adverse morphology changes observed in these organs. Additionally, PEG-AuNRs were detected in mouse feces, but not urine (**Figure 3-3d**), suggesting that the PEG-AuNRs were primarily eliminated via bile secretion.

To complement the circulation half-life, biodistribution, and organ uptake of PEG-AuNRs, complete blood count (CBC), hemoglobin (Hb), platelet (Plt), LDH (lactate

dehydrogenase), and white blood cell count with differentials (neutrophil, lymphocytes and eosinophils) were tested at different time points following intravenous administration of PEG-AuNRs, showing no significant changes. To test for additional adverse effects, body weight (Figure 3-4a), blood urea nitrogen levels (BUN, **Figure 3-4b**), and creatinine levels (CRE, **Figure 3-4c**) were also measured. PEG-AuNRs had no significant effect on body weight, nor was there any observed effect on BUN or CRE levels, suggesting that intravenous administration of these AuNRs has a minimal impact on renal function. In addition, serum glutamic pyruvate transaminase (ALT) and glutamic oxaloacetic transaminase (AST) levels were quantified to evaluate the effects on hepatic function after administration of PEG-AuNRs of treated mice. Both ALT and AST levels did not change significantly in the treated groups compared with the control group (**Figure 3-4d**).

To further characterize the accumulation of the PEG-AuNRs in the RES organs (i.e. liver and spleen), transmission electron microscopy (TEM) was utilized to visually observe particle uptake and organ tissue microstructure. no adverse changes were observed in the liver and spleen tissue microstructure for up to 15 months following intravenous administration of AuNRs (**Figure 3-3a)** PEG-AuNRs. This finding could be significant, especially since our previous studies have shown that the AuNRs exhibit greater potential as photothermal contrast agents in PPTT, suggesting their enhanced utility in cancer therapeutics.

Our previous studies, as well as that of other researchers in the field, have demonstrated the great success of AuNR-assisted PPTT in the ablation of head and neck tumor xenografts, indicating their strong potential as plasmonic photothermal contrast agents for

the treatment of cancer in the clinic. That being said, we also realize the limited knowledge available regarding several characteristics of this new generation of cancer treatment agents, including their biodistribution, long-term fate, toxicity, tumor affinity, and how these properties are influenced by tuning the particle size, and surface coating. Toxicity of PEGylated spherical AuNPs, specifically inflammation in the liver, has been observed in other studies, suggesting the potential for adverse effects with other AuNP-based treatment platforms. (32) Our present study suggests that the long-term effects of AuNRs (up to 15 months in a mouse model) are minimal, in terms of toxicity to major organs. Increasing PEG density on the surface of AuNRs can prolong circulation half-life, while addition of a tumor targeting peptide (HNSCP-1) increases tumor uptake of AuNRs. Overall, our long-term study suggests that AuNP-based therapeutics do not exhibit significant toxicities, and therefore could demonstrate great promise as a cancer treatment platform in the clinic.

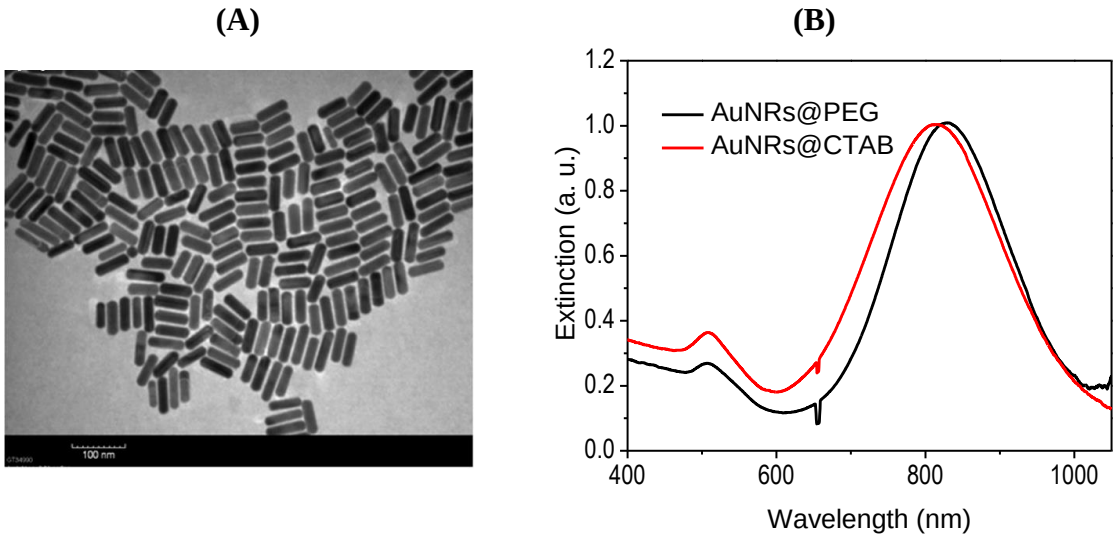

Figure 3-1 Characterization of AuNRs

(A) TEM of large rpods (Length 72±7 x Width 19±4 nm), (B) UV-Vis absorbance spectra of the large (Length 72 nm, black) CTAB-stabilized AuNRs. The SPR peaks of the large and small AuNRs were 767 nm.

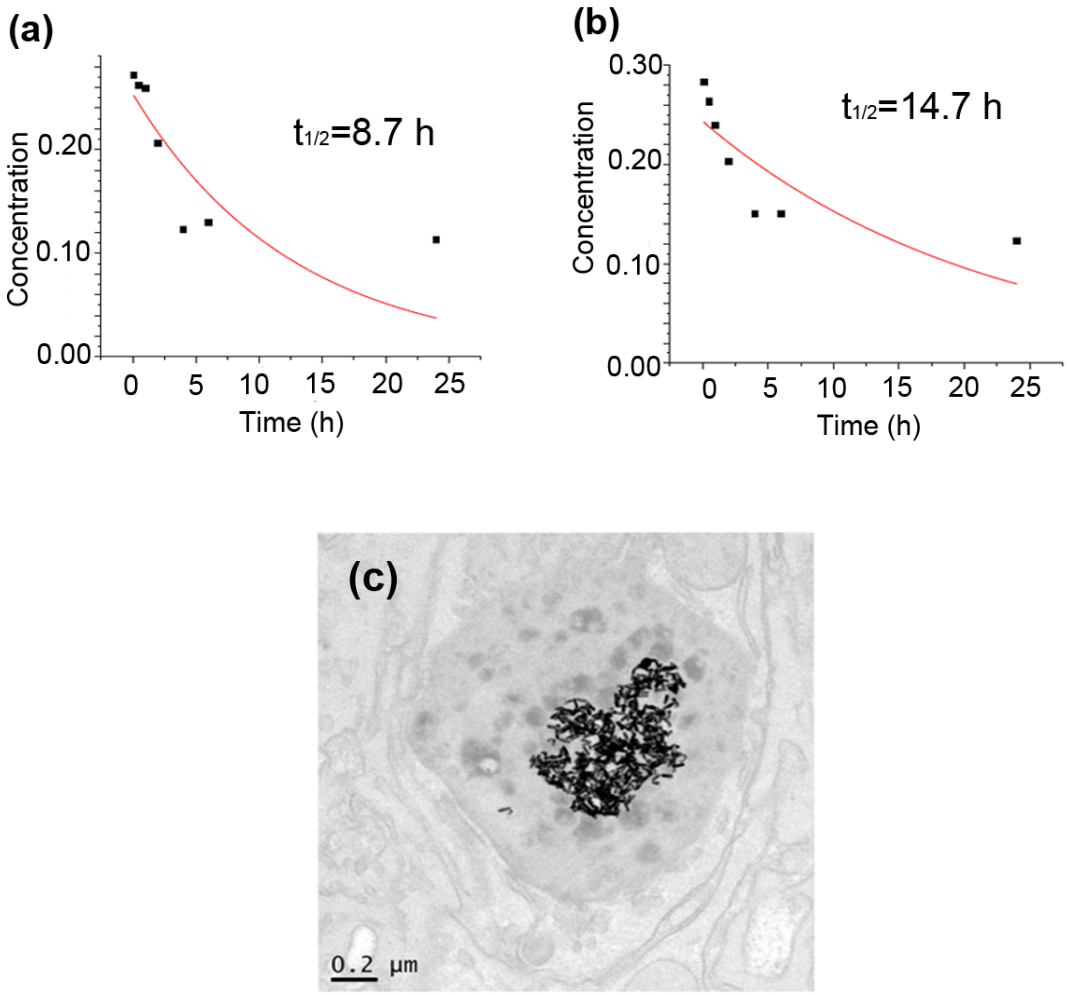

Figure 3-2: Blood half-life of PEG-conjugated AuNRs

(A) 500/AuNR and (B) 1000/AuNR. (C) TEM images shown that the 72 nm AuNRs showed no remarkable change in size or shape in the liver 15 months after systemic administration in mice.

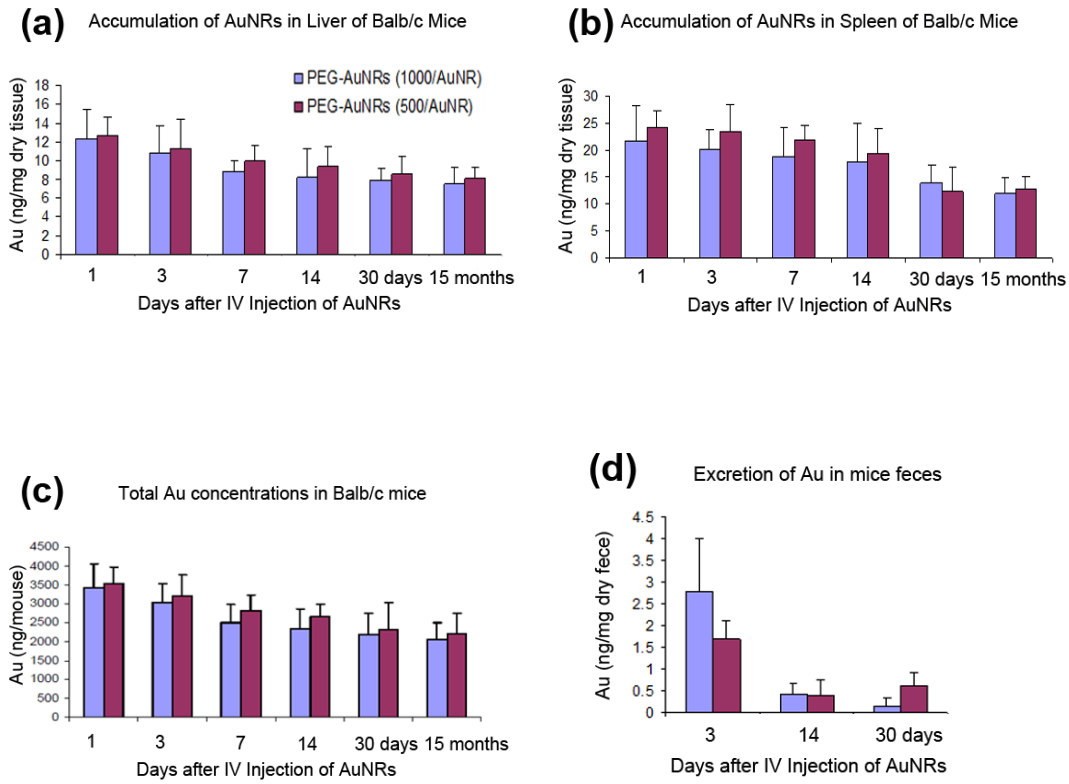

Figure 3-3. Au concentrations are shown in liver

(A) and spleen (B) of Balb/c mice at different time points after IV injection of a single dose of AuNRs (Au: 0.18mg/kg, 3 mice per group). Total Au concentrations in Balb/c mice (C) at different time points after IV injection of a single dose of AuNRs (Au: 0.18mg/kg, 3 mice per group). Excretion of Au in mice feces at different time points (D).

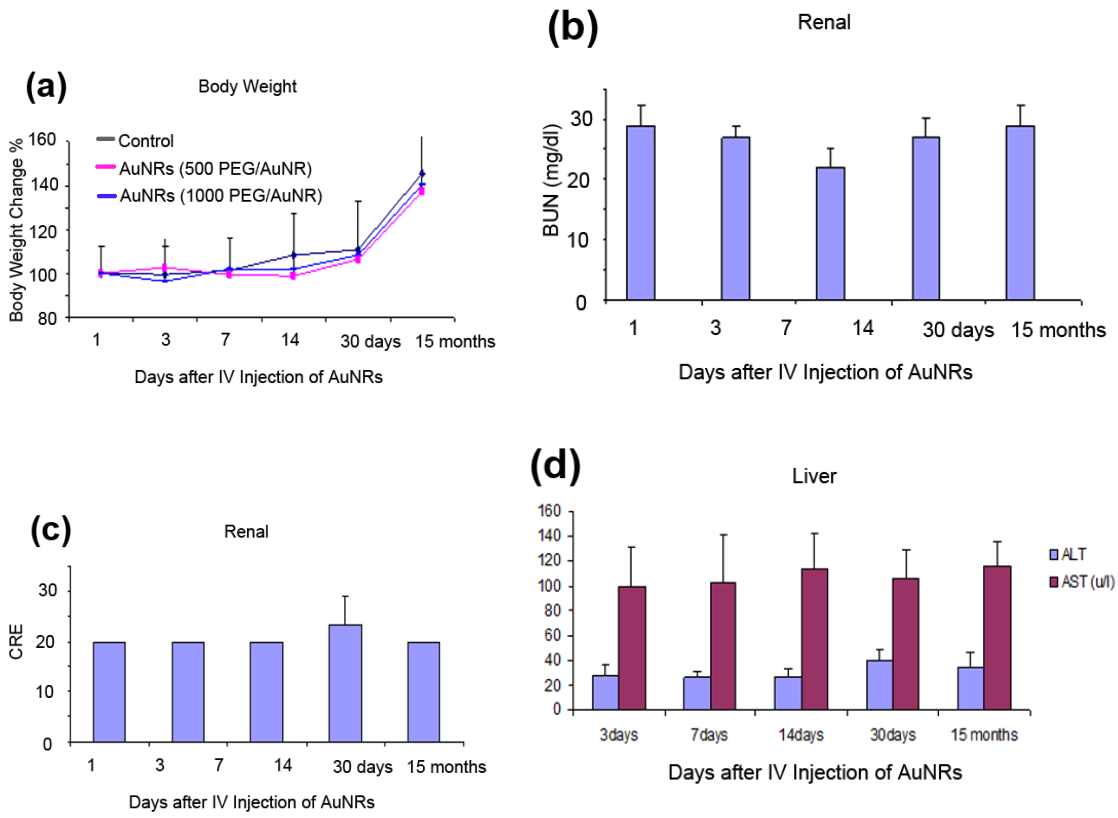

Figure 3-4 Toxicity

Body weight (A), renal (B, C) and liver (D) function changes in mice at different time points after IV injection of a single dose of the AuNRs (Au: 0.18mg/kg, 3 mice per group).

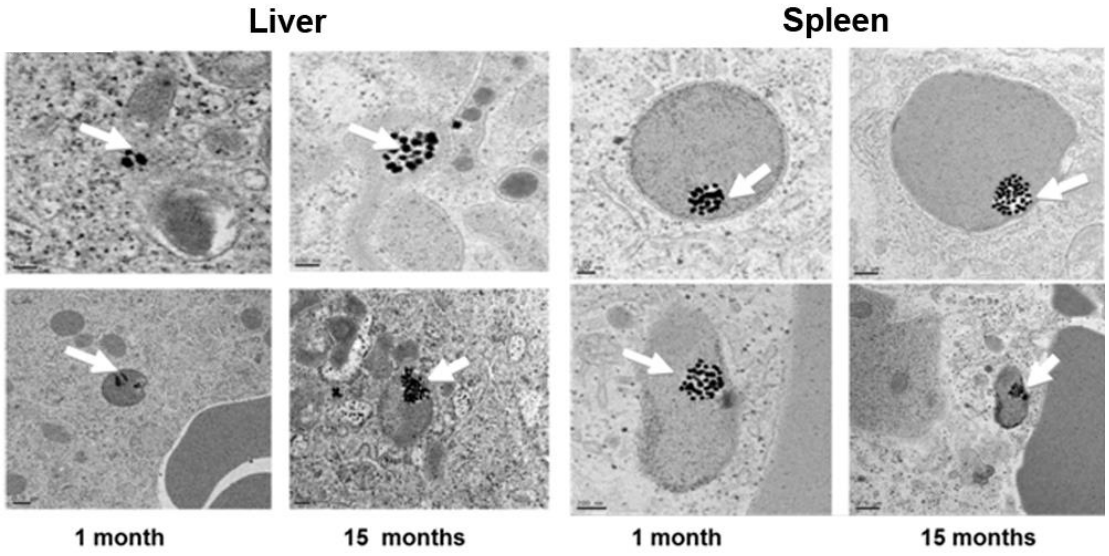

Figure 3-5. TEM images at tow time points AuNRs

(Au: 0.18mg/kg, 3 mice per group). 10000 PEG/AuNR (indicated by arrow) found in the liver and spleen without morphology changes (up to 15 months) when treated with AuNRs (72 nm length).

3.1.4 Conclusion and Future Look

This work gives the results of extensive long time study on the bio distribution and toxicity effect of gold nanorods (AuNR)s used in the plasmonic photothermal therapy of cancer in the xenograft mice. We tested the long-term toxicity and biodistribution of AuNRs in different mice organs. No toxicity was observed in the mouse model up to 15 months after injection of gold nanorods. The long-term safety profile of the AuNRs suggests their great potential utility in the cancer treatment in larger animals then clinical trails.

3.1.5 References

1. Peng, X. H., Mackey, M. A. Ali, M. R. K., Rahman, M. A., Raftery, E., Shin, H. J. C., Chen, Z. N., Chen, Z. G., Oyelere, A. K., Shin, D. M., and El-Sayed M. A. (2017) The Long-Term Effects of Gold Nanorods in a Mouse Model: Circulation, Biodistribution, and Toxicity. under preparation.

2. Huang, X. H.; Jain, P. K.; El-Sayed, I. H.; El-Sayed, M. A. (2008) Plasmonic photothermal therapy (PPTT) using gold nanoparticles. *Lasers in Medical Science*, 23, 217-228.

3. Dickerson, E. B.; Dreaden, E. C.; Huang, X. H.; El-Sayed, I. H.; Chu, H. H.; Pushpanketh, S.; McDonald, J. F.; El-Sayed, M. A. (2008) Gold nanorod assisted near-infrared plasmonic photothermal therapy (PPTT) of squamous cell carcinoma in mice. *Cancer Letters*, 269, 57-66.

4. Li, Z.; Huang, P.; Zhang, X.; Lin, J.; Yang, S.; Liu, B.; Gao, F.; Xi, P.; Ren, Q.; Cui, D. (2010) RGD-Conjugated Dendrimer-Modified Gold Nanorods for in Vivo Tumor Targeting and Photothermal Therapy. *Molecular Pharmaceutics*, 7, 94-104.

5. Nikbakht, H.; Gill, P.; Tabarraei, A.; Niazi, A. (2014) Nanomolecular detection of human influenza virus type A using reverse transcription loop-mediated isothermal amplification assisted with rod-shaped gold nanoparticles. *RSC Advances*, 4, 13575-13580.

6. Stacy, B. M.; Comfort, K. K.; Comfort, D. A.; Hussain, S. M. (2013) In Vitro Identification of Gold Nanorods through Hyperspectral Imaging. *Plasmonics*, 8, 1235-1240.

7. Loo, C.; Lin, A.; Hirsch, L.; Lee, M. H.; Barton, J.; Halas, N.; West, J.; Drezek, R. (2004) Nanoshell-enabled photonics-based imaging and therapy of cancer. *Technology in cancer research & treatment*, 3, 33-40.

8. Nie, S. M.; Xing, Y.; Kim, G. J.; Simons, J. W. (2007) Nanotechnology applications in cancer. In *Annual Review of Biomedical Engineering*, Annual Reviews: Palo Alto,; 9, 257-288.

9. Connor, E. E.; Mwamuka, J.; Gole, A.; Murphy, C. J.; Wyatt, M. D. (2005) Gold nanoparticles are taken up by human cells but do not cause acute cytotoxicity. *Small*, 1, 325-327.

10. Pernodet, N.; Fang, X. H.; Sun, Y.; Bakhtina, A.; Ramakrishnan, A.; Sokolov, J.; Ulman, A.; Rafailovich, M. (2006) Adverse effects of citrate/gold nanoparticles on human dermal fibroblasts. *Small*, 2, 766-773.

11. Cho, W. S.; Cho, M. J.; Jeong, J.; Choi, M.; Cho, H. Y.; Han, B. S.; Kim, S. H.; Kim, H. O.; Lim, Y. T.; Chung, B. H.; Jeong, J. (2009) Acute toxicity and pharmacokinetics of 13 nm-sized PEG-coated gold nanoparticles. *Toxicology and Applied Pharmacology*, 236, 16-24.

12. Sultana, S.; Djaker, N.; Boca-Farcau, S.; Salerno, M.; Charnaux, N.; Astilean, S.; Hlawaty, H.; de la Chapelle, M. L. (2015) Comparative toxicity evaluation of flower-shaped and spherical gold nanoparticles on human endothelial cells. *Nanotechnology*, 26, 12.

13. Sabella, S.; Brunetti, V.; Vecchio, G.; Galeone, A.; Maiorano, G.; Cingolani, R.; Pompa, P. (2011) Toxicity of citrate-capped AuNPs: an in vitro and in vivo assessment. *J Nanopart Res*, 13, 6821-6835.

14. Vecchio, G.; Galeone, A.; Brunetti, V.; Maiorano, G.; Sabella, S.; Cingolani, R.; Pompa, P. P. (2012) Concentration-Dependent, Size-Independent Toxicity of Citrate Capped AuNPs in Drosophila melanogaster. *Plos One*, 7, 11.

15. Tang, Y.; Shen, Y.; Huang, L.; Lv, G.; Lei, C.; Fan, X.; Lin, F.; Zhang, Y.; Wu, L.; Yang, Y. (2015) In vitro cytotoxicity of gold nanorods in A549 cells. *Environmental toxicology and pharmacology*, 39, 871-8.

16. Kilford, P. J.; Stringer, R.; Sohal, B.; Houston, J. B.; Galetin, A. (2009) Prediction of Drug Clearance by Glucuronidation from in Vitro Data: Use of Combined Cytochrome P450 and UDP-Glucuronosyltransferase Cofactors in Alamethicin-Activated Human Liver Microsomes. *Drug Metabolism and Disposition*, 37, 82-89.

17. Pan, Y.; Neuss, S.; Leifert, A.; Fischler, M.; Wen, F.; Simon, U.; Schmid, G.; Brandau, W.; Jahnen-Dechent, W. (2007) Size-dependent cytotoxicity of gold nanoparticles. *Small*, 3, 1941-1949.

18. Zhang, G. D.; Yang, Z.; Lu, W.; Zhang, R.; Huang, Q.; Tian, M.; Li, L.; Liang, D.; Li, C. (2009) Influence of anchoring ligands and particle size on the colloidal stability and in vivo biodistribution of polyethylene glycol-coated gold nanoparticles in tumor-xenografted mice. *Biomaterials*, 30, 1928-1936.

19. Axiak-Bechtel, S. M.; Upendran, A.; Lattimer, J. C.; Kelsey, J.; Cutler, C. S.; Selting, K. A.; Bryan, J. N.; Henry, C. J.; Boote, E.; Tate, D. J.; Bryan, M. E.; Katti, K. V.; Kannan, R. (2014) Gum arabic-coated radioactive gold nanoparticles cause no short-term local or systemic toxicity in the clinically relevant canine model of prostate cancer. *International journal of nanomedicine*, 9, 5001-11.

20. Fraga, S.; Brandão, A.; Soares, M. E.; Morais, T.; Duarte, J. A.; Pereira, L.; Soares, L.; Neves, C.; Pereira, E.; Bastos, M. d. L.; Carmo, H. (2014) Short- and long-term distribution and toxicity of gold nanoparticles in the rat after a single-dose intravenous administration. *Nanomedicine: Nanotechnology, Biology and Medicine*, 10, 1757-1766.

21. Bhalekar, M. R.; Pokharkar, V.; Madgulkar, A.; Patil, N.; Patil, N. (2009) Preparation and evaluation of miconazole nitrate-loaded solid lipid nanoparticles for topical delivery. *AAPS PharmSciTech*, 10, 289-96.

22. Huang, X. H.; El-Sayed, I. H.; Qian, W.; El-Sayed, M. A. (2006) Cancer cell imaging and photothermal therapy in the near-infrared region by using gold nanorods. *Journal of the American Chemical Society*, 128, 2115-2120.

23. Huang, X. H.; El-Sayed, I. H.; Qian, W.; El-Sayed, M. A. (2007) Cancer cells assemble and align gold nanorods conjugated to antibodies to produce highly enhanced, sharp, and polarized surface Raman spectra: A potential cancer diagnostic marker. *Nano Letters*, 7, 1591-1597.

24. Ali, M. R. K.; Panikkanvalappil, S. R.; El-Sayed, M. A. (2014) Enhancing the Efficiency of Gold Nanoparticles Treatment of Cancer by Increasing Their Rate of Endocytosis and Cell Accumulation Using Rifampicin. *Journal of the American Chemical Society*, 136, 4464-4467.

25. Nothelfer, E. M.; Zitzmann-Kolbe, S.; Garcia-Boy, R.; Kramer, S.; Herold-Mende, C.; Altmann, A.; Eisenhut, M.; Mier, W.; Haberkorn, U. (2009) Identification and Characterization of a Peptide with Affinity to Head and Neck Cancer. *Journal of Nuclear Medicine*, 50, 426-434.

26. Hong, F. D.; Clayman, G. L. (2000) Isolation of a peptide for targeted drug delivery into human head and neck solid tumors. *Cancer Research*, 60, 6551-6556.

27. Mackey, M. A.; Ali, M. R. K.; Austin, L. A.; Near, R. D.; El-Sayed, M. A. (2014) The Most Effective Gold Nanorod Size for Plasmonic Photothermal Therapy: Theory and In Vitro Experiments. *Journal of Physical Chemistry B*, 118, 1319-1326.

28. Nikoobakht, B.; El-Sayed, M. A. (2003) Preparation and growth mechanism of gold nanorods (NRs) using seed-mediated growth method. *Chemistry of Materials*, 15, 1957-1962.

29. Ali, M. R. K.; Snyder, B.; El-Sayed, M. A. (2012) Synthesis and Optical Properties of Small Au Nanorods Using a Seedless Growth Technique. *Langmuir*, 28, 9807-9815.

30. Bulaj, G.; Kortemme, T.; Goldenberg, D. P. (1998) Ionization-reactivity relationships for cysteine thiols in polypeptides. *Biochemistry*, 37, 8965-72.

31. James, W. D.; Hirsch, L. R.; West, J. L.; O'Neal, P. D.; Payne, J. D. (2007) Application of INAA to the build-up and clearance of gold nanoshells in clinical studies in mice. *Journal of Radioanalytical and Nuclear Chemistry*, 271, 455-459.

32. Pokharkar, V.; Dhar, S.; Bhumkar, D.; Mali, V.; Bodhankar, S.; Prasad, B. L. V. (2009) Acute and Subacute Toxicity Studies of Chitosan Reduced Gold Nanoparticles: A Novel Carrier for Therapeutic Agents. *Journal of Biomedical Nanotechnology*, 5, 233-239.

33. Kilfoy, B. A.; Zheng, T.; Holford, T. R.; Han, X.; Ward, M. H.; Sjodin, A.; Zhang, Y.; Bai, Y.; Zhu, C.; Guo, G. L.; Rothman, N.; Zhang, Y., (2009) International patterns and trends in thyroid cancer incidence, 1973-2002. *Cancer causes & control: CCC*, 20 (5), 525-31.

3.2 Gold Nanorods-assisted Plasmonic Photothermal Therapy of Cancer; Efficacy, Toxicity and Mechanistic Studies *in vivo* [1]

Gold nanorods (AuNRs)-assisted plasmonic photothermal therapy (AuNRs-PPTT) is a promising strategy for combating cancer, in which AuNRs absorb near infrared (NIR) light and convert it into heat, causing cell death mainly by apoptosis and/or necrosis. Developing a valid PPTT that induces cancer cell apoptosis and avoids necrosis *in vivo* and exploring its molecular mechanism of action is of great importance. Furthermore, assessment of the long-term fate of the AuNRs after treatment is critical for clinical usage. We first optimized the size, surface modification (rifampicin (RF) conjugation), and concentration (2.5 nM) of AuNRs and the PPTT laser power (2 W/cm^2) to achieve maximal induction of apoptosis. Second, we studied the potential mechanism of action of AuNRs-PPTT using quantitative proteomic analysis in mouse tumor tissues. Several death pathways were identified, mainly involving apoptosis and cell death by releasing neutrophil extracellular traps (NETs) (NETosis), which were more obvious upon PPTT using RF-conjugated AuNRs (AuNRs@RF) than with polyethylene glycol thiol (PEG)-conjugated AuNRs. Cytochrome c and p53-related apoptosis mechanisms were identified as contributing to the enhanced effect of PPTT with AuNRs@RF. Furthermore, Pin1 and IL18-related signaling contributed to the observed perturbation of the NETosis pathway by PPTT with AuNRs@RF. Third, we report for the first time a 15-month toxicity study that showed no long term toxicity of AuNRs *in vivo*. Together, these data demonstrate that our AuNRs-PPTT platform is effective and safe for cancer therapy in mouse models. These findings provide a strong framework for the translation of PPTT to the clinic.

3.2.1 Introduction

Plasmonic photothermal therapy (PPTT) has recently drawn considerable attention for cancer treatment, as plasmonic nanoparticles can effectively convert absorbed near infrared light into heat that ultimately kills cancer cells [2-5]. Gold nanorods (AuNRs) show unique physicochemical properties compared to other gold nanoparticles [6-7], in that they absorb and scatter NIR radiation (650−900 nm) strongly, and have suitable aspect ratios (length divided by width). AuNRs have been found to be one of the most effective photothermal contrast agents [8, 21, 9]. PPTT can induce cell death mainly via two pathways: necrosis and apoptosis [10]. During necrosis, the heat induced by PPTT (if above 50 ^{o}C) could disrupt the plasma membrane, causing the cellular components to leak out and cause inflammation, metastasis [11], and harm to surrounding normal tissues. Apoptosis is a programmed cell death pathway that triggers cancer cell death [12-13], attenuates inflammatory activities, and is regarded as a "cleaner" process of cell elimination. Skewing the response toward apoptotic cell death rather than necrotic death will minimize inflammatory responses that may promote the damage or destruction of healthy tissues. Therefore, modulating PPTT to trigger apoptosis would be more favorable in clinical settings [8, 14] It has been reported that different intracellular locations or shapes of nanoparticles potentially regulate the switch between necrosis and apoptosis [15]. In this study, we aimed to optimize the conditions of AuNRs-PPTT to trigger apoptosis rather than necrosis and examined the molecular impact of AuNRs-PPTT *in vivo* using western-blot analysis and mass spectrometry-based proteomics.

To optimize the efficacy of apoptosis induction, several aspects of the fabrication of AuNRs were considered, i.e. the size, dose and surface modifications of AuNRs, in order to enhance the internalization of AuNRs and the generation of heat. Effective internalization of AuNRs in tumor tissue is a significant challenge [16-19]_ENREF_12_ENREF_13. To increase the uptake of AuNRs, surface modification with ligands that assist endocytosis or block exocytosis has been used, aiming at greater nanoparticle retention inside cancer cells [20]. We have previously developed rifampicin (RF)-conjugated AuNRs for enhancing the internalization of AuNRs in tumor cells. RF was shown to enhance the entry of AuNRs into cells and decrease exocytosis from the cells [21]. However, detailed mechanisms of the behavior of RF-coated AuNRs *in vivo* have yet to be explored. Heat generation and dose of the AuNRs must also be considered [22].

To better understand the cellular responses to PPTT, more systematic studies *in vivo* are required. Most previous reports concerning the mechanism of PPTT were only conducted *in vitro* [15] and focus on a single protein or pathway. Several mechanisms have been proposed *in vitro*. Ali et al proposed heat shock protein 70 as a major player [14]. Pérez-Hernández et al reported that apoptosis during PTT using gold nanoprisms is mediated by proteins Bak and Bax, through the activation of protein Bid [15]. To better understand the mechanisms involved, systematic analysis such as mass spectrometry (MS)-based proteomics is necessary.

The safety profile of AuNRs remains largely undefined [23]. Gold is a chemically inert material. Therefore, it is generally considered biocompatible and has been used in some routine clinical practices for many years, e.g. in treating rheumatoid arthritis. Several studies have reported no significant short term toxicity of AuNPs (1 day to 3 months) [24-26]. You *et al*., [27] ENREF [29] have reported a lack of both acute and chronic toxicity over 3 months following multiple injections of PEGylated hollow gold nanospheres in mice. _ENREF_23_ENREF_23However, other studies have contradictorily reported that the presence of nanoparticles causes cytotoxicity such as actin stress [28], induces apoptosis, or causes inflammation in mouse livers [29]. Some studies have explored how gold nanoparticle exposure (aside from any heat-induced effects) impacts cells at the molecular level, affects pathways such as mitochondrial oxidative phosphorylation, and causes oxidative stress [30]. The dose-dependent effects of gold nanoparticles on biological systems have been widely recognized [31]. A high dose of NPs or the desorbed surfactants from their surface could result in "toxic" behavior [32, 33] Of concern for AuNRs is the incomplete purification of surfactant CTAB, which may cause cytotoxicity[34]. Therefore, the optimal dose and purification of AuNRs is of great importance in minimizing toxic effects. The preservation of spherical AuNPs without complete clearance over six months has been reported [35]. You *et al.,* [27] also reported slow clearance of gold nanoparticles from the body during the 3-month period. Such body deposition of metallic NPs over a long-period raises significant concerns regarding their long-term safety. Therefore, a comprehensive investigation of the organ uptake, biodistribution, longer-term fate and toxicity of AuNRs is essential to fundamentally understand their *in vivo* biological interactions and to use this knowledge to minimize their toxicity [25].

Here, we report for the first time the long-term *in vivo* fate of AuNRs 15 months after the initial administration, their biodistribution and associated toxicity in a BALB/c mouse model, and their efficacy in a head and neck squamous cell carcinoma (HNSCC) xenograft model. Our findings add to the current knowledge of AuNRs-PPTT *in vivo* in regulating apoptosis signaling and in providing an effective and safe potential new treatment. This study provides a strong framework for the translation of this approach to the clinic.

3.2.2 Experimental Methods

AuNRs synthesis, conjugation, and characterization*:* A seedless growth method was used for the synthesis of gold nanorods (AuNRs) with an average size of 25 ± 3 nm × 5.5 ± 0.8 nm (length x width) [36]. Briefly, $HAuCl_4$ (5.0 mL, 1.0 mM) was added to 5.0 mL of 0.2 M cetyltrimethylammonium bromide (CTAB) at room temperature. Then, 250 μL of 4.0 mM $AgNO_3$, 8 μL of 37% HCl and 70 μL of ascorbic acid (78.8 mM) was successively added and the solution was gently mixed. Immediately afterwards, 15 μL of 0.01 M ice-cold $NaBH_4$ was injected into the unstirred growth solution and allowed to react for 12 hrs. The synthesized AuNRs were then centrifuged at 21000 rcf for 50 min and re-dispersed in DI water, followed by a second centrifugation at 19000 rcf for 40 min to remove the extra CTAB. A seed-mediated growth method was used for the synthesis of AuNRs with an average size of 72 ± 7 nm × 16 ± 4 nm: where 4.0 mM of silver nitrate and 78.8 mM of ascorbic acid were added to a growth solution consisting of 0.2 M CTAB, 1.0 mM of $HAuCl_4$ and 0.01 M of $NaBH_4$. Then, CTAB stabilized AuNRs were purified by

centrifugation (10000 rcf for 50 min) and redispersed in DI H_2O, followed by a second centrifugation at 7000 rcf for 30 min. For AuNRs conjugated with PEG, we added mPEG-SH (1 mM) to the nanoparticles overnight to achieve about 20,000 ligands on each particle. For AuNRs conjugated with RF, we first added 50 ml of 0.5 mM bovine serum albumin (BSA) (Sigma-Aldrich, USA) to 1 nM AuNRs solution, which was then incubated for 3 h at room temperature. Then, 300 μL of 5 mM RF was added to the AuNRs solution and incubated for 3 hrs. After conjugation, the particles were centrifuged to remove the extra ligands. Transmission electron microscopy (TEM) was used to examine particle size and homogeneity. UV-Vis spectrometer and ZetaSizer 3000 (Malvern Instruments) were used to examine if the conjugation was successful. For BSA fluorescent quenching experiments, excitation and emission measurements were carried out on a Quanta Master™ 300 — phosphorescence/fluorescence spectrofluorometer. BSA was used at a concentration of 10^{-4} M. The number of RF molecules per AuNRs was calculated according to Ali et al, [37]based on the UV-Vis spectra. The dose of AuNRs were presented as molar concentration. For comparison with other studies, 5 nM = 1 O.D. (optical density) [36].

Dark-field images*:* MDA686TU cells were seeded on glass coverslips in complete growth medium for 24 h to achieve 40% final confluence. Cells were incubated with 2.5 nM AuNRs with RF or PEG conjugation in supplemented DMEM cell culture medium for 24 h. Dark field images were taken using an inverted microscope equipped with a dark field condenser and Lumenera Infinity2 CCD camera. 20 X objective lens was used to collect scattered light from the samples to produce dark field images.

Differential interference contrast (DIC) microscopy*:* MDA686TU cells were seeded on glass coverslips in complete growth medium for 24 h, then incubated with 2.5 nM AuNRs

with RF or PEG conjugation in supplemented DMEM cell culture medium for 24 h. For DIC imaging, an inverted Nikon Eclipse Ti-E microscope equipped with Perfect Focus System (PFS, 25 nm z-axial resolution) was used for imaging and z-stacks acquisitions under DIC microscopy. The DIC mode utilized a DIC polarizer and analyzer pair, a high resolution 100×I-R DIC slider, a high numerical aperture (N.A., 1.40) oil immersion condenser lens, a Nikon CFI Apo TIRF 100× (N.A., 1.49) oil immersion objective, and a 12 V/100 W halogen lamp as light source. Appropriate bandpass filters were placed in the light path. Z-stack movies were taken by a Hamamatsu ORCA-Flash 4.0 V2 CMOS camera (C11440-22CU, pixel size: 6.5 μm × 6.5 μm) with Camera Link interface using Micro-Manager and analyzed using NIH ImageJ and reconstructed in Amira. Fixed Hey cells on 22 mm × 22 mm glass coverslips were rinsed with DPBS at pH 7.4 and fabricated into a sandwiched chamber with two pieces of double-sided tape and a cleaned glass slide. PBS solution was added into the chamber to fill the space and the chamber was sealed with clear nail polish. The sample slide was then placed under the microscope for observation. Z-stacks were acquired using the Multi-Dimensional Acquisition function in Micro-Manger. DIC optical sectioning (shown as a video in Supporting Information) through the whole cell thickness was achieved by moving the objective on the motorized nosepiece using PFS at 65 nm/step at 33 ms (30 fps) exposure time.

Cell lines: Information and primary sources of HNSCC cell lines MDA686TU, Fadu, SqCC/Y1 were described elsewhere [38]. UD-SCC2, UM-SCC-47 cell lines were obtained from Dr. Ferris (University of Pittsburg Cancer Center). Cells were maintained in DMEM/F12 (1:1) medium supplemented with 10% heat-inactivated FBS in a 37°C, 5% CO_2 humidified incubator.

Cell viability assay: Sulforhodamine B (SRB) assay was used for cell viability determination [39]. Cells were seeded (5×10^3 cells/well) in a 96-well plate. 24 hrs later cells were treated with AuNRs for 24 hrs and exposed to laser for 2 min. Cells were fixed after another 24 hrs. Plates were stained with SRB and bound SRB was dissolved to assess OD at 492 nm using a microplate reader. The percentage of surviving cells was calculated based on the absorbance values relative to the non-treated samples.

Apoptosis assay: Apoptotic cells were identified and measured as described elsewhere [40]. Briefly, cells were collected and stained with Annexin V-phycoerythrene and 7-AAD (BD PharMingen) for 15 min at room temperature. Samples were measured using a fluorescence-activated cell sorting (FACS) caliber bench-top flow cytometer (Becton Dickinson). FlowJo software (Tree Star) was used for apoptosis analysis.

Western blot analysis: Western blot was incubated with primary followed by secondary antibodies and detected using enhanced chemiluminescence system as described [40]. Primary antibodies were anti-phospho-Akt, anti-total Akt, anti-phospho-Erk, anti-total Erk, anti-caspase3, anti-caspase3, anti-PARP from Cell Signaling, MA; anti-p21 from Santa Cruz Biotech, CA; and anti-β-actin from Sigma Aldrich. Secondary antibodies were from Santa Cruz Biotech. Western band quantification was performed using Image-Quant TL software (GE/Amersham Biosciences, Piscataway, NJ).

Nude mice bearing human HNSCC xenograft tumor model: Based on protocols approved by the Institutional Animal Care and Use Committee of Emory University, female nude mice (athymic nu/nu) aged 4–6 weeks were purchased from Taconic. Each mouse was injected with 5×10^6 MDA686TU cells subcutaneously in the right flank, and tumor volume

was monitored (volume = $0.5 \times L \times W^2$). Mice were randomized into groups once the tumors reached 70 mm^3. Mice were injected intratumorally with PBS or different concentrations of AuNRs, and exposed to different powers of NIR laser for 2 min (5 mice/group). Tumors were monitored every other day and mice were sacrificed on the 25th day after cancer cell transplantation. Tumors and organs were collected, measured and processed for paraffin embedding.

Immunohistochemistry: Upon deparaffinization and rehydration, tissue sections were permeabilized with 0.25% Triton-X-100/PBS for 5 min. Tissue sections were blocked with 2.5% horse serum for 30 minutes. To detect intracellular localization and expression levels of Ki67 proteins, we used mouse anti-human Ki-67 antibody (prediluted; Invitrogen, Carlsbad, CA) then counterstained cell nuclei using 4,6-diamidino-2-phenylindole (DAPI, Invitrogen, Carlsbad, CA). Mouse and rabbit IgG were used as negative controls.

Sample preparation for proteomics: 5×10^6 MDA686TU cells were injected into the right flank of nude mice. We injected a single dose of AuNRs@PEG (2.5 nM) or AuNRs@RF (2.5 nM) intratumorally followed by 2 min of 2 W/cm^2 NIR laser exposure when the tumors had reached 150 mm^3. 24 hours later we collected tumors for proteomics analysis. Each experiment was repeated twice. Mouse tumor tissues were homogenized, followed by ultrasonic tissue ablation with ice-cold lysis buffer (50 mM HEPES, pH 7.8, 150 mM NaCl 0.1% SDS, 0.5% sodium deoxycholate 1% Triton X 100 or NP-40, phosphatase inhibitors). The cells were then scraped down and the obtained mixtures homogenized with sonication and vortexing. Cell debris was removed by centrifugation at 18,000 g for 20 min at 4 °C. Four volumes of ice-cold acetone/ethanol/acetic acid (v/v/v = 50/50/0.1) was added to the supernatant to precipitate the proteins at -20 °C overnight. After centrifugation, the protein

pellet was re-dissolved in denaturing buffer (pH 8.0) containing 8 M urea and 50 mM HEPES, and the protein concentration was tested using a Bradford assay. The disulfide bonds in the protein solution were reduced by 2 mM dithiothreitol (DTT) at 37 °C for 2 h and subsequently alkylated by adding 6 mM iodoacetamide (IAA) and incubation in darkness at room temperature for 40 min [41]. Purified peptides were labelled with 6-plex TMT reagents (Thermo) following the manufacturer's protocol. Briefly, lyophilized peptides were dissolved in 100 µL of 100 mM triethylammonium bicarbonate (TEAB) buffer, pH= 8.5. Each channel of the TMT reagents was dissolved in 41 µL of anhydrous ACN and transferred into the peptide tube. The reaction was performed at room temperature for 1 h then was quenched by adding 8 µL of 5% hydroxylamine. Peptides from all six tubes were then mixed, desalted again using a tC18 Sep-Pak cartridge, and lyophilized overnight. For protein analysis, the peptide mixture was separated by high pH reversed-phase high-performance liquid chromatography (HPLC) into 20 fractions with a 40-min gradient of 5-55% ACN in 10 mM ammonium acetate (pH=10).

LC-MS/MS analysis and database search*:* After TMT labeling and purification, lyophilized peptide samples were dissolved in 10 µl solvent of 5% ACN and 4% FA, and 4 µl of the dissolved sample were loaded onto a microcapillary column packed with C18 beads (Magic C18AQ, 3 µm 200 Å, 100 µl x 16 cm, Michrom Bioresources) by a Dionex WPS-3000TPLRS autosampler (UltiMate 3000 thermostatted Rapid Separation Pulled Loop Wellplate Sampler). Peptides were separated by reversed-phase chromatography using an UltiMate 3000 binary pump with a 90-min gradient of 4-30% ACN (in 0.125% FA). Peptides were detected with a data-dependent Top15 method [42] in a hybrid dual-cell quadrupole linear ion trap – Orbitrap mass spectrometer (LTQ Orbitrap Elite,

ThermoFisher, with Xcalibur 3.0.63 software). For each cycle, one full MS scan (resolution: 60,000) in the Orbitrap at 106 AGC target was followed by up to 15 MS/MS for the most intense ions. The selected ions were excluded from further analysis for 90 seconds. Ions with single or unassigned charge were discarded. MS2 scans were performed in the orbitrap cell by activating with high energy collision dissociation (HCD) at 40% normalized collision energy with 1.2 m/z isolation width. All MS2 spectra were converted into mzXML format, and then searched using the SEQUEST algorithm (version 28) [43]. Spectra were matched against a database containing sequences of all proteins in the UniProt Human (*Homo sapiens*) database. The following parameters were used during the search: 20 ppm mass tolerance; fully digested with trypsin; up to 3 missed cleavages; fixed modifications: carbamidomethylation of cysteine (+57.0214), TMT modification of lysine (+229.1629) and N-terminus (+229.1629); variable modifications: oxidation of methionine (+15.9949). False discovery rates (FDR) of peptide and protein identifications were evaluated and controlled by the target-decoy method [44]. Each protein sequence was listed in both forward and reversed orders. Linear discriminant analysis (LDA), which is similar to other methods in the literature [45], was used to control the quality of peptide [46]. Peptides fewer than seven amino acid residues in length were discarded. Furthermore, peptide spectral matches were filtered to <1% FDR. An additional protein-level filter was applied in each dataset to reduce the protein-level FDRs (<1%).

Proteomics data analysis*:* For proteomics analysis, each experiment was repeated twice. The mean expression level of each protein was used for downstream analysis. Raw data were normalized using supervised normalization of microarray (SNM) [47]. Variance due to biological replicates was adjusted by setting them as variables in the model. Variance

explained by different experimental treatments (control, AuNRs@PEG-PPTT, and AuNRs@RF-PPTT) was fitted as a biological variable in the model. Hierarchical clustering was performed with statistical software R. Proteins identified as being affected were subjected to pathway analysis using the MetaCore from Thomson Reuters.

Short-term and long-term uptake fate of PEGylated AuNRs: BALB/C mice (male), 6 weeks of age, were injected via the tail vein with 200 µl solution of Au NRs (0.18mg/kg). At specified time points of 1 day, 3, 7, 14, 30 days and 15 months, mice were euthanized by pressurized CO_2 asphyxiation, 3 mouse each group. Liver, spleen, kidney and lung were collected, rinsed with distilled water and dried. The dried tissues were dissolved and assayed for Au using ICP-MS.

Histopathology evaluation: Liver, spleen, kidney and lung tissues were embedded in paraffin and cut at 5 um thickness. The tissues were stained with hematoxylin and eosin (Sigma) to assess histological alterations via microscopy.

Statistical Analysis: All results represent the average of at least three separate experiments and are expressed as mean +/- standard deviation or standard error. Statistical analysis was conducted using t test. *P*-value less than 0.05 was considered statistically significant.

3.2.3 Results and Discussion

Efficacy of AuNR@RF/PPTT in cellular growth inhibition *in vitro* (HNSCC cells) and in tumor growth reduction in a MDA686TU xenograft model

AuNRs were synthesized using a seedless growth technique [36]. AuNRs were conjugated with bovine serum albumin (BSA) as a protein carrier and linker to rifampicin (RF), as shown in schematic Figure 1A. Detailed descriptions of AuNRs synthesis, conjugation, cellular uptake and cytotoxicity measurements are in the supporting information. Briefly, transmission electron microscope (TEM) images (Figure B.1.A) show the average size of AuNRs (for small AuNRs: 25 (± 3) nm × 5.5 (± 0.8) nm (length × width); and for big AuNRs: 72 (± 7) nm × 16 (± 4) nm) and UV-Vis spectrum shows an absorbance centered near 800 nm, corresponding to the longitudinal surface plasmon resonance band of AuNRs (Figure B.1.B). Successful conjugation of BSA/RF molecules to the surface of AuNRs (AuNRs@BSA@RF) was proven by red-shift of the plasmon peak of AuNRs in the UV-Vis spectrum (Figure B.1.B), fluorimetry (**Figure B.1.C**) and zeta potential (**Figure B.1.D**). Successful uptake of AuNRs@RF was observed by 3-dimensional scanning differential interference contrast (DIC) microscopy (**Figure 1B and B.3**.), dark field images (Figure B.1.E) and UV-Vis absorbance (**Figure B.1.**F). After applying PPTT to AuNRs@RF, the release of RF molecules from the surface of AuNRs, as shown in schematic Figure 1A, was demonstrated by UV-Vis spectra (**Figure B.1.B**). After PPTT, the RF peaks of the particles (330 nm and 470 nm) disappeared, accompanied with the increased concentration of RF in the supernatant, indicating the release of surface RF. The number of RF molecules per AuNRs was calculated according to a previous study [37]. From the calculation, we found 657 rifampicin molecules present on each AuNRs@BSA, most of which was released after PPTT as shown in Figure B.1.B by the loss of RF peaks on AuNRs. Furthermore, DIC images (**Figure 1B**) show increases in the sizes of nanoparticle aggregates after PPTT, further supporting the release of surface ligands after PPTT (shown in Figure 1A) which

causes the particles to more easily aggregate. Similarly, AuNRs@PEG were also prepared, and their detailed characterization is described in supporting data **(Appendix Figure B.2.).**

The effectiveness of PPTT in the regulation of cell viability was examined in five HNSCC cell lines, MDA686TU, Fadu, UD-SCC2, UM-SCC-47, and SqCC/Y1. We applied different concentrations of AuNRs@PEG with 2 W/cm^2 laser to optimize the AuNRs concentration. We found inhibition of cell viability (~30-50%) following treatment with at least 2.5 nM AuNRs@PEG compared to non-treated cell lines after 72 h (**Appendix Figure B.4. A**). Furthermore, we compared the effectiveness of AuNRs@RF and AuNRs@PEG in MDA686TU cells. Interestingly, we observed that AuNRs@RF/PPTT reduced cell viability more efficiently than AuNRs@PEG/PPTT (Figure B.4.B). We also observed that treatment with both AuNRs@RF and AuNRs@PEG mainly induced apoptosis without obvious necrotic death (**Appendix Figure B.4.C**). These observations prompted us to further investigate the mechanistic details of AuNRs@RF action. In MDA686TU cells treated with AuNRs@PEG or AuNRs@RF followed by laser treatment, RF-conjugated AuNRs induced approximately twice as much apoptosis when compared to AuNRs@PEG/PPTT alone (**Figure 1C**) (**Appendix Figure B.4.B**). Western blot analysis revealed that AuNRs-PPTT induced apoptotic signaling molecules such as cleaved caspase 3 (effector caspase), followed by cleavage of substrate poly ADP-ribose polymerase (PARP) (**Figure 1D**). In addition, we observed that AuNRs@RF/PPTT reduced cell viability and proliferation, evidenced by reduction of Akt and Erk activation and upregulation of the cell cycle inhibitor protein, p21 (**Figure 1D**).

To optimize AuNRs concentration and laser power and assess anti-cancer therapeutic potential *in vivo*, we established a MDA686TU xenograft model. We applied three concentrations of AuNRs (conjugated with PEG or RF), 2.5, 5 and 10 nM; along with three different powers of laser, 0.5, 1 and 2 W/cm^2. In addition, we compared two different sizes of AuNRs@PEG (the characterization of big AuNRs is shown in **Figure B.5**.) due to their different heat conversion capacity. Nanoparticles (100 µL) were injected intratumorally and laser treatment was performed once on day 1. We included three control groups: PBS, AuNRs (without laser), and laser alone. Tumor progression data over 25 days in mice from each treatment group are presented in Figure 1E and supplementary Figure B.6. and B.7., with the corresponding mice shown in Figure 1F. We observed promising tumor growth inhibition with smaller-sized AuNRs@PEG. Over 25 days, tumor growth was reduced significantly in mice treated with AuNRs@PEG at all three concentrations only when the laser power was 2 W/cm^2 (Figure 1E). We observed that treatment with 10 nM and 5 nM AuNRs@PEG with 2 W/cm^2 laser reduced tumor growth by many fold compared to the control groups (PBS, laser only and AuNRs only) (Figure 1E) [control groups (PBS, Laser, AuNRs) vs treated groups (2.5, 5, 10 nM AuNRs@PEG-PPTT), $p<0.01$]. However, we observed skin wounding effects in mice at these concentrations (Figure 1F). Treatment with 2.5 nM AuNRs@PEG-PPTT had a moderate wounding effect, however, tumor growth increased after 20 days (Figure 1E). In comparison with 2.5 nM small AuNRs@PEG (25 nm length), treatment with 2.5 nM large (72 nm length) AuNRs@PEG-PPTT had no obvious effect on tumor inhibition (**Figure 3-6E**). Since AuNRs@RF-PPTT showed the most efficient apoptosis *in vitro* (**Figure 3-6C**), we were interested to see the effect *in vivo* in comparison to AuNRs@PEG-PPTT. We found that 2.5 nM AuNRs@RF-

PPTT efficiently reduced tumor growth to the same extent as 10 nM AuNRs@PEG-PPTT without any skin wounding (**Figure 3-6E, F**) [control groups (PBS, Laser, AuNRs) vs treated group (2.5 nM AuNRs@RF-PPTT), $p<0.01$]. All mice were sacrificed on day 25 and tumors were collected. Tumor weight was significantly reduced in mice treated with all concentrations of small AuNRs with 2 W/cm^2 laser (Figure B.6.) [control (PBS, Laser, AuNRs) vs treated groups, p <0.01], while large AuNRs (Figure B.6.) or lower laser power was unable to reduce tumor growth (Figure B.7.). The mice were monitored during and after tumor cell and nanoparticle injections. Movement, diet, and vital signs (ruffled fur, weight loss, and normal activity) were observed throughout the experiments. We did not observe any abnormalities other than the skin wounding effect at higher concentrations of AuNRs. IHC of mouse tumor tissues for the cell proliferation marker Ki67 (**Figure 3-6G**) suggested that AuNRs@RF (25 nm length) with 2 W/cm^2 laser significantly reduced cell viability, accompanied by the suppression of tumor growth progression without any skin wounding effect.

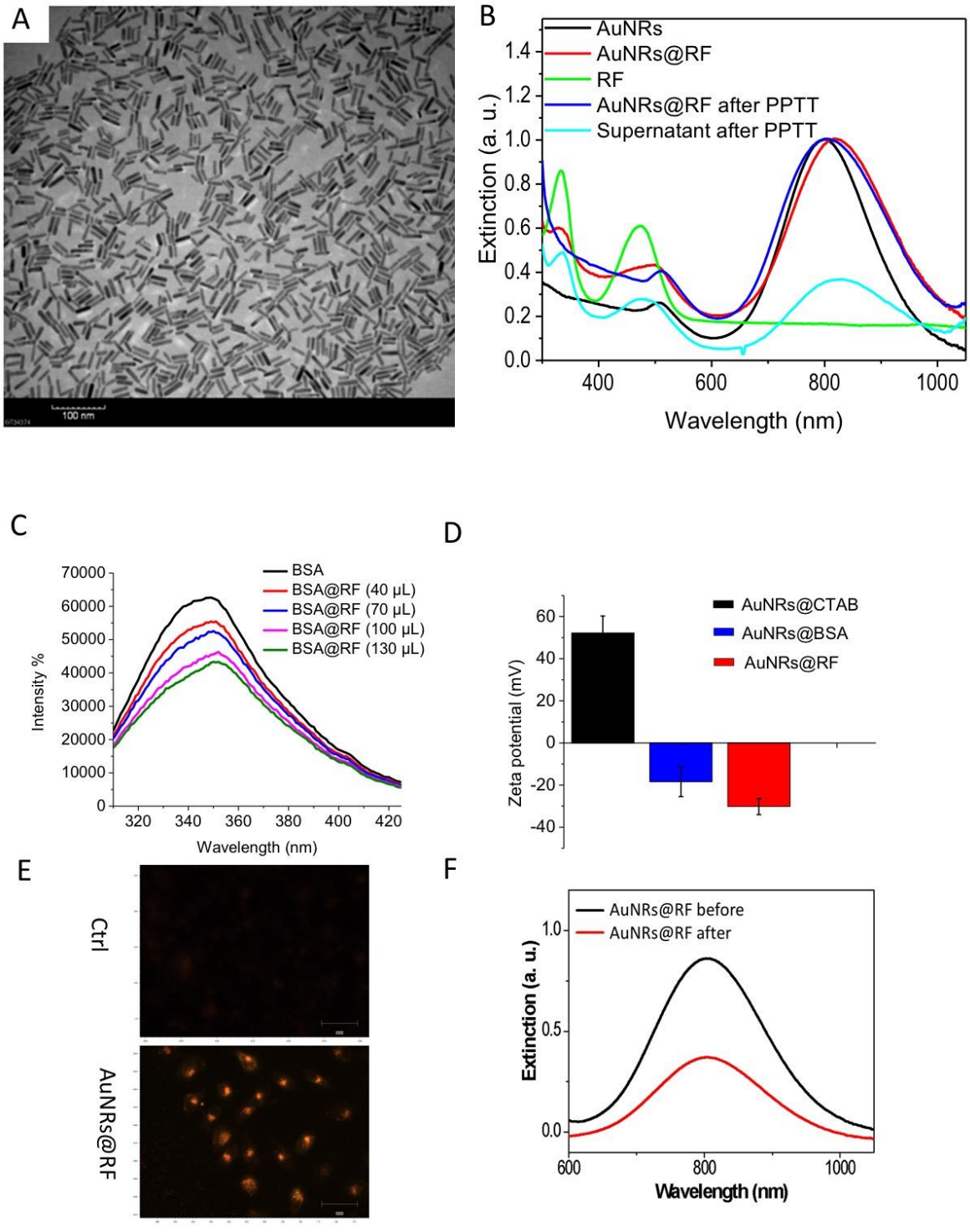

Figure 3-6. Efficacy of AuNRs@RF in vivo and in vitro

(A) Schematic showing the characterization and conjugation of AuNRs@Rifampicin, and the release of surface ligands after PPTT; (B) DIC images of optical sectioning of control sample (without nanoparticles), cells incubated with AuNRs@RF, and cells after PPTT. All scale bars are 10 μm; white arrows indicate AuNRs aggregates. (C) Comparative apoptosis analysis in MDA686TU HNSCC cells treated with AuNRs or AuNRs@RF and PPTT after 72h (error bars are mean ±SD, n=3); (D) Western blotting for the indicated proteins in MDA686TU HNSCC cell line after treatment with AuNRs@PEG-PPTT and AuNRs@RF-PPTT. A representative blot of three independent experiments is presented; (E) MDA686TU HNSCC tumor xenograft growth (tumor volume = 0.5×l×w2) progression in groups: PBS, 2 W/cm2 Laser, 10 nM small AuNRs@PEG as control groups; 5 nM, 10 nM small AuNRs@PEG with 2W/cm2 Laser; 2.5nM small and large AuNR@PEG with 2W/cm2 Laser; 2.5 nM AuNRs@RF with 2W/cm2 laser. First and only dose was given on Day 1 (tumor volume ~ 70 mm3) and tumor growth was monitored until Day 25 (endpoint of tumor volume 1800 mm3) (error bars are mean ±SEM, n=5). Statistical analysis (t-test) between control groups (PBS, Laser, AuNRs@PEG) vs treated groups (2.5, 5, 10 nM AuNRs@PEG-PPTT, 2.5 nM AuNRs@RF-PPTT) was p< 0.01 (F) Representative mouse from each of the indicated groups presented; (G) Ki67 expression detected in xenograft tissue by IHC analysis. Representative images shown from indicated groups (brown stain for Ki67 and nuclei were counterstained by hematoxylin, blue; magnification X200). For comparison with other studies, 5 nM = 1 O.D. (optical density) for small AuNRs36.

AuNRs@RF-PPTT induces stronger perturbation of apoptosis and cell death by releasing neutrophil extracellular traps (NETs) (NETosis) pathway:

We conducted quantitative proteomics experiments using tandem mass tags (TMT) to study alterations in protein expression levels in tumor tissues, identify the mechanisms responsible for the induction of apoptosis by AuNRs@PEG-PPTT and AuNRs@RF-PPTT, and explore why AuNRs@RF-PPTT was much more effective. Two biological replicates were conducted for AuNRs@PEG-PPTT-treated, AuNRs@RF-PPTT-treated, and control groups. Differentially expressed proteins identified in each experiment (AuNRs@PEG-PPTT and AuNRs@RF-PPTT) were compared (**Figure 3-7A**). In total, we measured 5222 proteins. For proteomics analysis, we set +/-0.5 as a threshold for fold

change (log 2) detection (**Figure 3-7B**). Following AuNRs@PEG-PPTT treatment, 532 proteins were decreased and 600 proteins were increased. AuNRs@RF-PPTT treatment led to downregulation of 558 and upregulation of 644 proteins (**Figure 3-7C**). Overlap in altered proteins (increased or decreased) is shown in **Figure 3-7D.**

Pathway analysis identified apoptosis-related pathways that were significantly regulated by AuNRs@RF-PPTT and AuNRs-PPTT compared to the control group (**Figure 3-7F**), including Granzyme B signaling, BAD phosphorylation, caspase cascade, and others. These pathways and associated increased proteins (Figure 2E and Table S1) may provide a mechanistic explanation for the apoptosis promoting effect of PPTT with AuNRs. Apoptosis-related proteins are listed in **Figure 3-7E** and a schematic illustration is shown in **Figure 3-7G**. A greater increase in cytochrome c and Apaf-1 protein expression was identified following AuNRs@RF-PPTT versus AuNRs@RF treatment. Cytochrome c and Apaf-1 form a complex leading to the activation of caspase-9, which activates caspase-3, inducing caspase-3 mediated apoptosis [48, 49]. In addition, we observed the activation of upstream signaling of p38alpha, which leads to ROS generation [50, 51] that can result in mitochondrial dysfunction-triggered apoptosis. We also observed increased levels of FANCD2, p53 and PTEN. FANCD2 is required for the maintenance of chromosomal stability, which is involved in the repair of DNA double-strand breaks [52, 53]. DNA damage can affect FANCD2 via FANCL [54, 55], whereas FANCD2 can further interact with BRCA1 [56, 57]. BRCA1 then activates CHK1 [58], which activates p53 [59]. Activated p53 then promotes apoptosis [60]. PTEN can also induce apoptosis via PI3K/AKT dependent and independent pathways [61] or other pathways [62-63]. We observed stronger apoptosis promotion, *i.e.*, greater upregulation of apoptosis-related

proteins, with AuNRs@RF-PPTT compared to AuNRs@PEG-PPTT treatment (**Figure 3-7E**). These observations at the molecular level are in agreement with the phenotypic study showing that AuNRs@RF-PPTT is more effective than AuNRs@PEG-PPTT *in vivo* and *in vitro*.

Interestingly, our proteomics analysis also revealed that treatment with AuNRs@RF-PPTT induced changes in the levels of several proteins involved in the NETosis pathway more strongly than AuNRs@PEG-PPTT (**Figure 3-7F**). NETosis refers to a specific form of neutrophil cell death caused by pathogen infection, which releases neutrophil extracellular traps (NETs). It has been recently reported that small NPs activate the NETosis pathway [64]. NETosis can be triggered by two pathways: directly by IL-18 [65-67] or by chromatin decondensation [68-71]. In this study, proteomics analysis identified nine proteins in the NETosis pathway. Specifically, a clear elevation of histone H2, histone H4, IL-18, and Pin1 were observed following AuNRs@RF-PPTT treatment; therefore, both pathways leading to NETosis were altered (Figure 2G). Since NETosis is related to endocytosis, we speculate that AuNRs@RF may be better taken up by cells resulting in enhanced NETosis. In summary, from proteomics analysis, we determined that AuNRs@RF-PPTT can induce apoptosis and NETosis more efficiently than AuNRs@PEG-PPTT.

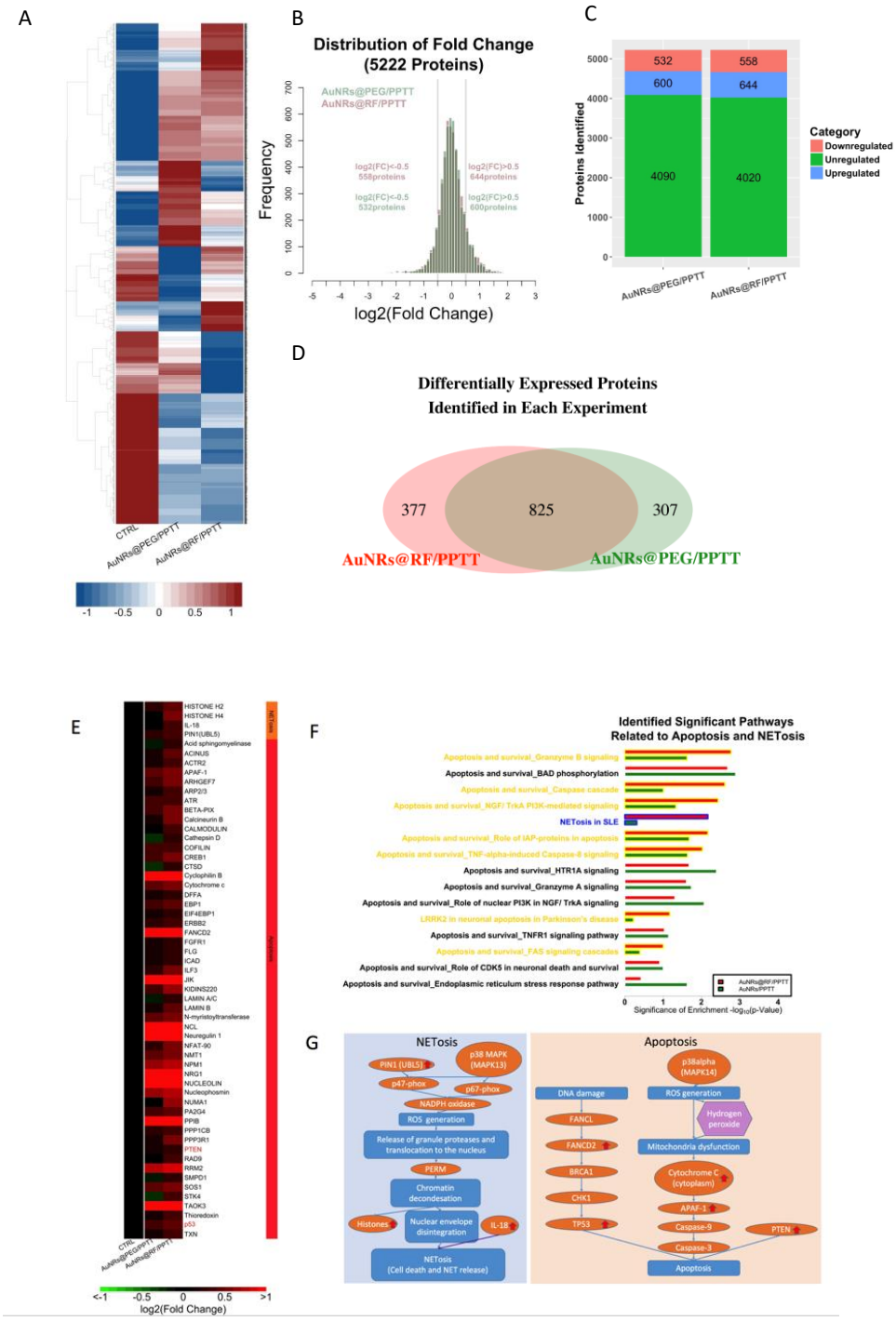

Figure 3-7 Quantitative proteomics

(A) Comprehensive heatmap showing the proteome perturbed by AuNRs@PEG-PPTT and AuNRs@RF-PPTT compared to control group; (B) Distribution of fold changes in proteins perturbed by AuNRs@PEG-PPTT and AuNRs@RF-PPTT compared to control group; (C) Bar graph showing numbers of proteins unregulated,

increased and decreased in each group; (D) Venn diagram showing the differentially expressed proteins identified in each group; (E) Heatmap for proteins related to apoptosis and NETosis contributing to the better efficacy of AuNRs@RF-PPTT compared to AuNRs@PEG-PPTT. The values of protein fold change are listed in Table S1; (F) Identified significant pathways related to apoptosis and NETosis; (G) Simplified pathway map of NETosis and apoptosis.

Long term effects of AuNRs on biodistribution and toxicity:

Treatment with AuNRs enhanced PPTT in Balb/C mice with a low dose of NIR light (**Figure 3-6E**), indicating their strong clinical potential. However, there is limited knowledge regarding several features of this new generation of AuNRs, including their biodistribution, long-term fate and toxicity. To assess toxicity, the histopathology of tissues from the liver, spleen, lung and kidney of mice was evaluated by a pathologist 1 month and 15 months after single intravenous (iv) injection of AuNRs@PEG. We did not observe any histopathological abnormalities in any of the mouse organs (**Figure 3-8A**). Furthermore, we monitored mice every week for 15 months following AuNRs@PEG injection and did not observe any clinical signs of toxicity including ruffled fur, impeded movement, signs of abnormal constitution, aberrant behavior, loss of weight, ocular or nasal discharge, respiratory distress, inability to walk, or diarrhea. TEM was utilized to visually observe AuNRs@PEG particle uptake and organ tissue microstructure. As seen in **Figure 3-8B**, AuNRs@PEG remained inside the cells without any structural changes. Measurement of Au levels in the tissues demonstrated that AuNRs@PEG were present mostly in the spleen and liver of mice (**Figure 3-8C, D**), and to a lesser extent in the kidney and lung (**Figure 3-8E, F**). To measure any gold excretion, we tested the amount of Au in the feces of mice at three different time points (1, 14 and 30 days) (Figure B.8.). We found that a very small

portion of injected Au was excreted whereas the major portion of Au accumulated mainly in the spleen and liver and was sustained without any structural modification over a long period (observed: up to 15 months). Au accumulated in mouse organs from the first day of treatment and remained in these tissues even 15 months later, without any evidence of toxicities.

AuNRs-PPTT is widely recognized as a promising strategy for combating cancer. Developing a valid PPTT *in vivo* that triggers cancer cell apoptosis (avoiding necrosis) and exploring its molecular mechanism of action is of great importance. In addition, exploring the long-term fate of the AuNRs after treatment is critical for clinical usage. In this systematic *in vivo* study, we 1) optimized the conditions of AuNRs-PPTT to induce apoptosis, 2) explored the molecular mechanisms of action of AuNRs-PPTT, and 3) revealed the long-term (15 month) fate of AuNRs, which indicated their lack of toxicity in mouse models. To optimize PPTT conditions to maximize tumor apoptosis, we evaluated the size, surface modification, and concentration of AuNRs and the PPTT laser power both *in vitro* (five HNSCC cell lines) and *in vivo* (MDA686TU xenograft mice model). Cell and tumor growth inhibition and apoptosis were clearly observed *in vitro* and *in vivo*. It is worth noting that among the 5 HNSCC cell lines, we have used UM-SCC-47, which is an HPV positive cell line. Our findings suggest that AuNRs-PPTT is equally effective against viral and non-viral derived tumors. Histopathological analysis of mice tissue revealed that a lower concentration (2.5 nM) of AuNRs@RF-PPTT significantly reduced cancer cell viability as shown by decreased Ki-67. Past attempts to induce apoptosis *in vitro* have applied a moderate hyperthermia [72] or targeted different cellular locations [8, 73-74].

Herein, by adjusting the surface modification and heat generation, we were able to generate efficient tumor apoptosis *in* vivo without any skin wounding.

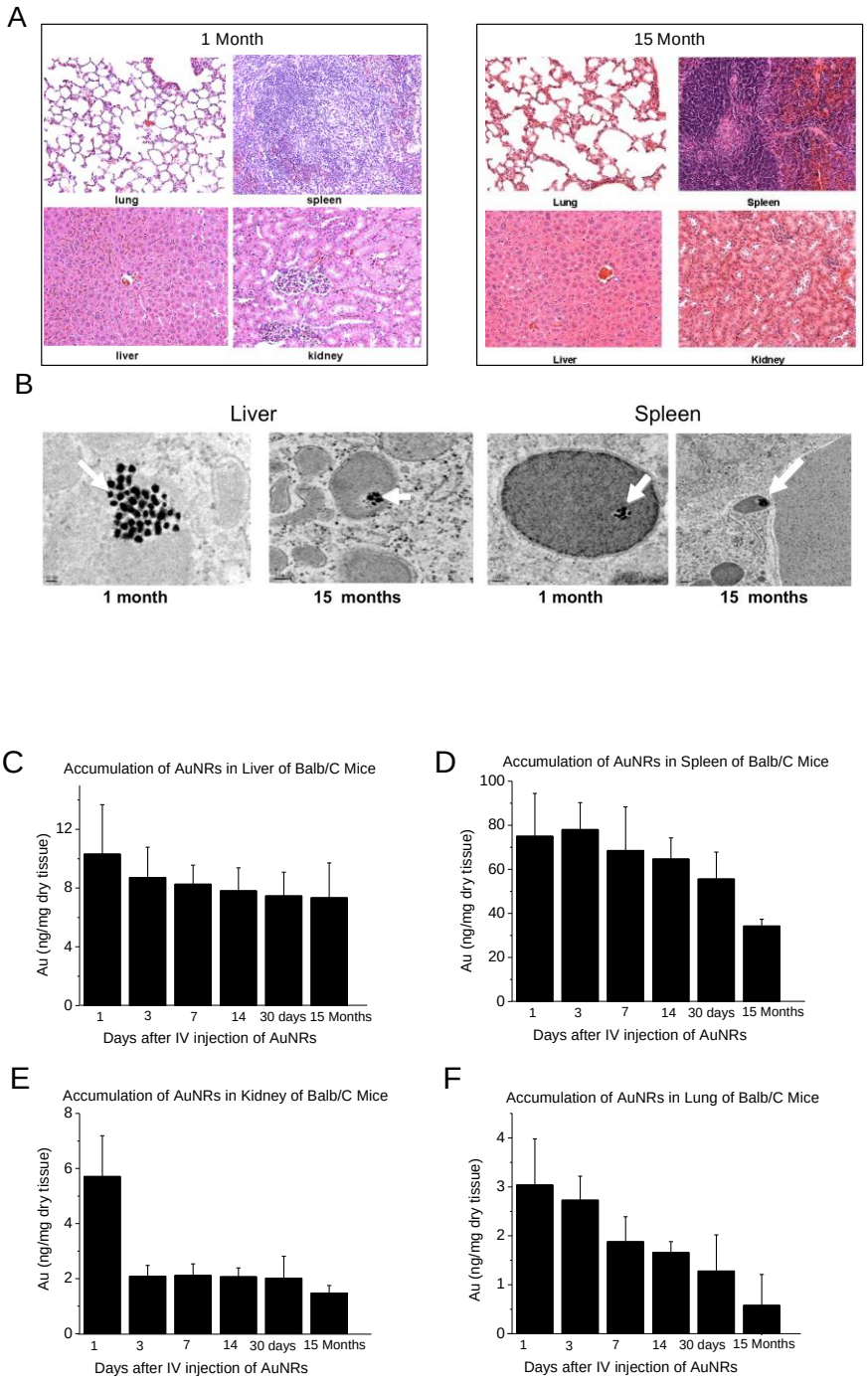

Figure 3-8. Effect of AuNRs on organ toxicity and accumulation

(A) Histopathological images of the liver, spleen, kidney and lung of Balb/c mice at different time points after IV injection of a single dose of AuNRs (Au: 0.18mg/kg, 3 mice per group); (B) TEM images at two time points AuNRs (Au: 0.18mg/kg, 3 mice per group). 10,000 PEG/AuNR (indicated by arrow) were found in the liver and

spleen without morphology changes (up to 15 months) when treated with 25 nm length AuNRs. (C-F) Accumulation of AuNRs in different organs over 15 months. Au concentrations are shown in the liver (C), spleen (D), kidney (E) and lung (F) of Balb/c mice at different time points after IV injection of a single dose of AuNRs (Au: 0.18mg/kg, 3 mice per group) (Error bars are mean ±SEM).

In our study we have optimized our treatment dose based on the tumor volume using very low doses (in nMs with 100 uL AuNPs injection volume) and intratumoral injection, which is more realistic for the clinical application of PPTT. In contrast, most earlier studies have injected the nanoparticles intravenously, at doses based on animal body weight (nanoparticle amount in mg/Kg body weight) [75-77]. Compared to other studies, we used a moderate laser intensity and low exposure time (0.5 to 2 W/cm^2 for 2 minutes)[78].

The effect of heat shock (hyperthermia) on the induction of cell apoptosis has been known for centuries. The mechanism of hyperthermia-induced apoptosis has been largely unclear until recently [79]. PPTT is not simply heat shock; instead, it could be regarded as a synergistic effect between nanoparticles and hyperthermia. We observed that both apoptosis and NETosis pathways were significantly affected after treatment with PPTT, especially AuNRs@RF-PPTT, which demonstrated a much stronger molecular impact on these pathways. Cytochrome c and p53-related apoptosis mechanisms were identified as contributing to the enhanced effect of PPTT with RF-conjugated AuNRs. Furthermore, Pin1 and IL18-related signaling contribute to the observed perturbation of the NETosis pathway by PPTT with RF-conjugated AuNRs. Upregulation of Pin1 has been shown to induce ROS production through phosphorylation of NADPH oxidase regulatory subunits p47-phox and p67-phox [68-70]. ROS production further leads to the release of PERM.

Histone H4 and histone H2 are subsequently degraded leading to chromatin decondensation, which is further enhanced by PERM. Eventually the integrity of the nuclear envelope is disrupted, resulting in cell rupturing [71]. The greater effect of AuNRs@RF-PPTT on NETosis may result from better uptake of AuNRs into the cells when conjugated with RF. It has been reported recently that cells entrap nanoparticles via formation of NETs, which are formed immediately following rapid damage to plasma membranes and instability of the lysosomal compartment induced by nanoparticle stimulation [64]. The significant effects observed in our study of AuNRs@RF-PPTT on the NETosis pathway may account for the greater efficacy of the RF conjugate.

After PPTT, we observed the aggregation of AuNRs@RF around cell nuclear membranes as shown by DIC microscopy (**Figure 1B**). Our proteomics study identified greater upregulation of nuclear lamin proteins (**Figure 2E**), which are responsible for nuclear shape and structure. Therefore, AuNRs@RF may harm nuclear membrane integrity through intrinsic cell defense mechanisms. On the other hand, lamins are known to impede cancer cell migration and invasion [80, 81] Lamin promotes cell-matrix adhesion and plays an important role in apoptosis by loosening epithelial cell contact with the extracellular matrix [82]. Lamins are targets for degradation in the apoptotic process, and accordingly are often used as markers for apoptosis [83].

There is to date limited knowledge regarding the biodistribution, long-term fate and toxicity of AuNRs. Thus, our studies of the toxicity of AuNRs are important to develop

safer treatments. To the best of our knowledge, this is the first report of a 15-month toxicity study of AuNRs in mice. Based on our findings, we can conclude that these AuNRs have great potential to be used in PPTT for the local treatment of cancers, supporting the efficient translation of AuNRs into clinical settings.

3.2.4 Conclusion and Future Outlook

We have optimized the efficacy and studied the molecular mechanisms of AuNRs-assisted plasmonic photothermal therapy, and examined the 15-month toxicity and fate of AuNRs in a mouse model. Together, these data demonstrate that our AuNRs-PPTT is highly effective and safe for local therapy for cancers. These findings provide a strong framework for translation of this approach to the clinic.

3.2.5 References

1. Ali, M. R. K., Rahman, M. A., Wu, Y., Han, T., Peng, X. H., Mackay, M. A., Wang, D., Shin, H. J., Chen, Z., Xiao, H., Wu, R., Tang, Y., Shin, D. M., El-Sayed, M. A. (2017) Gold Nanorods-assisted Plasmonic Photothermal Therapy of Cancer; Efficacy, Toxicity and Mechanistic Studies in vivo, *under third revision, PNAS.*

2. Huang, X.; El-Sayed, I. H.; Qian, W.; El-Sayed, M. A., (2006) Cancer Cell Imaging and Photothermal Therapy in the Near-Infrared Region by Using Gold Nanorods. *Journal of the American Chemical Society, 128* (6), 2115-2120.

3. Dickerson, E. B.; Dreaden, E. C.; Huang, X. H.; El-Sayed, I. H.; Chu, H. H.; Pushpanketh, S.; McDonald, J. F.; El-Sayed, M. A., (2008) Gold nanorod assisted near-infrared plasmonic photothermal therapy (PPTT) of squamous cell carcinoma in mice. *Cancer Letters*, *269* (1), 57-66.

4. Hirsch, L. R.; Stafford, R. J.; Bankson, J. A.; Sershen, S. R.; Rivera, B.; Price, R. E.; Hazle, J. D.; Halas, N. J.; West, J. L., (2003) Nanoshell-mediated near-infrared thermal therapy of tumors under magnetic resonance guidance. *Proceedings of the National Academy of Sciences of the United States of America*, *100* (23), 13549-13554.

5. Abadeer, N. S.; Murphy, C. J., (2016) Recent Progress in Cancer Thermal Therapy Using Gold Nanoparticles. *The Journal of Physical Chemistry C*, *120* (9), 4691-4716.

6. Steinmetz, N. F., (2010) "Cancer Nanotechnology: Methods and Protocols (Methods in Molecular Biology)" by Stephen R. Grobmyer (Editor), Brij M. Moudgil (Editor). *BioMedical Engineering OnLine*, *9* (1), 1-3.

7. Alkilany, A. M.; Thompson, L. B.; Boulos, S. P.; Sisco, P. N.; Murphy, C. J., (2012) Gold nanorods: Their potential for photothermal therapeutics and drug delivery, tempered by the complexity of their biological interactions. *Advanced Drug Delivery Reviews*, *64* (2), 190-199.

8. Ali, M. R.; Ibrahim, I. M.; Ali, H. R.; Selim, S. A.; El-Sayed, M. A., (2016) Treatment of natural mammary gland tumors in canines and felines using gold nanorods-assisted plasmonic photothermal therapy to induce tumor apoptosis. *International Journal of Nanomedicine*, *11*, 4849.

9. von Maltzahn, G.; Park, J. H.; Agrawal, A.; Bandaru, N. K.; Das, S. K.; Sailor, M. J.; Bhatia, S. N., (2009) Computationally guided photothermal tumor therapy using long-circulating gold nanorod antennas. *Cancer research*, *69* (9), 3892-900.

10. Pattani, V. P.; Shah, J.; Atalis, A.; Sharma, A.; Tunnell, J. W., (2015) Role of apoptosis and necrosis in cell death induced by nanoparticle-mediated photothermal therapy. *Journal of Nanoparticle Research*, *17* (1), 1-11.

11. Bonfil, R. D.; Bustuoabad, O. D.; Ruggiero, R. A.; Meiss, R. P.; Pasqualini, C. D., (1988) Tumor Necrosis Can Facilitate the Appearance of Metastases. *Clinical & Experimental Metastasis*, *6* (2), 121-129.

12. Hanahan, D.; Weinberg, R. A., (2011) Hallmarks of Cancer: The Next Generation. *Cell*, *144* (5), 646-674.

13. Danial, N. N.; Korsmeyer, S. J., (2004) Cell death: critical control points. *Cell*, *116* (2), 205-19.

14. Ali, M. R.; Ali, H. R.; Rankin, C. R.; El-Sayed, M. A., (2016) Targeting heat shock protein 70 using gold nanorods enhances cancer cell apoptosis in low dose plasmonic photothermal therapy. *Biomaterials*, *102*, 1-8.

15. Pérez-Hernández, M.; del Pino, P.; Mitchell, S. G.; Moros, M.; Stepien, G.; Pelaz, B.; Parak, W. J.; Gálvez, E. M.; Pardo, J.; de la Fuente, J. M., (2015) Dissecting the Molecular Mechanism of Apoptosis during Photothermal Therapy Using Gold Nanoprisms. *ACS Nano*, *9* (1), 52-61.

16. Oh, N.; Park, J. H., (2014) Endocytosis and exocytosis of nanoparticles in mammalian cells. *International Journal of Nanomedicine, 9,* 51-63.

17. Iyer, A. K.; Khaled, G.; Fang, J.; Maeda, H., (2006) Exploiting the enhanced permeability and retention effect for tumor targeting. *Drug Discovery Today, 11* (17–18), 812-818.

18. Maeda, H.; Wu, J.; Sawa, T.; Matsumura, Y.; Hori, K., (2000) Tumor vascular permeability and the EPR effect in macromolecular therapeutics: a review. *Journal of controlled release: official journal of the Controlled Release Society, 65* (1-2), 271-84.

19. Liu, X.; Chen, Y.; Li, H.; Huang, N.; Jin, Q.; Ren, K.; Ji, J., (2013) Enhanced retention and cellular uptake of nanoparticles in tumors by controlling their aggregation behavior. *ACS Nano, 7* (7), 6244-57.

20. Wilhelm, S.; Tavares, A. J.; Dai, Q.; Ohta, S.; Audet, J.; Dvorak, H. F.; Chan, W. C. W., (2016) Analysis of nanoparticle delivery to tumours. *Nature Reviews Materials, 1,* 16014.

21. Ali, M. R. K.; Panikkanvalappil, S. R.; El-Sayed, M. A., (2014) Enhancing the Efficiency of Gold Nanoparticles Treatment of Cancer by Increasing Their Rate of Endocytosis and Cell Accumulation Using Rifampicin. *Journal of the American Chemical Society, 136* (12), 4464-4467.

22. Mackey, M. A.; Ali, M. R. K.; Austin, L. A.; Near, R. D.; El-Sayed, M. A., (2014) The Most Effective Gold Nanorod Size for Plasmonic Photothermal Therapy: Theory and In Vitro Experiments. *Journal of Physical Chemistry B, 118* (5), 1319-1326.

23. Alkilany, A. M.; Murphy, C. J., (2010) Toxicity and cellular uptake of gold nanoparticles: what we have learned so far? *Journal of Nanoparticle Research, 12* (7), 2313-2333.

24. Connor, E. E.; Mwamuka, J.; Gole, A.; Murphy, C. J.; Wyatt, M. D., (2005) Gold nanoparticles are taken up by human cells but do not cause acute cytotoxicity. *Small, 1* (3), 325-327.

25. Axiak-Bechtel, A. M.; Upendran, A.; Lattimer, J. C.; Kelsey, J.; Cutler, C. S.; Selting, K. A.; Bryan, J. N.; Henry, C. J.; Boote, E.; Tate, D. J.; Bryan, M. E.; Katti, K. V.; Kannan, R., (2014) Gum arabic-coated radioactive gold nanoparticles cause no short-term local or systemic toxicity in the clinically relevant canine model of prostate cancer. *International Journal of Nanomedicine, 9*, 5001-5011.

26. Chen, H.; Dorrigan, A.; Saad, S.; Hare, D. J.; Cortie, M. B.; Valenzuela, S. M., (2013) In Vivo Study of Spherical Gold Nanoparticles: Inflammatory Effects and Distribution in Mice. *PLoS ONE, 8* (2), e58208.

27. You, J.; Zhou, J. L.; Zhou, M.; Liu, Y.; Robertson, J. D.; Liang, D.; Van Pelt, C.; Li, C., (2014) Pharmacokinetics, clearance, and biosafety of polyethylene glycol-coated hollow gold nanospheres. *Particle and Fibre Toxicology, 11*.

28. Pernodet, N.; Fang, X. H.; Sun, Y.; Bakhtina, A.; Ramakrishnan, A.; Sokolov, J.; Ulman, A.; Rafailovich, M., (2006) Adverse effects of citrate/gold nanoparticles on human dermal fibroblasts. *Small, 2* (6), 766-773.

29. Cho, Y. S.; Challa, S.; Moquin, D.; Genga, R.; Ray, T. D.; Guildford, M.; Chan, F. K., (2009) Phosphorylation-driven assembly of the RIP1-RIP3 complex regulates programmed necrosis and virus-induced inflammation. *Cell*, *137* (6), 1112-23.

30. Qu, Y.; Huang, Y.; Lu, X., (2013) Proteomic analysis of molecular biocompatibility of gold nanoparticles to human dermal fibroblasts-fetal. *Journal of biomedical nanotechnology*, *9* (1), 40-52.

31. Yildirimer, L.; Thanh, N. T. K.; Loizidou, M.; Seifalian, A. M., (2011) Toxicology and clinical potential of nanoparticles. *Nano Today*, *6* (6), 585-607.

32. Murphy, C. J.; Gole, A. M.; Stone, J. W.; Sisco, P. N.; Alkilany, A. M.; Goldsmith, E. C.; Baxter, S. C., (2008) Gold Nanoparticles in Biology: Beyond Toxicity to Cellular Imaging. *Accounts Chem Res*, *41* (12), 1721-1730.

33. Boisselier, E.; Astruc, D., (2009) Gold nanoparticles in nanomedicine: preparations, imaging, diagnostics, therapies and toxicity. *Chemical Society Reviews*, *38* (6), 1759-1782.

34. Niidome, T.; Yamagata, M.; Okamoto, Y.; Akiyama, Y.; Takahashi, H.; Kawano, T.; Katayama, Y.; Niidome, Y., (2006) PEG-modified gold nanorods with a stealth character for in vivo applications. *Journal of Controlled Release*, *114* (3), 343-347.

35. Sadauskas, E.; Danscher, G.; Stoltenberg, M.; Vogel, U.; Larsen, A.; Wallin, H., (2009) Protracted elimination of gold nanoparticles from mouse liver. *Nanomedicine : nanotechnology, biology, and medicine*, *5* (2), 162-9.

36. Ali, M. R. K.; Snyder, B.; El-Sayed, M. A., (2012) Synthesis and Optical Properties of Small Au Nanorods Using a Seedless Growth Technique. *Langmuir*, *28* (25), 9807-9815.

37. Ali, H. R.; Ali, M. R.; Wu, Y.; Selim, S. A.; Abdelaal, H. F.; Nasr, E. A.; El-Sayed, M. A., (2016) Gold Nanorods as Drug Delivery Vehicles for Rifampicin Greatly Improve the Efficacy of Combating Mycobacterium tuberculosis with Good Biocompatibility with the Host Cells. *Bioconjugate Chemistry*, *27* (10), 2486-2492.

38. Zhao, M.; Sano, D.; Pickering, C. R.; Jasser, S. A.; Henderson, Y. C.; Clayman, G. L.; Sturgis, E. M.; Ow, T. J.; Lotan, R.; Carey, T. E.; Sacks, P. G.; Grandis, J. R.; Sidransky, D.; Heldin, N. E.; Myers, J. N., (2011) Assembly and initial characterization of a panel of 85 genomically validated cell lines from diverse head and neck tumor sites. *Clin Cancer Res*, *17* (23), 7248-64.

39. Vichai, V.; Kirtikara, K., (2006) Sulforhodamine B colorimetric assay for cytotoxicity screening. *Nature protocols*, *1* (3), 1112-6.

40. Rahman, M. A.; Amin, A. R.; Wang, D.; Koenig, L.; Nannapaneni, S.; Chen, Z.; Wang, Z.; Sica, G.; Deng, X.; Chen, Z. G.; Shin, D. M., (2013) RRM2 regulates Bcl-2 in head and neck and lung cancers: a potential target for cancer therapy. *Clin Cancer Res*, *19* (13), 3416-28.

41. Wu, Y.; Wang, F. J.; Liu, Z. Y.; Qin, H. Q.; Song, C. X.; Huang, J. F.; Bian, Y. Y.; Wei, X. L.; Dong, J.; Zou, H. F., (2014) Five-plex isotope dimethyl labeling for quantitative proteomics. *Chemical Communications*, *50* (14), 1708-1710.

42. Xiao, H.; Wu, R., (2016) Quantitative investigation of human cell surface N-glycoprotein dynamics. *Chemical Science*.

43. Eng, J. K.; McCormack, A. L.; Yates, J. R., (1994) An approach to correlate tandem mass spectral data of peptides with amino acid sequences in a protein database. *Journal of the American Society for Mass Spectrometry, 5* (11), 976-989.

44. Elias, J. E.; Gygi, S. P., (2007) Target-decoy search strategy for increased confidence in large-scale protein identifications by mass spectrometry. *Nat Meth, 4* (3), 207-214.

45. Kall, L.; Canterbury, J. D.; Weston, J.; Noble, W. S.; MacCoss, M. J., (2007) Semi-supervised learning for peptide identification from shotgun proteomics datasets. *Nat Methods, 4* (11), 923-5.

46. Huttlin, E. L.; Jedrychowski, M. P.; Elias, J. E.; Goswami, T.; Rad, R.; Beausoleil, S. A.; Villén, J.; Haas, W.; Sowa, M. E.; Gygi, S. P., (2010) A tissue-specific atlas of mouse protein phosphorylation and expression. *Cell, 143* (7), 1174-1189.

47. Mecham, B. H.; Nelson, P. S.; Storey, J. D., (2010) Supervised normalization of microarrays. *Bioinformatics, 26* (10), 1308-1315.

48. Sakai, T.; Liu, L.; Teng, X.; Mukai-Sakai, R.; Shimada, H.; Kaji, R.; Mitani, T.; Matsumoto, M.; Toida, K.; Ishimura, K.; Shishido, Y.; Mak, T. W.; Fukui, K., (2004) Nucling recruits Apaf-1/pro-caspase-9 complex for the induction of stress-induced apoptosis. *J Biol Chem, 279* (39), 41131-40.

49. Yin, Q.; Park, H. H.; Chung, J. Y.; Lin, S. C.; Lo, Y. C.; da Graca, L. S.; Jiang, X.; Wu, H., (2006) Caspase-9 holoenzyme is a specific and optimal procaspase-3 processing machine. *Mol Cell*, *22* (2), 259-68.

50. Geering, B.; Simon, H. U., (2011) A novel signaling pathway in TNFalpha-induced neutrophil apoptosis. *Cell Cycle*, *10* (17), 2821-2.

51. Geering, B.; Gurzeler, U.; Federzoni, E.; Kaufmann, T.; Simon, H. U., (2011) A novel TNFR1-triggered apoptosis pathway mediated by class IA PI3Ks in neutrophils. *Blood*, *117* (22), 5953-62.

52. Barroso, E.; Pita, G.; Arias, J. I.; Menendez, P.; Zamora, P.; Blanco, M.; Benitez, J.; Ribas, G., (2009) The Fanconi anemia family of genes and its correlation with breast cancer susceptibility and breast cancer features. *Breast Cancer Res Treat*, *118* (3), 655-60.

53. Montes de Oca, R.; Andreassen, P. R.; Margossian, S. P.; Gregory, R. C.; Taniguchi, T.; Wang, X.; Houghtaling, S.; Grompe, M.; D'Andrea, A. D., (2005) Regulated interaction of the Fanconi anemia protein, FANCD2, with chromatin. *Blood*, *105* (3), 1003-9.

54. Longerich, S.; San Filippo, J.; Liu, D.; Sung, P., (2009) FANCI binds branched DNA and is monoubiquitinated by UBE2T-FANCL. *J Biol Chem*, *284* (35), 23182-6.

55. Yuan, F.; El Hokayem, J.; Zhou, W.; Zhang, Y., (2009) FANCI protein binds to DNA and interacts with FANCD2 to recognize branched structures. *J Biol Chem*, *284* (36), 24443-52.

56. Garcia-Higuera, I.; Taniguchi, T.; Ganesan, S.; Meyn, M. S.; Timmers, C.; Hejna, J.; Grompe, M.; D'Andrea, A. D., (2001) Interaction of the Fanconi anemia proteins and BRCA1 in a common pathway. *Mol Cell*, *7* (2), 249-62.

57. Taniguchi, T.; Garcia-Higuera, I.; Andreassen, P. R.; Gregory, R. C.; Grompe, M.; D'Andrea, A. D., (2002) S-phase-specific interaction of the Fanconi anemia protein, FANCD2, with BRCA1 and RAD51. *Blood*, *100* (7), 2414-20.

58. Yarden, R. I.; Pardo-Reoyo, S.; Sgagias, M.; Cowan, K. H.; Brody, L. C., (2002) BRCA1 regulates the G2/M checkpoint by activating Chk1 kinase upon DNA damage. *Nat Genet*, *30* (3), 285-9.

59. Goudelock, D. M.; Jiang, K.; Pereira, E.; Russell, B.; Sanchez, Y., (2003) Regulatory Interactions between the Checkpoint Kinase Chk1 and the Proteins of the DNA-dependent Protein Kinase Complex. *Journal of Biological Chemistry*, *278* (32), 29940-29947.

60. Norbury, C. J.; Zhivotovsky, B., (2004) DNA damage-induced apoptosis. *Oncogene*, *23* (16), 2797-808.

61. Weng, L.-P.; Brown, J. L.; Eng, C., (2001) PTEN induces apoptosis and cell cycle arrest through phosphoinositol-3-kinase/Akt-dependent and -independent pathways. *Human Molecular Genetics*, *10* (3), 237-242.

62. Qi, Y.; Liu, J.; Saadat, S.; Tian, X.; Han, Y.; Fong, G. H.; Pandolfi, P. P.; Lee, L. Y.; Li, S., (2015) PTEN induces apoptosis and cavitation via HIF-2-dependent Bnip3 upregulation during epithelial lumen formation. *Cell Death Differ*, *22* (5), 875-84.

63. Zhao, H.; Dupont, J.; Yakar, S.; Karas, M.; LeRoith, D., (2004) PTEN inhibits cell proliferation and induces apoptosis by downregulating cell surface IGF-IR expression in prostate cancer cells. *Oncogene, 23* (3), 786-94.

64. Muñoz, L. E.; Bilyy, R.; Biermann, M. H. C.; Kienhöfer, D.; Maueröder, C.; Hahn, J.; Brauner, J. M.; Weidner, D.; Chen, J.; Scharin-Mehlmann, M.; Janko, C.; Friedrich, R. P.; Mielenz, D.; Dumych, T.; Lootsik, M. D.; Schauer, C.; Schett, G.; Hoffmann, M.; Zhao, Y.; Herrmann, M., (2016) Nanoparticles size-dependently initiate self-limiting NETosis-driven inflammation. *Proceedings of the National Academy of Sciences*, *113* (40), E5856-E5865.

65. Yu, Y.; Su, K., (2013) Neutrophil Extracellular Traps and Systemic Lupus Erythematosus. *J Clin Cell Immunol*, *4*.

66. Kahlenberg, J. M.; Carmona-Rivera, C.; Smith, C. K.; Kaplan, M. J., (2013) Neutrophil extracellular trap-associated protein activation of the NLRP3 inflammasome is enhanced in lupus macrophages. *J Immunol, 190* (3), 1217-26.

67. Mitroulis, I.; Kambas, K.; Chrysanthopoulou, A.; Skendros, P.; Apostolidou, E.; Kourtzelis, I.; Drosos, G. I.; Boumpas, D. T.; Ritis, K., (2011) Neutrophil extracellular trap formation is associated with IL-1beta and autophagy-related signaling in gout. *PLoS One, 6* (12), e29318.

68. Makni-Maalej, K.; Boussetta, T.; Hurtado-Nedelec, M.; Belambri, S. A.; Gougerot-Pocidalo, M. A.; El-Benna, J., (2012) The TLR7/8 agonist CL097 primes N-formyl-methionyl-leucyl-phenylalanine-stimulated NADPH oxidase activation in human

neutrophils: critical role of p47phox phosphorylation and the proline isomerase Pin1. *J Immunol*, *189* (9), 4657-65.

69. El Benna, J.; Han, J.; Park, J. W.; Schmid, E.; Ulevitch, R. J.; Babior, B. M., (1996) Activation of p38 in stimulated human neutrophils: phosphorylation of the oxidase component p47phox by p38 and ERK but not by JNK. *Arch Biochem Biophys*, *334* (2), 395-400.

70. Dang, P. M.; Morel, F.; Gougerot-Pocidalo, M. A.; El Benna, J., (2003) Phosphorylation of the NADPH oxidase component p67(PHOX) by ERK2 and P38MAPK: selectivity of phosphorylated sites and existence of an intramolecular regulatory domain in the tetratricopeptide-rich region. *Biochemistry*, *42* (15), 4520-6.

71. Papayannopoulos, V.; Metzler, K. D.; Hakkim, A.; Zychlinsky, A., (2010) Neutrophil elastase and myeloperoxidase regulate the formation of neutrophil extracellular traps. *J Cell Biol*, *191* (3), 677-91.

72. Li, S.; Chien, S.; Branemark, P. I., (1999) Heat shock-induced necrosis and apoptosis in osteoblasts. *Journal of orthopaedic research : official publication of the Orthopaedic Research Society*, *17* (6), 891-9.

73. Wang, L.; Liu, Y.; Li, W.; Jiang, X.; Ji, Y.; Wu, X.; Xu, L.; Qiu, Y.; Zhao, K.; Wei, T.; Li, Y.; Zhao, Y.; Chen, C., (2011) Selective Targeting of Gold Nanorods at the Mitochondria of Cancer Cells: Implications for Cancer Therapy. *Nano Letters*, *11* (2), 772-780.

74. Kang, B.; Mackey, M. A.; El-Sayed, M. A., (2010) Nuclear Targeting of Gold Nanoparticles in Cancer Cells Induces DNA Damage, Causing Cytokinesis Arrest and Apoptosis. *Journal of the American Chemical Society*, *132* (5), 1517-1519.

75. von Maltzahn, G.; Park, J.-H.; Agrawal, A.; Bandaru, N. K.; Das, S. K.; Sailor, M. J.; Bhatia, S. N., (2009) Computationally Guided Photothermal Tumor Therapy Using Long-Circulating Gold Nanorod Antennas. *Cancer Research*, *69* (9), 3892-3900.

76. Lal, S.; Clare, S. E.; Halas, N. J., (2008) Nanoshell-Enabled Photothermal Cancer Therapy: Impending Clinical Impact. *Accounts of Chemical Research*, *41* (12), 1842-1851.

77. Melancon, M. P.; Lu, W.; Yang, Z.; Zhang, R.; Cheng, Z.; Elliot, A. M.; Stafford, J.; Olson, T.; Zhang, J. Z.; Li, C., (2008) targeting of hollow gold nanoshells directed at epidermal growth factor receptor for photothermal ablation therapy. *Molecular Cancer Therapeutics*, *7* (6), 1730-1739.

78. Moon, H. K.; Lee, S. H.; Choi, H. C., (2009) In vivo near-infrared mediated tumor destruction by photothermal effect of carbon nanotubes. *ACS Nano*, *3* (11), 3707-13.

79. Song, A. S.; Najjar, A. M.; Diller, K. R., (2014) Thermally induced apoptosis, necrosis, and heat shock protein expression in 3D culture. *Journal of biomechanical engineering*, *136* (7).

80. Short, B., (2014) Lamin-A provides stiff resistance to cell migration. *The Journal of cell biology*, *204* (5), 626-626.

81. van der Zee, J. A.; van Eijck, C. H.; Hop, W. C.; Biermann, K.; Dicheva, B. M.; Seynhaeve, A. L.; Koning, G. A.; Eggermont, A. M.; Ten Hagen, T. L., (2012) Tumour

basement membrane laminin expression predicts outcome following curative resection of pancreatic head cancer. *Br J Cancer*, *107* (7), 1153-8.

82. Esco, M. A.; Wang, Z.; McDermott, M. L.; Kurpakus-Wheater, M., (2001) Potential role for laminin 5 in hypoxia-mediated apoptosis of human corneal epithelial cells. *Journal of cell science*, *114* (Pt 22), 4033-40.

83. Broers, J. L.; Ramaekers, F. C., (2014) The role of the nuclear lamina in cancer and apoptosis. *Advances in experimental medicine and biology*, *773*, 27-48.

3.3 Treatment of Natural Mammary Gland Tumors in Canines and Felines Using Gold Nanorods-Assisted Plasmonic Photothermal Therapy to Induce Tumor Apoptosis [1]

Plasmonic photothermal therapy (PPTT) is a cancer therapy in which gold nanorods are injected at the site of a tumor before near-infrared light is transiently applied to the tumor causing localized cell death. Previously, PPTT studies have been carried out on xenograft mice models. Herein, we report a study showing the feasibility of PPTT as applied to natural tumors in the mammary glands of dogs and cats, which more realistically represent their human equivalents at the molecular level. We optimized a regime of three low PPTT doses at 2-week intervals that ablated tumors mainly via apoptosis in thirteen natural mammary gland tumors from seven animals. Histopathology, X-ray, blood profiles, and comprehensive examinations were used for both the diagnosis and the evaluation of tumor statuses before and after treatment. Histopathology results showed an obvious reduction in the cancer grade shortly after the first treatment and a complete regression after the third treatment. Blood tests showed no obvious change in liver and kidney functions. Similarly, X-ray diffraction showed no metastasis after 1 year of treatment. In conclusion, our study suggests the feasibility of applying the gold nanorods-PPTT on natural tumors in dogs and cats without any relapse or toxicity effects after 1 year of treatment.

3.3.1 Introduction

Plasmonic nanoparticles (NPs) exhibit unique physical and chemical properties that can be utilized for both cancer treatment and diagnosis. In plasmonic photothermal therapy

(PPTT), NPs such as gold nanorods (AuNRs) absorb near-infrared (NIR) light resulting in hyperthermia, thereby inducing tumor ablation. In PPTT, cancer cells show a much higher uptake of NPs than normal cells. Although many traditional cancer therapies with drugs or radiation cause side effects due to their toxicity to normal cells, PPTT has fewer side effects mainly because of its selectivity to cancer cells. In PPTT, two selective targeting methods can be applied: 1) active targeting and 2) passive targeting. In active targeting, specific surface modifications (ligands) of NPs can recognize and bind to the receptors on the surface of cancer cells. On the other hand, in passive targeting, NPs are usually injected directly to solid tumor and accumulate inside the tumor mainly via the enhanced permeability and retention effect. The enhanced permeability and retention effect has been regarded as a primary rationale for the delivery of NPs due to the leaky tumor blood vasculature. Then, the tumor will be irradiated with laser, causing localized heat for killing cancer cells [2–6] These attributes of PPTT make it a superior alternative in cancer treatment.

Among all plasmonic gold NPs, three types have shown the greatest potential for use in cancer PPTT: gold nanocages, gold nanoshells (AuNSs), and AuNRs.[7-9] These three types of NPs have been synthesized with specific sizes and shapes designed to enable absorption of NIR radiation and allow for subsequent heat transmission. Due to the toxicological properties that could result from the presence of unused silver (Ag) on the interior of the nanocage during its synthesis, the widespread use of gold nanocages for the treatment of cancer is not likely to occur.[10] The AuNSs plasmon wavelength is dependent on the ratio of the thickness of the shell to the core diameter.[1] Thus far, the use of AuNSs has been limited to the US Food and Drug Administration-approved use of the AuNSs AuroLase®

(Nanospectra Biosciences, Inc., Houston, TX, USA) for PPTT clinical trials of head and neck cancer.[1] One challenge of using AuNSs is the difficulty of synthesizing them with a uniform ratio of shell to core radii. AuNRs exhibit a longitudinal NIR surface plasmon resonance band that is directly proportional to its aspect ratio (length/width). Among all plasmonic gold NPs, AuNRs are regarded as one of the most feasible options for absorbing NIR laser radiation. [11-14] For example, a recent publication compared the efficacy of AuNRs with that of AuNSs and found that AuNRs intrinsically have greater absorption efficacy per gram of gold and longer circulation half-life in vivo.[15] Additionally, PPTT-AuNRs studies have shown encouraging results with no significant toxicological side effects in vivo (xenograft mice model).[16-19]

PPTT can induce cell death primarily by two pathways: necrosis and apoptosis [20]. During necrosis, the heat induced from PPTT disrupts the plasma membrane causing the cytoplasmic components to leak out and inflammation to occur within the cell. However, apoptosis is a highly regulated cell death pathway and would thus be a cleaner way for eliminating cancer cells. Therefore, modulating PPTT to trigger apoptosis would be more favorable in clinical studies. It has been reported that different intracellular locations or shapes of NPs regulate the switch between necrosis and apoptosis [21, 22]. In this study, we were able to cause cancer cell apoptosis in vitro and in vivo by adjusting the laser exposure time.

The primary novelty of this study was the extension of AuNRs-assisted PPTT to natural tumors in animals larger than ones used in any previous study. Mammary gland tumors of epithelial origin are very common neoplasms of canines and felines. The similarity of molecular and biological machinery of canines/felines and that of humans suggests the

suitability of using mammary tumors of these animals as a model for the study of human mammary tumors [23-25]. The second novelty was the optimization of AuNRs-PPTT's conditions to generate tumor apoptosis as a favorable cell death mechanism (rather than necrosis) [12, 26-27]. Herein, we directly injected the PEGylated AuNRs to the mammary tumors of each canine/feline as opposed to intravenous injection, as our previous study showed a better efficacy for intratumoral injection than intravenous injection,[1] although the latter could be helpful for some applications (especially for tumors that are not accessible for direct injection of AuNR) [8]. We tested PPTT on canine and feline natural mammary gland tumors. To minimize side effects, we optimized PPTT dosages to enable a slow cancer cell apoptosis. Using our optimized protocol, adjusting the photothermic temperature to 44°C, we could ablate 100% of tumors in seven animals without any relapse or toxicity effect after 1 year from the tumor treatment.

3.3.2 Experimental methods

Synthesis and surface modification of AuNRs

AuNRs were prepared according to the literature [28]. Briefly, $HAuCl_4$ (5 mL, 1 mM; Sigma-Aldrich, St. Louis, MO, USA) was added to 5 mL of cetyltrimethylammonium bromide (CTAB, 0.20 M; Sigma-Aldrich). $AgNO_3$ (250 μL, 4 mM; Sigma-Aldrich) was then added and the pH of the solution adjusted to 1–1.15. Around 70 μL of ascorbic acid (78.8 mM; Sigma-Aldrich) was added to the solution until the solution became clear. Ice-cold $NaBH_4$ (15 μL, 0.01 M; Sigma-Aldrich) was injected into the unstirred growth solution immediately and then allowed to react for 6 hours. The resulting AuNRs had

dimensions of approximately 25×5 nm (see "Formulation and characterization of the AuNRs" section, Figure 1). AuNRs were concentrated by centrifuging at 19,745 rcf for 15 minutes. The pellet was redispersed in water and centrifuged at 19,745 rcf for an additional 15 minutes. Then methoxy polyethylene glycol (PEG) thiol (m-PEG-Th, PEG; Laysan Bio, Arab, AL, USA) was added to the CTAB-conjugated AuNRs and was incubated overnight in a shaker. A final ratio of about 20,000 PEG molecules per NP was achieved after centrifugation to remove unconjugated PEG.

Characterization of AuNRs

The characterization of AuNRs was carried out using a Cary 500 UV–Vis Spectrometer (Agilent Technologies, Santa Clara, CA, USA) for the spectroscopic measurements, and a JEOL 100 CX transmission electron microscope (TEM) (JEOL Ltd., Tokyo, Japan) was used to image the samples. Zeta potentials were measured using a ZetaSizer 3000 HAS (Malvern Instruments, Worcestershire, UK). Zeta potential was tested to characterize the surface conjugation with PEG. Ellman's reagents (react with free -SH group; Sigma-Aldrich) were used to quantify the number of PEG molecules bound to the surface of the AuNRs [29] Ellman's reagent reacts with free -SH group and can be measured calorimetrically at 412 nm. By subtracting the absorbance of the residual PEG, in the supernatant solution after PEG conjugation and centrifugation, from the original absorbance of the solution before adding to AuNRs, we can calculate the number of PEG molecules on the surface of AuNRs by Beer's law. The results of characterization are described below (see "Formulation and characterization of the AuNRs" section).

Animal diagnosis, ultrasonography, and X-ray examination

The animals were admitted to the clinic of Department of Surgery, Faculty of Veterinary Medicine, Cairo University. All pets' owners claimed that their animals did not receive any treatment before their arrival at the university. Histopathology tests were used to diagnose the tumors as adenocarcinoma without any skin invasion, except for one tumor (Case 1, Tumor 6). Seven animals were included in this study, five canines (females) and two felines (females), and the total number of tumors was thirteen. All animals were handled in accordance with Association for Assessment and Accreditation of Laboratory Animal Care and Office of Laboratory Animal Welfare guidelines under the direction of the Institutional Animal Care and Use Committee. Ultrasonography examination was performed with a real-time Toshiba medical company ultrasound system (Toshiba, Tokyo, Japan), using multifrequency probes (7 microns convex and 7 MHz linear probe) with displayed depth of 4–6 mm. The scans and photographs were taken on Polaroid in both longitudinal and transverse scans. At the tumor site, the animal's hair was clipped and shaved, and subsequently, sonographic gel was applied to the skin of the animals. Radiographic recordings were taken with an X-ray machine (Fischer, Berlin, Germany). The radiographic setting factors were 58 to 70 kVp, 10 mAs, and 90 cm focal spot–film distance. The radiographic exposures were conducted, dorsoventrally and right laterally. The tumor dimensions were measured using calipers and confirmed with sonar.

Performing PPTT in animals

Each animal was subjected to three sessions of PPTT treatment in 2-week intervals using an 808 nm diode laser with a power of 5.8 W/cm^2 and a spot size of around 5.6 mm^2. An effective dose of AuNRs solution (7.5 nM AuNRs) for each 100 cm^3 was used, and the amount used was scaled up based on the volume of the tumor and injected directly into the

tumor. Five minutes after injection, the entirety of the tumor was irradiated with the laser. The AuNRs concentration was decreased by 50% for each subsequent treatment. The temperature increase of a tumor during the laser irradiation was measured by placing a 33-gauge hypodermic thermocouple (OMEGA Engineering, Inc., Stamford, CT, USA) needle directly inside the tumor (42°C–44°C). The results of PPTT in animals, histopathology evaluation (see "Histopathology evaluation for animals" section), blood analysis (see "Blood analysis" section), X-ray (see "Animal diagnosis, ultrasonography, and X-ray examination" section) are discussed in "Applying PPTT to animals" and "The physiological status of animals after 1 year from treatment" sections.

Histopathology evaluation for animals

The detailed pathologic evaluation of tumors was conducted by the members of the pathology department, Faculty of Veterinary Medicine, Cairo University. Histopathological analysis was performed on 5 μm sections from tumor tissue that were fixed in 10% buffered formalin. The samples were stained with hematoxylin and eosin to assess pathology.

Blood analysis

Blood analyses tests for examining the liver and kidney functions of the animals were conducted before and after treatment. The tests were performed according to the manufacturer's instructions using diagnostic kits of the StatLab Spectrum Diagnostics in Egypt. Absorption spectrometry with six light-emitting diodes as optical light source was used. The kits were purchased from Egyptian Company for Biotechnology (Obour city industrial area, Egypt).

Cell culture and PPTT optimization in vitro and in vivo

To examine the in vitro efficacy of PPTT and optimize the treatment condition (see "Optimization of PPTT toward generating cancer cell apoptosis" section), MCF-7 breast cancer cells (human adenocarcinoma; American Type Culture Collection, Manassas, VA, USA) were cultured in Dulbecco's Modified Eagles' medium (Corning Incorporated, Corning, NY, USA) supplemented with 10% v/v fetal bovine serum, 1% penicillin/streptomycin at 37°C in a 5% CO_2 humidified atmosphere. For incubation, the growth media was removed from the cell cultures that had NPs and replaced with identical media containing PEGylated AuNRs (2.5 nM) overnight, and an 808 nm diode laser (power: 5.8 W/cm^2; spot size around 5.6 mm) was used on the cells. The level of cell ablation was related to the time of PPTT. Two time scales were used: 2 and 5 minutes.

For optimizing the PPTT condition in vivo, we applied PEGylated AuNRs (2.5 nM) for two different time periods (2 and 5 minutes) using an 808 nm diode laser (power: 5.8 W/cm^2; spot size around 5.6 mm). The result of optimization is shown in Supplementary material.

Apoptosis/necrosis assay in vitro

MCF-7 cells (human breast cancer cells) were washed with phosphate-buffered saline and then trypsinized (Clonetech, Mountain View, CA, USA).[29] After trypsinization, cells were centrifuged and washed with phosphate-buffered saline. Cells were then resuspended in 493 µL 1× annexin binding buffer (Invitrogen, Thermo Fisher Scientific, Waltham, MA, USA) with 2 µL working propidium iodide (PI; BioLegend, San Diego, CA, USA) 100 µg/mL and 5 µL annexin-V–fluorescein isothiocyanate (BioLegend) and then incubated at

room temperature for 15 minutes. Subsequently, cells were filtered and subjected to flow cytometry using a BSR LSR II flow cytometer (BD Biosciences, San Jose, CA, USA). Samples were excited with a 488 nm laser, and fluorescein isothiocyanate was detected in FL-1 by a 525/30 BP filter, whereas PI was detected in FL-2 by a 575/30 BP filter. FlowJo software (Tree Star Inc., Ashland, OR, USA) was used to count annexin V+ cells from at least 10,000 events.

3.3.3 Results and Discussion

Formulation and characterization of the AuNRs

Based on our previous study in vitro, AuNRs with average length × width (26×5 nm) showed enhanced efficacy of PPTT, which was driven from the high ratio of the absorbed light to scattered light, [30-32] we synthesized AuNRs with similar dimensions using our reported method, [28] and these AuNRs are shown in the TEM image (**Figure 3-9A**). To absorb the near-IR laser light for performing PPTT, AuNRs were generated with an aspect ratio of about 5 and with a surface plasmon resonance wavelength of ~800 nm (Figure 1B). The approximate length and width were 26±3 nm and 5±0.8 nm, respectively, which was obtained by counting the length and width distributions of 100 particles (**Figure 3-9C** and **D**). After synthesis, AuNRs were successfully coated with mPEG-Th as shown by their zeta potential of −17.1±7.83 mV (**Figure 3-9F**), while as-synthesized AuNRs had a positive zeta potential (**Figure 3-9E**) because of positively charged CTAB. The number of PEG molecules per particle was observed to be approximately 20,000 PEG/AuNR.

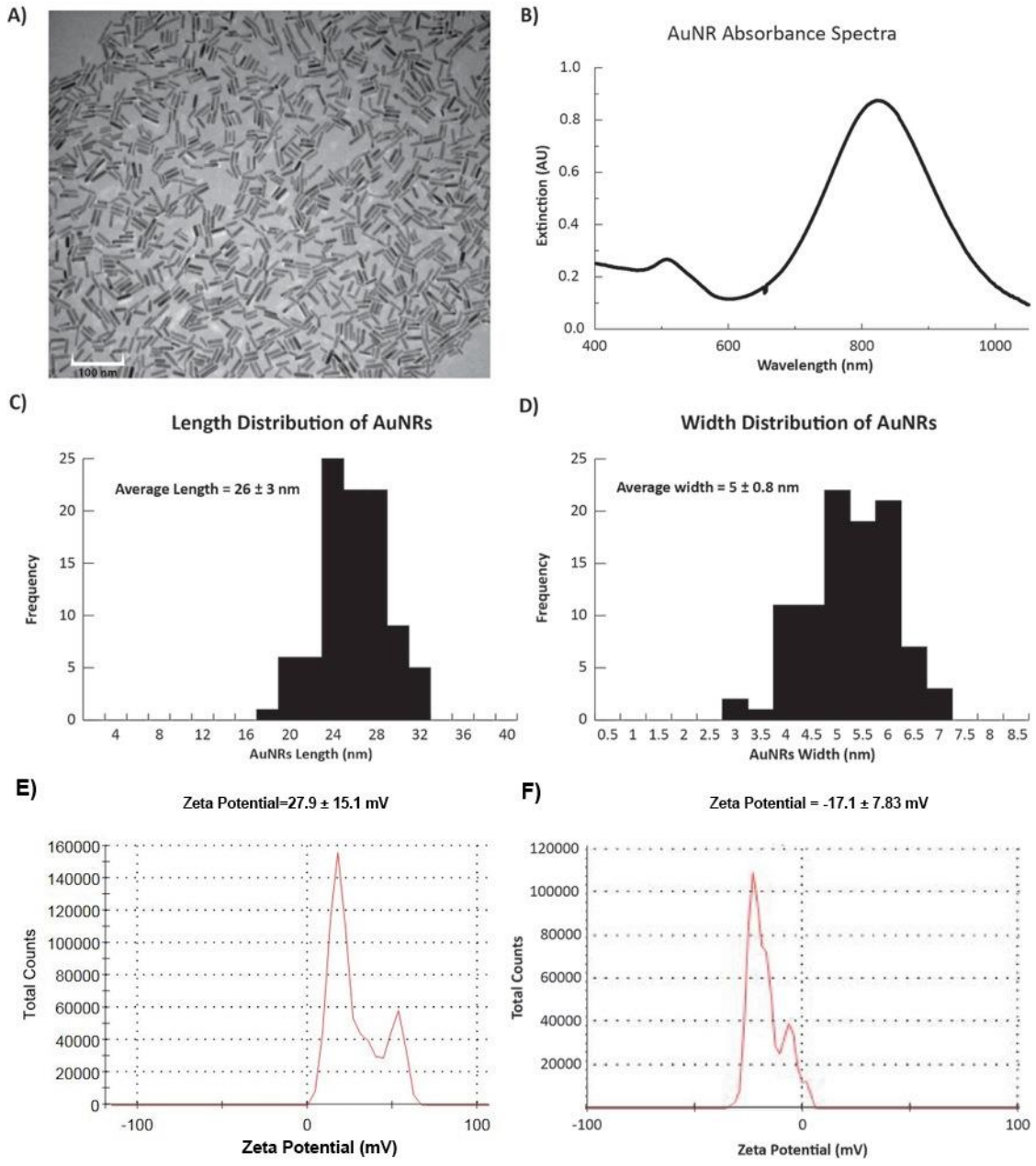

Figure 3-9. Characterization of PEGylated AuNRs rods (length 26±3 nm, width 5±0.8 nm):

(A) TEM image with 100 nm scale bar. (B) UV–Vis absorbance spectra showing the SPR peaks of AuNRs. (C) Corresponding histograms of the lengths of the 100 AuNRs particles counted. (D) Corresponding histograms of the widths of the 100 AuNRs particles counted. (E) Zeta potential data of the as-synthesized rods. (F) Zeta potential data of PEGylated AuNRs.

Optimization of PPTT toward inducing cancer cell apoptosis. We developed a mild PPTT strategy that induced cell apoptosis using a reduced laser exposure time. We conducted PPTT in vitro (MCF-7 cells) and in vivo (mammary gland tumor) by irradiating the tumors for 2 or 5 minutes. The control sample that incubated with AuNRs but without laser treatment were shown in **Appendix Figure B.9. B**. After 2 minutes of laser irradiation, 42.7% and 2.89% of the population underwent apoptosis or necrosis, respectively (Figure B.9.C), whereas 5 minutes of laser irradiation caused 20.17% and 15.5% of apoptosis or necrosis, respectively. The data demonstrates that a 5-minute irradiation time predominantly leads to necrosis (heating up to about 52°C), while on the other hand, a 2-minute irradiation time mainly results in apoptosis (**Appendix Figure B.9. D**, heating up to 42°C –44°C). This result is very comparable with the former study which showed that a low dose of heat induces apoptosis, whereas a high dose (heating above 50°C) induces necrosis.[21] For thermal damage of cells, Sapareto et al [33] proposed "cumulative equivalent minutes at 43°C (CEM43) apop" as a method to calculate the thermal dose applied. Using their methods, we calculated that the CEM43 of 5-minute irradiation is more than 500 times that of 2-minute irradiation. When laser was applied without AuNRs injection, no obvious temperature increase was observed.

Then, we used a preliminary optimal laser time on a single mammary gland tumor in a dog. We applied PPTT with two different irradiation times (2 and 5 minutes) to both sides of a single tumor. It was concluded that 2 minutes of irradiation caused a gentle change within the tumor, whereas 5 minutes of irradiation caused a very severe burning (Figure B.9.E). We related our thermal dosage to the average temperature that arose from the animal or cells after a 2-minute irradiation. In both cases, the temperatures are similar (42°C–44°C).

Based on these preliminary experiments, we selected the 2-minute irradiation time as the optimal irradiation time for complete tumor treatment for all tumor groups.

Applying PPTT to animals

After establishing the dosage of an effective laser application time, the PPTT optimized conditions were conducted multiple times (0, 2, and 4 weeks) and tumor volumes evaluated every 2 weeks until complete regression, as shown in **Figure 3-10**. Before any PPTT treatment, tumors of all the animals showed variant growth, and after PPTT, obvious tumor regression was observed. All thirteen tumors with variant volumes regressed with an average half-life of about 2 weeks and completely disappeared within 6–8 weeks. Images of tumor change and relevant histopathology in Case 7(feline) show the tumor regression process (Tumor 6: open tumor and Tumor 10: close tumor). Although both tumors have different malignancy stages (Table 1: Blood profile for each case before treatment and 1 year after cure), the images indicate that both tumors respond positively to the treatment, and no tissue burning was seen after gentle treatments. Histopathological examinations were carried out on tumors to investigate the malignancy of the tumors before and after PPTT. Photographic images (**Figure 3-11**), and also complete images of the case (Figure B.10.), showed the tumor statuses before, during, and after treatments. As shown in **Figure 3-11A**, before treatment, Case 7 (Tumor 6) was diagnosed with well-differentiated and highly malignant adenocarcinoma according to histopathology. **Figure 3-11A** showed that the cells were arranged either in tubular pattern or solid masses, in which the acini were arranged in groups and surrounded by fibrous connective tissue stroma. The stroma was infiltrated with inflammatory cells, mainly macrophages and lymphocytes. The acini were lined by secretory cells without a basement membrane, and the nucleus appeared to be

deeply basophilic with an enlarged, clear nucleolus. Poorly undifferentiated neoplastic mass characterized by a cluster of neoplastic cells with deeply basophilic cytoplasm and a vesiculated nucleus was observed. The tumor mass appeared highly cellular with low fibrous connective tissue stroma and loss of Grade IV acinar pattern (solid carcinoma).

Two weeks after the second treatment and before the third treatment, histopathology showed absence of epithelial lining of acini and basement membrane, indicating a decrease in malignancy. Also, it revealed the atrophy of acini with dense fibrous connective tissue proliferation. The mammary lobule appeared as involution stage Grade I (**Figure 3-11B**). Finally, after the third treatment, there was complete regression of the tumors. Additionally, 1 year after the third treatment, no relapses were observed for Case 7 (feline) (**Figure 3-11C** and **E**).

Furthermore, in Case 2 (canine), X-ray image showed there was no metastasis in the internal organs, and ultrasound image showed the tumor location, shape, and dimensions (Figure B.11.). Tumor statuses before, during, or after treatments are seen in **Figure 3-12**, and other photographs for Case 2 are shown in Figure B.12. For the tissue sections, moderately undifferentiated tumor mass characterized by basophilic cells with condensed nuclear chromatin lining the acini are observed (**Figure 3-12A**). The connective tissue stroma was infiltrated with mononuclear cells of mainly lymphocyte and macrophage origin but also contained some multinucleated giant tumor cells (Grade III). On the other hand, after treatment (**Figure 3-12B**) histopathology revealed some necrosis of acini accompanied with cellular stroma (Grade 0). No metastasis was observed based on X-ray diffraction images (**Figure 3-13**). Similarly, Case 3 has been explained in the Supplementary material, along with photographic images taken before treatment, 2 weeks

after treatment, and 1 year after treatment (Figure B.13., photographs). Histopathology images for Case 3 before treatment shows the tumor grade change from Grade III before treatment to Grade 0 after the treatment (Figure B.14.). Furthermore, the X-ray images before and after treatment show there is no metastasis in both statuses (Figure B.15.).

Images of tumor change and relevant histopathology in Case 7 (feline) show the tumor regression process (Tumor 6: open tumor and Tumor 10: close tumor). Although both tumors have different malignancy stages (Table 1), the images indicate that both tumors responded positively to the treatment, and no tissue burning appeared after the gentle treatments. The regression curve as shown in **Figure 3-10** shows a dramatic tumor regression with normal hair growth. Furthermore, 1 year after the completion of treatment, no subject exhibited signs of relapse or effects of toxicity, and even the hair grew back naturally.

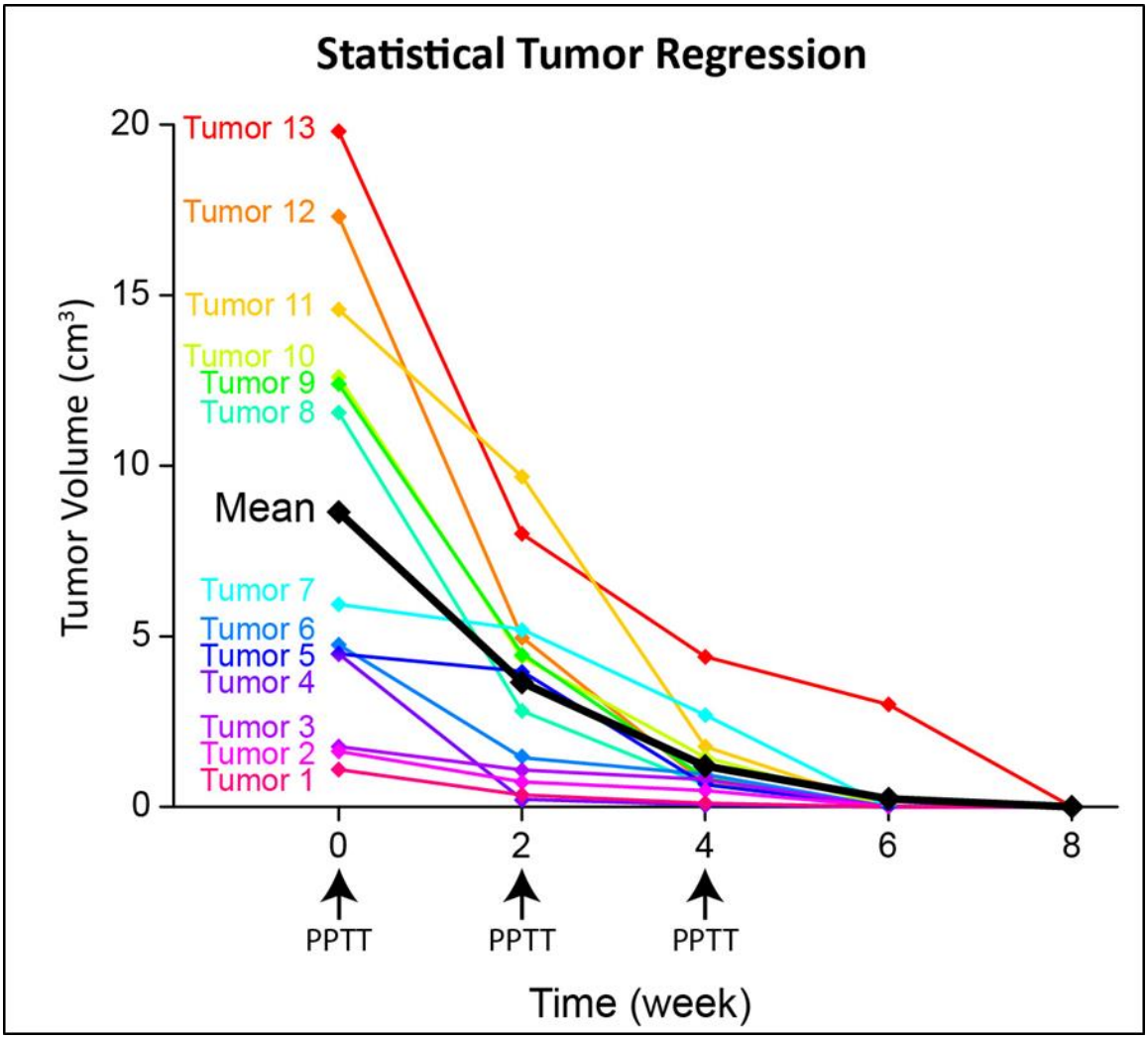

Figure 3-10. Regression curves of 13 tumors of variable volumes from multiple PPTT treatment (labeled with "arrow").

Notes: The mean of the regression ("black line") shows the general efficacy of the treatment.

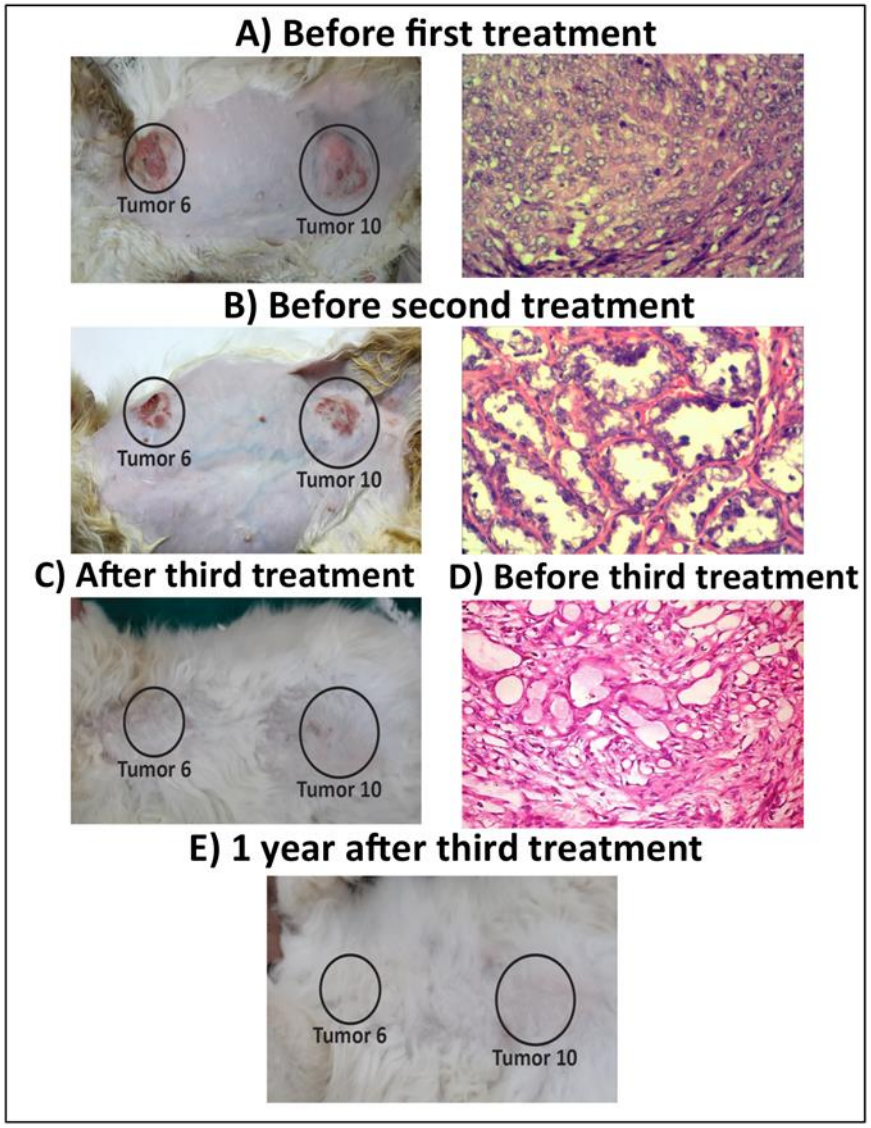

Figure 3-11. Photographs for Case 7 (feline) with two tumors (Tumor 6: anterior thoracic opened tumor; and Tumor 10: caudoinguinal tumors)

Histopathology images (Tumor 6) showing the tumor regression before and/or after each treatment. Notes: After 1 year of treatment, no relapse is observed (E). After 1 year, the tumors completely disappeared, thus we were unable to take histopathology data for the animals. Magnification of histopathology images stained with H&E: (A) and (D) ×100; (B) ×200. Abbreviation: H&E, hematoxylin and eosin.

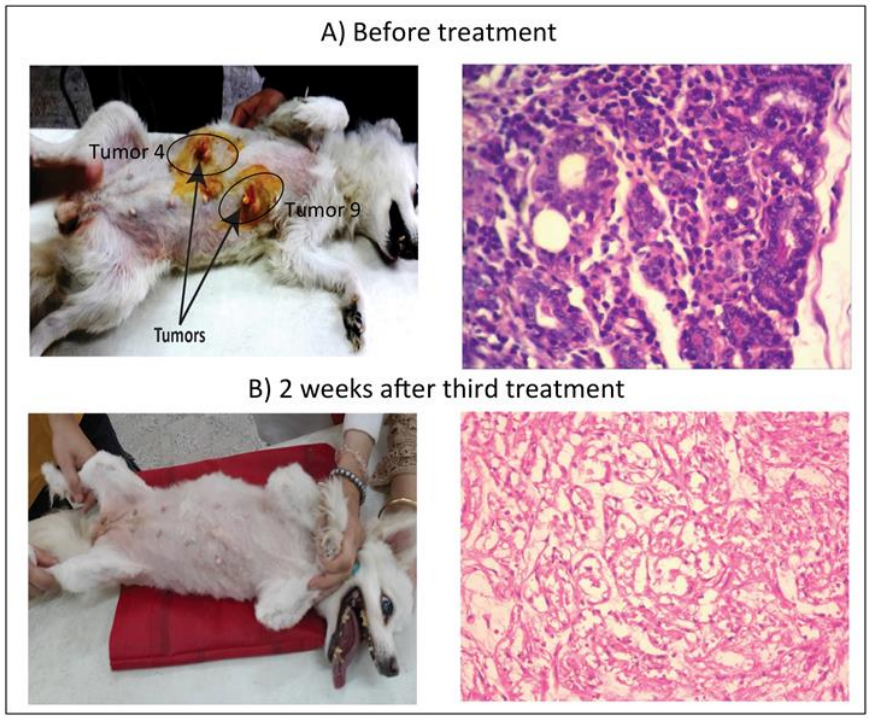

Figure 3-12. Photographs for Case 2 (canine; Tumor 4: left caudothoracic and Tumor 9: right abdominal mammary gland) and histopathology images (Tumor 4) showing the tumor status before treatment (A) and after regression (B).

Notes: Magnification of histopathology images stained with H&E: ×100. Abbreviation: H&E, hematoxylin and eosin.

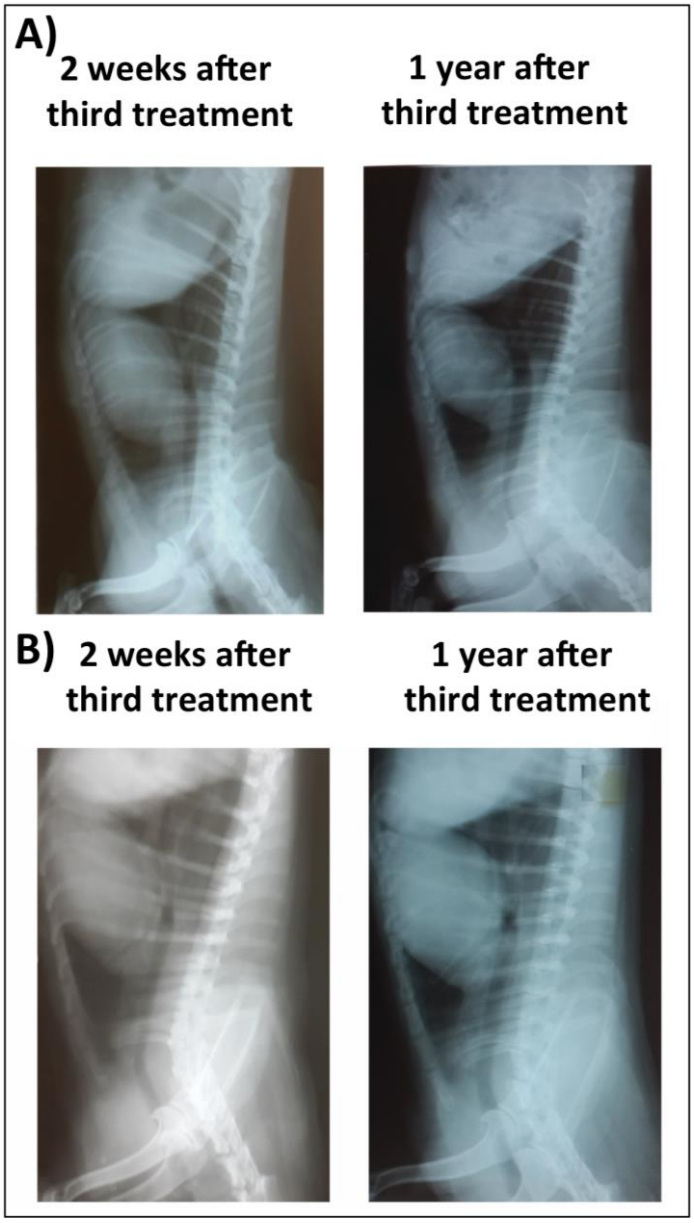

Figure 3-13 X-ray lateral exposure for Case 7 (feline)

(A) and Case 2 (canine) (B). Notes: Left: 2 weeks after third treatment and right: 1 year after third treatment showing that there is no metastasis. The physiological status of animals after 1 year from treatment

Short-term toxicity of AuNRs-PPTT was regarded as minimal because of the normal behavior and the animal's activity, diet, body weight, and appearance. In addition, the study of AuNRs toxicity on mice models has proved its short-term safety.[15,20] For long-term safety, a complete blood profile picture for all the cases was examined at two different times: once before the treatment and once1 year after treatment. The objective was to follow-up the animals 1 year after their final treatment and check for any changes in anatomical function (liver and kidney) as well as their overall health (eg, body weight, physical activity, and body skin). No significant change was observed in liver (alanine transaminase and aspartate transaminase) and kidney (urea and creatinine) functions when comparing before treatment and 1 year after treatment, although some animals in did have abnormal initial blood analysis results before treatment, which might be due to their different health or diet conditions (**Table 1**). In summary, this result suggests no obvious change in liver and kidney functions and that PPTT is safe even after 1 year.

Our data suggests that administering AuNRs in conjunction with very low photothermal conditions of 42°C–44°C for 2 minutes to canines and felines with natural tumors triggers apoptosis, which is more favorable for tumor treatment than necrosis. We tracked the animals after treatment for 1 year and found no tumor relapse or metastasis, or any negative physiological changes, indicating that there is no toxicity when using optimized AuNRs-PPTT conditions. We did not observe changes in liver and kidney function 1 year after treatment. In addition, the normal behavior and animal's activity, diet, body weight, and appearance indicate no biotoxicity of AuNRs. To our knowledge, this is the first study supporting the efficacy and safety of AuNRs-PPTT applied to natural mammary tumors in canines and felines.

A previous study has reported that AuNRs-PPTT can induce cell apoptosis following the common mitochondrial alternative pathway, reactive oxygen species production, Ca^{2+} release, mitochondrial membrane potential change, cytochrome C release, and the subsequent activation of the caspase family.[34-38] Besides this, other potential mechanisms of PPTT-induced apoptosis have been reported, such as initiating Golgi apparatus–endoplasmic reticulum dysfunction by albumin-conjugated gold NPs [39-42] and nuclear damage by harming the de novo RNA biosynthesis [43]. Further studies are needed to gain a better understanding of the mechanism of NP-based photothermal therapy.

Most cancer therapeutic strategies target a tumor's microenvironment, such as inflammatory tumor–associated macrophages (TAMs) and cancer-associated fibroblasts (CAFs), as they are considered to be key players in promoting tumorigenesis [21] It has been published that TAMs and CAFs have high uptake toward gold NPs [44-46]. Our results showed complete clearance of the tumor with no relapse or metastasis. Therefore, we expect that PPTT has a significant effect on a tumor's microenvironment, which is most likely related to the high uptake of AuNRs and therefore consistent with the higher photothermal response for CAFs and TAMs in the tumor microenvironment [47-48]. Further studies will be conducted to examine the effect of AuNRs-PPTT on changing a tumor's microenvironment.

Table 1: Blood profile for each case before treatment and 1 year after cure

Case no.	Animal species	Age/year	Tumor location	Tumor size/grade	Renal functions						Liver functions					
					Urea (mg/dL)			Creatinine (mg/dL)			ALT (U/L)			AST (U/L)		
					Before	After 1 year	Normal range	Before	After 1 year	Normal range	Before	After 1 year	Normal range	Before	After 1 year	Normal range
1	Dog Griffon	10	12-left anterior thoracic	T3/VI	15	14.9	5–25	0.82	0.71	0.5–1.6	84	88	5–107	156	135	5–55
2	Dog Griffon	11	9-right abdominal	T3/III	28	34	5–25	0.87	0.91	0.5–1.6	49	84.4	5–107	84	61	5–55
			4-left caudothoracic	T1/III												
3	Dog Griffon	7	13-right abdominal	T3/III	26	24.2	5–25	1.6	1.1	0.5–1.6	115	117	5–107	142	123	5–55
			2-left caudothoracic	T1/III												
4	Dog Griffon	5	8-right cranioinguinal	T3/III	27	26.8	5–25	0.96	0.85	0.5–1.6	72	76	5–107	140	96	5–55
5	Dog Griffon	13.5	7-left cranioinguinal	T3/VI	15	20	5–25	1.2	1.1	0.5–1.6	76	88	5–107	35	42	5–55
			5-left cranioinguinal	T2/VI												
			3-left inguinal lymph node	T3/III												
6	Cat Shirazi	11	11-right caudoinguinal	T2/III	38.7	35.6	14–36	1.6	1.4	0.6–2.4	56.2	58.4	10–100	34.5	36.2	10–100
			1-left craniothoracic	T1/III												
7	Cat Shirazi	4	6-left anterior thoracic	T2/IV	26.4	24.9	14–36	1.8	1.3	0.6–2.4	19	25	10–100	16	14	10–100
			10-right post caudoinguinal	T3/IV												

Abbreviations: ALT, alanine transaminase; AST, aspartate transaminase.

3.3.4 Conclusion and Future Look

We developed a three PPTT treatment regime with 2-week intervals to gradually suppress the natural tumors of dogs and cats without causing any burning of the tumor or affecting the nearby healthy cells. The results show a complete tumor regression in the seven animals (thirteen tumors). Furthermore, 1 year after the completion of treatment, no signs of relapse or effects of toxicity were observed. This evidence shows not only the efficacy of AuNRs-PPTT as a proposed treatment, but also its viability as a safer alternative to conventional treatments. All animals were subjected to AuNRs-PPTT and showed no relapse , toxicity or metastasise effect even 1 year after treatment.

3.3.5 References

1. M.R. Ali, I.M. Ibrahim, H.R. Ali, S.A. Selim, M.A. El-Sayed. (2016) Treatment of natural mammary gland tumors in canines and felines using gold nanorods-assisted plasmonic photothermal therapy to induce tumor apoptosis, *International Journal of Nanomedicine* 11, 4849.

2. Maeda H, Wu J, Sawa T, Matsumura Y, Hori K. (2000) Tumor vascular permeability and the EPR effect in macromolecular therapeutics: a review. *J Control Release.* 65(1–2), 271–284.

3. Li WQ, Sun CY, Wang F, et al. (2013) Achieving a new controllable male contraception by the photothermal effect of gold nanorods. *Nano Lett.* 13(6):2477–2484.

4. Liu X, Chen Y, Li H, et al. (2013) Enhanced retention and cellular uptake of nanoparticles in tumors by controlling their aggregation behavior. *ACS Nano.* 7(7), 244–6257.

5. Duan X, Li Y. (2013) Physicochemical characteristics of nanoparticles affect circulation, biodistribution, cellular internalization, and trafficking. *Small.* 9(9–10),1521–1532.

6. Mackey MA, Saira F, Mahmoud MA, El-Sayed MA. (2013) Inducing cancer cell death by targeting its nucleus: solid gold nanospheres versus hollow gold nanocages. *Bioconjug Chem.* 24(6):897–906.

7. Dreaden EC, Mackey MA, Huang X, Kang B, El-Sayed MA. (2011) Beating cancer in multiple ways using nanogold. *Chem Soc Rev.* 40:3391–3404.

8. Bagley AF, Hill S, Rogers GS, Bhatia SN. (2013) Plasmonic photothermal heating of intraperitoneal tumors through the use of an implanted near-infrared source. *ACS nano.* 7 (9):8089-8097.

9. Bardhan R, Lal S, Joshi A, Halas NJ. (2011) Theranostic nanoshells: from probe design to imaging and treatment of cancer. *Acc Chem Res.* 44(10):936–946.

10. Ali MRK, Panikkanvalappil SR, El-Sayed MA. (2014) Enhancing the efficiency of gold nanoparticles treatment of cancer by increasing their rate of endocytosis and cell accumulation using rifampicin. *J Am Chem Soc.* 136(12):4464–4467.

11.Zhang ZJ, Wang J, Nie X, Wen T, Ji YL, Wu XC, Zhao YL, Chen CY. (2014) Near Infrared Laser-Induced Targeted Cancer Therapy Using Thermoresponsive Polymer Encapsulated Gold Nanorods. *Journal of the American Chemical Society 136*: 7317-7326.

12.Eghtedari M, Oraevsky A, Copland JA, Kotov NA, Conjusteau A, Motamedi M. (2007) High sensitivity of in vivo detection of gold nanorods using a laser optoacoustic imaging system. *Nano Letters 7*: 1914-1918.

13.Jang B, Park JY, Tung CH, Kim IH, Choi Y. (2011) Gold Nanorod-Photosensitizer Complex for Near-Infrared Fluorescence Imaging and Photodynamic/Photothermal Therapy In Vivo. *Acs Nano 5*:1086-1094.

14.Ratto F, Matteini P, Rossi F, Menabuoni L, Tiwari N, Kulkarni SK, Pini R. (2009) Photothermal effects in connective tissues mediated by laser-activated gold nanorods. *Nanomedicine-Nanotechnology Biology and Medicine 5*: 143-151.

15.Dickerson EB, Dreaden EC, et al. (2008) Gold nanorod assisted near-infrared plasmonic photothermal therapy (PPTT) of squamous cell carcinoma in mice. *Cancer Lett.* 269(1):57–66.

16.Goodrich GP, Bao LL, Gill-Sharp K, Sang KL, Wang J, Payne JD. (2010) Photothermal therapy in a murine colon cancer model using near-infrared absorbing gold nanorods. *Journal of Biomedical Optics 15*.

17.Li ZM, Huang P, Zhang XJ, Lin J, Yang S, Liu B, Gao F, Xi P, Ren QS, Cui DX. (2010) RGD-Conjugated Dendrimer-Modified Gold Nanorods for in Vivo Tumor Targeting and Photothermal Therapy. *Molecular Pharmaceutics 7*: 94-104.

18.Niidome T, Akiyama Y, Shimoda K, Kawano T, Mori T, Katayama Y, Niidome Y. (2008) In vivo monitoring of intravenously injected gold nanorods using near-infrared light. Small 4: 1001-1007.

19.Niidome T, Akiyama Y, Yamagata M, Kawano T, Mori T, Niidome Y, Katayama Y. (2009) Poly(ethylene glycol)-Modified Gold Nanorods as a Photothermal Nanodevice for Hyperthermia. *Journal of Biomaterials Science-Polymer Edition 20*: 1203-1215.

20.Pattani VP, Shah J, Atalis A, Sharma A, Tunnell JW. (2015) Role of apoptosis and necrosis in cell death induced by nanoparticle-mediated photothermal therapy. *J Nanoparticle Res.* 17(1):11.

21. Song AS, Najjar AM, Diller KR. (2014) Thermally induced apoptosis, necrosis, and heat shock protein expression in 3D culture. *J Biomech Eng.* 136(7).

22. Perez-Hernandez M, del Pino P, Mitchell SG, et al. (2015) Dissecting the molecular mechanism of apoptosis during photothermal therapy using gold nanoprisms. *ACS Nano.* 9(1):52–61.

23. Shafiee R, Javanbakht J, Atyabi N, et al. (2013) Diagnosis, classification and grading of canine mammary tumours as a model to study human breast cancer: an Clinico-Cytohistopathological study with environmental factors influencing public health and medicine. *Cancer Cell Int.* 13:79.

24. . Shafiee R, Javanbakht J, Atyabi N, et al. (2013) Comparative value of clinical, cytological, and histopathological features in feline mammary gland tumors; an experimental model for the study of human breast cancer. *Diagn Pathol.* 8:136.

25. Manesh JY, Shafiee R, Pedram B, Malayeri HZ, Mohajer S, Ahmadi S, Ahmadi S, Javanbakht J, Mokarizadeh A, Khadivar F. (2014) Improving the diagnosis, treatment, and biology patterns of feline mammary intraepithelial lesions: a potential model for

human breast masses with evidence from epidemiologic and cytohistopathologic studies. *Tumour Biol.* 35(12):12109-17

26. Yu M, Guo F, Tan F, Li N. (2015) Dual-targeting nanocarrier system based on thermosensitive liposomes and gold nanorods for cancer thermo-chemotherapy. *J Control Release.* 215:91–100.

27. Zhou T, Yu MF, Zhang B, Wang LM, Wu XC, Zhou HJ, Du YP, Hao JF, Tu YP, Chen CY, Wei TT. (2014) Inhibition of Cancer Cell Migration by Gold Nanorods: Molecular Mechanisms and Implications for Cancer Therapy. *Advanced Functional Materials*. 24 (44):6922-6932.

28. Ali MRK, Snyder B, El-Sayed MA. (2012) Synthesis and optical properties of small Au nanorods using a seedless growth technique. *Langmuir.* 28(25):9807–9815.

29. Ellman GL. (1959) Tissue sulfhydryl groups. *Arch Biochem Biophys.* 82(1):70–77

30. Ali MRK., Ali, HR., Rankin, CR., and El-Sayed, MA. (2016) Targeting heat shock protein 70 using gold nanorods enhances cancer cell apoptosis in low dose plasmonic photothermal therapy. *Biomaterials*. *102*, 1-8.

31. Mackey MA, Ali MRK, Austin LA, Near RD, El-Sayed MA. (2014) The most effective gold nanorod size for plasmonic photothermal therapy: theory and in vitro experiments. *J Phys Chem B.* 118(5):1319–1326.

32. Oldenburg SJ, Averitt RD, Westcott SL, Halas NJ. (1998) Nanoengineering of optical resonances. *Chem Physics Lett.* 288(2–4):243–247.

33. Sapareto SA, Dewey WC. (1984) Thermal dose determination in cancer therapy. *Int J Radiat Oncol Biol Phys.* 10(6):787–800.

34.. Yang L, Tseng Y-T, Suo G, et al. (2015) Photothermal therapeutic response of cancer cells to aptamer–gold nanoparticle-hybridized graphene oxide under nir illumination. *ACS Appl Mater Interfaces.* 7(9):5097–5106.

35. Nam J, La W-G, Hwang S, et al. (2013) pH-responsive assembly of gold nanoparticles and "spatiotemporally concerted" drug release for synergistic cancer therapy. *ACS Nano.* 7(4):3388–402

36. von Maltzahn G, Park JH, Agrawal A, et al. (2009) Computationally guided photothermal tumor therapy using long-circulating gold nanorod antennas. *Cancer Res.* 69(9):3892–3900.

37. Huang XH, Kang B, Qian W, et al. (2010) Comparative study of photothermolysis of cancer cells with nuclear-targeted or cytoplasm-targeted gold nanospheres: continuous wave or pulsed lasers. *J Biomed Opt.* 15(5):7

38. Kang B, Austin LA, El-Sayed MA. (2014) Observing real-time molecular event dynamics of apoptosis in living cancer cells using nuclear-targeted plasmonically enhanced raman nanoprobes. *ACS Nano.* 8(5):4883–4892.

39. Zhang S, Li Y, He X, et al. (2014) Photothermolysis mediated by gold nanorods modified with EGFR monoclonal antibody induces Hep-2 cells apoptosis in vitro and in vivo. *Int J Nanomedicine.* 9:1931–1946.

40. Mocan L, Matea C, Tabaran FA, et al. (2015) Photothermal treatment of liver cancer with albumin conjugated gold nanoparticles initiates Golgi Apparatus-ER dysfunction and caspase-3 apoptotic pathway activation by selective targeting of Gp60 receptor. *Int J Nanomedicine.* 10:5435–5445.

41. Cheng L, Yang K, Chen Q, Liu Z. (2012) Organic stealth nanoparticles for highly effective in vivo near-infrared photothermal therapy of cancer. *ACS Nano.* 6(6):5605–5613.

42. Liu X, Tao H, Yang K, Zhang S, Lee ST, Liu Z. (2011) Optimization of surface chemistry on single-walled carbon nanotubes for in vivo photothermal ablation of tumors. *Biomaterials.* 32(1):144–151.

43. Kodiha M, Hutter E, Boridy S, Juhas M, Maysinger D, Stochaj U. (2014) Gold nanoparticles induce nuclear damage in breast cancer cells, which is further amplified by hyperthermia. *Cell Mol Life Sci.* 71(21):4259–4273.

44. Ward C, Langdon SP, Mullen P, et al. (2013) New strategies for targeting the hypoxic tumour microenvironment in breast cancer. *Cancer Treat Rev.* 39(2):171–179.

45. Luo YP, Zhou H, Krueger J, et al. (2006) Targeting tumor-associated macrophages as a novel strategy against breast cancer. *J Clin Invest.* 116(8):2132–2141.

46. Madsen SJ, Christie C, Hong SJ, et al. (2015) Nanoparticle-loaded macrophage-mediated photothermal therapy: potential for glioma treatment. *Lasers Med Sci.* 30(4):1357–1365.

47. Costa EC, Gaspar VM, Marques JG, Coutinho P, Correia IJ. (2013) Evaluation of Nanoparticle uptake in co-culture cancer models. *PLoS One.* 8(7):13.

48. Calvo F, Ege N, Grande-Garcia A, et al. (2013) Mechanotransduction and YAP-dependent matrix remodelling is required for the generation and maintenance of cancer-associated fibroblasts. *Nat Cell Biol.* 15(6):637–646.

CHAPTER 4. GOLD NANOPARTICLES INHIBIT CANCER CELL MIGRATION

Moustafa Ali and Yue Wu have equally contributed to designing, performing, analyzing, and writing the research in this chapter.

4.1 Nuclear membrane-targeted gold nanoparticles inhibit cancer cell migration and invasion

If we can prevent cancer cell migration (i.e. stops metastasis), not too many people would die of cancer. Recent studies have showed that gold nanoparticles (AuNPs) can suppress metastasis by slowing down the migration speed of cancer cells. Since nuclear stiffness of the cell largely decreases cell migration, our hypothesis is that targeting AuNPs to the cell nucleus region could enhance nuclear stiffness, and therefore inhibit cell migration. Our results show that upon nuclear targeting of AuNPs, the ovarian cancer cell motilities decrease more significantly than non-targeted AuNPs. Furthermore, using atomic force microscopy, we observed an enhanced cell nuclear stiffness. In order to understand the mechanism of cancer cell migration/invasion inhibition, firstly, the exact locations of the targeted AuNPs were clearly imaged using a high-resolution three-dimensional imaging microscope, which showed that the AuNPs were trapped at the nuclear membrane. Meanwhile, we observed a greatly increased expression level of lamin A/C protein, which is located in the inner nuclear membrane and functions as a structural component of the nuclear lamina to enhance nuclear stiffness. We propose that the AuNPs that are trapped at the nuclear membrane both: 1) add to the mechanical stiffness of the nucleus and 2)

stimulate the overexpression of lamin A/C located around the nuclear membrane, thus increasing nuclear stiffness and slowing cancer cell migration and invasion.

4.1.1 Introduction

Metastasis, a process in which cancer cells migrate to other locations of the human body, is responsible for most cancer-related mortality. It usually begins with local invasion to the surrounding tissues, followed by intravasation into the lymph and blood microvasculature before the cancer cells finally colonize within the microenvironment of other locations in the patient's body. [2, 3] Many treatments for inhibiting metastasis are based on drugs that target specific proteins that promote the cell migration process; however, past attempts to develop anti-metastasis drugs have not been efficacious in clinical trials.[4] Moreover, in many cases, the anti-cancer drugs that target specific proteins might lose their efficacy after several months of treatment due to protein mutations, thus conferring drug resistance to cancer cells,[5] and could also cause side effects on healthy tissues.[6]

Recent advances in nanomedicine provide us with a great opportunity to avoid the drawbacks of current drugs. [5-11] Nanoparticles have been widely used in cancer diagnosis and cancer therapy thanks to their intrinsic chemical, physical and optical properties. [10, 12-14] Nanoparticles with proper surface modifications can target tumors selectively, [8, 15-18] and their effects on cancer cell migration or metastasis have drawn attention from many researchers. [19-22] In 2013, Murphy *et al.* reported that gold nanoparticles (AuNPs) with different surface charges and sizes can affect cancer cell migration. [19] In 2014, Chor Yong Tay *et al.* [21] found that after incubation with nano-

ceramics, such as titania, silica and hydroxyapatite, cells showed significantly impaired wound healing capability by disruption of the intracellular microtubule assembly. In the same year, Zhou *et al.* [22] showed that gold nanorods (AuNRs) coated with bovine serum albumin (BSA) exhibited reduced cell migration and invasion by impairing ATP synthesis, which subsequently inhibits the F-actin cytoskeletal assembly and decreases cancer cell migration.[22] Arvizo *et al.* used non-specific targeted gold nanospheres (AuNSs) to inhibit cancer cell migration by abrogating MAPK signaling and reversing the epithelial-mesenchymal transition.[16] For most of the related works, non-specific targeted nanoparticles have been used, for instance, Zhou *et al.*[22] used BSA coated AuNRs that showed inhibitory effects on cancer cell migration, but the high concentration of AuNRs (50-200 μM) that they used might be an obstacle for clinical usage. To maintain the nanoparticle effect on slowing the cancer cell migration with a minimized amount of nanoparticles, the intracellular locations of nanoparticles could be an important factor to consider. It is thus promising to design nanoparticles that can target specific intracellular regions to enhance the inhibition of cancer cell migration.

Mechanical stiffness of cancer cells has been shown to grade metastatic potential in patient tumor cells, [23] as well as in cultured cancer cell lines. [24, 25] Lower stiffness is related to more invasive cells. [26] In eukaryotic cells, the nucleus contains most of the cell's genetic material and controls cell activities by transcriptional regulation. It is the largest and stiffest organelle in most cells and largely determines the cell migration ability. [27-29] Lamin A/C (LMNA) proteins are an important factor in nuclear stiffness. They form a dense protein network that connects the nuclear membrane and chromatin structures on the interior of the nuclear membrane. Recent studies have shown that nuclear lamin A protein

scales with tissue stiffness [30] and generate a barrier to cells migrate through three-dimensional (3D) environments. [31] It is shown that lamin A/C deficiency hampers cell mechanics, polarization, and migration. [32, 33]

Here, targeted AuNPs were used to locate the AuNPs to the cells, because of their specific physical and chemical properties and better biocompatibility than other nanomaterials such as nano-ceramics or silver nanoparticles. [18, 34] By targeting and locating the AuNPs to the cell in a manner to modulate the stiffness of its nucleus, we could improve the inhibition effect on cell migration. In our experiment, we used three ligands, methoxy-polyethylene glycol thiol (PEG) for increasing the biocompatibility of AuNPs, RGD (RGDRGDRGDRGDPGC) peptides for binding to the surface integrin of cancer cells and enhancing endocytosis, and nuclear localization signal (NLS, CGGGPKKKRKVGG) peptides for targeting the AuNPs to the nucleus. Cell migration or invasion abilities have been measured, and the results show a clear decrease in these functions after the nuclear targeting of the nanoparticles. For studying the cell mechanical response, atomic force microscope (AFM) showed that the two types of AuNPs (***i.e.*** AuNRs and AuNSs) both significantly enhanced the nuclear stiffness. A high-resolution 3D optical imaging system showed the exact location of the nanoparticles, which were trapped at the nuclear membrane. The levels of lamin A/C were found to be elevated upon nanoparticle incubation, which could be an explanation for the observed enhanced nuclear stiffness causing inhibition of cell motility upon gold nanoparticle treatment.

4.1.2 Experimental Methods

Gold nanoparticle synthesis, conjugation and characterization: Gold nanospheres (AuNSs) with an average diameter of 35 nm were synthesized using the citrate reduction method. [35] Briefly, 100 mL of 0.254 mM $HAuCl_4.3H_2O$ solution was heated till boiling, and then reduced by adding 2.5 mL of 0.35% of trisodium citrate. The solution was then left heating until it turned wine red, followed by cooling under water flow. The citrate stabilized AuNSs were centrifuged under 5000 g for 10 min and redispersed in deionized (DI) water to remove extra citrate and be ready for conjugation.

Gold nanorods (AuNRs) with an average size of 25 x 6 nm (length x width) were synthesized using a seedless growth method. [36] Briefly, 5 ml of 1.0 mM $HAuCl_4$ was added to a mixture of 5 mL of 0.20M CTAB, 250 ul of 4.0 mM $AgNO_3$ and 8 μL of 37% HCl. For reduction, 70 μL of 78.8 mM ascorbic acid was added, followed by immediate injection of 15 μL of 0.01M of ice-cold $NaBH_4$. The solution was left undisturbed for 12 hrs, then centrifuged at 21000 rpm for 50 min and redispersed in DI water followed by a second centrifugation at 19000 rpm for 40 min to remove the extra CTAB. TEM was used to measure the sizes and homogeneity of the nanoparticles.

AuNSs and AuNRs were then conjugated according to previous work, [37, 16] to achieve nuclear and cytoplasmic targeting. For nuclear targeting, first, mPEG-SH (1 mM) was added to the nanoparticles for overnight to achieve about 1000 ligands on each particle. Then, the PEGylated nanoparticles (1 nM) were treated with RGD (1 mM) and NLS (1 mM) to achieve 10^4 and 10^5 molar excess, respectively. The solution was then allowed to shake overnight at room temperature. Excess ligands were removed by centrifugation. For preparing BSA conjugated nanoparticles, BSA (4.5 mM) was added to the nanoparticles and left for 3 h to incubate. UV-vis spectrometer and zetasizer was used to test the

conjugation. Surface modification causes red shift of UV-vis spectra due to the change in the dielectric constant of the surrounding environment of Au nanoparticles.

Cell culture and AuNPs incubation: The ovarian cancer HEY A8 cell lines were grown in RPMI-1640 media supplemented with 10% FBS and 1% antibiotic-antimycotic solution (R10 medium). Cells were kept in a humidified incubator at 37 ^{o}C and under 5% CO_2. After achieving 50% confluence, the cells were incubated with functionalized AuNSs or AuNRs in supplemented DMEM cell culture medium for 24 h. The concentration of nanoparticles was carefully chosen to avoid cytotoxicity or perturbation to the cell cycle. [38]

Apoptosis/necrosis assay: The HEY A8 cells were collected by trypsinization and washed with cold PBS twice. Then, cells were the dispersed in 493 mL of Annexin V binding buffer before labeling by 5 μL of Annexin V FITC (BioLegend) and 2 μL of PI (BioLegend, 100 μg/ mL). The mixture was then incubated for 15 min at room temperature. The cells were subjected to flow cytometry analysis using a BSR LSR II flow cytometer (BD Biosciences). For excitation, a 488 nm laser was applied. FITC and PI were detected in FL-1 and FL-2 using 525/30 and 575/30 BP filters, separately. Standard compensation using unstained and single-stained cells was conducted before performing actual experiments. FlowJo software (Tree Star Inc.) was used for data analysis. At least 10 000 events were collected for each experiment. [57]

Cell motility assay: HEY cells were seeded on uncoated 24-well plate at a sub-confluent density for 24 hours. Then the cells were treated with nanoparticles of varying shapes and conjugated motifs before returning them to incubator for 12 hours to facilitate particle

uptake. After the incubation period, cells were stained with nuclear dye Hoechst 33342 (dilution 1: 10,000) for 30-60 minutes. Cells were maintained at 37°C and 5% carbon dioxide throughout the experiment using an environmental cell chamber (InVivo Scientific). For observation, a Nikon Eclipse Ti inverted epifluorescent microscope was used and both bright field (BF) and DAPI images were taken at multiple xy positions at 12 minute time interval for 6-8 hours at 10x magnification. The locations of cell nuclei, segmented from fluorescent images, were tracked in MATLAB to define cell traces. The cell migration coefficients and directional velocities were determined by fitting the traces to the persistent random walk model. Briefly, mean square displacements were calculated from the two-dimensional tracking data and was used for fitting the following equation,

$$\langle d^2(\tau)\rangle = 4\mu\{t - P[1 - e^{-t/P}]\}$$

Where P= persistence time and μ=migration coefficient.

Trans-well invasion assay: The Cultured 24 Well BME Cell Invasion Assay kit (Trevigen) was used according to the manufacturer's instructions. For these studies, HEY cells were seeded and grown in a 6 well plate to 60-80% confluency before treating with nanoparticles in serum free media for 24 hours. Cells were then detached, spun down and re-suspended in serum free media. We also counted the cell number at this time to adjust the density to 500,000 cells/mL. Then 50,000 cells (100 μL) were added for each condition to the top surface of transwell inserts with 8 μm membrane pores coated with basement membrane matrix (BME). Cells were allowed to migrate toward the 10% FBS containing media in bottom chamber acting as the chemo attractant for a period of 32 hours. After the desired incubation time, non-migratory cells were gently removed from the top of each

transwell using q-tips and the migrated cells at the bottom surface were detached using detaching buffer and incubated with Calcein AM. A plate reader was used to measure the fluorescence intensity, which is positively related to the number of trans-well cells.

Atomic Force Microscopy: AFM mechanical measurements [39, 40] of HEY A8 cells were obtained using an MFP 3-D AFM (Asylum Research, Santa Barbara, CA) on a vibration isolation table (Herzan, Laguna Hills, CA). A silicon nitride cantilever (Bruker, Camarillo, CA) was used for the experiments. The pyramidal tip had a half angle of 35° and the radius of curvature of the point of the tip was 20 nm. Measurements were performed on cells plated to the glass bottom of the Fluorodish and in culture media at room temperature. For eliminating the effect of the overlapping neighboring cells on the stiffness, single cells were measured. Thermal calibration [41] yielded the cantilever spring constant, k=28.01pN/nm. A measurement rate of 0.39 Hz was used. The 5 nN force trigger resulted in indentations of approximately 4 μm for typical cells. Cells were optically located using a Nikon Eclipse Ti microscope (Nikon, Melville, NY). Force-displacement curves were recorded to obtain the Young's modulus of each cell. Two distinct sets of measurements were performed with the AFM. The first investigated changes in mean cell stiffness between populations treated with AuNPs@NLS and an untreated control population. The second set of measurements investigated subcellular elasticity of nucleus. For the first set of measurements, the cantilever probe was positioned over the individual cells for indentation and measurement. For the second set, the probe was positioned over the perinuclear region.

Cell Imaging Using DIC Microscopy: An inverted Nikon Eclipse Ti-E microscope equipped with Perfect Focus System (PFS, 25 nm z-axial resolution) was used for imaging

and z-stacks acquisitions under differential interference contrast (DIC) microscopy. The DIC mode utilized a pair of DIC polarizer and analyzer, a high resolution 100×I-R DIC slider, a high numerical aperture (N.A., 1.40) oil immersion condenser lens, a Nikon CFI Apo TIRF 100× (N.A., 1.49) oil immersion objective, and a 12 V/100 W halogen lamp as light source. Appropriate bandpass filters were placed in the light path. The z-stack movies were taken by a Hamamatsu ORCA-Flash 4.0 V2 CMOS camera (C11440-22CU, pixel size: 6.5 μm × 6.5 μm) with Camera Link interface using Micro-Manager and analyzed using NIH ImageJ and reconstructed in Amira. Fixed HEYA8 cells on 22 mm × 22 mm glass coverslips were rinsed with DPBS at pH 7.4 and fabricated into a sandwiched chamber with two pieces of double-sided tape and a cleaned glass slide. PBS solution was added into the chamber to fill the space and the chamber was then sealed by clear nail polish. The so-formed sample slide was then place under the microscope for observation. Z-stacks were acquired using the Multi-Dimensional Acquisition function in Micro-Manger. More specifically, the DIC optical sectioning through the whole cell thickness was achieved by moving the objective on the motorized nosepiece using PFS at 65 nm/step at 33 ms (30 fps) exposure time.

Scratch assay: The scratch assay has been performed according to former report. [42] Cells were cultured in a 6 well plate to a confluent monolayer. A p200 pipet tip was used to scrape the cell monolayer in a straight line to create an empty gap. The debris was then remove by washing the cells once with culture medium and then replace with 2 ml of fresh medium. Then the cells were imaged shortly after and 12 hours after scratch.

Western blot: Briefly, cells were lysed in RIPA buffer (20 mM Tris pH 7.4, 150 mM NaCl, 2 mM EDTA, 2 mM EGTA, 0.1% Sodium Deoxycholate, 1% Triton X-100, 0.1% SDS)

containing protease inhibitors (Sigma-Aldrich). BCA assay (Pierce) was performed to measure the protein concentration and equal amounts of protein were loaded on a SDS-PAGE gel. After SDS-PAGE, the resulting gels were transferred to PVDF membranes (Millipore) overnight. Afterwards, the gel was blocked with 5% milk in TBS (20 mM Tris, 150 mM NaCl). A rabbit polyclonal antibody to Lamin A/C was used as the primary antibody (Bethyl Laboratories, Inc.) overnight in 4 °C with shaking. A goat anti rabbit HRP labeled antibody was used as the secondary antibody (Jackson Immuno Research Laboratories). Blots were washed 3 times for 20 m in TBS after primary and secondary antibodies. Konica Minolta developer and Hyglo enhanced chemiluminescence (Denville) were used to develop the immunoblots.

Immunofluorescence labeling and confocal microscopy: Cells were cultured on confocal chamber slides (MATECH Co. USA). After gold nanoparticle treatment, [18] cells were fixed in 4% Paraformaldehyde/0.1% Glutaraldehyde for 10 min at room temperature the wash with PBS. Cells were then permeabilized with 0.1% Triton X-100 for 5 min at room temperature. Cells were then blocked with 5% BSA and incubated with the primary antibody as stated in the Western-blot method for overnight. Cells were then incubated for 1 h with an Alexa Fluor 488 secondary antibody (Invitrogen) for 1 h before mounting with Prolong Gold (Invitrogen). Lastly images were taken with a Zeiss LSM 700-405 confocal microscope and the fluorescence intensity was quantified in Image J.

Data: To determine the Young's modulus, IGOR Pro software (Wavemetrics, Portland, OR) was used to apply the Hertzian contact model [43-45] from 10-90% of the maximum indentation of the extension force-displacement curve. Due to the unequal sample size and heteroscedasticity of the AFM data, overall statistical significance of differences in mean

cell stiffness and nuclear stiffness between cells treated with AuNPs@NLS was tested using Welch's analysis of variance (ANOVA). Post-hoc analysis was performed using the Games-Howell test. The analyses were performed with the alpha type error set at 0.05.

4.1.3 Results and Discussion

Au nanoparticles synthesis, conjugation, cellular uptake and cytotoxicity measurement

The AuNRs with an average size of 25 (± 2) × 5 (± 0.5) nm were synthesized using a seedless method, [36] as shown in **Figure 1a** (TEM figure) and a surface plasmon resonance (SPR) peak centered ~ 800 nm (UV-Vis spectrum in **Figure 1d**). The AuNSs with an average size of 35 ± 2 nm that absorb at 535 nm wavelength of light were synthesized using citrate reduction method were shown in **Figure 4-1b** and **Figure** 4-1**e** (TEM and UV-Vis spectrum).

Gold nanoparticles (AuNPs) were functioned with three ligands, methoxy-polyethylene glycol thiol (PEG), RGD (RGDRGDRGDRGDPGC) peptides and nuclear localization signal (NLS, CGGGPKKKRKVGG) peptides, as shown in schematic **Figure 4-1c**. In details, first, we conjugated the PEG to the surface of the AuNPs surface in order to enhance the biocompatibility. [46] Then, the second ligand, RGD binds to surface integrins which are highly expressed on the surface of the cancer cells than the normal ones to enhance the receptor-mediated endocytosis of the nanoparticles selectively to the cancer cells. [47] The third ligand, which is NLS, a peptide sequences that recognized by importin

and translocate into the nucleus. [48] Successful surface modification of AuNRs@PEG@RGD/NLS (AuNRs@NLS) is evident in the red-shift of the plasmon peak of AuNRs to longer wavelengths, from 800 nm for the as-synthesized cetyl-trimethy ammonium bromide (CTAB) coated AuNRs to 805 nm for PEGylated AuNRs, and finally to 825 nm for the RGD and NLS modified AuNRs (**Figure 4-1d)**. Similarly, the surface plasma peak of AuNSs@PEG@RGD/NLS (AuNSs@NLS) was also red-shifted (**Figure 4-1e**), which is in agreement with our former publication. [37]

Furthermore, the zeta potential of the AuNRs at the different conjugating stages of the three ligands were measured (**Table C.1.**) to confirm the surface modifications. In details, the as-synthesized CTAB coated AuNRs has highly positive surface charge (50.9 ± 7.97 mV) as CTAB is a highly cationic surfactant. After PEG modification, the AuNRs become negatively charged (-13.6 ± 11.8 mV). The zeta potential of the AuNRs becomes positive again (14.9 ± 3.13 mV) after further modification with RGD and NLS peptides (Table S1). Also, the zeta potential of the AuNSs@NLS proved their successful surface modification (**Appendix Table C.1.**), similar to the previous studies. [37]

To examine the cytotoxicity of the AuNPs, the XTT cell proliferation assay was conducted and no significant change of the cell viability was observed for nanoparticles at frequently used concentrations 0.5, 2.5 and 5 nM (for AuNRs) [18, 49] (**Figure 4-2a and Figure** 4-2**b**), and 0.05, 0.1 and 0.2 nM concentrations (for AuNSs). [37, 50] Apoptosis/necrosis assay was also conducted for 5 nM of the AuNRs or 0.2 nM of the AuNSs (**Figure 4-2c, Figure 4-2d and Figure 4-2e**) using flow cytometry. Therefore, the results indicate that the concentrations of the AuNRs used in this study are lower than that affecting cell viability or inducing apoptosis.

The uptake of AuNPs@NLS was monitored using dark-field (DF) microscopy and UV-Vis absorption. The HEY A8 cells, which were previously identified to be highly invasive cell line, [51] were incubated with 2.5 nM of AuNRs@NLS or 0.05 nM of AuNSs@NLS for 24 hrs. As shown in the DF image (**Appendix Figure C.1. a and b**), clear internalization of both AuNPs (AuNRs@NLS and AuNSs@NLS) was observed. Furthermore, for evaluating the AuNPs uptake to the HEY A8 cells, the UV-Vis spectra have been collected for the AuNPs in culture media before incubation with cells, compared with the ones after 24 h cell incubation (**Appendix Figure C.1. c and d**), which showed the decrease of peak intensity that, indicate the portion of AuNRs being uptaken by cells.

Non-targeted AuNPs with bovine serum albumin (BSA) coating were also fabricated. Successful surface modification of AuNPs@BSA (both AuNRs@BSA and AuNSs@BSA) is evident in the red-shift of the surface plasmon peak of AuNPs to longer wavelengths (**Appendix Figure C.2. a and b**). Zeta potential of AuNRs after BSA modification became negatively charged (-19.6 ± 9.89 mV, **Table C.1.**) due to the negative charge of BSA, while the as-synthesized CTAB coated AuNRs has highly positive surface charge (50.9 ± 7.97 mV, **Appendix Table C.1.**). The AuNSs@BSA also has a negative zeta potential of -15.2 ± 12.5 mV (**Appendix Table C.1.**). No toxicity effect of AuNPs@BSA was observed, as shown in **Appendix Figure C.2. c and d**.

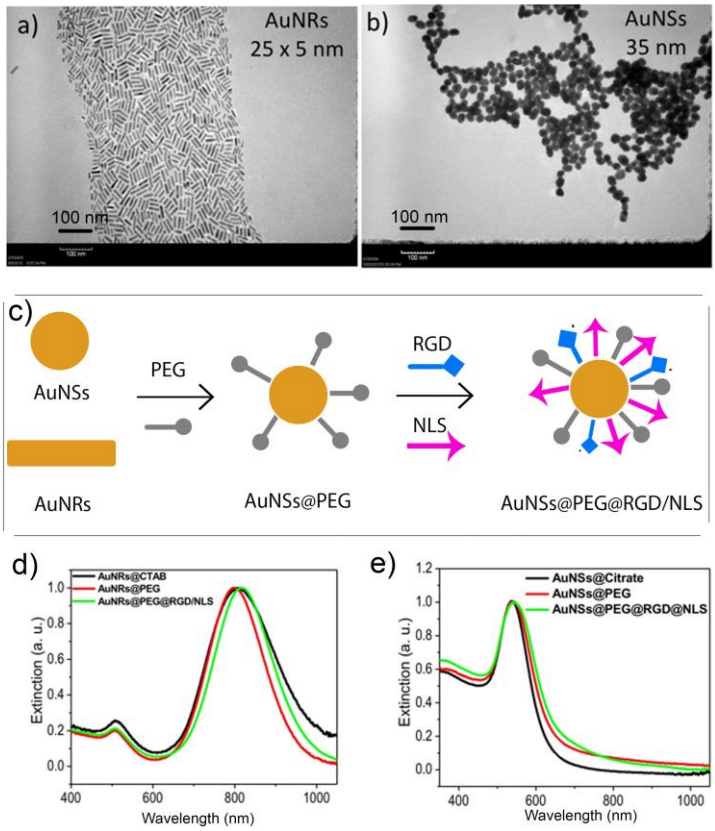

Figure 4-1. Characterization of Au nanoparticles

(A) Transmission Electron Microscopic (TEM) image of gold nanorods (AuNRs) and (B) TEM image of gold nanospheres (AuNSs), Scale bar = 100 nm. (C) Schematic figure of Au nanoparticle conjugation with PEG, RGD and NLS peptides. (D) UV-Vis extinction spectra of the unconjugated AuNRs (black spectrum), AuNRs@PEG (red spectrum), and AuNRs@PEG@RGD/NLS (green spectrum), (E) UV-Vis extinction spectra of the unconjugated AuNSs (black spectrum), AuNSs@PEG (red spectrum), and AuNSs@PEG@RGD/NLS (green spectrum).

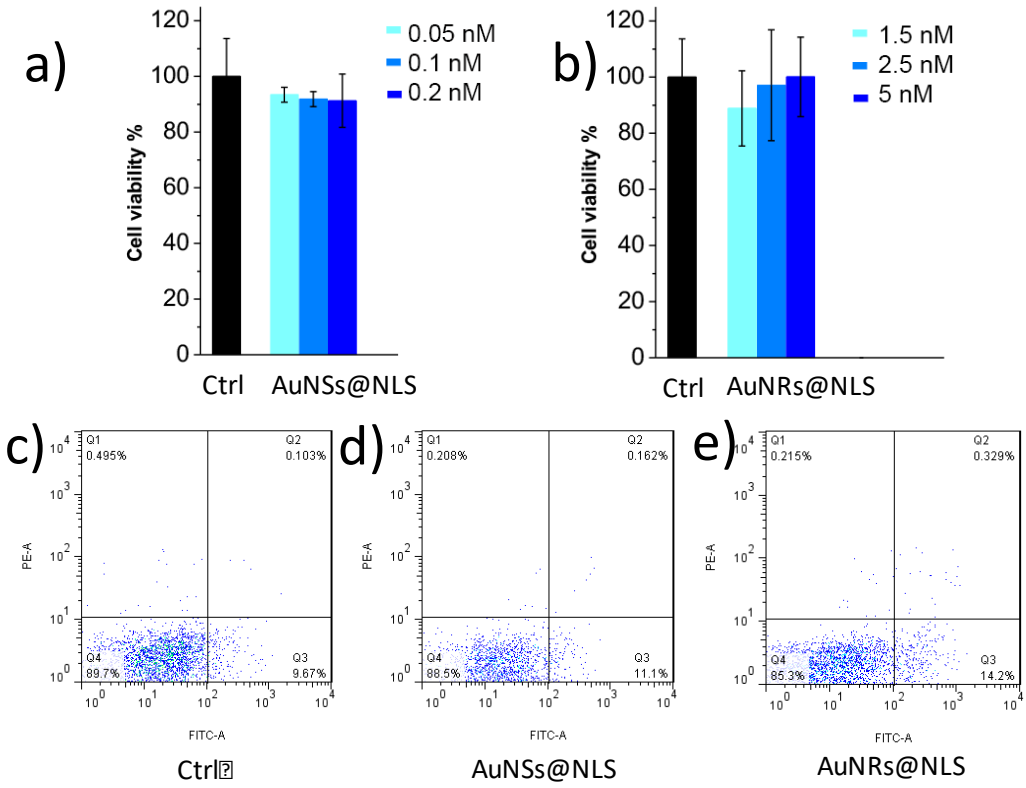

Figure 4-2. Au nanoparticles cytotoxicity measurements and cellular uptake

(A) Cell viability measurement (XTT assay) of HEY-A8 cells after 24 h incubation with AuNSs@NLS at concentrations 0.05 nM (light blue), 0.1 nM (medium blue) and 0.2 nM (dark blue). (B) Cell viability (XTT) assay for cells after 1.5 nM (light blue), 2.5 nM (medium blue) and 5 nM (dark blue) of AuNRs@NLS incubation with HEY-A8 cells for 24h. (C, D, and E) Flow cytometry experiment for apoptosis/necrosis assay (C, Ctrl; D, cells incubated with 0.2 nM of AuNSs@NLS ; (E) cells incubated with 5 nM of AuNRs@NLS).

Nuclear targeting gold nanoparticles inhibit cancer cell migration and invasion

To test the cell motility, HEYA8 cells were incubated with AuNPs for 12 hours before staining with fluorescent nuclear dye. Cells were then placed on an inverted epi-fluorescent microscope equipped with a cell culture chamber for continuous bright field and fluorescence imaging. The cell migration coefficients were then determined from the images. As shown in Figure 3a, both nuclear-targeted AuNRs and AuNSs inhibit the motility of HEY A8 cells. The average migration coefficient of the cells decreases from 3 x 10^{-10} by a factor of 3-10. (**Figure 4-3**a and Supporting Video Information for motility). We conducted a control experiment of non-targeted AuNPs coated with BSA, (AuNPs@BSA, characterization information in the Supporting Information and **Figure 2**). The motility assay shows that there is no apparent inhibition of AuNRs@BSA or AuNSs@BSA on cell migration (**Figure 4-3b**). The scratch assay was conducted to evaluate the migration ability. Results (**Figure 4-3c**) indicate that the control cells had a completely healed "wound" after 12 h following AuNPs incubation, while the ones treated with AuNRs@NLS and AuNSs@NLS were not completely healed after 12 h.

In order to examine the invasion ability of HEY A8 cells after their treatment with the nuclear membrane-targeted AuNPs, the trans-well invasion assay was performed. The cells that invaded the basement membrane extract (BME) after 32 h were dissociated and stained with Calcein AM, a fluorescent dye that labels living cells. A control experiment has been performed to eliminate the possibility that gold nanoparticles could quench the fluorescence from Calcein AM (**Appendix Figure C.3.**). A significant decrease in fluorescence intensity was observed in the AuNPs treated groups, indicating the inhibition of the invasion ability of HEY A8 cells particles (Figure 3d). In general, the cell migration,

and invasion abilities of HEY A8 cells were inhibited effectively by both AuNRs@NLS and AuNSs@NLS.

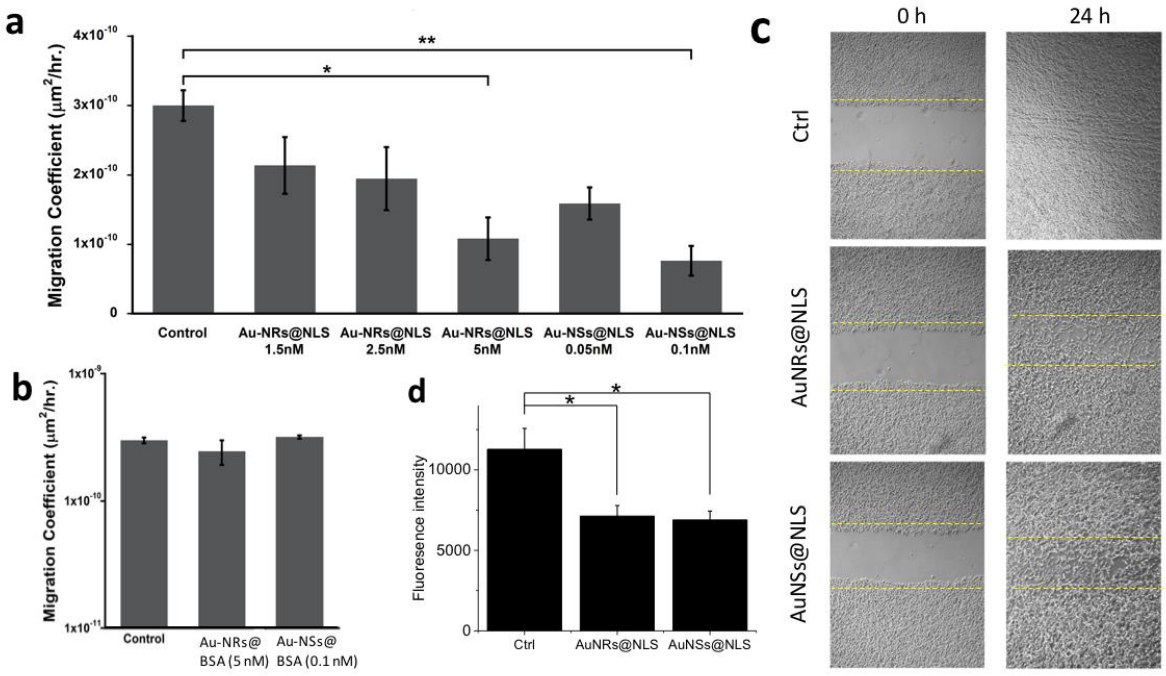

Figure 4-3. Effect of AuNPs (2.5 nM AuNRs@NLS and 0.1 nM AuNSs@NLS if not mentioned) on motility and invasion of HEY A8 cells

Cell migration study was performed to determine the effects of both AuNRs@NLS and AuNSs@NLS (A), and AuNRs@BSA (5 nM) and AuNSs@BSA (0.1 nM) (B) on the HEY A8 cells motility (error bar ±SEM). (C) Scratch assay of cells incubated with AuNRs@NLS and AuNSs@NLS displayed arrested healing/closing of the scratch. (D) Invasion assay of cells without AuNPs or with AuNRs@NLS and AuNSs@NLS treatment (error bar ± SD). *P < 0.05, **P < 0.01, ***P<0.001.

Nuclear targeting gold nanoparticles enhance nuclear stiffness

Next, we tested our hypothesis that the nuclear-targeted AuNPs can enhance nuclear stiffness. Cell stiffness as quantified by the Young's modulus has been used as a biomarker of the metastatic potential of cancer cells. [19] For AFM measurements (**Figure 4-4a**), a

beaded cantilever was lowered on top of the individual cells, producing an indentation in those cells and corresponding deflection of the AFM cantilever, which allowed for the measurement of cell stiffness. An overhead image of AFM cantilever tip next to HEY A8 cells with nanoparticles was shown in **Figure 4-4b**. The distribution of Young's moduli of individual cells, as well as that of the cell nucleus, from different nanoparticle treatments and the control is depicted in **Figure 4-4c** and **Figure 4-4d**. In our study, both AuNSs@NLS and AuNRs@NLS exhibit significant increase in the cell stiffness (**Figure 4-4c**), which is similar to previous observations that nanoparticles could increase cell stiffness. [52, 53] For the nuclear stiffness, as shown in **Figure 4d**, the mean nuclear Young's modulus of the cells treated with AuNPs (AuNRs and AuNSs) were also significantly higher than the mean nuclear Young's modulus of the untreated cells, in agreement with the results of the overall cell stiffness. In addition, we observed the increase of gold nanoparticle amount could increase the nuclear stiffness, as shown in **Appendix Figure C.4.**

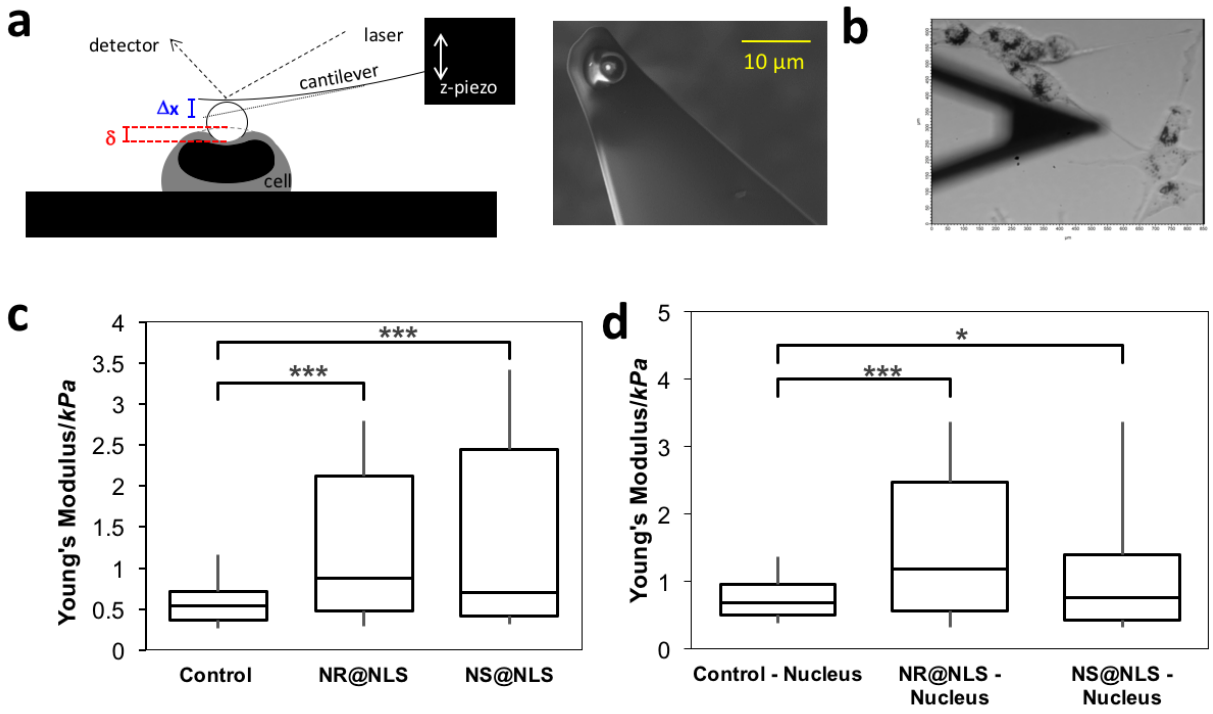

Figure 4-4. Stiffness distribution of cells:

(A) Schematic of measurements on cells with AFM; δ is indentation, Δx is cantilever deflection. To measure bulk cellular stiffness, a beaded cantilever was used to increase cell-probe surface area. (B) Overhead image of AFM cantilever tip next to HEY A8 cells with nanoparticles (C) Box-and-whisker plots of stiffness of single cells for different nanoparticles treatment, the percentiles are 10%, 25%, 50%, 75%, and 90%. Overall difference between means is significant (p-value calculated from ANOVA); (D) Box-and-whisker plots of nuclear stiffness. *P < 0.05, **P < 0.01, ***P<0.001.

AuNPs accumulate at nuclear membrane resolved by three-dimensional microscopy

Resolving the exact localizations of AuNPs regarding the nuclear membranes [54, 55] is a crucial, yet highly challenging, step in our attempt to understand the effects of AuNPs on the inhibition of cell migration. Most commonly used optical microscopy methods, such as confocal fluorescence microscopy and dark field (DF) microscopy, do not offer the

accurate locations of the nuclear membranes and AuNPs simultaneously, and they usually suffer from high background. On the other hand, TEM, despite its high resolving power, is limited by the high costs and tedious sample preparation to gain the full 3D distribution of AuNPs inside the cells. To circumvent these challenges, we employed a recently-developed differential interference contrast (DIC) microscopy-based 3D imaging method to visualize and locate plasmonic AuNPs inside the cells. [56-58] As shown in **Figure 4-5a**, the cells were placed in a sandwiched chamber. DIC optical sectioning was performed on the whole cell thickness. The arrow indicates the scanning optical sectioning of the cell, directed from layer 1 (close to the surface of the cover glass) to layer 2 (middle of the cell) and to layer 3 (top of the cell) (**Figure 4-5 and Appendix Figure C.5-6**, and Videos in the Supporting Information). The DIC microscope, which was equipped with a set of high numerical aperture (NA = 1.4), oil-immersion condenser and objective, features a shallow depth of field in optical sectioning of a 3D specimen to generate sharply focused images. More importantly, the nuclear membranes are clearly visible under the DIC microscope to allow the determination of the relative positions of the nuclear membranes and AuNPs.

Figure 4-5b to Figure 4-5d shows the AuNSs@NLS locations inside the HEY A8 cells. The black spots in the figures are the nanoparticle aggregates, which are shown clearly surrounding the nucleus from difference optical sections. Similarly, **Figure 4-5e to Figure 4-5g** shows a similar distribution of AuNRs@NLS inside HEY A8 cells. Both AuNRs@NLS and AuNSs@NLS aggregates were located predominantly on the nuclear membranes, while the internalization of nanoparticles inside the nucleus was rarely found, which was likely due to the large sizes of the nanoparticles and their aggregates compared to the nuclear pores (around 9~12 nm [59]).

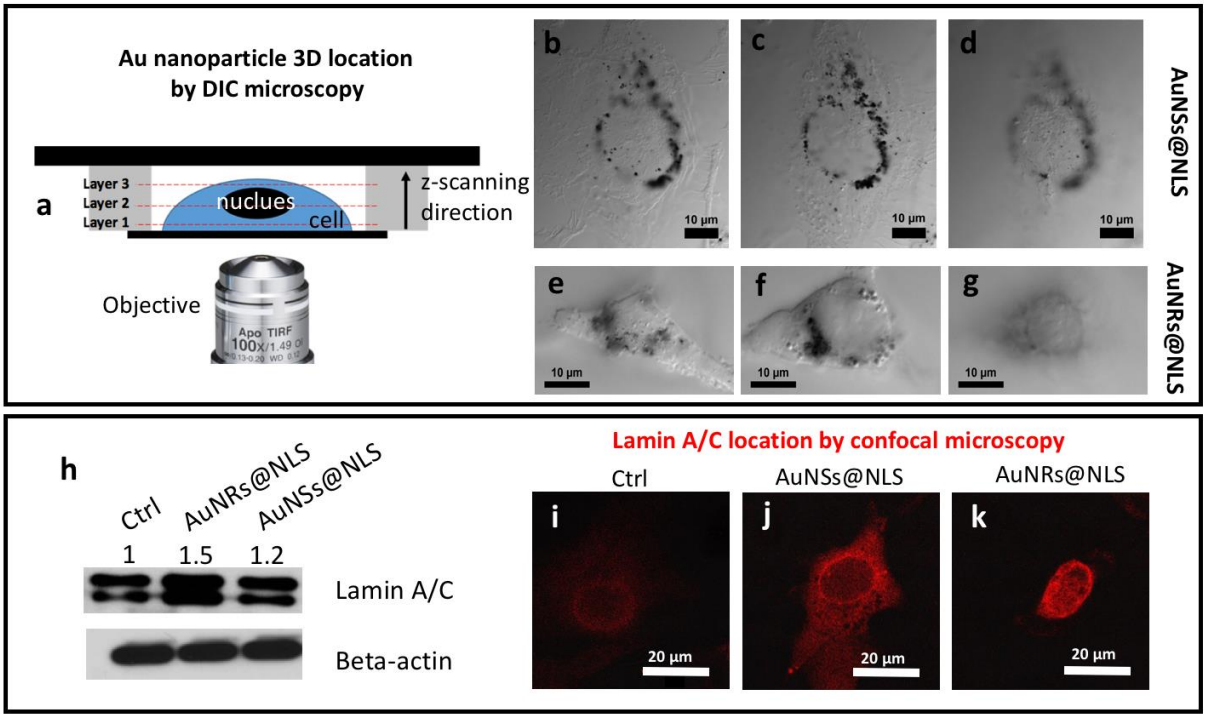

Figure 4-5. Locations of AuNPs inside the HEYA8 cell (up) and lamin A/C protein location/expression (down) inside the HEY A8 cell

(A) Scheme of the cell sample in sandwiched chamber for 3 dimensional DIC microscope imaging. Z-axis scanning step is 65 nm from the bottom (close to the attached glass surface) to the top of the cell. Three layers from the bottom, middle, and the top of the cell, for cells incubated with 0.1 nM of AuNSs@NLS (B-D) and 2.5 nM of AuNRs@NLS (E-G) were imaged, corresponding to frame 75, 235, and 395 (AuNSs@NLS) and frame 49, 179, and 285 (AuNRs@NLS) of the movies in the Supporting Information. (H) Western-blot results of lamin A/C, with beta-actin as reference protein. (I, J and K) Lamin A/C localization by confocal microscope of (I) cells without or (J) with AuNSs@NLS or (K) AuNSs@NLS incubation.

Nuclear targeting gold nanoparticles cause lamin A/C protein increase

Lamins, especially lamin A/C, are intermediate filament proteins found at nearly all cell nuclei and contribute to nuclear stiffness and stability. (60), (61) Nuclear lamins interact with the membrane-associated proteins to form the nuclear lamina (30-100 nm thick), which is located in the interior of the nuclear membrane. It has been reported that lamin A/C-deficient cells exhibit severely reduced nuclear stiffness. [30, 61] To further understand the biological mechanism for why nuclear membrane-targeting AuNPs increase nuclear stiffness and inhibit cancer cell migration, we measured the expression level of lamin A/C in Western-blots (**Figure 4-5h**) and confocal microscopy imaging after immuno-staining (**Figure 4-5**). The results indicate a clear overexpression of lamin A/C after incubation with AuNSs@NLS or AuNRs@NLS. As shown in **Figure 4-5i, Figure 4-5j and Figure 4-5k**, the fluorescence signal from lamin A/C was increased as a circle-surrounding the nucleus, which is in agreement with the location of nuclear lamina.

AuNPs conjugated with a nuclear localization signal were thought to be able to internalize into the nucleus. [54, 62] In our study we clearly observed most of the NLS conjugated gold nanoparticles aggregated around the nuclear membrane. Western blot experiment showed that the endocytosis and nuclear transportation has been activated upon nanoparticle incubation (**Appendix Figure C.7.**), due to the increased expression level of dynamin protein (a GTPase responsible for endocytosis in the eukaryotic cell) and GTP-binding nuclear protein Ran (involved in the transport into and out of the cell nucleus). Since the cellular and nuclear transportation are all activated, the trapping of AuNPs at the nuclear membrane was most likely due to the large size of the gold nanoparticles aggregates compared to the nuclear pores.

It has been widely reported that following the entry of nanoparticles, they traffic through early endosomes to late endosomes and lysosomes (endolysosomal trafficking). [63, 64] To achieve nuclear membrane targeting, nanoparticles need to escape from the endosome and/or lysosomes. There are several well-established mechanisms explaining the cytosolic release of the NPs from endosomes or lysosomes. One of the most popular mechanism is through the charge interactions. The cationic nanoparticles could interact with the negatively charged phosphor lipid membrane, followed by "proton sponge" effect, causing endosomal membrane rupturing [65, 66] and nanoparticle escaping. In our study, the positively charged AuNRs@NLS. [67] could have the similar mechanism to escape from the endosome. In our results, most of the nanoparticles finally locates surrounding the cell nucleolus after incubation with cells overnight (**Figure 4-5b toFigure 4-5g** and Supporting movies HEYA8_AuNSs@NLS.avi and HEYA8_AuNSs@NLS.avi), indicating a good efficacy that gold nanoparticles escape from the endosome/lysosomes and target the nuclear membrane. Meanwhile, the above results show that the effect of endosome degradation [68] of the surface conjugated peptides might be very minor.

Coincident with the increased nuclear stiffness by the AuNPs is the aggregation of the AuNPs at the nuclear membrane and the increase of the Lamin A/C expression, which is located at the inner side of nuclear membrane. Lamin A/C is known to maintain the mechanical strength of the nucleus, [69] and is thus consistent with an inhibited cell migration. In our results, a clearly increased expression level of Lamin A/C was observed. Thus, we propose that the increase of nuclear stiffness not only due to the mechanical contribution of the presence of gold nanoparticles, but could also due to the increase of Lamin A/C. How AuNPs increase Lamin A/C is not yet well explored in literature. **Figure**

Figure 4-5c shows AuNPs closely contact with the nuclear membrane, which could potentially disturb the membrane integrity. Therefore, we propose it could be a cellular defense mechanism as lamin is known to remain the mechanical strength of nucleus. Interestingly, nuclear lamin-associated proteins, such as emerin, which stabilizes nuclear architecture for maintaining the structural integrity, [68, 70, 71] are also increased as the AuNPs are added at the nuclear membrane as shown in **Figure C.7.** To investigate this mechanism, further studies such as proteomics and high-resolution imaging could be fruitful to elucidate the exact role of the AuNPs in inhibiting cell migration.

The clearance of nanoparticles from body after treatment has great importance to the evaluation of long-term effect of nanoparticles. While small nanoparticles (hydrodynamic diameter less than 5.5 nm) can be discard rapidly and efficiently through renal/urinary excretion. [72] big nanoparticles (over 18 nm) tend to accumulate in liver and spleen. [73] Such body deposition of metallic NPs over a long-time raises significant concerns regarding their long-term safety. A decrease of the liver content of gold has been reported after 1 month from 0.54% to the 0.07%. [74] The fate and the body elimination pattern of gold nanoparticles are not well studied. Future work will be focused on studying the effect of gold nanoparticles for preventing and treating the metastasis in animals.

4.1.4 Conclusion and Future Outlook

this is the first study showing that nuclear membrane-targeting AuNPs can increase nuclear stiffness and thereby inhibit cell migration and invasion. Compared with the previous studies with non-targeted AuNPs at relatively high amount (50-200 μM of AuNRs@BSA

[22] and 5-20 μg AuNSs@Citrate [20]), the nuclear membrane-targeted AuNPs showed higher inhibition effects at significantly lower concentrations (0.1 nM for 35 nm AuNSs and 2.5 nM for 25 × 5 nm AuNRs). The AuNPs were found to be trapped on the nuclear membranes from mapping the 3D distributions of the AuNPs under a DIC microscope. The trapping of AuNPs at the nuclear membranes could possibly: 1) add to the mechanical stiffness of the nucleus, and, 2) stimulate the overexpression of lamin A/C, which is known to lead to nuclear stiffness and thus slows down cancer cell migration. This new insight takes us one step closer to fully understand the effects on AuNPs on the inhibition of metastasis.

4.1.5 References

1. Ali, M. R. K., Wu, Y., Ghosh, D., Do, B. H., Chen, K. Dawson, M. R., Fang, N. Sulchek, T. A., Mostafa A. El-Sayed. (2017) Nuclear membrane-targeted gold nanoparticles inhibit cancer cell migration and invasion, *ACS Nano*, accepted.

2. Fidler, I. J. (2003) The pathogenesis of cancer metastasis: the 'seed and soil' hypothesis revisited. Nature reviews. *Cancer 3*, 453-458.

3. Hanahan, D., Weinberg, R, A. (2011) Hallmarks of Cancer: The Next Generation. *Cell 144*, 646-674.

4. Weber, G. F. (2013) Why does cancer therapy lack effective anti-metastasis drugs? *Cancer letters 328*, 207-211.

5. Morgillo, F., Lee, H. Y. (2005) Resistance to epidermal growth factor receptor-targeted therapy. *Drug resistance updates : reviews and commentaries in antimicrobial and anticancer chemotherapy 8*, 298-310.

6. Anonymous (2005) Effects of chemotherapy and hormonal therapy for early breast cancer on recurrence and 15-year survival: an overview of the randomised trials. *Lancet (London, England) 365*, 1687-1717.

7. Murphy, C. J., et al. (2008) Gold Nanoparticles in Biology: Beyond Toxicity to Cellular Imaging. *Accounts Chem Res 41*, 1721-1730.

8. Hirsch, L. R., et al. (2003) Nanoshell-mediated near-infrared thermal therapy of tumors under magnetic resonance guidance. *Proceedings of the National Academy of Sciences 100*, 13549-13554.

9. Peer, D., et al. (2007) Nanocarriers as an emerging platform for cancer therapy. *Nature nanotechnology 2*, 751-760.

10. Ali, M. R., Ibrahim, I. M., Ali, H. R., Selim, S. A., El-Sayed, M. A. (2016) Treatment of natural mammary gland tumors in canines and felines using gold nanorods-assisted plasmonic photothermal therapy to induce tumor apoptosis. *International Journal of Nanomedicine 11*, 4849.

11. Ali, H. R., et al. (2016) Gold Nanorods as Drug Delivery Vehicles for Rifampicin Greatly Improve the Efficacy of Combating Mycobacterium tuberculosis with Good Biocompatibility with the Host Cells. *Bioconjugate Chemistry 27*, 2486-2492.

12. Jun, Y-w, et al. (2005) Nanoscale Size Effect of Magnetic Nanocrystals and Their Utilization for Cancer Diagnosis via Magnetic Resonance Imaging. *Journal of the American Chemical Society 127*, 5732-5733.

13. Jain, P. K., Lee, K. S., El-Sayed, I. H., El-Sayed, M. A. (2006) Calculated Absorption and Scattering Properties of Gold Nanoparticles of Different Size, Shape, and Composition: Applications in Biological Imaging and Biomedicine. *The Journal of Physical Chemistry B 110*, 7238-7248.

14. Ali, M. R., Panikkanvalappil, S. R., El-Sayed, M. A. (2014) Enhancing the efficiency of gold nanoparticles treatment of cancer by increasing their rate of endocytosis and cell accumulation using rifampicin. *Journal of the American Chemical Society 136*, 4464-4467.

15. Danhier, F., Feron, O., Preat, V. (2010) To exploit the tumor microenvironment: Passive and active tumor targeting of nanocarriers for anti-cancer drug delivery. *Journal of controlled release : official journal of the Controlled Release Society 148*, 135-146.

16. Ali, M. R. K., Panikkanvalappil, S. R., El-Sayed, M. A. (2014) Enhancing the Efficiency of Gold Nanoparticles Treatment of Cancer by Increasing Their Rate of Endocytosis and Cell Accumulation Using Rifampicin. *Journal of the American Chemical Society 136*, 4464-4467.

17. Dickerson, E. B., et al. (2010) Chemosensitization of cancer cells by siRNA using targeted nanogel delivery. BMC Cancer 10(1):10.

18. Ali, M. R. K., Ali, H. R., Rankin, C. R., El-Sayed, M. A. (2016) Targeting heat shock protein 70 using gold nanorods enhances cancer cell apoptosis in low dose plasmonic photothermal therapy. Biomaterials 102, 1-8.

19. Yang, J. A., Phan, H. T., Vaidya, S., Murphy, C. J. (2013) Nanovacuums: Nanoparticle Uptake and Differential Cellular Migration on a Carpet of Nanoparticles. *Nano Letters 13*, 2295-2302.

20. Arvizo, R. R., et al. (2013) Inhibition of tumor growth and metastasis by a self-therapeutic nanoparticle. *Proceedings of the National Academy of Sciences of the United States of America 110*, 6700-6705.

21. Tay, C. Y., et al. (2014) Nanoparticles strengthen intracellular tension and retard cellular migration. Nano Lett 14(1):83-88.

22. Zhou, T., et al. (2014) Inhibition of Cancer Cell Migration by Gold Nanorods: Molecular Mechanisms and Implications for Cancer Therapy. *Advanced Functional Materials 24*, 6922-6932.

23. Swaminathan, V., et al. (2011) Mechanical stiffness grades metastatic potential in patient tumor cells and in cancer cell lines. *Cancer research 71*, 5075-5080.

24. Cross, S. E., et al. (2008) AFM-based analysis of human metastatic cancer cells. *Nanotechnology 19*, 384003.

25. Wirtz, D., Konstantopoulos, K., Searson, P. C. (2011) The physics of cancer: the role of physical interactions and mechanical forces in metastasis. *Nature reviews Cancer 11*, 512-522.

26. Lautscham, L. A., et al. (2015) Migration in Confined 3D Environments Is Determined by a Combination of Adhesiveness, Nuclear Volume, Contractility, and Cell Stiffness. *Biophysical journal 109*, 900-913.

27. Dahl, K. N., Ribeiro, A. J. S., Lammerding, J. (2008) Nuclear Shape, Mechanics, and Mechanotransduction. *Circulation Research 102*, 1307.

28. Isermann, P., Lammerding, J. (2013) Nuclear Mechanics and Mechanotransduction in Health and Disease. *Current Biology 23*, R1113-R1121.

29. McGregor, A. L., Hsia, C. R., Lammerding, J. (2016) Squish and squeeze-the nucleus as a physical barrier during migration in confined environments. *Current opinion in cell biology 40*, 32-40.

30. Swift, J., et al. (2013) Nuclear lamin-A scales with tissue stiffness and enhances matrix-directed differentiation. *Science 341*, 1240104.

31. Harada, T., et al. (2014) Nuclear lamin stiffness is a barrier to 3D migration, but softness can limit survival. *The Journal of cell biology 204*, 669-682.

32. Lee, J. S., et al. (2007) Nuclear lamin A/C deficiency induces defects in cell mechanics, polarization, and migration. *Biophys J 93*, 2542-2552.

33. Davidson, P. M., Denais, C., Bakshi, M. C., Lammerding, J. (2014) Nuclear deformability constitutes a rate-limiting step during cell migration in 3-D environments. *Cell Mol Bioeng 7*, 293-306.

34. Mackey, M. A., Ali, M. R. K., Austin, L. A., Near, R. D., El-Sayed, M. A. (2014) The Most Effective Gold Nanorod Size for Plasmonic Photothermal Therapy: Theory and In Vitro Experiments. *The Journal of Physical Chemistry B 118*, 1319-1326.

35. Turkevich, J., Stevenson, P. C., Hillier, J. (1951) A Study Of The Nucleation And Growth Processes In The Synthesis Of Colloidal Gold. *Discussions of the Faraday Society 11*, 55-75.

36. Ali, M. R. K., Snyder, B., El-Sayed, M. A. (2012) Synthesis and Optical Properties of Small Au Nanorods Using a Seedless Growth Technique. *Langmuir 28*, 9807-9815.

37. Kang, B., Austin, L. A., El-Sayed, M. A. (2014) Observing real-time molecular event dynamics of apoptosis in living cancer cells using nuclear-targeted plasmonically enhanced Raman nanoprobes. *ACS nano 8*, 4883-4892.

38. Austin, L. A., et al. (2015) Cytotoxic effects of cytoplasmic-targeted and nuclear-targeted gold and silver nanoparticles in HSC-3 cells - A mechanistic study. *Toxicology in Vitro 29*, 694-705.

39. Bao, G., Suresh, S. (2003) Cell and molecular mechanics of biological materials. *Nature Materials 2*, 715-725.

40. Cross, S. E., Jin, Y. S., Rao, J., Gimzewski, J. K. (2007) Nanomechanical analysis of cells from cancer patients. *Nature Nanotechnology 2*, 780-783.

41. Cross, S. E., Jin, Y. S., Rao, J., Gimzewski, J. K. (2007) Nanomechanical analysis of cells from cancer patients. *Nat Nanotechnol 2*, 780-783.

42. Liang, C. C., Park, A. Y., Guan, J. L. (2007) In vitro scratch assay: a convenient and inexpensive method for analysis of cell migration in vitro. Nature protocols 2(2):329-333.

43. Hutter JL & Bechhoefer J (1993) Calibration Of Atomic-Force Microscope Tips (VOL 64, PG 1868, 1993). *Rev Sci Instrum 64*, 3342-3342.

44. Renger, A. (1989) Johnson, K. L., Contact Mechanics. Cambridge etc., Cambridge University Press 1985. XII, 452 pp., £ 17.50 P/B. ISBN 0521347963. *ZAMM - Journal of Applied Mathematics and Mechanics / Zeitschrift für Angewandte Mathematik und Mechanik 69*, 214-214.

45. Xu, W. W., Chahine, N., Suchek, T. (2011) Extreme Hardening of PDMS Thin Films Due to High Compressive Strain and Confined Thickness. *Langmuir 27*, 8470-8477.

46. Prencipe, G., et al. (2009) PEG Branched Polymer for Functionalization of Nanomaterials with Ultralong Blood Circulation. *J Am Chem Soc 131*, 4783-4787.

47. Ruoslahti, E., Pierschbacher, M. D. (1986) Arg-Gly-Asp - A Versatile Cell Recognition Signal. *Cell 44*, 517-518.

48. Kalderon, D., Roberts, B. L., Richardson, W. D., Smith, A. E. (1984) A Short Amino-Acid Sequence Able To Specify Nuclear Location. *Cell 39*, 499-509.

49. Ali, H. R., et al. (2016) Gold Nanorods as Drug Delivery Vehicles for Rifampicin Greatly Improve the Efficacy of Combating Mycobacterium tuberculosis with Good Biocompatibility with the Host Cells. *Bioconjugate Chem 27*, 2486-2492.

50. Panikkanvalappil, S. R., Hira, S. M., Mahmoud, M. A., El-Sayed, M. A. (2014) Unraveling the Biomolecular Snapshots of Mitosis in Healthy and Cancer Cells Using Plasmonically-Enhanced Raman Spectroscopy. *J Am Chem Soc 136*, 15961-15968.

51. Xu, W. W., et al. (2012) Cell Stiffness Is a Biomarker of the Metastatic Potential of Ovarian Cancer Cells. *Plos One 7*.

52. Pietuch, A., et al. (2015) Mechanical properties of MDCK II cells exposed to gold nanorods. *Beilstein Journal of Nanotechnology 6*, 223-231.

53. Lee, C. W., et al. (2016) Membrane roughness as a sensitive parameter reflecting the status of neuronal cells in response to chemical and nanoparticle treatments. *Journal of Nanobiotechnology 14*.

54. Kang, B., Mackey, M. A., El-Sayed, M. A. (2010) Nuclear Targeting of Gold Nanoparticles in Cancer Cells Induces DNA Damage, Causing Cytokinesis Arrest and Apoptosis. *J Am Chem Soc 132*, 1517.

55. Patel, S., et al. (2014) NanoScript: A Nanoparticle-Based Artificial Transcription Factor for Effective Gene Regulation. *Acs Nano 8*, 8959-8967.

56. Wang, G. F., Stender, A. S., Sun, W., Fang, N. (2010) Optical imaging of non-fluorescent nanoparticle probes in live cells. *Analyst 135*, 215-221.

57. Stender, A. S., et al. (2013) Single Cell Optical Imaging and Spectroscopy. *Chem Rev 113*, 2469-2527.

58. Sun, W., Wang, G., Fang, N., Yeung, E. S. (2009) Wavelength-Dependent Differential Interference Contrast Microscopy: Selectively Imaging Nanoparticle Probes in Live Cells. *Anal Chem 81*, 9203-9208.

59. Paine, P. L. (1975) Nucleocytoplasmic Movement Of Fluorescent Tracers Microinjected Into Living Salivary-Gland Cells. *Journal of Cell Biology 66*, 652-657.

60. Pajerowski, J. D., Dahl, K. N., Zhong, F. L., Sammak, P. J., Discher, D. E. (2007) Physical plasticity of the nucleus in stem cell differentiation. *Proceedings of the National Academy of Sciences of the United States of America 104*, 15619-15624.

61. Lammerding, J., et al. (2006) Lamins A and C but not lamin B1 regulate nuclear mechanics. *J Biol Chem 281*, 25768-25780.

62. Dreaden, E. C., Mackey, M. A., Huang, X. H., Kang, B., El-Sayed, M. A. (2011) Beating cancer in multiple ways using nanogold. *Chemical Society Reviews 40*, 3391-3404.

63. Sandin, P., Fitzpatrick, L. W., Simpson, J. C., Dawson, K. A. (2012) High-Speed Imaging of Rab Family Small GTPases Reveals Rare Events in Nanoparticle Trafficking in Living Cells. *Acs Nano 6*, 1513-1521.

64. Kim, A. J., Boylan, N. J., Suk, J. S., Lai, S. K., Hanes, J. (2012) Non-degradative intracellular trafficking of highly compacted polymeric DNA nanoparticles. *Journal of Controlled Release 158*, 102-107.

65. Chu, Z. Q., et al. (2015) Rapid endosomal escape of prickly nanodiamonds: implications for gene delivery. *Scientific Reports 5*.

66. Morille, M., Passirani, C., Vonarbourg, A., Clavreul, A., Benoit, J. P. (2008) Progress in developing cationic vectors for non-viral systemic gene therapy against cancer. *Biomaterials 29*, 3477-3496.

67. Ali, M. R. K., et al. (2016) Simultaneous Time-Dependent Surface-Enhanced Raman Spectroscopy, Metabolomics, and Proteomics Reveal Cancer Cell Death Mechanisms Associated with Gold Nanorod Photothermal Therapy. *Journal of the American Chemical Society 138*, 15434-15442.

68. Rowat, A. C., Lammerding, J., Ipsen, J. H. (2006) Mechanical properties of the cell nucleus and the effect of emerin deficiency. *Biophysical journal 91*, 4649-4664.

69. Ge, Y., Bruno, M., Wallace, K., Winnik, W., Prasad, R. Y. (2011) Proteome profiling reveals potential toxicity and detoxification pathways following exposure of BEAS-2B cells to engineered nanoparticle titanium dioxide. *Proteomics 11*, 2406-2422.

70. Lammerding, J., et al. (2005) Abnormal nuclear shape and impaired mechanotransduction in emerin-deficient cells. *Journal of Cell Biology 170*, 781-791.

71. Berk, J. M., Tifft, K. E., Wilson, K. L. (2013) The nuclear envelope LEM-domain protein emerin. *Nucleus-Austin 4*, 298-314.

72. Choi, H. S., et al. (2007) Renal clearance of quantum dots. *Nature Biotechnology 25*, 1165-1170.

73. Semmler-Behnke, M., et al. (2008) Biodistribution of 1.4-and 18-nm Gold Particles in Rats. *Small 4*, 2108-2111.

74. Sadauskas, E., et al. (2009) Protracted elimination of gold nanoparticles from mouse liver. *Nanomedicine-Nanotechnology Biology and Medicine 5*, 162-169.

4.2 Targeting Cancer Cell Integrins Using Gold Nanorods in Photothermal Therapy Inhibits Its Migration by Affecting Cytoskeleton Proteins [1]

Metastasis is responsible for the majority of cancer-related deaths, while the current clinical treatments are not effective. Recently, gold nanoparticles were discovered to inhibit cancer cell migration and prevent metastasis. However, high doses of gold nanoparticles were necessary to achieve good inhibition efficacy, which is not favorable for clinical applications. Moreover, the mechanism behind remains largely unexplored. Cytoskeletons are cell structure proteins closely related to migration. Within this process, surface receptor integrins, play one of the most important roles in controlling the cytoskeletons. Herein, we developed a novel strategy to inhibit cancer cell migration using gold nanorods (AuNRs) conjugated with RGD peptides, for targeting cancer cell integrins, with 1000 times less particle dosage. AuNRs were further activated with 808 nm near infrared (NIR) light to generate plamonic photothermal therapy (PPTT), which was controlled not to affect the cell viability or proliferation. Our results demonstrated a decreased cell migration speed. Changes in cell morphology, observed as cytoskeleton protrusions known as lamellipodia and filopodia, were reduced after treatment. The Western-blot analysis indicated that the down-stream effectors of integrin were attracted towards the anti-migration direction. Proteomics results indicated broad perturbations in four signaling pathways: Rho GTPases, actin, microtubule, and kinases related pathways. When we applied PPTT, it further inhibited the cancer cell migration by remodeling the cell cytoskeleton proteins. In summary, the ability of targeting AuNRs to the cancer cell integrins and the introduction of PPTT stimulated wide-range regulating the migration pathways, which provides a potential novel medical application for controlling cancer metastasis.

4.2.1 Introduction

Metastasis is a process that enables cancer cells to spread to other sites of the body, and is responsible for most cancer-related deaths [2-4]. The migration of cancer cells from one site to another requires dramatic remodeling of the cell cytoskeleton [2, 4-6]. Studies on the changes of cytoskeleton components could provide novel therapeutic approaches to prevent cancer cell migration and metastasis [5]. The targeting of cytoskeletal components, such as actin or tubulin [7-8], or regulatory proteins, such as Rho-ROCK or LIM kinases, has been shown to inhibit the invasive and metastatic behavior of cancer cells [9-10]. However, the pharmacological inhibitors of cytoskeleton have not been very effective in clinical trials due to their non-specific targeting of cytoskeleton in the normal cells that might cause side effects, such as cardiotoxicity [5, 8, 11]. Moreover, in many cases, the anti-cancer drugs that target specific proteins might lose their efficacy after several months of treatment due to mutations of the proteins that result in the rise of drug resistance in cancer cells [12, 13].

Recent advancements in nanomedicine provide us with great opportunities to avoid the drawbacks of commonly used drugs [14-15]. Due to their small sizes and surface modifications, nanoparticles, in general, can target tumors selectively [16]. Because of these intrinsic properties, nanoparticles are widely used in cancer diagnosis and therapy [17-18]. The recent discovery of nanoparticles' effect on inhibiting cancer cell migration or metastasis has drawn the attention of many researchers [19,20-22]. Among them, several groups have reported that this inhibition effect of nanoparticles is closely related to the cytoskeletons. Tay *et al*. found that TiO_2, SiO_2, and hydroxyapatite nanoparticles could disrupt the intracellular microtubule assembly, thus strengthening the intracellular tension

and retarding cellular migration [19]. Soenen et al also reported that high concentrations of iron oxide nanoparticles within cells affect the cellular cytoskeleton and focal adhesion kinase-mediated signaling [23]. Zhou *et al*. showed gold nanorods (AuNRs) can inhibit F-actin cytoskeletal assembly and decrease cancer cell migration [21]. However, current studies use high concentrations of nanoparticles in μM, which might be an obstacle when considering the translation to clinical usage [19, 21, 23]. Additionally, several types of nanoparticles, including TiO_2, SiO_2, iron oxide, *etc*. have been found to exhibit toxicity when used in relatively high concentrations [24, 25, 26]. In order to maintain the nanoparticles' effect on slowing cancer cell migration with a limited amount of nanoparticles, an intelligent design and delivery of nanoparticles to regulate the cytoskeleton promises to be crucial in helping the development of novel and effective anti-metastasis therapy.

Gold nanorods (AuNRs), due to their unique chemical, physical and optical properties, have been used in drug delivery [27], bio-imaging [28], and the plasmonic photothermal therapy (PPTT) of cancer [29-31]. It has been reported that heat stress affects the cytoskeleton and induces their rearrangements [32-34]. The use of AuNRs allows us to apply near infra-red laser (NIR) to generate heat efficiently through non-radioactive processes [14, 35-36]. NIR light as a low energetic (safe) light might deeply penetrate the tissues to activate the AuNRs' effects on cytoskeletal proteins and inhibit migration. Our previous study has shown success in treating natural mammary gland tumors in dogs and cats using AuNRs assisted plasmonic photothermal therapy (PPTT), where all the cases did not have cancer relapse and metastasis [37], hinting the potential effect of PPTT on

inhibiting cancer metastasis. Therefore, to overcome the drawbacks of using nanoparticles, four aspects were considered to better the nanoparticle design to achieve effective inhibition of cancer cell migration: 1) Lower the concentration of nanoparticles to nM dosage, as a means for lowering toxicity. 2) Enhance the selectivity to the cancerous cells. 3) Apply NIR light to activate the AuNRs' effects on cytoskeletal proteins and inhibit migration. 4) Most importantly, enhancing the migration inhibition effect by targeting AuNRs to integrin proteins to remodel the cytoskeleton.

Integrins are major adhesion and signaling receptor proteins that play an important role in regulating cytoskeleton [38-40], by providing a physical linkage between the cytoskeleton and the extracellular matrix (ECM), and receiving signals from the ECM [41]. They could perturb the down-stream cell adhesion and migration pathways and modulate the cytoskeleton, thus regulating cell motility and migration [42-43]. Numerous studies have reported differentially expressed integrins in many cancers. For instance, inducing the expression of the αv or β3 integrin subunit in cancer cell lines increases their metastatic potential [44-45]. The Arg-Gly-Asp (RGD) peptides are known for specific binding to a wide number of surface integrins, including αvβ3, α3β1 and α5β1integrins. [46-48]

In our work, RGD peptides were conjugated on the surface of AuNRs to achieve the selective targeting of integrin. Near infrared (NIR) light was applied to the AuNRs to generate mild heat. The concentration of the AuNRs and heat were kept well below the threshold of those that might affect cell viability or proliferation. We compared both non-

targeted and integrin-targeted gold nanorods (AuNRs@RGD). Results indicated that, while both types of AuNRs decreased cell migration speed, the targeted ones did so with a greater effect. After applying NIR light, cell motility was further decreased. We have performed a proteomics study to understand the molecular mechanism, explaining how and why AuNRs have a wide-range effect in perturbing cytoskeleton proteins and cell migration pathways. Compared to the drugs comprised of small molecules that target only a single protein, AuNRs show great promise as a novel anti-metastasis strategy to be developed for clinical usage.

4.2.2 Experimental methods

Instrumentation. Gold nanoparticles were imaged using a JEOL 100CX-2 transmission electron microscope (TEM) microscope, and their average size was then measured by ImageJ software. UV−vis spectra were obtained using an Ocean Optics HR4000CG UV-NIR spectrometer. An inverted Nikon Eclipse Ti-E microscope equipped with Perfect Focus System (PFS, 25 nm z-axial resolution) was used for imaging under differential interference contrast (DIC) microscopy. Proteomics analysis was done on a hybrid dual-cell quadrupole linear ion trap − Orbitrap mass spectrometer LTQ Orbitrap Elite (Thermo Fisher) with Xcalibur 3.0.63 software. Flow cytometry experiments were conducted on a BD LSR II Flow Cytometer (BD Biosciences).

Synthesis, conjugation and characterization of AuNRs:

Gold nanorods (AuNRs) with an average size of 25 x 6 nm (length x width) were synthesized using a seedless growth method [49]. 5 ml of 1.0 mM $HAuCl_4$ was added to a solution of 5 mL of 0.2 M CTAB, 250 μL of 4.0 mM $AgNO_3$, and 8 μL of 37% HCl. Then, 70 μL of 78.8 mM ascorbic acid was added, followed by immediate injection of 15 μL of 0.01M of ice-cold $NaBH_4$. The solution was left undisturbed for 12 hours. The particles were centrifuged at 21000 g for 50 min and dispersed in DI water, followed by a second centrifugation at 19000 g for 40 min to remove the extra CTAB. TEM was used to measure the sizes and homogeneity of the nanoparticles.

After rinsing them with water, AuNRs were then conjugated with different surface ligands (PEG and RGD). For AuNRs@PEG, mPEG-SH (1 mM) was added to the nanoparticles overnight to achieve about 5000 ligands on each particle. For preparing AuNRs@RGD, first, mPEG-SH (1 mM) was added to the nanoparticles overnight to achieve about 1000 ligands on each particle. Then, the PEGylated nanoparticles (1 nM) were treated with RGD (1 mM) to achieve 10000 molar excess. The solution was then allowed to shake overnight at room temperature. Excess of ligands were removed by centrifugation. UV-vis spectrometer and zetasizer were used to test the conjugation.

Cell culture, AuNRs treatments and PPTT:

Cells were grown in Dulbecco's modified Eagles' medium (DMEM, Mediatech) containing 10% (v/v) fetal bovine serum (FBS, Mediatech) and 1% antimycotic solution (Mediatech) at 37 ^oC in a humidified incubator under 5% CO_2. Cells were cultured in 60 mm dishes for 24 hours followed by incubation with AuNRs for 24 hours. Then, a CW 808 nm laser (5.8 W/cm^2, spot size 5.6 mm) was applied to the cells. To cover the entire area

of the culture dish, the laser was applied spot by spot using scanning with each spot undergoing two minutes of laser exposure time. The cells were then harvested for MS analysis, with a final confluence about 80-90%.

Sample preparation for proteomics experiment:

After treatment for 24 hours, cells were washed twice using PBS. Cell lysates were prepared by directly adding the lysis buffer (150 mM NaCl, 50 mM HEPES, pH =7.4, 0.1% SDC, 10 units/ mL benzonase, protease inhibitor cocktail) to the cells followed by scraping and collecting on ice. Lysates were vortexed for 90 s (30 s x 3 times, 2 min pause), sonicated on ice, and centrifuged at 18000 g for 15 min at 4 ^{o}C. The supernatant solutions were saved and proteins were precipitated by adding 4 x excess volumes of ice-cold precipitation solvents (acetone: ethanol: acetic acid=50:50:0.1) and stored at -20 ^{o}C overnight. After centrifugation, the protein pellet was re-dissolved in an 8 M urea, 50 mM HEPES solution (pH=8) [50].

Protein disulfide bonds were reduced using 1 mM dithiothreitol (DTT) followed by alkylation with 5.5 mM iodoacetamide. After the lysate were diluted two times, (final urea concentration 4 M) endoproteinase Lys-C (1:100 w/w) was added to digest proteins for 4 hours. Then, modified sequencing grade trypsin (1:100 w/w) was used for further digestion in a more diluted solution with the final urea concentration of 1 M for overnight [51]. Protein concentration was measured by Bradford assay.

RPLC-MS/MS Analysis for label-free quantitative proteomics:

The proteomics analysis was conducted using the previous reported method [52]. Briefly, purified and dried peptide samples from the previous step were dissolved in 10 μL solvent with 5% acetonitrile and 4% FA, and 4 μL of the resulting solutions were loaded onto a microcapillary column packed with C18 beads (Magic C18AQ, 3 μm, 200 Å, 100 μm x 16 cm, Michrom Bioresources) by a Dionex WPS-3000TPLRS autosampler (UltiMate 3000 thermostatted Rapid Separation Pulled Loop Wellplate Sampler). A reversed-phase liquid chromatography (RPLC) using an UltiMate 3000 binary pump was used for Peptides separation, with a 110 min gradient of 8-38% ACN (with 0.125% FA). Peptides were detected with a data-dependent Top20 method, *i.e.* for each cycle, one full MS scan (resolution: 60,000) in the Orbitrap was followed by up to 20 MS/MS in the ion trap for the most intense ions. The selected ions were excluded from further analysis for 90 seconds. Ions with singly or unassigned charge were not sequenced. Maximum ion accumulation times were 1000 ms for each full MS scan and 50 ms for MS/MS scans. The sample at each condition was repeated 6 times (2 biological and 3 technique replicates) for label-free quantification.

Apoptosis/necrosis assay:

After removing the cell culture media, and cells were washed with PBS and collected after trypsinization followed by washing with cold PBS twice again. Then, the cells were dispersed in a mixture of 493 mL of Annexin V binding buffer, 5 μL of Annexin V FITC (BioLegend), and 2 μL of propidium iodide PI (BioLegend, 100 μg / mL) and incubated for 15 min at room temperature. The cells were then filtered and subjected to flow cytometry analysis using a BSR LSR II flow cytometer (BD Biosciences). A 488 nm laser was applied for excitation, and FITC was detected in FL-1 using a 525/30 BP filter while

PI was detected in FL-2 using a 575/30 BP filter. Standard compensation using unstained and single-stained cells was done before running actual experiments. FlowJo software (Tree Star Inc.) was used for analysis of the viable, apoptotic and necrotic cells from at least 10000 events.

Cell Imaging Using DIC Microscopy: The DIC mode utilized a pair of DIC polarizer and analyzer, a high resolution 100×I-R DIC slider, a high numerical aperture (N.A., 1.40) oil immersion condenser lens, a Nikon CFI Apo TIRF 100× (N.A., 1.49) oil immersion objective, and a 12 V/100 W halogen lamp as light source. Appropriate bandpass filters were placed in the light path. Fixed HEYA8 cells on 22 mm × 22 mm glass coverslips were rinsed with PBS at pH 7.4 and fabricated into a sandwiched chamber with two pieces of double-sided tape and a cleaned glass slide. PBS solution was then added into the chamber to fill the space, and the chamber was then sealed by clear nail polish. The so-formed sample slide was then place under the microscope for observation.

Scratch assay: The scratch assay has been performed according to a former report [53]. Cells were cultured in a 6 well plate to a confluent monolayer. A p200 pipet tip was used to scrape the cell monolayer in a straight line to create an empty gap. The debris was then removed by washing the cells once with a culture medium and then replaced with 2 mL of fresh medium. Then, the cells were imaged immediately after scratch and 12 hours after scratch.

Proteomics data analysis: Two biological replications and three MS technical replications for each condition (control, AuNRs@PEG, AuNRs@PEG/NIR, AuNRs@RGD, AuNRs@RGD/NIR) were conducted. Raw data from proteomics was normalized using

supervised normalization of the microarray (SNM) [54]. In the SNM procedure, variance due to biological and technical replicates were adjusted by setting them as variables in the model. Variance explained by different experimental treatments (control, AuNRs@PEG, and AuNRs@PEG+NIR for PEG-conjugated AuNRs group; control, AuNRs@RGD, and AuNRs@RGD+NIR for RGD-conjugated AuNRs group) was fitted as a biological variable in the model. Hierarchical clustering was done with statistical software R [55]. Proteomics data was log2 transformed before analysis of variance (ANOVA) which was used to detect differential levels of proteins between control and treatment groups. We fitted models with treatment conditions and fixed effects. We set P-value threshold at 0.1 to select differential proteins. The proteins identified as being affected were subjected to pathway analysis using the MetaCore pathway analysis software ("MetaCore from Thomson Reuters").

Western-blot analysis: Briefly, cells were lysed in RIPA buffer (20 mM Tris pH 7.4, 150 mM NaCl, 2 mM EDTA, 2 mM EGTA, 0.1% Sodium Deoxycholate, 1% Triton X-100, 0.1% SDS) containing protease inhibitors (Sigma-Aldrich). BCA assay (Pierce) was performed to measure the protein concentration, and equal amounts of protein were loaded on a SDS-PAGE gel. After SDS-PAGE, the resulting gels were transferred to PVDF membranes (Millipore) overnight. Afterwards, the gel was blocked with 5% milk in TBS (20 mM Tris, 150 mM NaCl). The primary antibodies (Bethyl Laboratories, Inc.) was incubated with the membrane overnight in 4 °C with shaking, followed by adding the secondary antibodies (Jackson Immuno Research Laboratories). Blots were washed three times for 20 m in TBS after primary and secondary antibodies.

4.2.3 Results and Discussion

AuNR Fabrication, Characterization, Cell Uptake and Cytotoxicity Study:

AuNRs with size of 25 (± 3) × 6 (± 1) nm (length × width) and aspect ratio of 4.2 were synthesized according the seedless method [49], as shown in the transmission electron microscope (TEM) in **Figure 4-6A**. The as-synthesized AuNRs were washed twice with water to remove cetyltrimethylammonium bromide (CTAB) to decrease the cytotoxicity and for the next step of surface modification. Polyethylene glycol thiol (PEG) were applied to formulate AuNRs@PEG to increase the biocompatibility [56]. For achieving integrin targeting, the PEGylated particles were further functionalized with RGD, which bind to the integrin on the surface of cancer cells and enhance the receptor-mediated endocytosis of the nanoparticles [46]. Surface modification causes red shift of UV-Vis spectra due to the change in the dielectric constant of the surrounding environment of AuNRs. The longitudinal surface plasmon resonance (SPR) band of AuNRs is 771 nm (as shown in the UV-Vis spectra in **Figure 4-6B**). After PEGylation, the SPR band red-shifts to 785 nm for AuNRs@PEG. Further red-shift to 796 nm for AuNRs@RGD was observed indicating the surface binding of RGD (**Figure 4-6B**). In addition, the zeta potentials of the AuNRs at different stages were measured to confirm the surface modifications. As shown in **Figure 4-6C**, the as-synthesized CTAB coated AuNRs has very positive surface charge of 22.9 ± 15.1 mV as the CTAB is a highly cationic surfactant. After PEG modification, the AuNRs became negatively charged (-10.2 ± 6.73 mV). The zeta potential of the AuNRs became positive again after further modification of the RGD peptides. The characterization results are consistent with the results from our and other groups, which indicates the successful conjugation of the RGD peptides to the surface of AuNRs [52, 57].

Successful internalization of AuNRs within the cells was observed as monitored by dark-field (DF) microscope (**Figure 4-6D-F**), where the brightness of the scattering light from AuNRs indicates the internalized amount. The human oral squamous cell carcinoma (HSC-3) cells were incubated with 2.5 nM of AuNRs for 24 hrs. For AuNRs@RGD, clear scattering light of AuNRs was observed while AuNRs@PEG did not show high uptake when compared to the AuNRs@RGD. The difference in uptake of these two types of AuNRs is due to the binding of RGD to the surface integrin that enhances the endocytosis of AuNRs [58]. For further confirmation, the internalization of AuNRs was also measured by UV-Vis spectra (**Figure C.8.A**) and the differential interference contrast (DIC) microscopy (**Figure C.8.B-D**). To measure the cell viability and apoptosis status, flow cytometry was used, which indicated the 2.5 nM of AuNRs@PEG and AuNRs@RGD did not affect the cell viability or cause apoptosis (**Figure 4-6G**). A NIR laser was applied for 1 min to raise the temperature of the culture media to about 42 ± 1 ^{o}C. As the temperature increased, there was no obvious change in the cell viability and no sign of apoptosis/necrosis (**Figure 4-6G-K**). In addition, that no apoptosis occurred in the cells after AuNRs incubation and slight NIR exposure, was further confirmed by our Western-blot results (**Figure 4-6L**), as BAX, an important protein that participate in initiation of apoptotic signaling [59], didn't show increase.

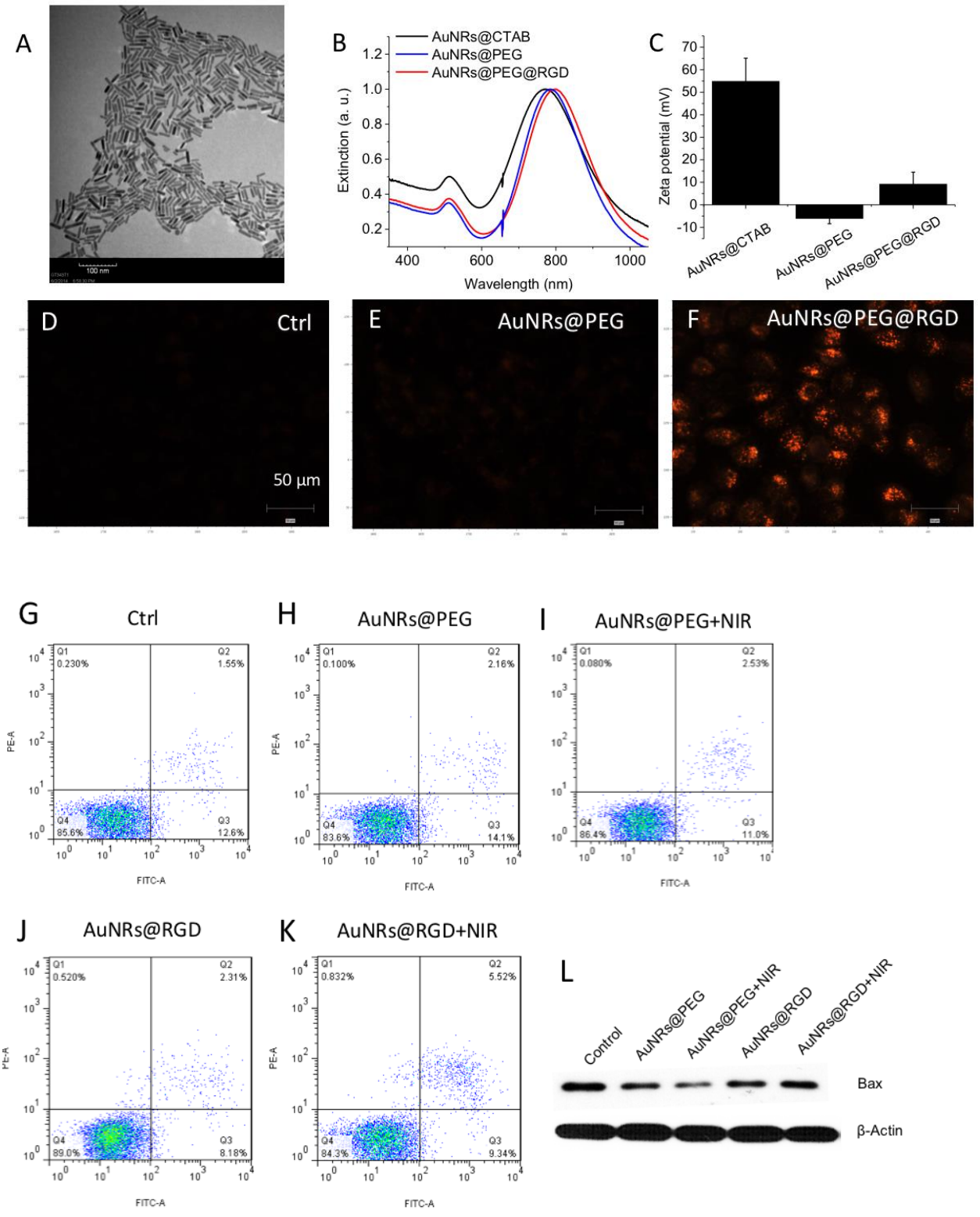

Figure 4-6. AuNRs synthesis, characterization, HSC-3 cellular uptake and cytotoxicity study

(A) Transmission electron microscopy (TEM) image of AuNRs. (B) UV-Vis spectrum of AuNRs with different surface ligands. Black: the as-synthesized AuNRs with CTAB on the surface; Blue: PEGylated AuNRs; Red: AuNRs conjugated with PEG and RGD. (C) Zeta potential shows the surface charge before/after conjugations. (D-F) Dark field image of cells without AuNRs, incubated with AuNRs@PEG or AuNRs@RGD, respectively. (G-K) Cell viability/apoptosis/necrosis assay of cells under different treatments, using flow cytometry. Q1: necrotic cells; Q2: late apoptotic cells; Q3: early apoptotic cells; Q4: viable cells. (L) Western blotting for the Bax protein after four groups of treatments.

AuNRs inhibit cancer cell migration and invasion ability

To evaluate the AuNRs effect on cancer cell migration, we conducted scratch assay [53] on the monolayers of cells that were incubated with or without AuNRs for 24 hours. After introducing a "scratch" or "wound" into a cell culture, images were captured immediately and 12 hours after the scratch. **Figure 4-7A** indicates that cells in the control group had the "wound" completely healed, while cells treated with AuNRs were not completely healed. In addition, NIR light exposure demonstrated an enhanced inhibition effect on cancer cell migration. Integrin-targeting AuNRs (AuNRs@RGD) have a greater inhibition effect than non-targeted AuNRs (AuNRs@PEG).

As mentioned above, the cell motility decreased upon the AuNR treatment. It is well known that the cell morphology change is closely related to the cell motility, which is initiated through two types of membrane protrusions: lamellipodia and filopodia. They contain a big occupancy of integrins [60] and play major roles in leading cancer cell migration and invasion [61-62]. As shown in the scheme of **Figure 4-7B**, lamellipodia are flat, sheet-like structures, while filopodia are needle-like protrusions from actin. To study the cell morphology change (lamellipodia and filopodia), differential interference contrast (DIC)

microscopy was used. The control sample exhibited a normal and extended lamellipodia and filopodia. After treating with AuNRs@RGD alone, the cell shape tended to become round after AuNRs@RGD internalization and contains less amount of lamellipodia and filopodia, compared with control. When we applied AuNRs@RGD and NIR light, the area of lamellipodia was further decreased. The morphology changes of integrin-rich lamellipodia and filopodia indicate that the integrin targeted gold nanorods with or without laser are effective in changing the cytoskeleton structures, a probable cause for the decrease in motility.

To study the molecular mechanism, we checked the expression levels of several proteins that closely associated with integrin and cell migration to examine their response after AuNRs treatment. Two important down-stream regulators of integrin, Src and ERK1/2 were found to be down-regulated with the AuNRs treatment when compared with the control (**Figure 4-7C**). Src is a critical protein which bridges between integrin and Rho signaling, which is the main regulator of cytoskeleton [63]. ERK1/2 is a mitogen-activated protein kinase, which plays a crucial role in cell migration [38, 64]. The decrease of Src and ERK1/2 indicates that targeting the surface integrin using AuNRs@RGD could block the down-stream regulators of integrin signaling [65], which contributes to the inhibition of cell migration by AuNRs. Moreover, in a further investigation of integrin-related proteins, **Figure 4-7C** showed that E-cadherin and PTEN, were up-regulated upon AuNRs treatments, which contributes to the inhibition of cancer migrations [66-69].

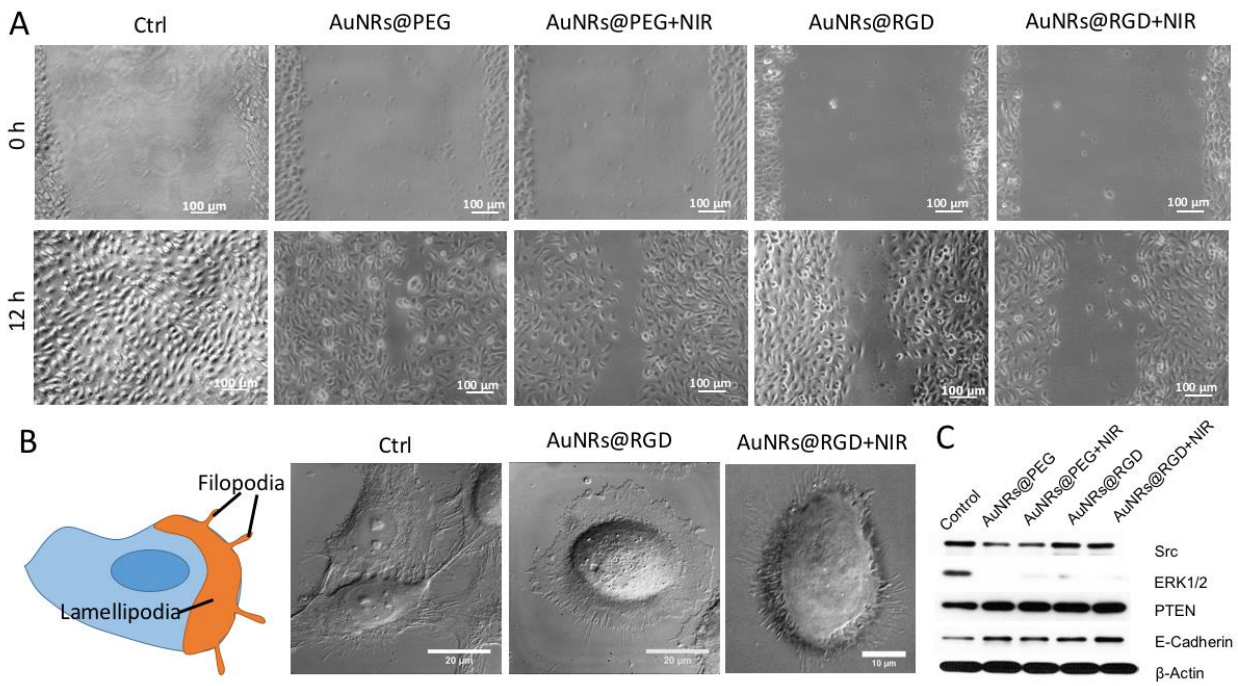

Figure 4-7. Cell shape changes upon cell movement

(A) Imaging of cell movement using scratch assay of cells incubated with AuNRs@RGD displayed arrested healing/closing of the scratch. (B) Shows the change in the cell shape using DIC images of cells before and after gold AuNRs treatments. (C) Western-blot analysis of integrin and migration related proteins in AuNRs@PEG (with or without laser) and AuNRs@RGD (with or without laser).

Proteomics analysis reveals the inhibition of migration pathways:

To gain a global view of proteome change, label-free quantitative proteomics was conducted to identify and quantify protein expression changes in HSC-3 cells after incubation with AuNRs. Proteomics results indicated a wide range of perturbations of proteins in migration-related pathways after AuNRs treatment. In this experiment, cells were lysed and proteins were then extracted, digested, and analyzed by mass spectrometry (MS). Two biological replications and three technical replications for each condition were

conducted. In total, over 4000 proteins were identified and about 1800 common proteins were quantified in four treatment groups (AuNRs@PEG, AuNRs@PEG+NIR, AuNRs@RGD, and AuNRs@RGD+NIR) **(Figure 4-9A)**. Hierarchical clustering analysis on similarity matrix of proteomics data was carried out to show the reproducibility of the experiments. The clustering analysis results **(Figure C.9. A and B)** indicate that most experiments from the control group or experimental groups were clustered together correspondingly, indicating a good reproducibility of the proteomics experiments. Differential analysis was conducted to obtain the proteins with significant changes at their expression level (**Figure C.9. C-F**). The number of up-regulated and down-regulated proteins in each group is shown in **Figure C.9. G**. Comparison of differentially expressed proteins identified in the four treatments is shown in the Venn diagram **(Figure C.9. H)**, showing the number of common and unique proteins in different groups. Expression levels of key proteins in these pathways are shown as a heatmap in **Figure 4-8B**, where a wide range of cytoskeleton proteins were observed to be affected in the four groups. Pathway analysis indicated perturbation of signaling pathways related to cell migration in all groups (**Figure 4-8C**), including cytoskeleton remodeling process, Rho GTPase signaling, integrin-mediated cell migration and invasion, *etc*. Maps of these pathways are shown in **Figure C.10**. It is worth noting that according to the pathway analysis results, AuNRs@RGD+NIR is the most effective for inhibiting cancer cell migration, as it shows the greatest significance in affecting the migration related pathways; AuNRs@RGD is more effective than AuNRs@PEG, and the NIR light increase the efficacy of the treatment (**Figure 4-8C**).

A scheme (**Figure 4-9**) was concluded from the pathway maps (**Figure C.10.**) to illustrate the change of the key protein players in the migration pathways. As shown in **Figure 4-9**, AuNRs regulate the cell migration by affecting the cytoskeleton in four main ways: 1) Rho GTPases, 2) actin, 3) microtubule, and 4) kinases related signaling pathways.

1) Rho GTPases signaling was greatly affected. Rho GTPases regulates actin cytoskeleton,[70-72] which plays an important role in cellular contractility by directly controlling the balance between myosin II and actin, and initiates the force needed for cell migration.[73-74] [75]As shown in the scheme (**Figure 4-9**), many key proteins in Rho GTPase signaling pathways were perturbed, including ROCK, MYHC, MELC, MLCP, RhoA, α-actinin, talin, etc. as shown in **Figure 4-8B**. All the four treatments applied exhibit effect for wide regulation of Rho signaling, to different extents. Among the 4 treated groups, the AuNRs@RGD+NIR group has the highest statistically significant p-value ($1.5x10^{-10}$), reflecting this group's highest efficacy in inhibiting the cancer migrations pathways (**Figure 4-8C**).
2) Actin-binding proteins were down-regulated after AuNRs incubation (**Figure 4-8B**), including alpha-actinin, talin, vinculin, *etc.* In the integrin-mediated signaling pathway, the activated integrins recruit actin-binding proteins, which include talin and vinculin, and coupled to the actin cytoskeleton [76]. Our results indicated that the connectivity between integrin and actin cytoskeleton was decreased, demonstrating the blocking effect of AuNRs on the migration pathways.
3) Microtubule-associated proteins MAP2 and MAP4 were significantly down-regulated (**Figure 4-8B** and **Figure 4-9**), indicating the rearrangement of microtubules, which is one of the most important cytoskeleton structures [77].

4) A large variety of kinases related to integrin signaling pathways were perturbed, including integrin linked kinase (ILK), NF-κB, the epidermal growth factor receptor (EGFR), caveolin, *etc* (**Figure 4-8B** and **Figure** 4-9). These proteins are closely associated with integrin regulation and cell migration [78]. It has been reported that the overexpression of ILK could promote the migration and invasion of colorectal cancer cells via NF-κB signaling [79]. In our results, the down-regulation of ILK and NF-κB exhibited a reduced cancer cell migration ability. In addition, EGFR, a surface receptor for epidermal growth factor decreased. The down regulation of EGFR was also confirmed in the Western-blot results which agrees with our proteomics results (**Figure 4-8B** and **Figure 4-9**). EGFR is regarded as an important target for anticancer therapeutics [80]. Furthermore, STAT3, which can be activated by tyrosine phosphorylation in response to the addition of EGFR [81] and can promote cell migration, was also down-regulated in all the AuNRs treated samples (**Figure 4-8D**).

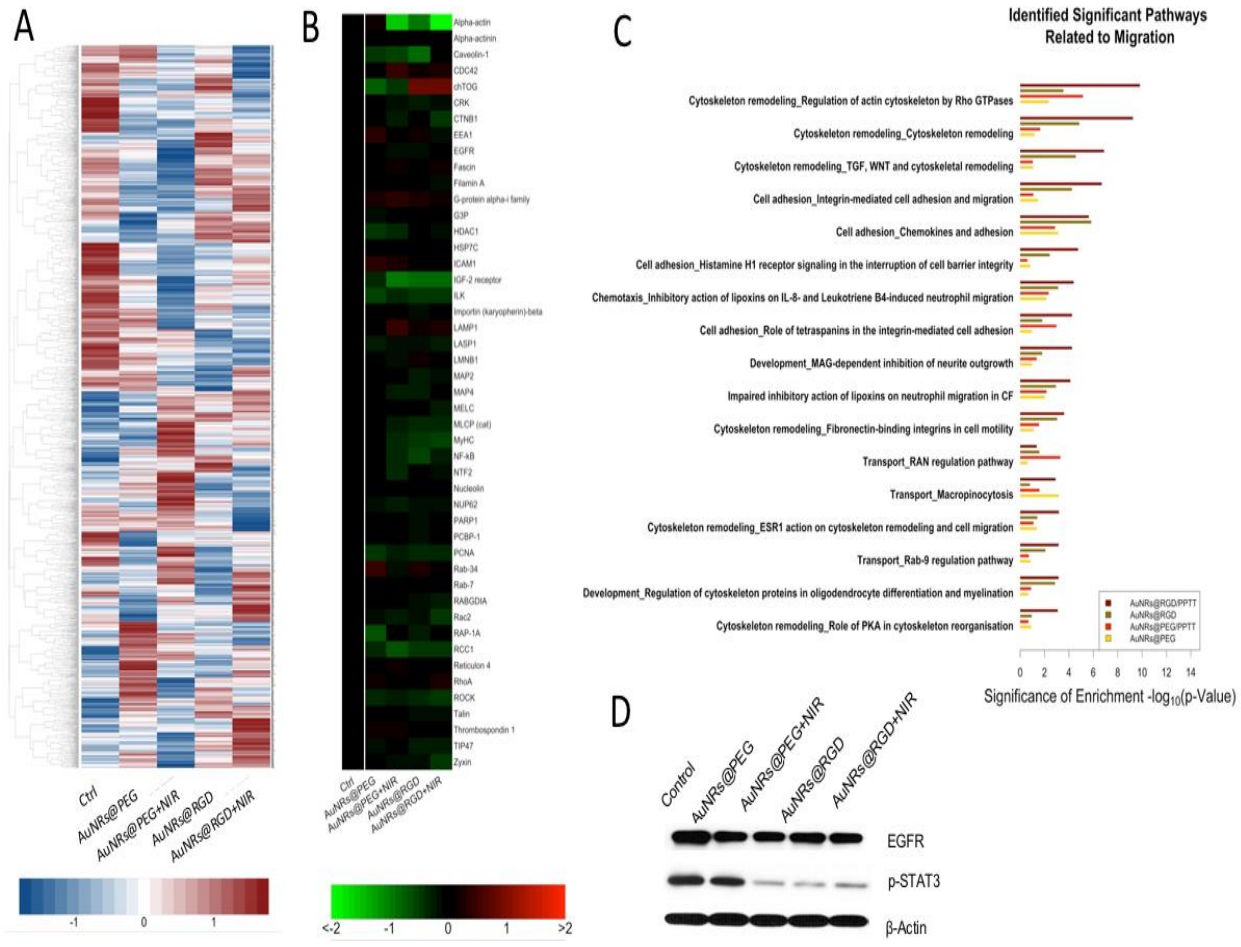

Figure 4-8. Experimental results of proteomics in the four treatment groups (AuNRs@PEG, AuNRs@PEG+NIR, AuNRs@RGD, and AuNRs@RGD+NIR)

(A) Heatmap showing the expression levels of all the quantified proteins. (B) Heatmap showing identified proteins contributing to migration inhibition. (C) Bar graph showing identified significant pathways related to migration. (D) Western-blot analysis of integrin and migration related proteins.

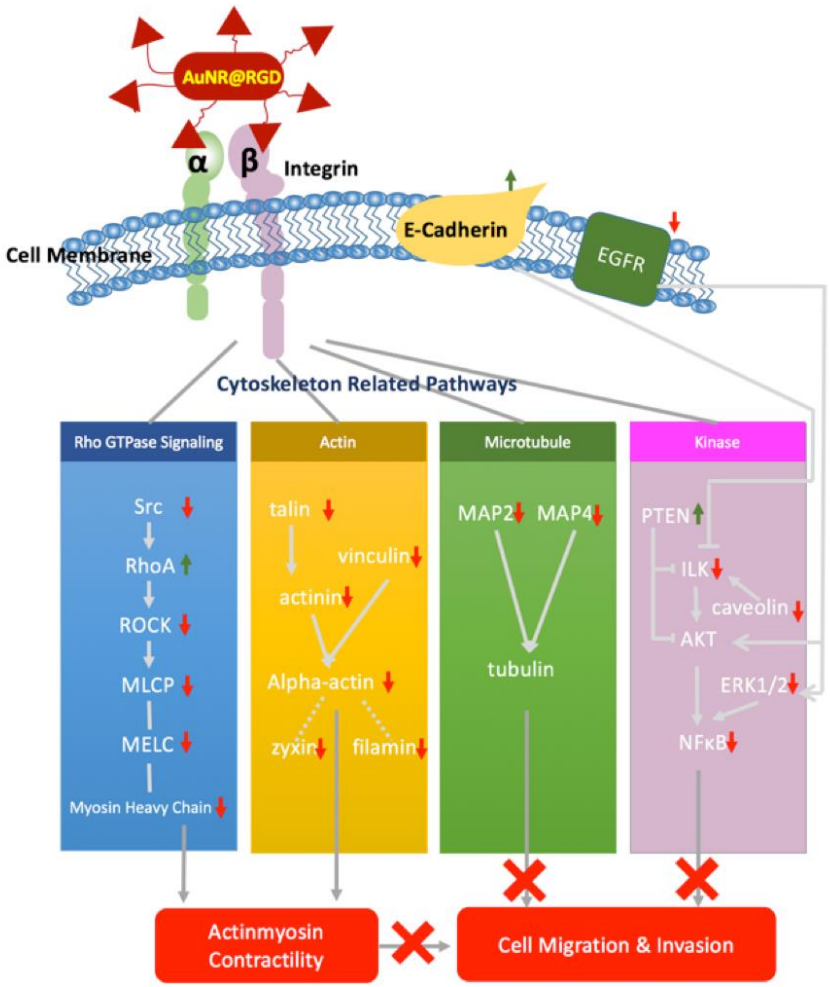

Figure 4-9 Scheme representing the mechanisms involved in inhibiting cell migration upon AuNR treatments

When the AuNRs@RGD (in red) target the alpha/beta integrins, four different cytoskeleton proteins pathways are regulated: Rho (blue), Actin (yellow), Microtubule (green), and Kinase (pink) which all affect the cell contractility and thus inhibit cell migration (shown in red at the bottom of the figure).

Current advances of nanoscience and nanomedicine enable us to fabricate "intelligent" nanomaterials that can specifically target subcellular locations of cells or cancer cells in living animals [82-83]. Our previous study has shown success in treating natural mammary gland tumors in dogs and cats using AuNRs assisted plasmonic photothermal therapy

(PPTT), where all the cases did not have cancer relapse and metastasis [37], hinting the potential effect of PPTT on inhibiting cancer metastasis. Herein, we reported that AuNRs assisted PPTT were able to greatly inhibit cancer cell migration than AuNRs alone (while the latter is also effective). Furthermore, integrins have been observed to be overexpressed in many types of cancer cells, which are closely involved in cancer cell migration because of their ability to regulate cytoskeleton proteins. In our work, targeting AuNRs to cancer cell surface protein integrins could enhance the inhibition effect on cancer cell migration, based on phenotype level results (cell migration speed and cell morphology) as well as molecular level results (Western blot and proteomics).

Cell morphology change was cytoskeleton protrusions, namely lamellipodia and filopodia, that form the leading edge for cell movement. These cytoskeleton protrusions were reduced after treating them with AuNRs@RGD. Furthermore, after applying NIR light, a greater morphological change was observed. Integrins are often found in the tips or alone in the shaft of filopodia and lamellipodia, which creates the "sticky fingers" and facilitate the migration and invasion [84-85].

The reason for this morphological change has been explored in our Western blot analysis, which indicated that the integrin related proteins were obviously affected, resulting in inhibition of cell migration pathways. As shown in **Figure 4-7C**, four integrin related proteins, Src, ERK1/2, PTEN, and E-cadherin had altered expressions. Src and ERK1/2, two important down-stream regulators of integrin have crucial roles in cytoskeleton regulation, were found to be down-regulated upon the AuNRs treatment. The decrease of

Src and ERK1/2 is mainly due to the targeting of the surface integrin using AuNRs@RGD, which could block the down-stream regulators of integrin signaling. Similar effects regarding nanoparticles that could target and block the function of proteins were previously reported [86]. Moreover, two proteins, E-cadherin and PTEN, were up-regulated upon the AuNRs treatments. Recent discoveries have shown that E-cadherins have cross-talk with integrin signaling [87] that alter cytoskeletal organization [66]. Loss of E-cadherin is often associated with tumor invasive progressing [67]. In addition, the tumor suppressor protein PTEN has been reported to inhibit integrin-mediated cell migration, spreading, and adhesion [68-69]. Our results indicated the up-regulation of E-cadherins and PTEN, which contributes to the inhibition of cancer migrations, and down-regulation of MAPs, similar to previous reports 88. The above results indicate that integrin-targeting AuNRs and NIR light exposure possibly change the cytoskeleton structure and shrink lamellipodia and filopodia thus impairing cell migration.

Moreover, for obtain a systematic understanding the AuNRs' inhibition effect on cancer cell migration, proteomics experiment was performed. A scheme (**Figure 4-9)** concluded from the pathway maps illustrates the changes of four groups of proteins in migration pathways. Among these proteins, the most important is those participating in actomyosin contraction, which create the intracellular tension [89]. Actomyosin contraction is generated by active myosin II binding to actin filaments (thus termed actomyosin). Rho GTPases family is a predominant regulator in actomyosin contraction by phosphorylating the myosin light chain, promoting the cross-linking of actin by myosin, and enhancing actomyosin contact [90]. Integrin signaling networks can initiate the regulation of the Rho GTPases through Src [74, 91], and then to Rho-associated kinase (ROCK, a

serine/threonine kinase), a downstream effector of Rho which plays a major role in the rearrangements of the actomyosin cytoskeleton [92-93]. Myosin light-chain phosphorylation (MLCP) is regulated by ROCK, which is necessary for the formation and maintenance of stress fibers and form a modulatory apparatus for acto-myosin contraction through modulation of myosin [92]. In our results, the expression levels of many key proteins (such as Src, ROCK, MELC, MLCP and MyHC) were changed (**Figure 4-9**), indicating the disruption of actomyosin contraction, which might prevent the traction force from generating during the migration process.

The effect of AuNRs on focal adhesion through targeting integrin was also observed, as the expression levels of the associated proteins were altered, including alpha-actinin, talin, vinculin, filamin, *etc*. Focal adhesions are structures that contains integrin and other associated proteins and form links between the intracellular actin cytoskeleton and ECM [94]. The binding of talin to integrin is regarded as a common final step of the cell signaling cascades that control integrin activation [95]. In addition, higher concentrations of talin can be observed in regions where focal adhesion complexes are formed96. Furthermore, vinculin links actin filaments to ECM through talin and integrin [97], and filamin is widely engaged in the integrin-actin cytoskeleton interaction [98]. The observed down regulation of these focal adhesion complex-associated proteins indicated the integrin-targeting nanoparticles could negatively affect the connection between integrin and the cytoskeleton.

4.2.4 Conclusion and Future Outlook

Metastasis is the main cause of cancer-related deaths. However, the current clinical treatments for anti-metastasis is not effective. This work aim at developing a novel strategy to inhibit cancer cell migration using gold nanorods. The surface functioned gold nanorods target integrins, which greatly affect the down-stream cytoskeleton proteins and impair cancer cell migration. When we apply the near-infrared light, the heat generated could further inhibit migration by remodeling the cytoskeleton. This work provides a new strategy for combating cancer metastasis.

The body deposition of metallic nanoparticles raises significant concerns regarding their long-term safety. While small nanoparticles (hydrodynamic diameter < 5.5 nm) can be excreted efficiently through urinary system, [99] bigger nanoparticles (> 18 nm in diameter) accumulate in organs such as the liver and spleen [100] and decrease slowly 101. Our results showed that when compared to the non-targeted AuNRs, the integrin-targeted AuNRs showed a larger enhanced effect on migration inhibition with a nanoparticle concentration at the nanomolar scale (1000x lower than the literature values [19, 21, 23]. The minimized amount of gold nanoparticles we applied is beneficial to decrease the nanoparticles' long-term effects. Future work will be focused on testing the effect of gold nanoparticles on preventing and treating cancer metastasis in animals.

4.2.5 References

1. Ali, M. R. K., Wu, Y., Han, T., Xiao, H., Chen, K., Tang, Y., Fang, N., Wu, R., El-Sayed, M. A. (2017) Targeting Cancer Cell Integrins Using Gold Nanorods in

Photothermal Therapy Inhibits Its Migration by Affecting Cytoskeleton Proteins, PNAS second revision.

2. Chaffer, C. L.; Weinberg, R. A., (2011) A Perspective on Cancer Cell Metastasis. *Science*, *331* (6024), 1559-1564.

3. Talmadge, J. E.; Fidler, I. J., (2010) AACR Centennial Series: The Biology of Cancer Metastasis: Historical Perspective. *Cancer Research*, *70* (14), 5649-5669.

4. Fidler, I. J., (2003) Timeline - The pathogenesis of cancer metastasis: the 'seed and soil' hypothesis revisited. *Nature Reviews Cancer*, *3* (6), 453-458.

5. Fife, C. M.; McCarroll, J. A.; Kavallaris, M., (2014) Movers and shakers: cell cytoskeleton in cancer metastasis. *British Journal of Pharmacology*, *171* (24), 5507-5523.

6. Hanahan, D.; Weinberg, R. A., (2011) Hallmarks of Cancer: The Next Generation. *Cell*, *144* (5), 646-674.

7. Dumontet, C.; Jordan, M. A., (2010) Microtubule-binding agents: a dynamic field of cancer therapeutics. *Nat Rev Drug Discov*, *9* (10), 790-803.

8. Stehn, J. R.; Haass, N. K.; Bonello, T.; Desouza, M.; Kottyan, G.; Treutlein, H.; Zeng, J.; Nascimento, P. R. B. B.; Sequeira, V. B.; Butler, T. L.; Allanson, M.; Fath, T.; Hill, T. A.; McCluskey, A.; Schevzov, G.; Palmer, S. J.; Hardeman, E. C.; Winlaw, D.; Reeve, V. E.; Dixon, I.; Weninger, W.; Cripe, T. P.; Gunning, P. W., (2013) A Novel Class of Anticancer Compounds Targets the Actin Cytoskeleton in Tumor Cells. *Cancer Research*, *73* (16), 5169-5182.

9. Patel, R. A.; Liu, Y.; Wang, B.; Li, R.; Sebti, S. M., (2014) Identification of novel ROCK inhibitors with anti-migratory and anti-invasive activities. *Oncogene, 33* (5), 550-555.

10. Prudent, R.; Vassal-Stermann, E.; Nguyen, C. H.; Pillet, C.; Martinez, A.; Prunier, C.; Barette, C.; Soleilhac, E.; Filhol, O.; Beghin, A.; Valdameri, G.; Honore, S.; Aci-Seche, S.; Grierson, D.; Antonipillai, J.; Li, R.; Di Pietro, A.; Dumontet, C.; Braguer, D.; Florent, J. C.; Knapp, S.; Bernard, O.; Lafanechere, L., (2012) Pharmacological Inhibition of LIM Kinase Stabilizes Microtubules and Inhibits Neoplastic Growth. *Cancer Research, 72* (17), 4429-4439.

11. Banerjee, S.; Hwang, D. J.; Li, W.; Miller, D. D., (2016) Current Advances of Tubulin Inhibitors in Nanoparticle Drug Delivery and Vascular Disruption/Angiogenesis. *Molecules, 21* (11).

12. Morgillo, F.; Lee, H. Y., (2005) Resistance to epidermal growth factor receptor-targeted therapy. *Drug Resist Update, 8* (5), 298-310.

13. Holohan, C.; Van Schaeybroeck, S.; Longley, D. B.; Johnston, P. G., (2013) Cancer drug resistance: an evolving paradigm. *Nature Reviews Cancer, 13* (10), 714-726.

14. Murphy, C. J.; Gole, A. M.; Stone, J. W.; Sisco, P. N.; Alkilany, A. M.; Goldsmith, E. C.; Baxter, S. C., (2008) Gold Nanoparticles in Biology: Beyond Toxicity to Cellular Imaging. *Accounts Chem Res, 41* (12), 1721-1730.

15. Moghimi, S. M.; Hunter, A. C.; Murray, J. C., (2005) Nanomedicine: current status and future prospects. *Faseb J, 19* (3), 311-330.

16. Petros, R. A.; DeSimone, J. M., (2010) Strategies in the design of nanoparticles for therapeutic applications. *Nat Rev Drug Discov, 9* (8), 615-627.

17. Hirsch, L. R.; Stafford, R. J.; Bankson, J. A.; Sershen, S. R.; Rivera, B.; Price, R. E.; Hazle, J. D.; Halas, N. J.; West, J. L., (2003) Nanoshell-mediated near-infrared thermal therapy of tumors under magnetic resonance guidance. *Proceedings of the National Academy of Sciences of the United States of America*, *100* (23), 13549-13554.

18. Peer, D.; Karp, J. M.; Hong, S.; FaroKHzad, O. C.; Margalit, R.; Langer, R., (2007) Nanocarriers as an emerging platform for cancer therapy. *Nat Nanotechnol, 2* (12), 751-760.

19. Tay, C. Y.; Cai, P. Q.; Setyawati, M. I.; Fang, W. R.; Tan, L. P.; Hong, C. H. L.; Chen, X. D.; Leong, D. T., (2014) Nanoparticles Strengthen Intracellular Tension and Retard Cellular Migration. *Nano Letters*, *14* (1), 83-88.

20. Yang, J. A.; Phan, H. T.; Vaidya, S.; Murphy, C. J., (2013) Nanovacuums: Nanoparticle Uptake and Differential Cellular Migration on a Carpet of Nanoparticles. *Nano Letters*, *13* (5), 2295-2302.

21. Zhou, T.; Yu, M. F.; Zhang, B.; Wang, L. M.; Wu, X. C.; Zhou, H. J.; Du, Y. P.; Hao, J. F.; Tu, Y. P.; Chen, C. Y.; Wei, T. T., (2014) Inhibition of Cancer Cell Migration by Gold Nanorods: Molecular Mechanisms and Implications for Cancer Therapy. *Advanced Functional Materials, 24* (44), 6922-6932.

22. Pan, Y. L.; Wu, Q.; Qin, L.; Cai, J. Y.; Du, B., (2014) Gold Nanoparticles Inhibit VEGF(165)-Induced Migration and Tube Formation of Endothelial Cells via the Akt Pathway. *Biomed Research International*.

23. Soenen, S. J. H.; Nuytten, N.; De Meyer, S. F.; De Smedt, S. C.; De Cuyper, M., (2010) High Intracellular Iron Oxide Nanoparticle Concentrations Affect Cellular Cytoskeleton and Focal Adhesion Kinase-Mediated Signaling. *Small*, *6* (7), 832-842.

24. Yildirimer, L.; Thanh, N. T. K.; Loizidou, M.; Seifalian, A. M., (2011) Toxicology and clinical potential of nanoparticles. *Nano Today*, *6* (6), 585-607.

25. Lin, W. S.; Huang, Y. W.; Zhou, X. D.; Ma, Y. F., (2006) In vitro toxicity of silica nanoparticles in human lung cancer cells. *Toxicology and Applied Pharmacology*, *217* (3), 252-259.

26. Pan, Z.; Lee, W.; Slutsky, L.; Clark, R. A. F.; Pernodet, N.; Rafailovich, M. H., (2009) Adverse Effects of Titanium Dioxide Nanoparticles on Human Dermal Fibroblasts and How to Protect Cells. *Small*, *5* (4), 511-520.

27. Ali, H. R.; Ali, M. R.; Wu, Y.; Selim, S. A.; Abdelaal, H. F.; Nasr, E. A.; El-Sayed, M. A., (2016) Gold Nanorods as Drug Delivery Vehicles for Rifampicin Greatly Improve the Efficacy of Combating Mycobacterium tuberculosis with Good Biocompatibility with the Host Cells. *Bioconjugate Chemistry*, *27* (10), 2486-2492.

28. Wang, N.; Zhao, Z.; Lv, Y.; Fan, H.; Bai, H.; Meng, H.; Long, Y.; Fu, T.; Zhang, X.; Tan, W., (2014) Gold nanorod-photosensitizer conjugate with extracellular pH-driven tumor targeting ability for photothermal/photodynamic therapy. *Nano Research*, *7* (9), 1291-1301.

29. Wang, J.; Zhu, G.; You, M.; Song, E.; Shukoor, M. I.; Zhang, K.; Altman, M. B.; Chen, Y.; Zhu, Z.; Huang, C. Z.; Tan, W., (2012) Assembly of Aptamer Switch Probes and

Photosensitizer on Gold Nanorods for Targeted Photothermal and Photodynamic Cancer Therapy. *ACS Nano*, *6* (6), 5070-5077.

30. Ali, M. R.; Ali, H. R.; Rankin, C. R.; El-Sayed, M. A., (2016) Targeting heat shock protein 70 using gold nanorods enhances cancer cell apoptosis in low dose plasmonic photothermal therapy. *Biomaterials*, *102*, 1-8.

31. Sugimoto, H.; Chen, T.; Wang, R.; Fujii, M.; Reinhard, B. M.; Dal Negro, L., (2015) Plasmon-Enhanced Emission Rate of Silicon Nanocrystals in Gold Nanorod Composites. *ACS Photonics*, *2* (9), 1298-1305.

32. Parrotta, L.; Faleri, C.; Cresti, M.; Cai, G., (2016) Heat stress affects the cytoskeleton and the delivery of sucrose synthase in tobacco pollen tubes. *Planta*, *243* (1), 43-63.

33. Coakley, W. T., Hyperthermia effects on the cytoskeleton and on cell morphology. (1987) *Symposia of the Society for Experimental Biology*, *41*, 187-211.

34. Gavrilova, L. P.; Korpacheva, I. I.; Semushina, S. G.; Yashin, V. A., (2013) Heat shock induces simultaneous rearrangements of all known cytoskeletal filaments in normal interphase fibroblasts. *Cell and Tissue Biology*, *7* (1), 54-63.

35. Dickerson, E. B.; Dreaden, E. C.; Huang, X. H.; El-Sayed, I. H.; Chu, H. H.; Pushpanketh, S.; McDonald, J. F.; El-Sayed, M. A., (2008) Gold nanorod assisted near-infrared plasmonic photothermal therapy (PPTT) of squamous cell carcinoma in mice. *Cancer Letters*, *269* (1), 57-66.

36. Huang, X. H.; El-Sayed, I. H.; Qian, W.; El-Sayed, M. A., (2006) Cancer cell imaging and photothermal therapy in the near-infrared region by using gold nanorods. *Journal of the American Chemical Society, 128* (6), 2115-2120.

37. Ali, M. R.; Ibrahim, I. M.; Ali, H. R.; Selim, S. A.; El-Sayed, M. A., (2016) Treatment of natural mammary gland tumors in canines and felines using gold nanorods-assisted plasmonic photothermal therapy to induce tumor apoptosis. *International Journal of Nanomedicine, 11*, 4849.

38. Hood, J. D.; Cheresh, D. A., (2002) Role of integrins in cell invasion and migration. *Nature Reviews Cancer, 2* (2), 91-+.

39. DeMali, K. A.; Wennerberg, K.; Burridge, K., (2003) Integrin signaling to the actin cytoskeleton. *Current opinion in cell biology, 15* (5), 572-82.

40. Ridley, A. J.; Schwartz, M. A.; Burridge, K.; Firtel, R. A.; Ginsberg, M. H.; Borisy, G.; Parsons, J. T.; Horwitz, A. R., (2003) Cell migration: Integrating signals from front to back. *Science, 302* (5651), 1704-1709.

41. Howe, A.; Aplin, A. E.; Alahari, S. K.; Juliano, R. L., (1998) Integrin signaling and cell growth control. *Curr Opin Cell Biol, 10* (2), 220-231.

42. Chattopadhyay, N.; Wang, Z.; Ashman, L. K.; Brady-Kalnay, S. M.; Kreidberg, J. A., (2003) α3β1 integrin–CD151, a component of the cadherin–catenin complex, regulates PTPμ expression and cell–cell adhesion. *The Journal of Cell Biology, 163* (6), 1351-1362.

43. Zhang, F.; Tom, C. C.; Kugler, M. C.; Ching, T. T.; Kreidberg, J. A.; Wei, Y.; Chapman, H. A., (2003) Distinct ligand binding sites in integrin alpha3beta1 regulate matrix adhesion and cell-cell contact. *J Cell Biol*, *163* (1), 177-88.

44. Feldinghabermann, B.; Mueller, B. M.; Romerdahl, C. A.; Cheresh, D. A., (1992) Involvement of Integrin Alpha-V Gene-Expression in Human-Melanoma Tumorigenicity. *J Clin Invest*, *89* (6), 2018-2022.

45. Filardo, E. J.; Brooks, P. C.; Deming, S. L.; Damsky, C.; Cheresh, D. A., (1995) Requirement of the Npxy Motif in the Integrin Beta-3 Subunit Cytoplasmic Tail for Melanoma Cell-Migration in-Vitro and in-Vivo. *J Cell Biol*, *130* (2), 441-450.

46. Ruoslahti, E.; Pierschbacher, M. D., (1986) Arg-Gly-Asp: A versatile cell recognition signal. *Cell 44*, 517-518.

47. Ruoslahti, E., (1996) RGD and other recognition sequences for integrins. *Annual Review of Cell and Developmental Biology*, *12*, 697-715.

48. Humphries, J. D.; Byron, A.; Humphries, M. J., (2006) Integrin ligands at a glance. *Journal of cell science*, *119* (19), 3901-3903.

49. Ali, M. R. K.; Snyder, B.; El-Sayed, M. A., (2012) Synthesis and Optical Properties of Small Au Nanorods Using a Seedless Growth Technique. *Langmuir*, *28* (25), 9807-9815.

50. Wu, Y.; Wang, F. J.; Liu, Z. Y.; Qin, H. Q.; Song, C. X.; Huang, J. F.; Bian, Y. Y.; Wei, X. L.; Dong, J.; Zou, H. F., (2014) Five-plex isotope dimethyl labeling for quantitative proteomics. *Chemical Communications*, *50* (14), 1708-1710.

51. Choudhary, C.; Kumar, C.; Gnad, F.; Nielsen, M. L.; Rehman, M.; Walther, T. C.; Olsen, J. V.; Mann, M., (2009) Lysine acetylation targets protein complexes and co-regulates major cellular functions. *Science, 325* (5942), 834-40.

52. Ali, M. R. K.; Wu, Y.; Han, T.; Zang, X.; Xiao, H.; Tang, Y.; Wu, R.; Fernandez, F. M.; El-Sayed, M. A., (2016) Simultaneous Time-dependent Surface Enhanced Raman Spectroscopy, Metabolomics and Proteomics Reveal Cancer Cell Death Mechanisms Associated with Au-Nanorod Photo-thermal Therapy. *Journal of the American Chemical Society*. 138, 15434–15442.

53. Liang, C. C.; Park, A. Y.; Guan, J. L., (2007) In vitro scratch assay: a convenient and inexpensive method for analysis of cell migration in vitro. *Nature protocols, 2* (2), 329-333.

54. Mecham, B. H.; Nelson, P. S.; Storey, J. D., (2010) Supervised normalization of microarrays. *Bioinformatics, 26* (10), 1308-1315.

55. R Core Team (2016) *R: A Language and Environment for Statistical Computing*, R Foundation for Statistical Computing.

56. Prencipe, G.; Tabakman, S. M.; Welsher, K.; Liu, Z.; Goodwin, A. P.; Zhang, L.; Henry, J.; Dai, H., (2009) PEG Branched Polymer for Functionalization of Nanomaterials with Ultralong Blood Circulation. *Journal of the American Chemical Society*, *131* (13), 4783-4787.

57. Kang, B.; Austin, L. A.; El-Sayed, M. A., (2014) Observing real-time molecular event dynamics of apoptosis in living cancer cells using nuclear-targeted plasmonically enhanced Raman nanoprobes. *ACS Nano, 8* (5), 4883-92.

58. Kim, Y.-H.; Jeon, J.; Hong, S. H.; Rhim, W.-K.; Lee, Y.-S.; Youn, H.; Chung, J.-K.; Lee, M. C.; Lee, D. S.; Kang, K. W.; Nam, J.-M., (2011) Tumor Targeting and Imaging Using Cyclic RGD-PEGylated Gold Nanoparticle Probes with Directly Conjugated Iodine-125. *Small*, *7* (14), 2052-2060.

59. Elmore, S., (2007) Apoptosis: a review of programmed cell death. *Toxicologic pathology*, *35* (4), 495-516.

60. Guillou, H.; Depraz-Depland, A.; Planus, E.; Vianaya, B.; Chaussy, J.; Grichine, A.; Albiges-Rizo, C.; Block, M. R., (2008) Lamellipodia nucleation by filopodia depends on integrin occupancy and downstream Rac1 signaling. *Experimental Cell Research*, *314* (3), 478-488.

61. Lauffenburger, D. A.; Horwitz, A. F., (1996) Cell migration: A physically integrated molecular process. *Cell*, *84* (3), 359-369.

62. Yamaguchi, H.; Condeelis, J., (2007) Regulation of the actin cytoskeleton in cancer cell migration and invasion. *Biochimica Et Biophysica Acta-Molecular Cell Research*, *1773* (5), 642-652.

63. Arthur, W. T.; Petch, L. A.; Burridge, K., (2000) Integrin engagement suppresses RhoA activity via a c-Src-dependent mechanism. *Curr Biol*, *10* (12), 719-22.

64. Huang, C.; Jacobson, K.; Schaller, M. D., (2004) MAP kinases and cell migration. *Journal of cell science*, *117* (20), 4619-4628.

65. Chen, P. S.; Wang, M. Y.; Wu, S. N.; Su, J. L.; Hong, C. C.; Chuang, S. E.; Chen, M. W.; Hua, K. T.; Wu, Y. L.; Cha, S. T.; Babu, M. S.; Chen, C. N.; Lee, P. H.; Chang, K.

J.; Kuo, M. L., (2007) CTGF enhances the motility of breast cancer cells via an integrin-alpha v beta 3-ERK1/2-dependent S100A4-upregulated pathway. *Journal of cell science, 120* (12), 2053-2065.

66. Chen, A.; Beetham, H.; Black, M. A.; Priya, R.; Telford, B. J.; Guest, J.; Wiggins, G. A.; Godwin, T. D.; Yap, A. S.; Guilford, P. J., (2014) E-cadherin loss alters cytoskeletal organization and adhesion in non-malignant breast cells but is insufficient to induce an epithelial-mesenchymal transition. *BMC Cancer*, *14*, 552.

67. Onder, T. T.; Gupta, P. B.; Mani, S. A.; Yang, J.; Lander, E. S.; Weinberg, R. A., (2008) Loss of E-cadherin promotes metastasis via multiple downstream transcriptional pathways. *Cancer Res*, *68*, 3645-54.

68. Tamura, M.; Gu, J.; Matsumoto, K.; Aota, S.; Parsons, R.; Yamada, K. M., (1998) Inhibition of cell migration, spreading, and focal adhesions by tumor suppressor PTEN. *Science*, *280*, 1614-7.

69. Cai, D.; Chen, S. C.; Prasad, M.; He, L.; Wang, X.; Choesmel-Cadamuro, V.; Sawyer, J. K.; Danuser, G.; Montell, D. J., (2014) Mechanical feedback through E-cadherin promotes direction sensing during collective cell migration. *Cell*, *157*, 1146-59.

70. Etienne-Manneville, S.; Hall, A., (2002) Rho GTPases in cell biology. *Nature*, *420*, 629-35.

71. Ridley, A. J.; Hall, A., (1992) The small GTP-binding protein rho regulates the assembly of focal adhesions and actin stress fibers in response to growth factors. *Cell*, *70*, 389-99.

72. Nobes, C. D.; Hall, A., (1995) Rho, rac, and cdc42 GTPases regulate the assembly of multimolecular focal complexes associated with actin stress fibers, lamellipodia, and filopodia. *Cell*, *81*, 53-62.

73. Friedl, P.; Wolf, K., (2003) Tumour-cell invasion and migration: diversity and escape mechanisms. *Nat Rev Cancer*, *3*, 362-74.

74. Parsons, J. T.; Horwitz, A. R.; Schwartz, M. A., (2010) Cell adhesion: integrating cytoskeletal dynamics and cellular tension. *Nat Rev Mol Cell Biol*, *11*, 633-43.

75. Heasman, S. J.; Ridley, A. J., (2008) Mammalian Rho GTPases: new insights into their functions from in vivo studies. *Nat Rev Mol Cell Biol*, *9*, 690-701.

76. Friedl, P.; Gilmour, D., (2009) Collective cell migration in morphogenesis, regeneration and cancer. *Nat Rev Mol Cell Biol*, *10*, 445-57.

77. Takemura, R.; Okabe, S.; Umeyama, T.; Kanai, Y.; Cowan, N. J.; Hirokawa, N., (1992) Increased microtubule stability and alpha tubulin acetylation in cells transfected with microtubule-associated proteins MAP1B, MAP2 or tau. *Journal of cell science*, *103*, 953-64.

78. Bock-Marquette, I.; Saxena, A.; White, M. D.; DiMaio, J. M.; Srivastava, D., (2004) Thymosin beta 4 activates integrin-linked kinase and promotes cardiac cell migration, survival and cardiac repair. *Nature*, *432*, 466-472.

79. Yan, Z.; Yin, H.; Wang, R.; Wu, D.; Sun, W.; Liu, B.; Su, Q., (2014) Overexpression of integrin-linked kinase (ILK) promotes migration and invasion of

colorectal cancer cells by inducing epithelial–mesenchymal transition via NF-κB signaling. *Acta Histochemica*, *116*, 527-533.

80. Ciardiello, F.; Tortora, G., Epidermal growth factor receptor (EGFR) as a target in cancer therapy: understanding the role of receptor expression and other molecular determinants that could influence the response to anti-EGFR drugs. *European Journal of Cancer 39* (10), 1348-1354.

81. Zhong, Z.; Wen, Z.; Darnell, J. E., Jr., Stat3: a STAT family member activated by tyrosine phosphorylation in response to epidermal growth factor and interleukin-6. *Science* 1994, *264* (5155), 95-8.

82. Qian, X. M.; Peng, X. H.; Ansari, D. O.; Yin-Goen, Q.; Chen, G. Z.; Shin, D. M.; Yang, L.; Young, A. N.; Wang, M. D.; Nie, S. M., In vivo tumor targeting and spectroscopic detection with surface-enhanced Raman nanoparticle tags. *Nature Biotechnology* 2008, *26* (1), 83-90.

83. El-Sayed, I. H.; Huang, X. H.; El-Sayed, M. A., Surface plasmon resonance scattering and absorption of anti-EGFR antibody conjugated gold nanoparticles in cancer diagnostics: Applications in oral cancer. *Nano Letters* 2005, *5* (5), 829-834.

84. Galbraith, C. G.; Yamada, K. M.; Galbraith, J. A., Polymerizing actin fibers position integrins primed to probe for adhesion sites. *Science* 2007, *315* (5814), 992-995.

85. Mattila, P. K.; Lappalainen, P., Filopodia: molecular architecture and cellular functions. *Nature Reviews Molecular Cell Biology* 2008, *9* (6), 446-454.

86. Yoo, S. I.; Yang, M.; Brender, J. R.; Subramanian, V.; Sun, K.; Joo, N. E.; Jeong, S. H.; Ramamoorthy, A.; Kotov, N. A., Inhibition of Amyloid Peptide Fibrillation by Inorganic Nanoparticles: Functional Similarities with Proteins. *Angewandte Chemie-International Edition* 2011, *50* (22), 5110-5115.

87. Canel, M.; Serrels, A.; Frame, M. C.; Brunton, V. G., (2003) E-cadherin-integrin crosstalk in cancer invasion and metastasis. *Journal of cell science* 2013, *126*, 393-401.

88. Gu, J. G.; Tamura, M.; Yamada, K. M., (1998) Tumor suppressor PTEN inhibits integrin- and growth factor-mediated mitogen-activated protein (MAP) kinase signaling pathways. *Journal of Cell Biology*, *143*, 1375-1383.

89. Beningo, K. A.; Hamao, K.; Dembo, M.; Wang, Y. L.; Hosoya, H., (2006) Traction forces of fibroblasts are regulated by the Rho-dependent kinase but not by the myosin light chain kinase. *Archives of Biochemistry and Biophysics*, *456*, 224-231.

90. Jaffe, A. B.; Hall, A., (2005) Rho GTPases: biochemistry and biology. *Annu Rev Cell Dev Biol*, *21*, 247-69.

91. Schwartz, M. A.; Shattil, S. J., (2000) Signaling networks linking integrins and rho family GTPases. *Trends Biochem Sci*, *25* (8), 388-91.

92. Amano, M.; Nakayama, M.; Kaibuchi, K., (2010) Rho-kinase/ROCK: A key regulator of the cytoskeleton and cell polarity. *Cytoskeleton (Hoboken)*, *67* (9), 545-54.

93. Matsui, T.; Amano, M.; Yamamoto, T.; Chihara, K.; Nakafuku, M.; Ito, M.; Nakano, T.; Okawa, K.; Iwamatsu, A.; Kaibuchi, K., (1996) Rho-associated kinase, a novel

serine/threonine kinase, as a putative target for small GTP binding protein Rho. *EMBO J*, *15* (9), 2208-16.

94. Kanchanawong, P.; Shtengel, G.; Pasapera, A. M.; Ramko, E. B.; Davidson, M. W.; Hess, H. F.; Waterman, C. M., (2010) Nanoscale architecture of integrin-based cell adhesions. *Nature*, *468* (7323), 580-U262.

95. Tadokoro, S.; Shattil, S. J.; Eto, K.; Tai, V.; Liddington, R. C.; de Pereda, J. M.; Ginsberg, M. H.; Calderwood, D. A., (2003) Talin binding to integrin beta tails: a final common step in integrin activation. *Science*, *302* (5642), 103-6.

96. Parri, M.; Chiarugi, P., (2010) Rac and Rho GTPases in cancer cell motility control. *Cell Commun Signal*, *8*, 23.

97. Case, L. B.; Baird, M. A.; Shtengel, G.; Campbell, S. L.; Hess, H. F.; Davidson, M. W.; Waterman, C. M., (2015) Molecular mechanism of vinculin activation and nanoscale spatial organization in focal adhesions. *Nat Cell Biol*, *17* (7), 880-892.

98. van der Flier, A.; Sonnenberg, A., (2001) Structural and functional aspects of filamins. *Biochimica et Biophysica Acta (BBA) - Molecular Cell Research*, *1538* (2–3), 99-117.

99. Choi, H. S.; Liu, W.; Misra, P.; Tanaka, E.; Zimmer, J. P.; Ipe, B. I.; Bawendi, M. G.; Frangioni, J. V., (2007) Renal clearance of quantum dots. *Nature Biotechnology*, *25* (10), 1165-1170.

100. Semmler-Behnke, M.; Kreyling, W. G.; Lipka, J.; Fertsch, S.; Wenk, A.; Takenaka, S.; Schmid, G.; Brandau, W., (2008) Biodistribution of 1.4-and 18-nm Gold Particles in Rats. *Small*, *4* (12), 2108-2111.

101. Sadauskas, E.; Danscher, G.; Stoltenberg, M.; Vogel, U.; Larsen, A.; Wallin, H., (2009) Protracted elimination of gold nanoparticles from mouse liver. *Nanomedicine-Nanotechnology Biology and Medicine*, *5* (2), 162-169.

PUBLICATIONS

[1] **Ali, M. R. K.;** Kassam K.; Wu, Y.; El-Sayed, M. A; Fabrication and Charactrization of Gold Nanorods, Especially Second Window Near IR. **Under preparation**

[2] **Ali, M. R. K.;** Chapman S.; Wu, Y.; El-Sayed, M. A; The Synthesis and Optical Properties of Different Sizes of Gold nanobones (AuNBs) and their self-assembly in water. **Under preparation**

[3] **Ali, M. R. K,** Farghaly, H.; Ali, H.R, Selim, S.A, El-Sayed, M.A. Plasmonic Photothermal therapy decrease bleeding **under preparation**

[4] Peng, X.; Mackey, M.: **Ali, M. R. K.;** Rahman, M. A.; Zhao, Z; Chen, G.Z.; Tang, R.; Shin, D.M.; El-Sayed. M.A.; The Long-Term Effects of Gold Nanorods in a Mouse Model: Circulation, Biodistribution, and Toxicity**. under preparation**

[5] **Ali, M. R. K.;** Wu, Y.; Han, T.; Zang, X.; Xiao, H.; Tang, Y.; Wu, R.; El-Sayed, M. A; Targeting Cancer Cell Integrins Using Gold Nanorods in Photothermal Therapy Inhibits Its Migration by Affecting Cytoskeleton Proteins. **PNAS**, **second revision**

[6] **Ali, M. R. K**.; Wu, Y.; Ghosh, D.; Do, B. H.; Chen, K.; Dawson, M. R.; Fang, N.; Sulchek, T. A.Δ; El-Sayed M. A. Nuclear membrane-targeted gold nanoparticles inhibit cancer cell migration and invasion **ACS nano 2017, DOI:** 10.1021/acsnano.6b08345

[7] **Ali, M. R. K**.; Rahman, M. A.; Wu, Y.; Han, T.; Zhao, Z; Chen, G.Z.; Xiao, H.; Tang, Y.; Wu, R.; Shin, D.M. ; El-Sayed, M.A.; Efficacy, long-term toxicity, and mechanistic studies of gold nanorods photothermal therapy of cancer in xenograft mice. **PNAS. 2017**: **DOI**:10.1073/pnas.1619302114

[8] **Ali, M. R. K**.; Wu, Y.; Han, T.; Zang, X.; Xiao, H.; Tang, Y.; Wu, R.; Fernandez, F. M.; El-Sayed, M. A. Simultaneous Time-dependent Surface Enhanced Raman Spectroscopy, Metabolomics and Proteomics Reveal Cancer Cell Death Mechanisms Associated with Au-Nanorod Photo-thermal Therapy. **JACS, 2016**, *138*, 15434-15442.

[9] **Ali, M. R. K**.; Ali, H. R.; Rankin, C. R.; El-Sayed, M. A. Targeting Heat Shock Protein 70 using Gold Nanorods Enhances Cancer Cell Apoptosis in Low Dose Plasmonic Photothermal Therapy. **Biomaterials 2016**, *102*, 1.

[10] Rahman, M. A.; **Ali, M. R. K**.; Zhao, Z; Chen, G.Z; El-Sayed, M.A.; Shin, D.M. Optimizing the antitumor efficacy of AuNR-assisted plasmonic photothermal therapy and its molecular impact. ***Cancer Research*** **2016,** *76, 3903-3903* **(Equal contributions)**

[11] Ali, H. R.; **Ali, M. R. K.**; Wu, Y.; Selim, S. A.; Abdelaal, H. F. M.; Nasr, E. A.; El-Sayed, M. A. Gold Nanorods as Drug Delivery Vehicles for Rifampicin Greatly Improve the Efficacy of Combating Mycobacterium tuberculosis with Good Biocompatibility with the Host Cells. ***Bioconjugate Chemistry.*** **2016**, 27, 2486-2492. **(Equal contributions)**

[12] Amira A Gamal Eldin, Mona A.M. Abo-Zeid, Sherien M. El-Daly, Mahmoud T. Abo-Elfadl, Cinderella A. Fahmy, **Ali, M. R. K.;** El-Sayed, M. A, "In Vivo Genotoxicity of Gold Nanorods in Mouse Bone Marrow Compared with Cyclophosphamide" **Nano Biomed. Eng**., 2016, 8(4): 306-314.

[13] Mackey, M. A.; **Ali, M. R. K.;** Austin, L. A.; Near, R. D.; El-Sayed, M. A. The most effective gold nanorod size for plasmonic photothermal therapy: theory and in vitro experiments. ***Journal of Physical Chemistry B*** **2014**, *118*, 1319.

[14] **Ali, M. R. K.**; Panikkanvalappil, S. R.; El-Sayed, M. A. Enhancing the efficiency of gold nanoparticles treatment of cancer by increasing their rate of endocytosis and cell accumulation using rifampicin. ***JACS*** **2014**, *136*, 4464.

[15] **Ali, M. R. K.;** Snyder, B.; El-Sayed, M. A. Synthesis and optical properties of small Au nanorods using a seedless growth technique. **Langmuir 2012**, *28*, 9807-

APPENDIX A: CHAPTER 2

ADDITIONAL FIGURES AND TABLES

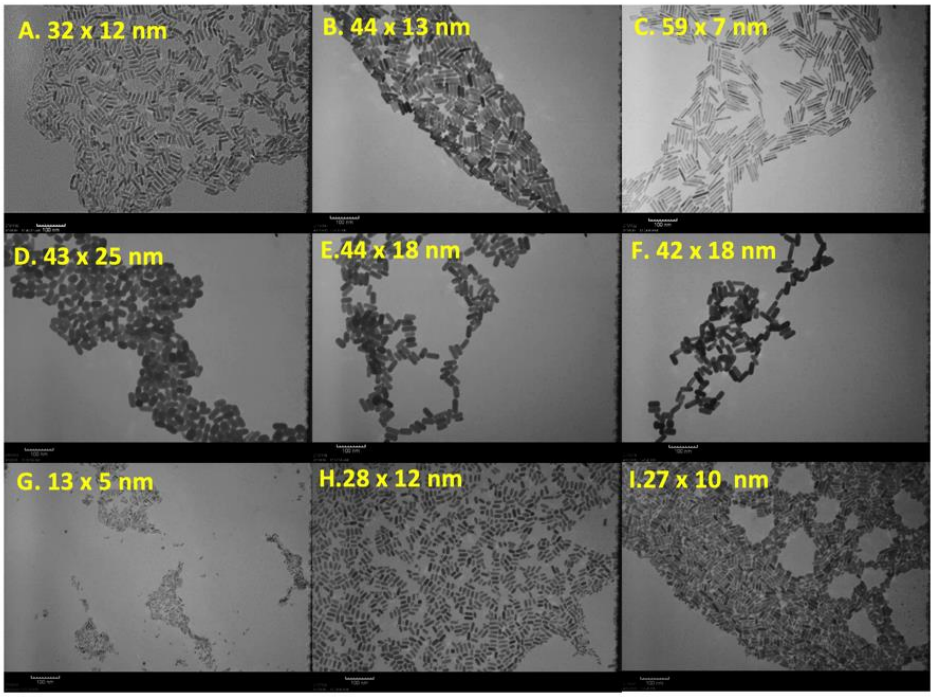

Sample	λ (nm)
A	712
B	775
C	1032
D	590
E	526
F	690
G	720
H	680
I	732

Figure A.1. TEM of different sizes of AuNRs: A, B, D, E, F, H, and I have been prepared using by seed growth technique. Howevere: C, and G samples has been prepared by seedless growth technique in (synthesis in section 2.1.2.4). (Right), their equivalent wavelengths listed in the table.

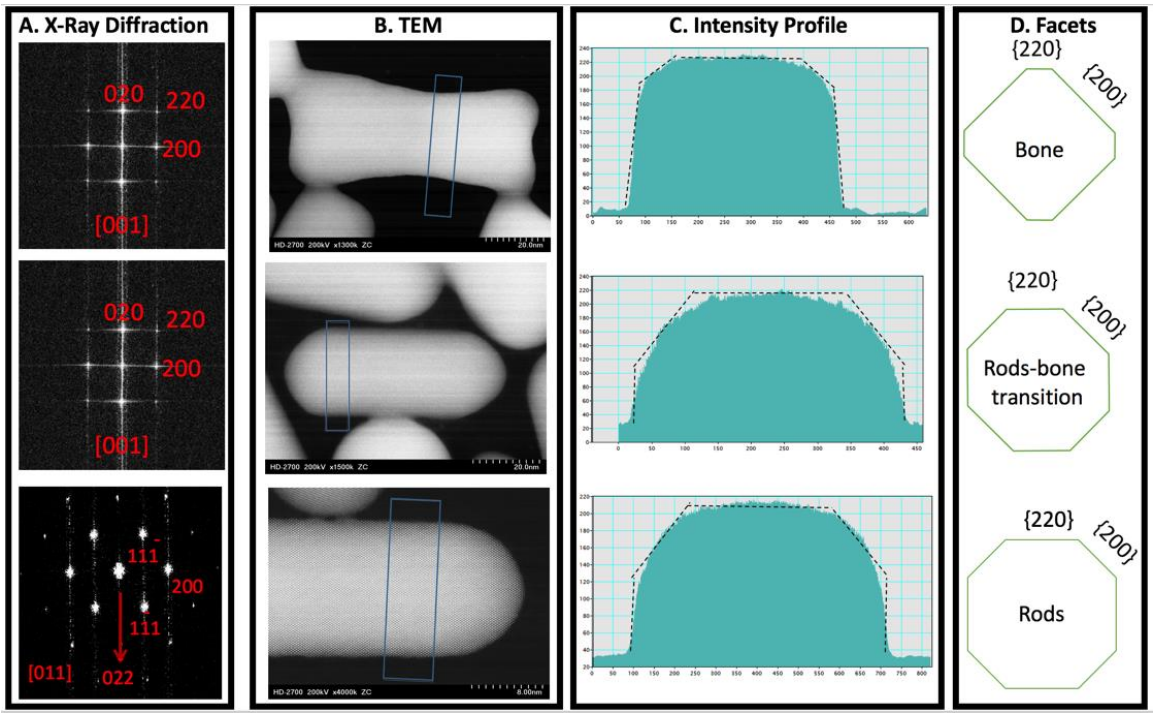

Figure A.2. Comparison between Au nanorods and Au nanobones growth: A) shows the different diffractions between rods and bones. B). 3D visualizations of tomographic reconstructions of both types of nanorods and the one in between (semibone). Crystal facets are visible in both tomographic reconstructions. D) High-resolution STEM projections of both nanorods oriented along the [220] direction. C) the intensity profile acquired from the first projection corresponds to a model where the morphology is composed of {220} and {200} facets. C) The intensity profile acquired from the projection of the rod grown with the 5-bromosalysilic acid clearly shown the effect of the negative surfactant on producing a completely different structure.

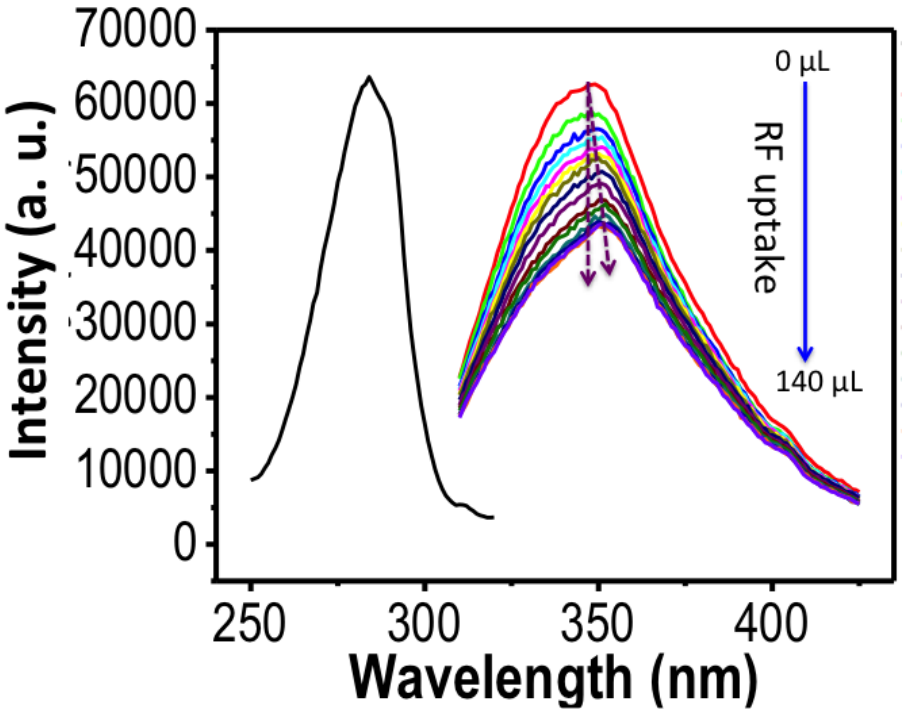

Figure A.3. Emission spectra of AuNRs@BSA (10^{-4} M) after the addition of various amounts of RF (10^{-4} M) from 0.0 to 140 µL at an increment of10 µL.

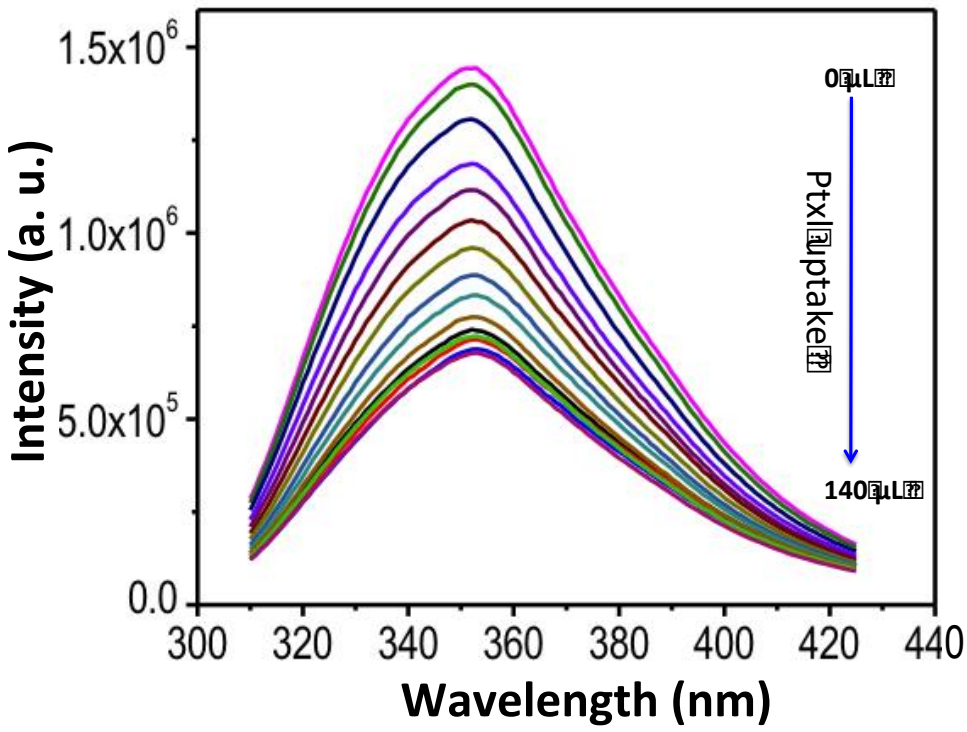

Figure A.4. Emission spectra of BSA (10^{-4} M) after the addition of various concentrations of Ptxl (10^{-4} M) from 0.0 to 140 µL at an increment of 10 µL.

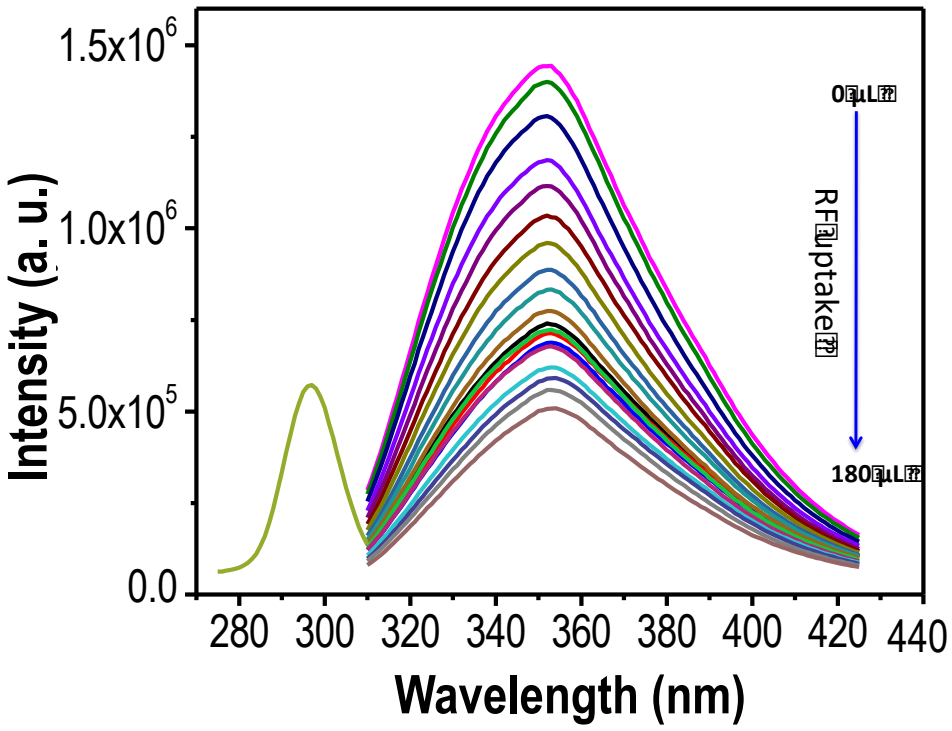

Figure A.5. Emission spectra of BSA (10^{-4} M) after the addition of various concentrations of RF (10^{-4} M) from 0.0 to 180 µL at an increment of 10 µL.

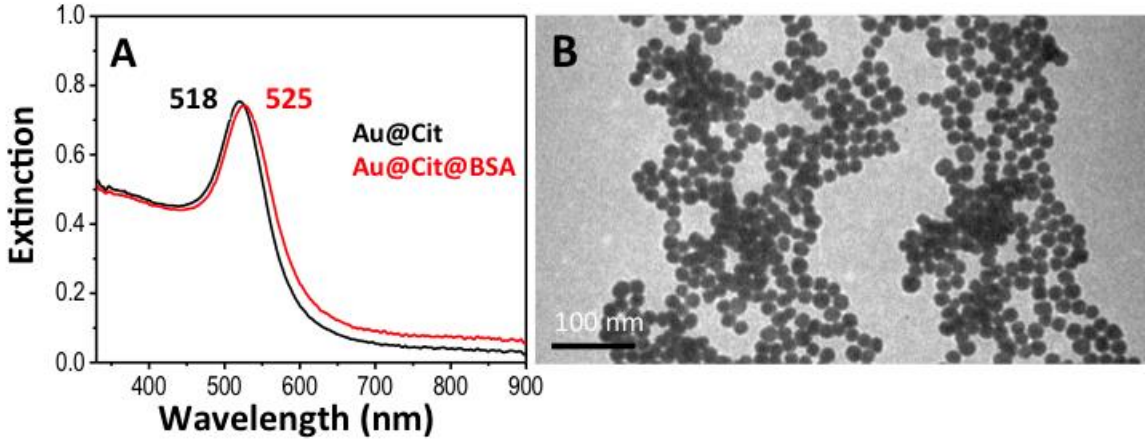

Figure A.6. A and B are the extinction spectrum and TEM image of AuNSs, respectively. Extinction spectrum of AuNSs@BSA also given in A (red trace).

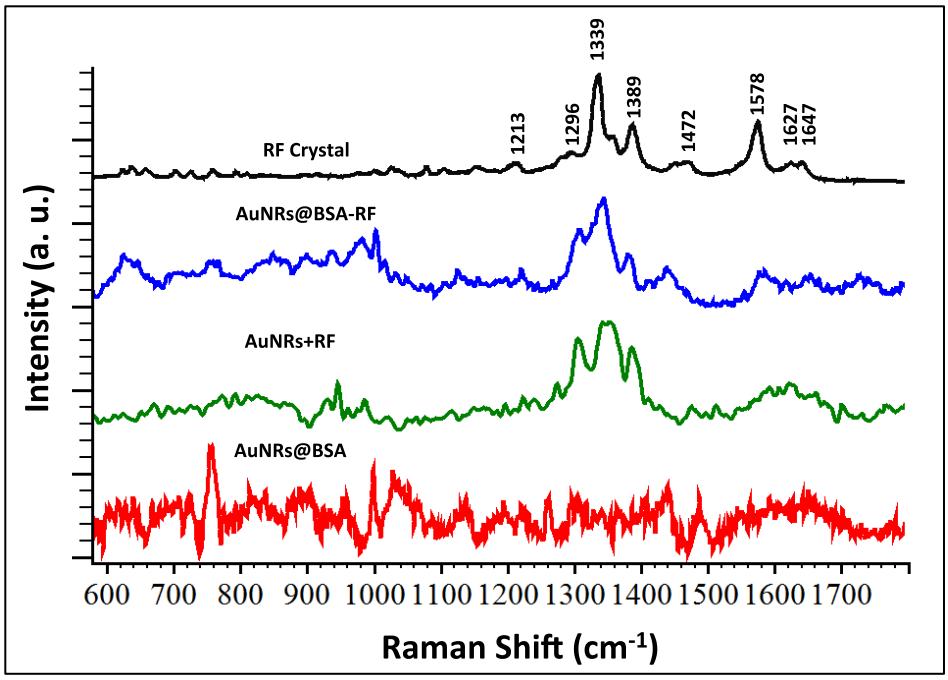

Figure A.7. SERS spectra of various RF conjugated and non-conjugated bAuNRs. Spectra of pure RF and bAuNRS@BSA are also included. Main Raman bands of RF is marked in the figure.

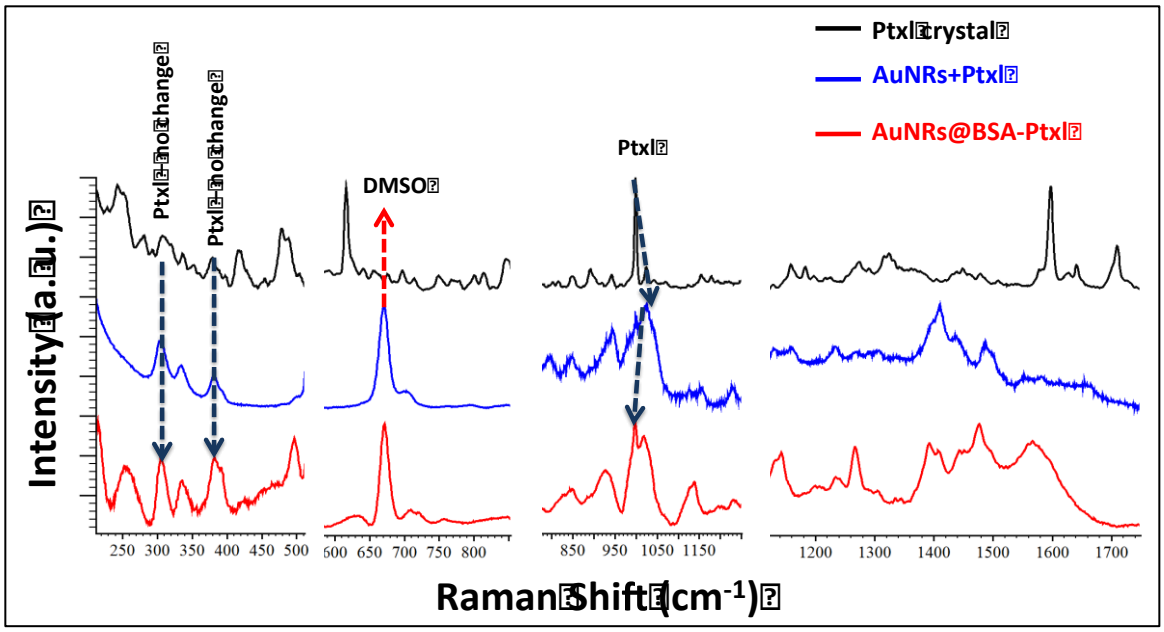

Figure A.8. SERS spectra of Ptxl-conjugated and non-conjugated AuNRs. Spectrum of pure Ptxl is also included.

The AuNRs@BSA-RF showed clear Raman features of RF, which was in concordance with the Raman features of pure RF[1]. Absence of Raman features of CTAB or BSA can be due to their low Raman cross-section compared to the RF. In the SERS spectra of RF with non-conjugated AuNRs (Fig. S5), the ring stretching vibrations (1578, 1389, and 1339 cm^{-1}) and carbonyl stretching vibration (1627 cm^{-1}) shifted towards higher wavenumber side (1618, 1390, 1356, and 1651 cm^{-1}, respectively) compared to the normal Raman spectra.[1] Whereas, after conjugation with BSA, these bands slightly shifted towards lower wavenumber side, which clearly indicates the conjugation of the RF with BSA. This shift can be attributed to the hydrogen bonding interactions between the RF and the amino acids present in the binding sites of BSA. All the SERS spectra were measured in the solution state.

Due to the hydrophobic nature of the molecule, paclitaxel is practically insoluble in water. For this reason, dimethylsulfoxide (DMSO) was chosen to be the solvent to increase its solubility. The SERS band appeared at 668 cm^{-1} was the characteristic peaks of DMSO, which was taken as an internal standard (Fig. S6). Raman band at 987 cm^{-1} appeared in the spectrum of the drug/BSA complex, which is attributed to the paclitaxel._ENREF_5[2] 600 and 1340 cm^{-1} appearing in the spectrum of paclitaxel disappeared from the spectrum of the complex (Fig. S6). All of these changes in the spectrum illustrate that there exist high affinity of the paclitaxel to the BSA, hence the binding.

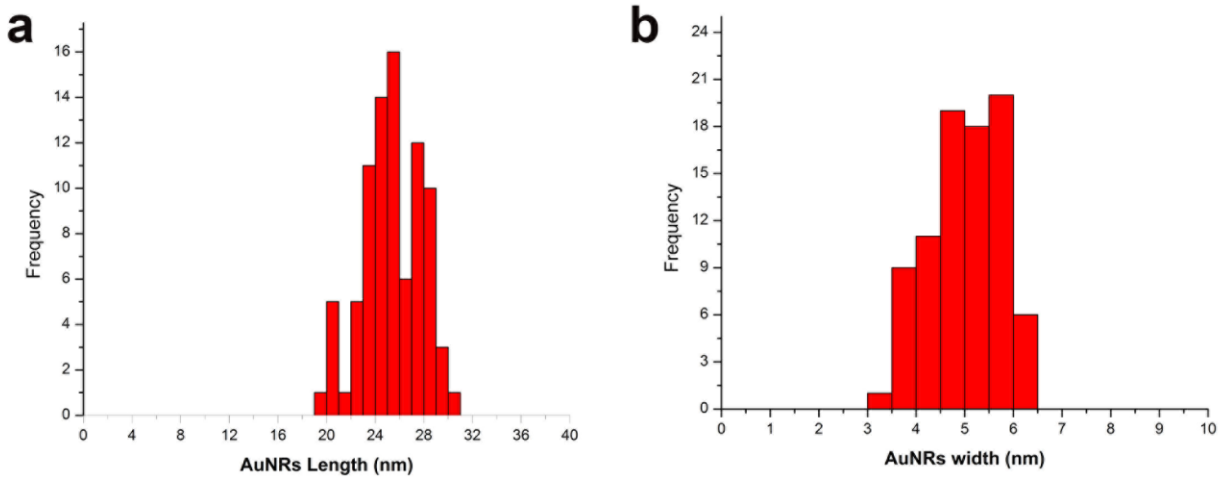

Figure A.9. Length **(a)** and width **(b)** distributions of 80 AuNRs counted.

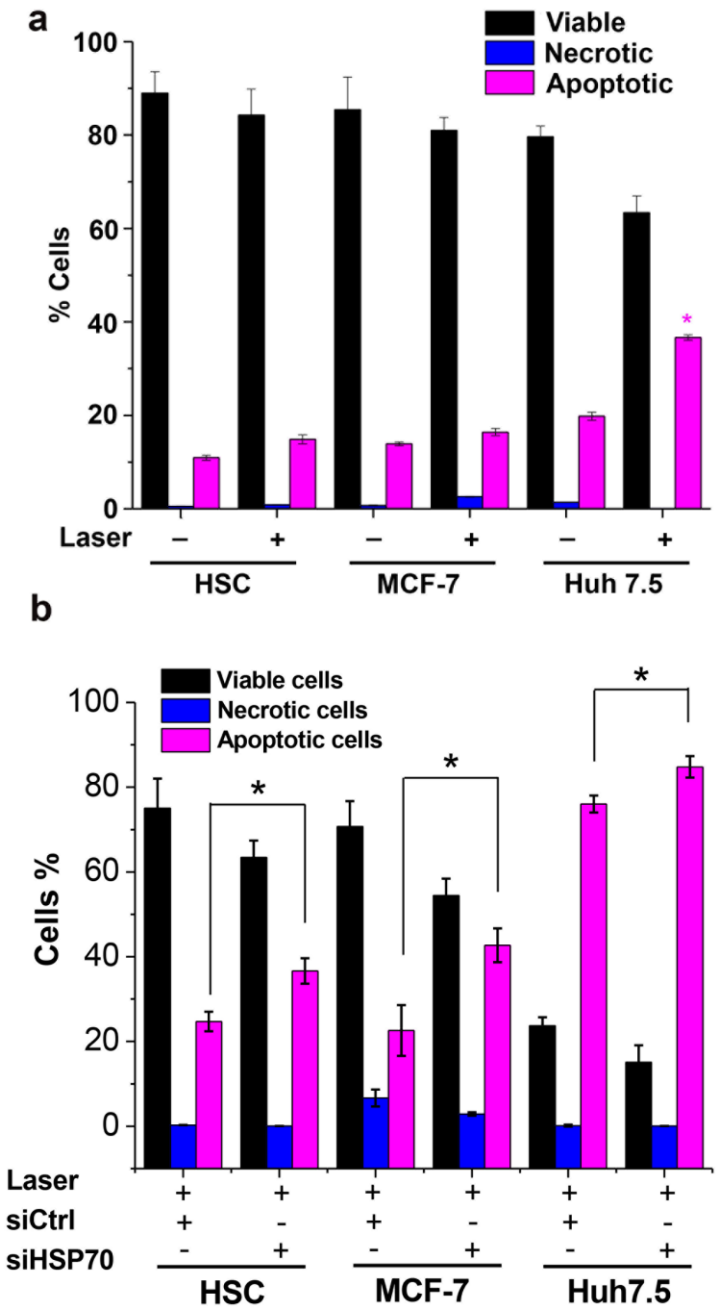

Figure A.10. **(a)** Histograms were generated from flow cytometry data of Annexin V+ Huh7.5 (human hepatocellular carcinoma), MCF-7 (human breast cancer) or HSC (human squamous carcinoma) cells with (PPTT) and without (Ctrl) laser treatment, showing the viable, nectotic and apoptotic cell populations. **(b)** Histograms were generated from flow cytometry data of Annexin

V+ cells after PPTT that were also treated with a control siRNA (siCtrl) or a siRNA against HSP70 (siHSP70).

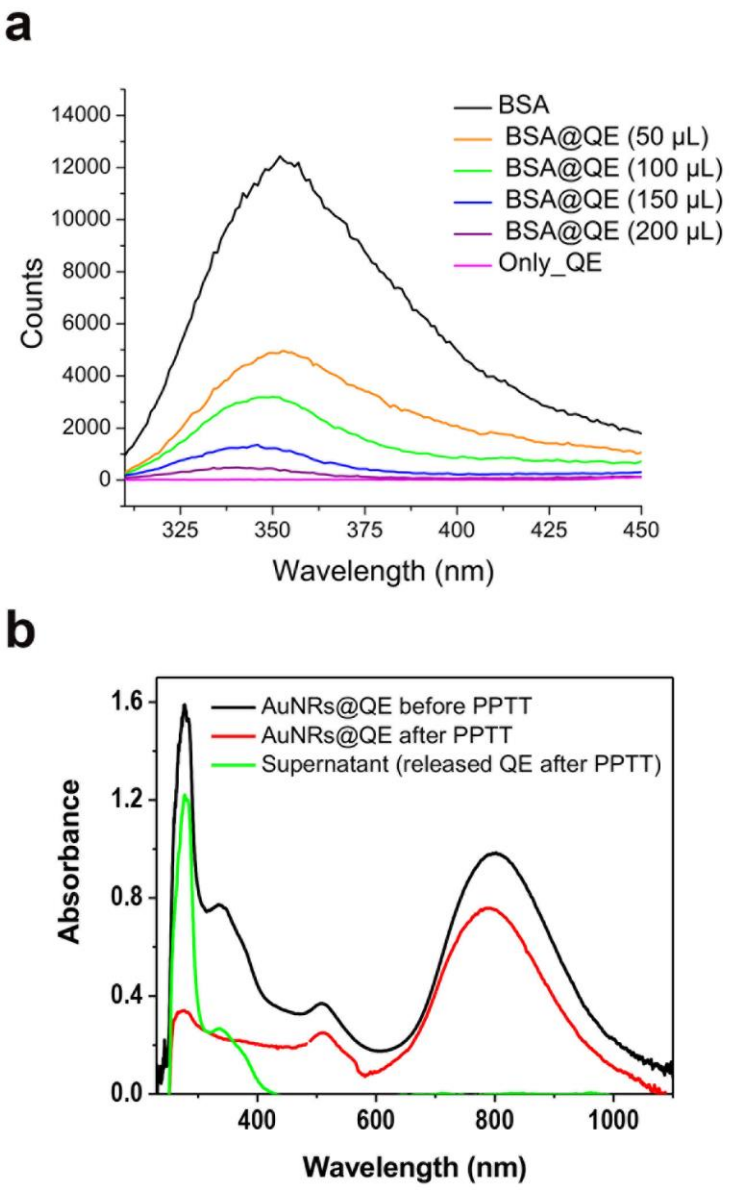

Figure A.11. (a) Fluorescence emission spectra of AuNRs@BSA (10-3 M) after the addition of various amounts of QE (10-3 M) at an increment of 50 µL. BSA-QE -1 (50 µL) BSA-QE -2 (100 µL). BSA-QE -3 (150 µL). BSA-QE -4 (200 µL). **(b)** UV-Vis spectra showing QE release from AuNRs after PPTT. 1 nM of the AuNRs@ QE in solution has been irradiates exposed to a near Infra-red (NIR) CW laser (808 nm, M2W dragon laser)

at 5.8 W / cm2 for 2 minutes with a spot size of approximately 5.6 mm. Then we separated the AuNRs from the supernatant using centrifugation (15 min at 14 500 RPM). Both the supernatant and the pellet were examined using UV-Vis spectrometer. Green line shows the supernatant has QE absorbance at 370 nm, indicating the successful release of QE from the surface of AuNRS after PPTT.

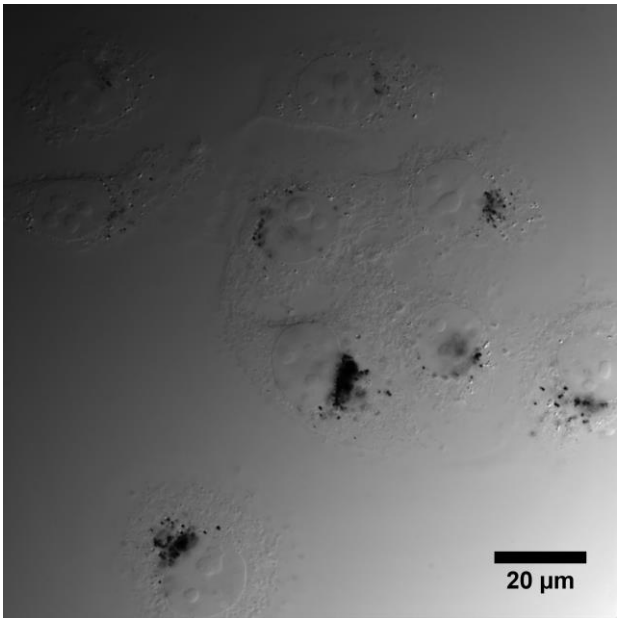

Figure A.12. Differential interference contrast (DIC) microscopy image of the AuNRs@NLS after incubation with the HSC-3 cells for 24 hours.

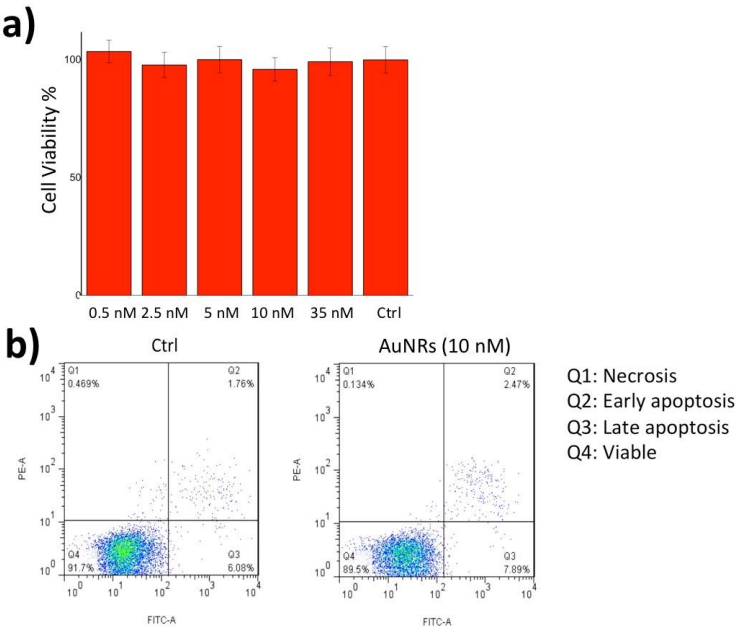

Figure A.13. Cell viability (XTT assay) (a) and flow cytometry (apoptosis/necrosis assay) (b) results for HSC cells incubated with AuNRs.

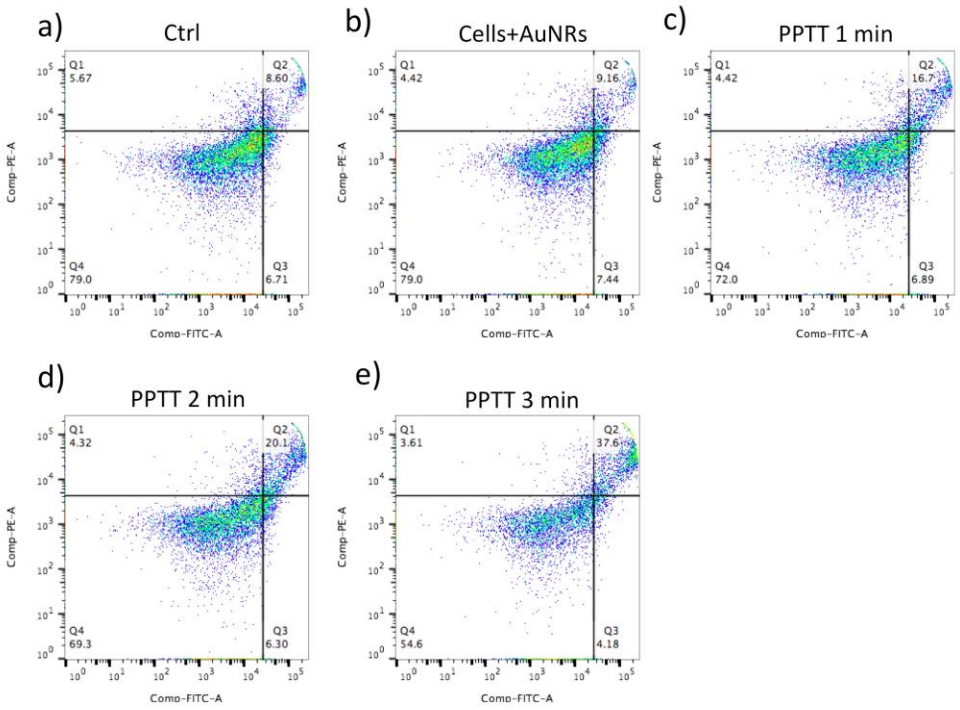

f)

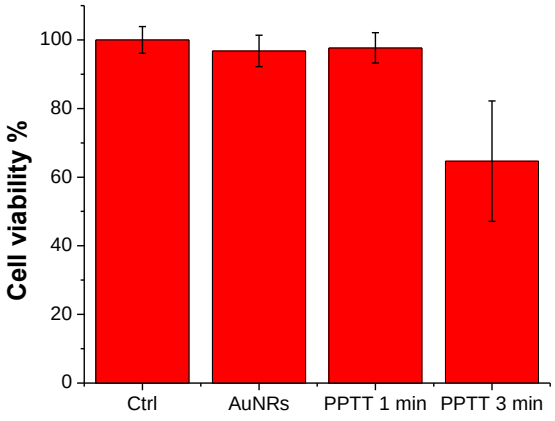

Figure A.14. Apoptosis/necrosis assay (a to e) and cell viability assay (f) for the HSC-3 samples treated with PPTT at different time; Q1 (necrosis), Q2 (apoptosis), Q3 (early apoptosis) and Q4 (early apoptosis).

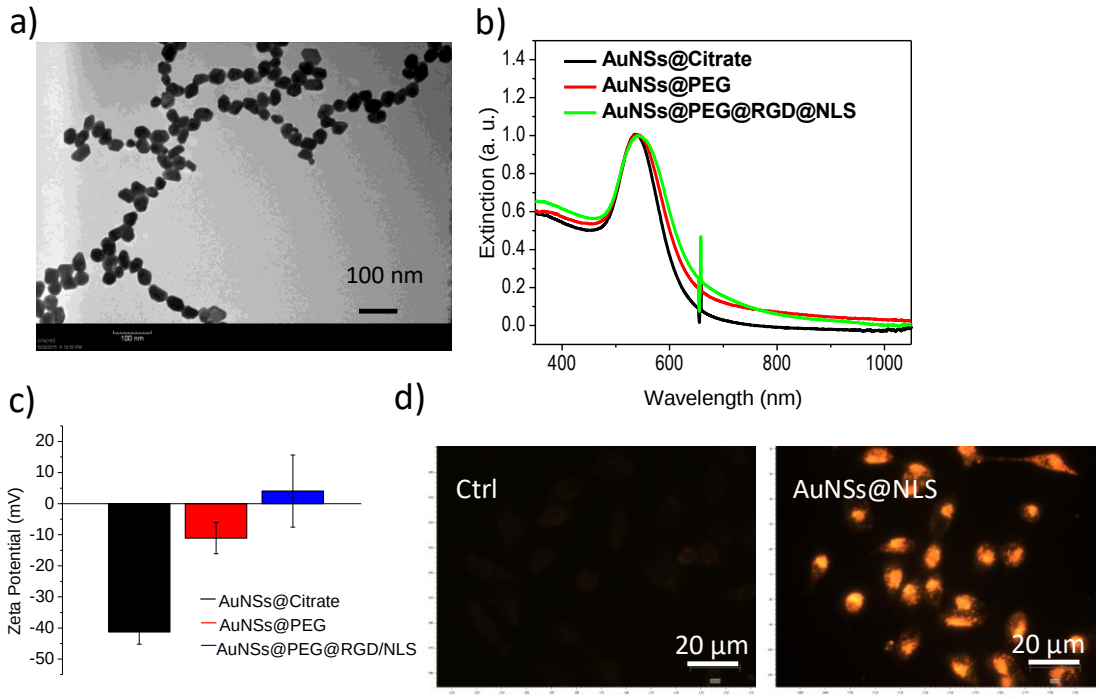

Figure A.15. Characterization of AuNSs@PEG@RGD@NLS. (a) Transmission electron microscope (TEM) image of conjugated gold nanospheres (AuNSs). Scale bar = 100 nm. (b) UV-Vis absorption spectra of the unconjugated AuNSs (black spectrum), PEG conjugated AuNSs (red spectrum) and AuNSs conjugated with NLS (green spectrum). (c) Zeta potential of AuNSs with different conjugations. (d) The dark field images of HSC-3 cells with or without AuNRs@NLS incubation for 24 hours. Scale bar = 20 μm.

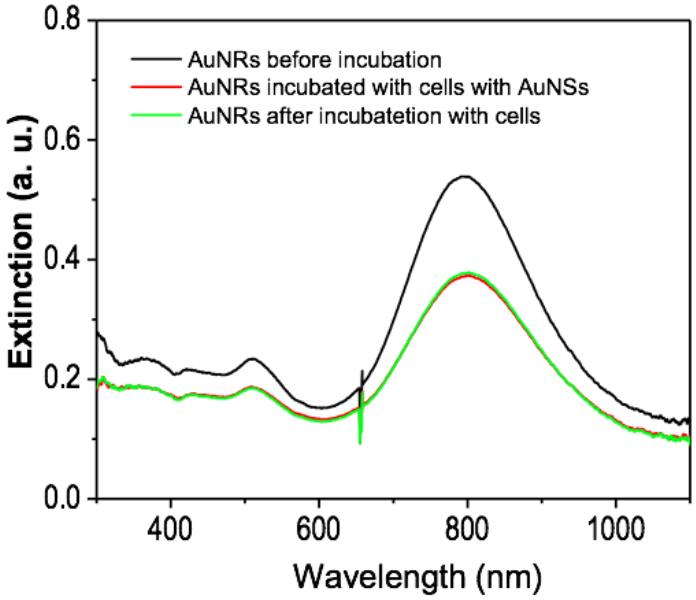

Figure A.16. The uptake of AuNRs by HSC-3 cells before and after 24 h incubation. The pre-existence of AuNSs does not affect the further internalization of AuNRs.

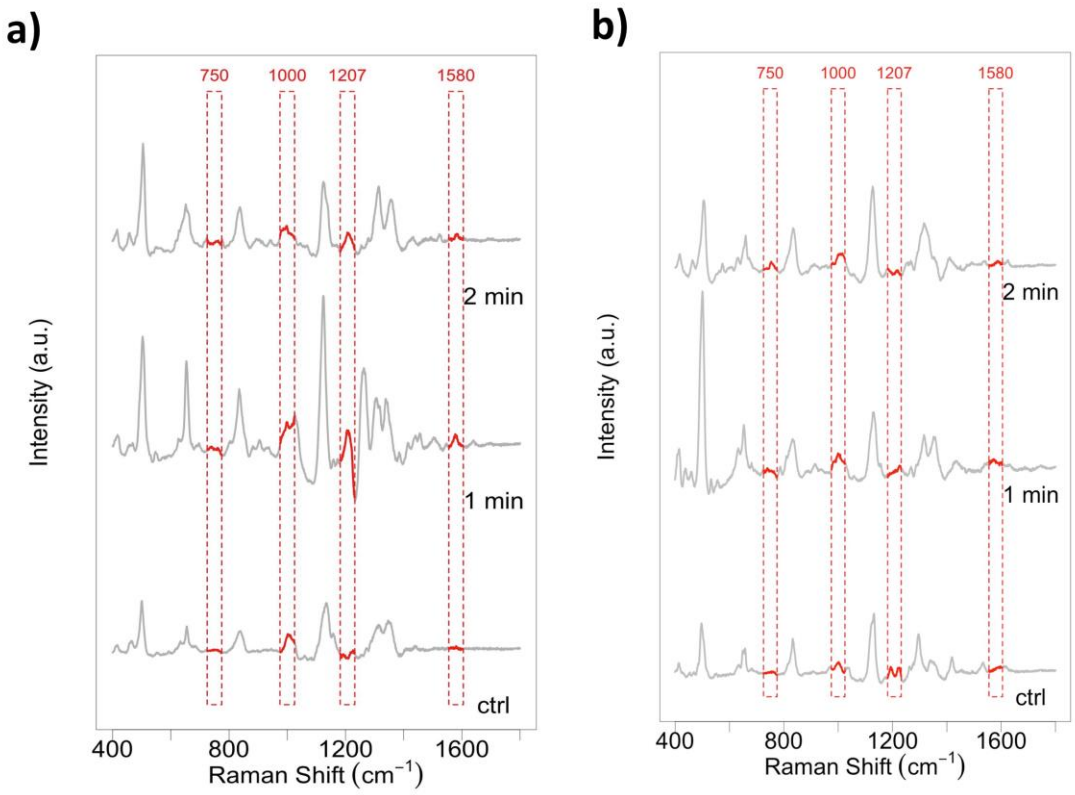

Figure A.17. SERS spectra of a) PPTT on cells with AuNSs alone (without AuNRs) and b) cell incubated with AuNRs but no laser exposure.

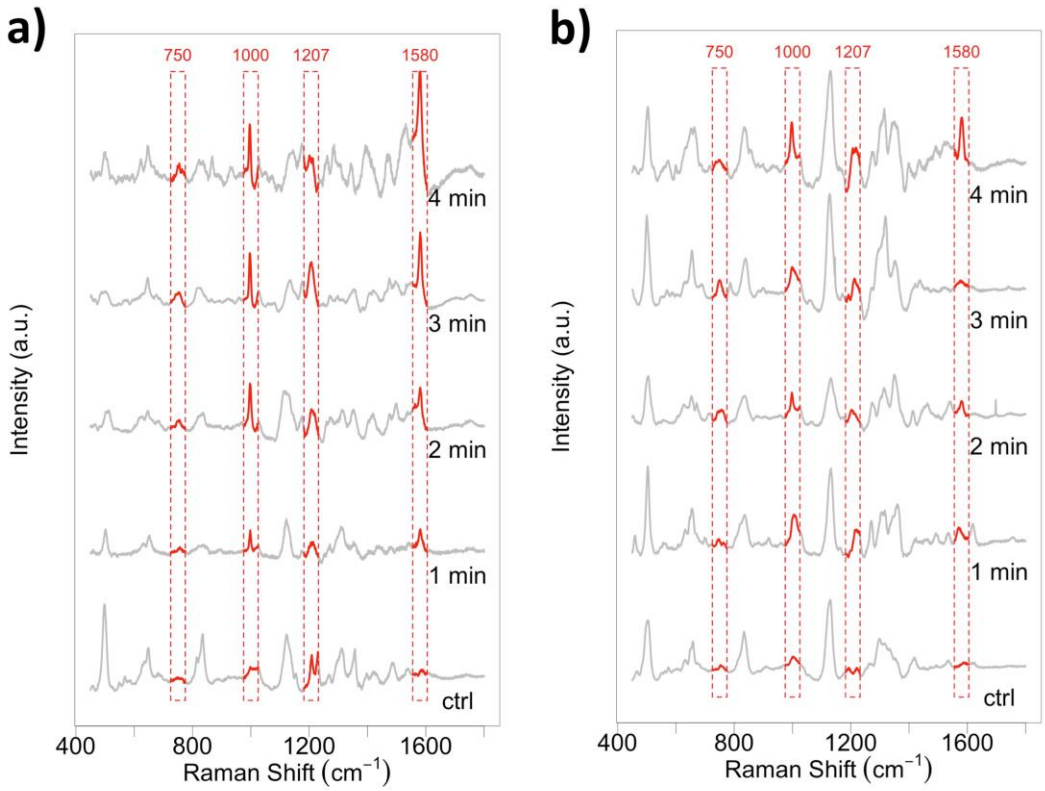

Figure A.18. Additional SERS spectra collected from single HSC-3 cell (incubated with AuNRs 24 h prior to PPTT) under NIR laser exposure of (808 nm diode laser 5.8 w/cm2) at different times (1 and 2 minutes).

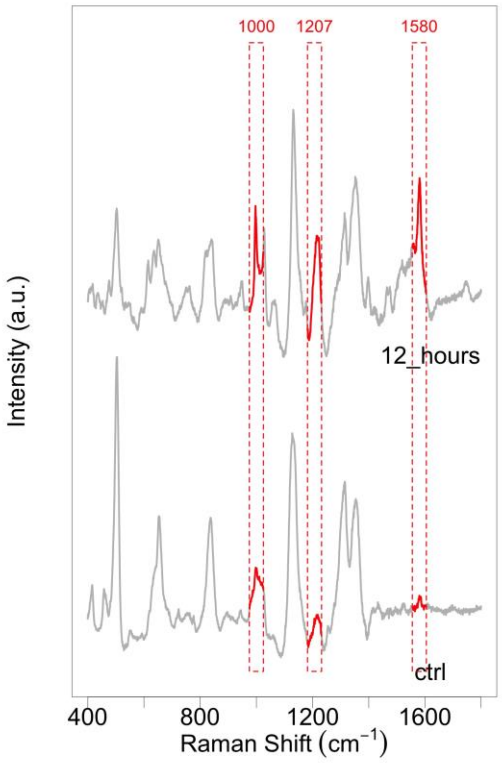

Figure A.19. SERS spectra collected from single HSC-3 cell 12 hours after PPTT (incubated with AuNRs 24 h prior to PPTT, under NIR laser exposure of 808 nm diode laser 5.8 w/cm^2).

a)

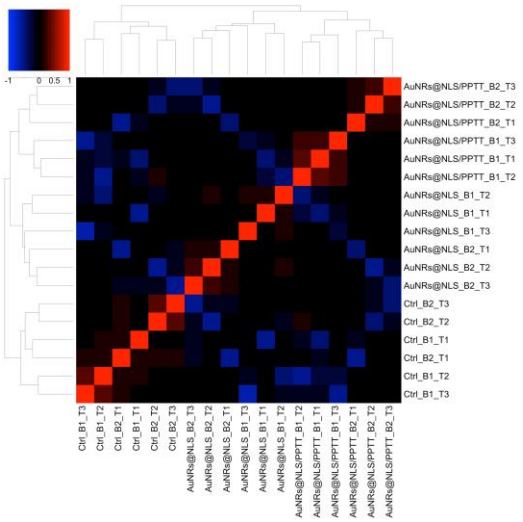
AuNRs@NLS/PPTT_B2_T3
AuNRs@NLS/PPTT_B2_T2
AuNRs@NLS/PPTT_B2_T1
AuNRs@NLS/PPTT_B1_T3
AuNRs@NLS/PPTT_B1_T1
AuNRs@NLS/PPTT_B1_T2
AuNRs@NLS_B1_T2
AuNRs@NLS_B1_T1
AuNRs@NLS_B1_T3
AuNRs@NLS_B2_T1
AuNRs@NLS_B2_T2
AuNRs@NLS_B2_T3
Ctrl_B2_T3
Ctrl_B2_T2
Ctrl_B1_T1
Ctrl_B2_T1
Ctrl_B1_T2
Ctrl_B1_T3

b)

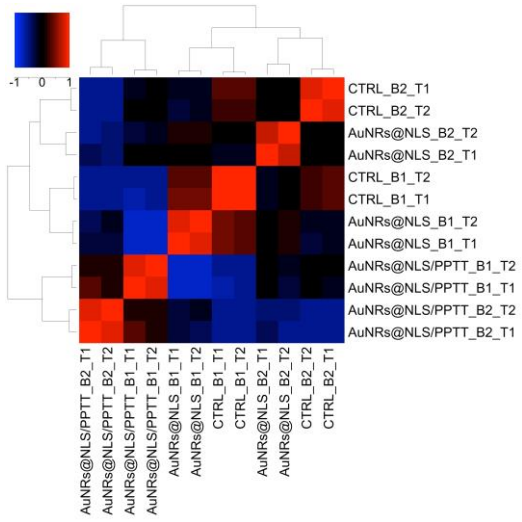
CTRL_B2_T1
CTRL_B2_T2
AuNRs@NLS_B2_T2
AuNRs@NLS_B2_T1
CTRL_B1_T2
CTRL_B1_T1
AuNRs@NLS_B1_T2
AuNRs@NLS_B1_T1
AuNRs@NLS/PPTT_B1_T2
AuNRs@NLS/PPTT_B1_T1
AuNRs@NLS/PPTT_B2_T2
AuNRs@NLS/PPTT_B2_T1

c)

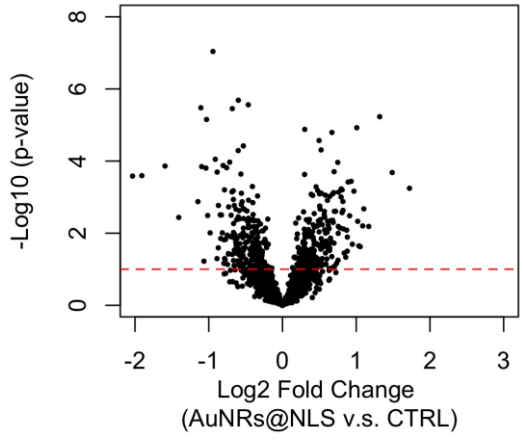
-Log10 (p-value)
Log2 Fold Change
(AuNRs@NLS v.s. CTRL)

d)

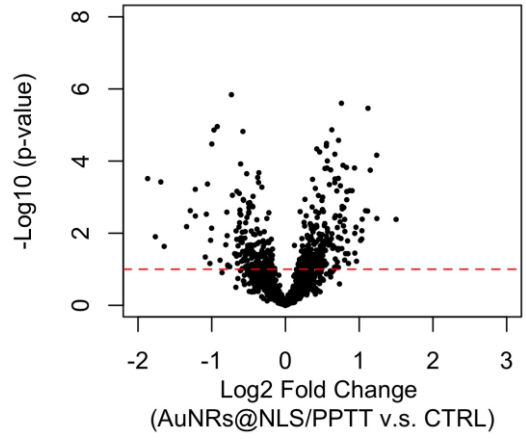
-Log10 (p-value)
Log2 Fold Change
(AuNRs@NLS/PPTT v.s. CTRL)

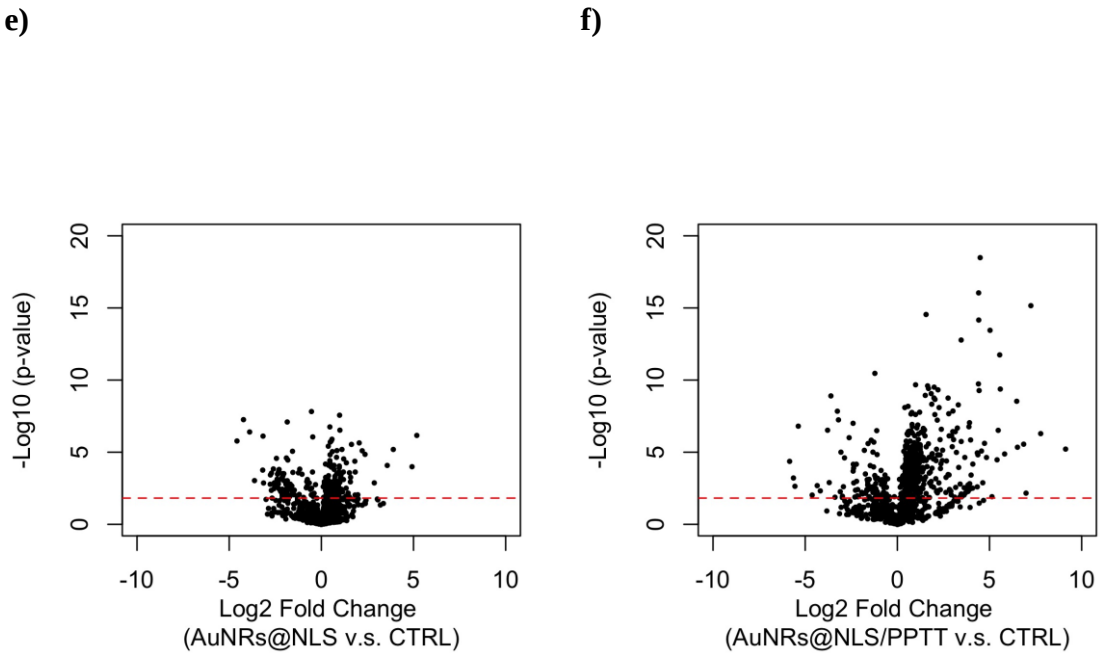

Figure A.20. Clustering analysis and differential analysis of proteomics and metabolomics data. (a) Clustering analysis of proteomics data. Two biological replicates (labeled as B1 and B2) and three MS technical replicates (labeled as T1, T2, and T3) were conducted. Clustering analysis indicated good reproducibility for the proteomics experiments. (b) Clustering analysis of metabolomics data. Two biological replicates (labeled as B1 and B2) and two MS technical replicates (labeled as T1 and T2) were conducted. Clustering analysis indicated good reproducibility for the metabolomics experiments. (c) Volcano plot showing that 434 proteins were differentially expressed in AuNR@NLS group compared to control group (p=0.1). In total, 1341 proteins are identified. (d) Volcano plot showing that 402 proteins were differentially expressed in AuNR@NLS/PPTT group in contrast to control group (p=0.1). (e) Volcano plot showing that 238 metabolomics features were

differentially expressed in AuNR@NLS group compared to control group (FDR=0.05, corresponding to p=0.015). A total of 1122 metabolomics features were detected in metabolite extracts, corresponding to 152 metabolites with primary ion ($[M-H]^-$). (f) Volcano plot showing that 483 metabolomics features were differentially expressed in AuNR@NLS/PPTT group in contrast to control group (FDR=0.05, corresponding to p=0.015).

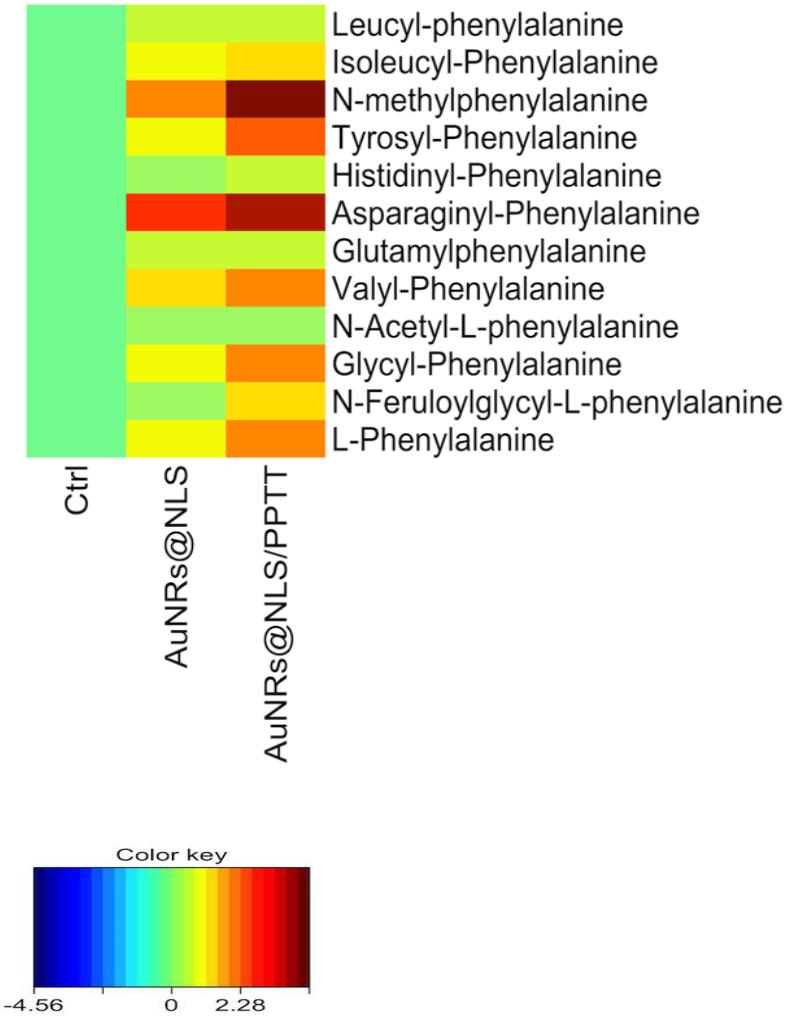

Figure A.21. Heat map showing fold change (log_2) of key metabolites related to phenylalanine metabolism in treatment experiments (AuNRs@NLS, AuNRs@NLS/PPTT) compared to control group.

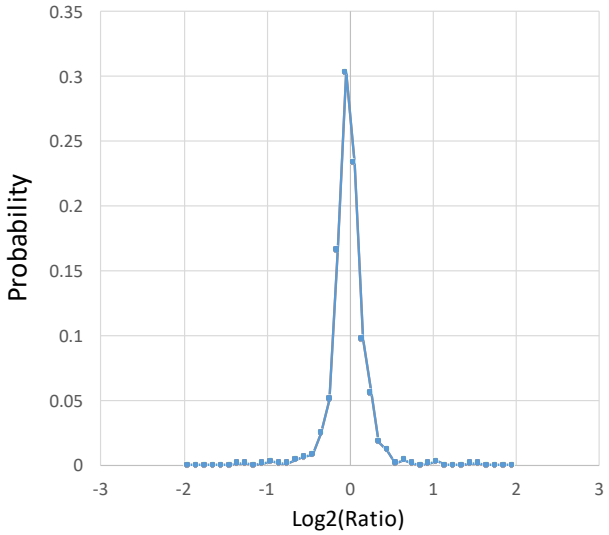

Figure A.22. Quantification accuracy examination of proteomics workflow: Log_2 ratio distributions of quantified peptides from 2 identical test samples (yeast whole proteome sample), each sample having 3 technical replicates.

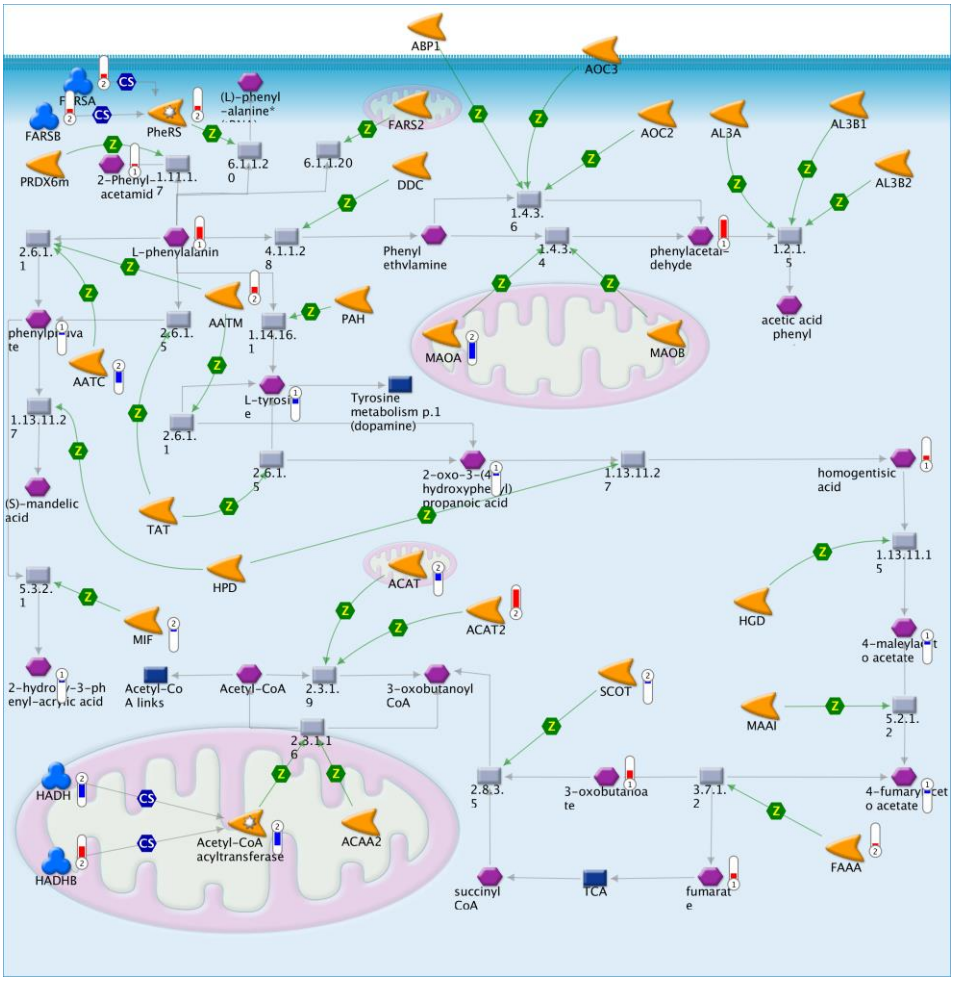

Figure A.23. Pathway map showing that the phenylalanine metabolism pathway was perturbed after PPTT and key proteins (HADHA, ACAT1) were down-regulated, which triggers apoptosis. (Red) means up-regulation after PPTT, (blue) means down-regulation after PPTT. In the thermometer sign, 1 refers to metabolomics results, 2 refers to proteomics results. The thermometers are filled to various degrees, corresponding to the amount by which the markers were up-regulated or down-regulated.

Note: in the figure, “Acetyl-CoA acyltransferase” represents “hydroxyacyl-CoA dehydrogenase/3-ketoacyl-CoA thiolase/enoyl-CoA hydratase (trifunctional protein), alpha subunit”, which is a protein complex catalyzing the 3-hydroxyacyl-CoA dehydrogenase and enoyl-CoA hydratase activities. HADHA and HADHB are both subunits of this protein complex. HADHA is down-regulated, while the HADHB is up-regulated. However, the down-regulation of HADHA is the rate limiting step forming the effective protein complex. Therefore, the activity of protein complex Acetyl-CoA acyltransferase is down-regulated, contributing to the mitochondria mediated apoptosis process.

ACAT1 is acetyl-CoA acetyltransferase 1, which is a mitochondrially localized enzyme that catalyzes the reversible formation of acetoacetyl-CoA from two molecules of acetyl-CoA. ACAT2 is cytosolic localized acetyl-CoA acetyltransferase 2, which involved in lipid metabolism. The mitochondrial isoform ACAT1 is down-regulated hints its perturbation contributes to mitochondria mediated apoptosis processes, while the cytosolic isoform ACAT2 is not related to this process.

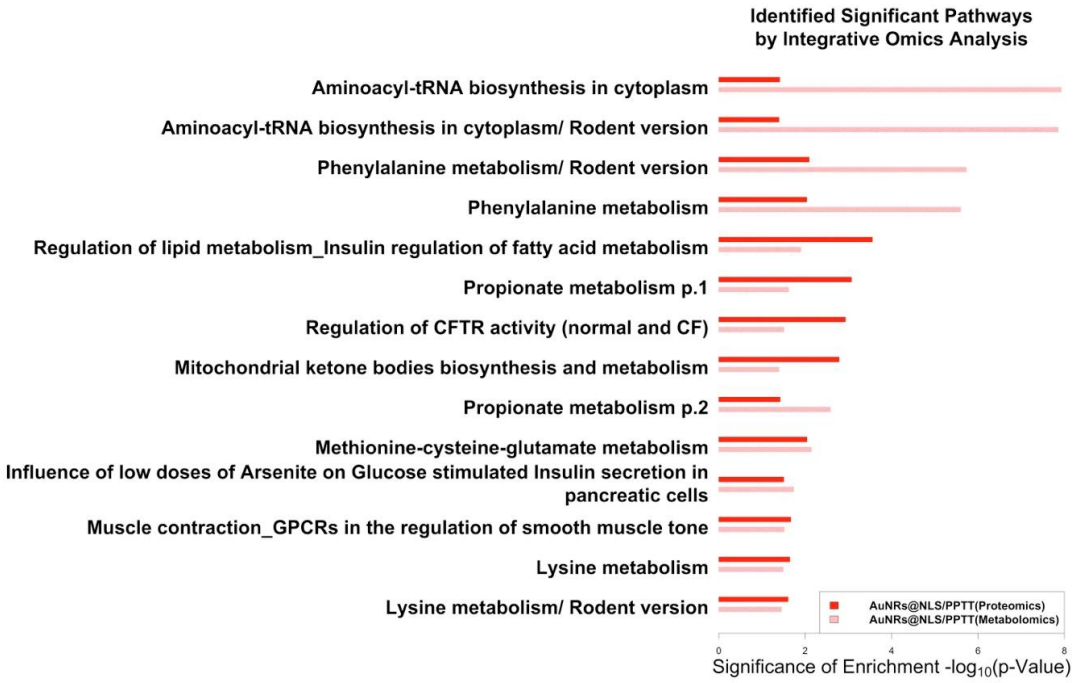

Figure A.24. Significant pathways identified from proteomics (red bars) and metabolomics (light pink bars) that perturbed by photothermal therapy.

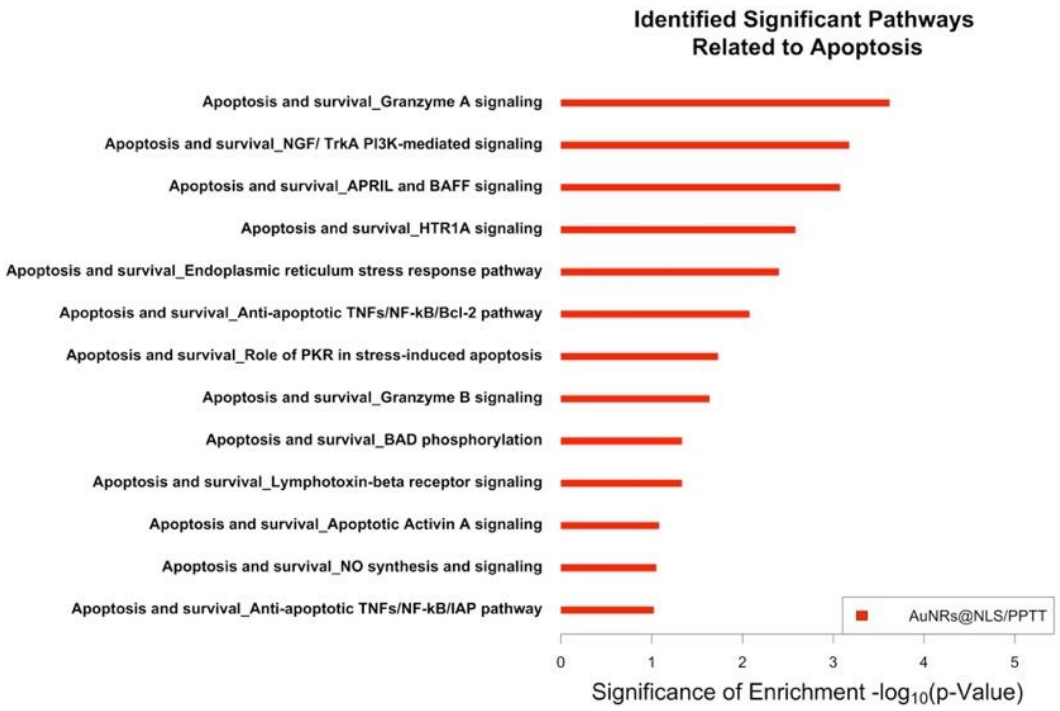

Figure A.25. Other apoptosis pathways revealed by proteomics results.

Table A.1. Zeta potential of 1m of conjugated nanorods (AuNRs) at different conjugations conditions; AuNRs@ CTAB, AuNRs conjugated to BSA, AuNRs conjugated to RF, AuNRs conjugated QE.

Nanoparticle type	Zata potential
AuNRs with citrate	22.9 ± 15.1 mV
AuNRs@BSA	-8.08 ± 4.97 mV
AuNRs@BSA@RF	-21.7 ± 5.55 mV
AuNRs@BSA@QE	-11.7 ± 5.47 mV

Table A.2. Zeta potential results for AuNRs with different surface modifications

Nanoparticles	Zeta potential value/ mV
CTAB-coated AuNRs	22.9±15.1
AuNRs@PEG	-10.2±6.73
AuNRs@PEG@RGD/NLS	35.7± 8.96

Table A.3. Tentative assignment of Raman bands in the SERS spectra collected from HSC cells (Panikkanvalappil, S. R. et al, 2014; Panikkanvalappil, S. R. et al, 2016)

Wavenumber (cm^{-1})	Tentative assignments of SERS bands
495-510	-S-S-
640−660	-C-S-
820−850	Tyr and lipids O−C−C−N symmetric stretches
990-1010	Phe ring breathing
748-758	pyrrole breathing mode ν15 in cytochrome c
1012−1030	In-plane bending mode of Phe and ring breathing of Trp
1200−1210	C_6H_5−C stretch of Phe and Tyr
1584−1592	Phe

Tyr = Tyrosine; Phe = Phenylalanine; Trp =Tryptophan.

APPENDIX B: CHAPTER 3

ADDITIONAL FIGURES AND TABLES

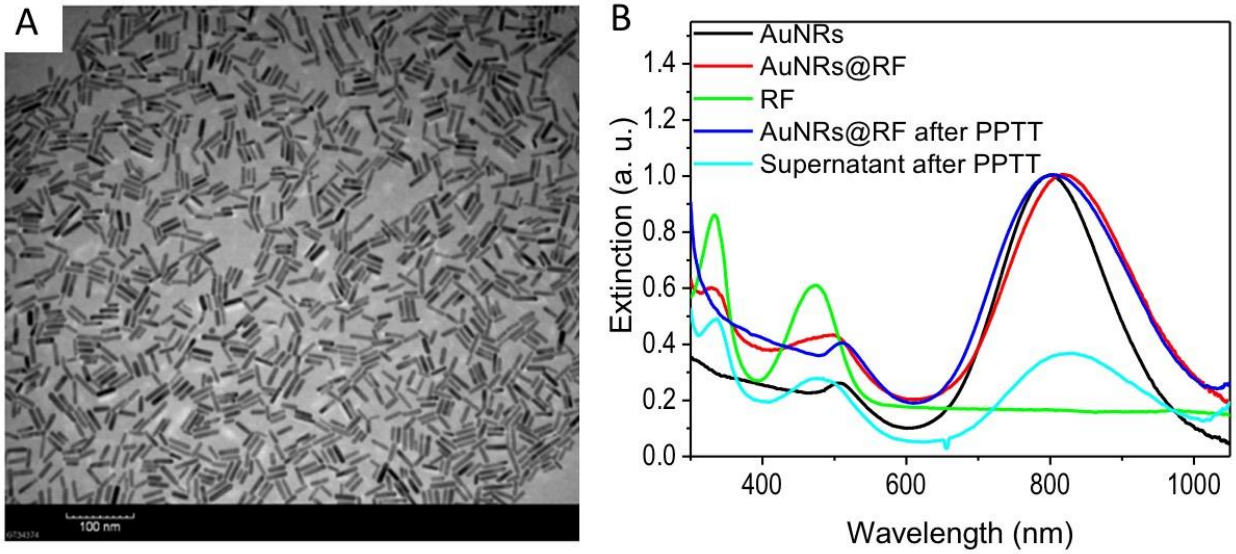

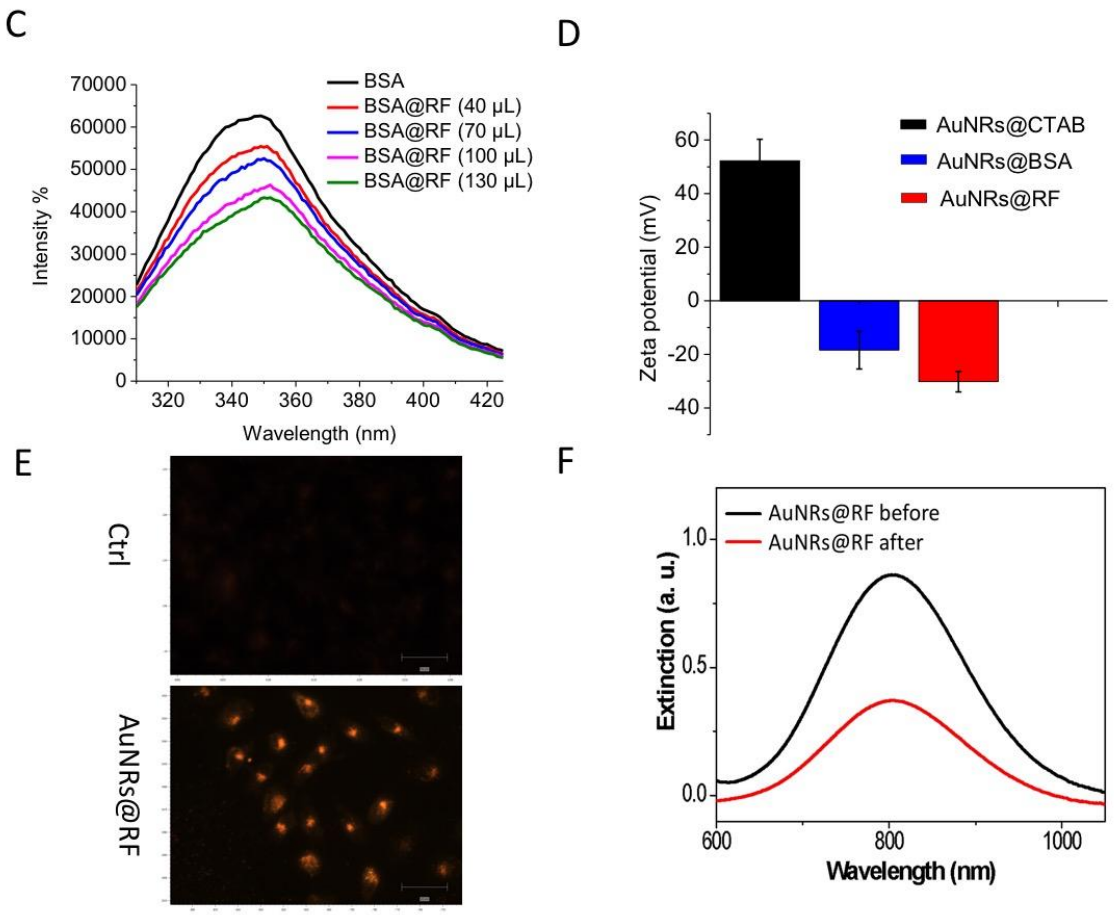

Figure B.1. Characterization and TU686 cell uptake of rifampicin-conjugated AuNRs@RF. (A) Transmission electron microscopic (TEM) image of conjugated nanorods (AuNRs). Scale bar = 100 nm; **(B)** UV-vis absorption spectra of the as-synthesized AuNRs (black line), BSA and RF conjugated AuNRs@RF (red line), free RF in solution (green line), AuNRs after PPTT (blue) and the supernatant after PPTT (cyan); **(C)** BSA fluorescent emission quenching of BSA (10^{-4} M) after adding various amounts of RF (10^{-4} M) from 0 to 130 μL; **(D)** Zeta potential of AuNRs with different surface ligands: cetyl trimethylammonium bromide (CTAB), BSA, BSA+RF; **(E)** Dark field microscopic imaging showing TU686 cellular uptake of 2.5 nM AuNRs@RF after 24 h incubation.

Scale bar = 50 μm; **(F)** UV-vis absorption spectra of the nanoparticle-media mixture before and after incubation with cells.

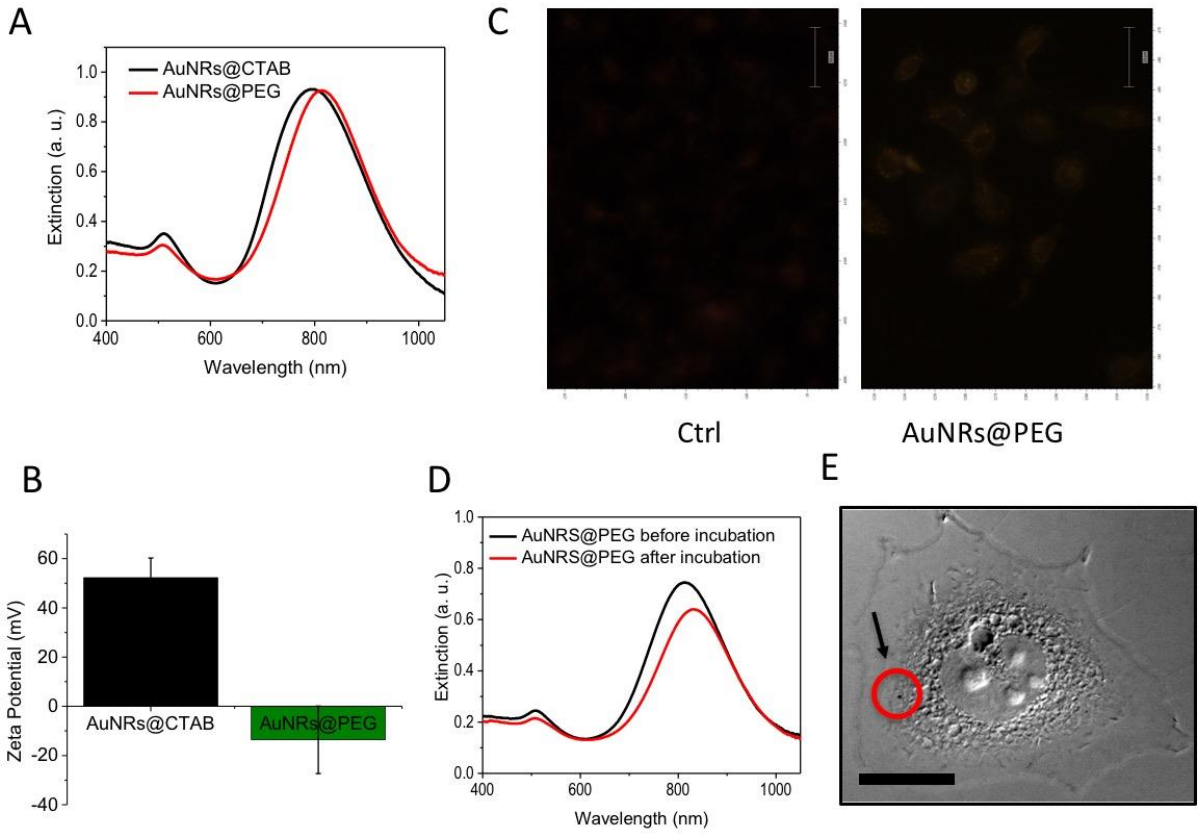

Figure B.2. Characterization of AuNRs@PEG (25 × 5.5 nm). (A) UV-Vis spectra showing the surface plasmon peaks of as-synthesized AuNRs and the red-shifted peak of PEGylated AuNRs; **(B)** Zeta potential of AuNRs@CTAB (black) and AuNRs@PEG (green); **(C)** Dark field images of cells with and without 2.5 nM AuNRs@PEG incubation for 24 h. Scale bar = 50 μm; **(D)** UV-Vis spectra showing the intensities of AuNRs plasmon peaks before and after incubation with cells; **(E)** DIC images of cells incubated with 2.5

nM AuNRs@PEG. The red circle and black arrow indicate a nanoparticle aggregate inside the cell. Scale bars are 10 μm. For comparison with other studies, 5 nM = 1 O.D. (optical density) for small AuNRs (35).

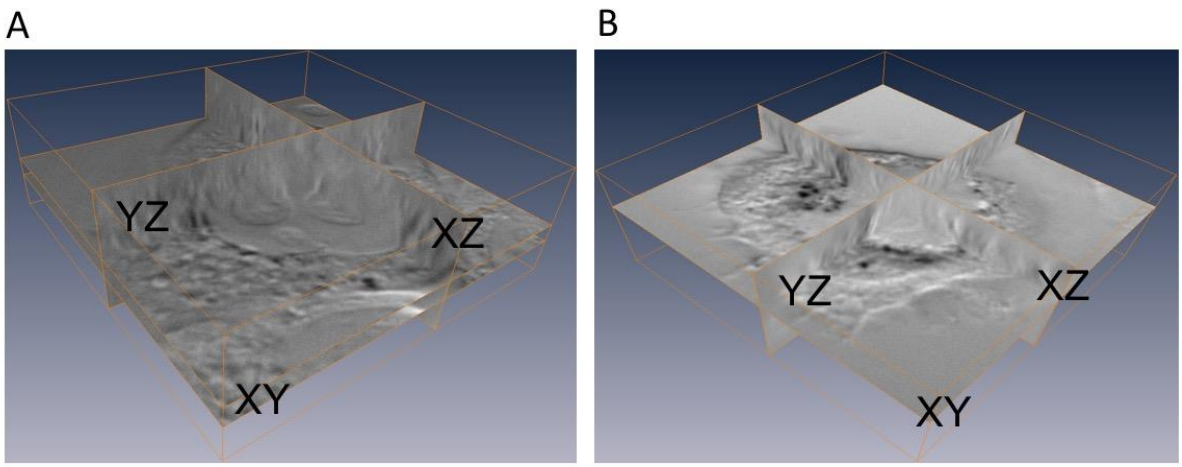

Figure B.3. Three dimensional reconstruction of AuNRs@RF inside cells. Z-stacks were acquired using the Multi-Dimensional Acquisition function in Micro-Manger. More specifically, the DIC optical sectioning through the whole cell thickness was achieved by moving the objective on the motorized nosepiece using PFS at 65 nm/step at 33 ms (30 fps) of AuNRs@RF inside cells. (A) cells incubated with AuNRs@RF; (B) cells after PPTT. (For more details, see supporting videos "3D DIC imaging of AuNRs@RF inside TU686 cells" and "3D DIC imaging of AuNRs@RF inside TU686 cells, after PPTT")

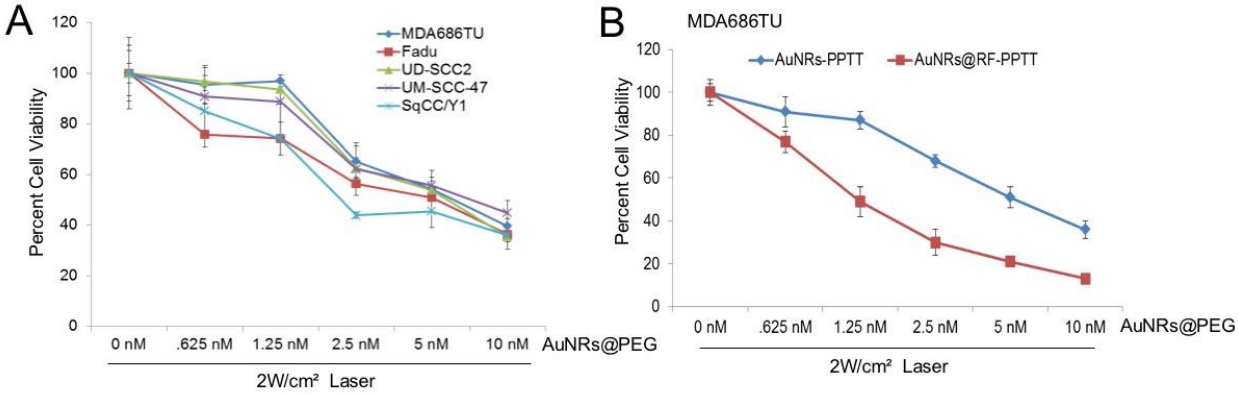

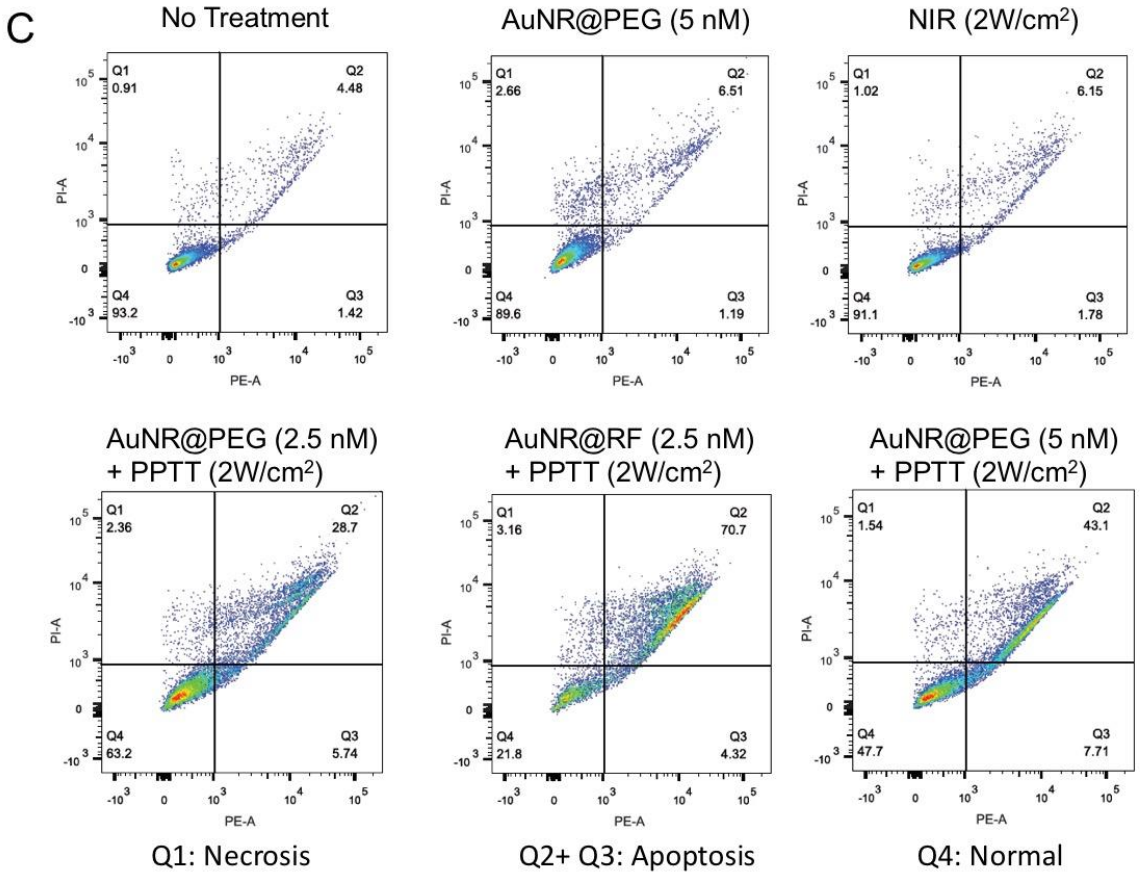

Figure B.4. AuNRs-PPTT efficiently inhibits cell viability and induces apoptosis *(in vitro*). (A) Cell viabilities of five HNSCC cell lines under treatment with various concentrations of small AuNR for 2h followed by 2 W/cm^2 NIR laser power for 2 min. 72h after laser treatment, cell viability was analyzed by SRB assay. The percentage of cell viability was then calculated based on the absorbance values relative to the non-treated samples. Error bars are mean ± SD from 3 independent experiments; **(B)** Cell viability analysis as above of MDA686TU cells 72h after treatment with AuNRs@PEG-PPTT and AuNRs@RF-PPTT (error bars are mean ±SD from 3 independent experiments). **(C)**

Apoptosis/necrosis assay of cells treated with PPTT under different conditions. Q1: necrosis cells; Q2+Q3: apoptosis cells; Q4: normal cells. For comparison with other studies, 5 nM = 1 O.D. (optical density) for small AuNRs (35).

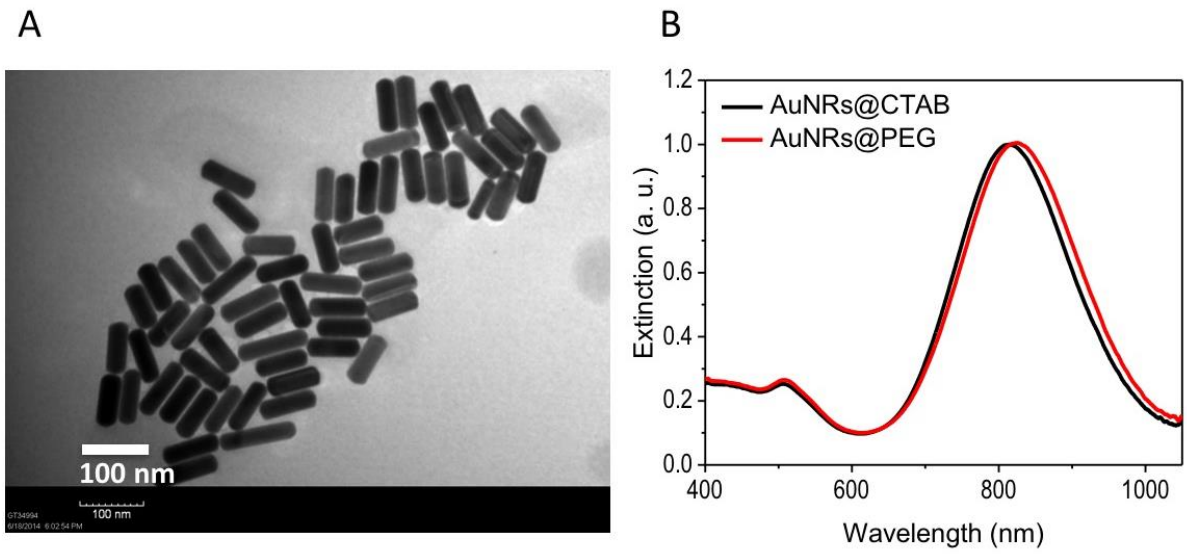

Figure B.5. Characterization of large AuNRs with size of 72 (± 7) nm × 16 (± 4) nm. **(A)** TEM image; **(B)** UV-Vis absorption spectra of AuNRs before and after PEG conjugation.

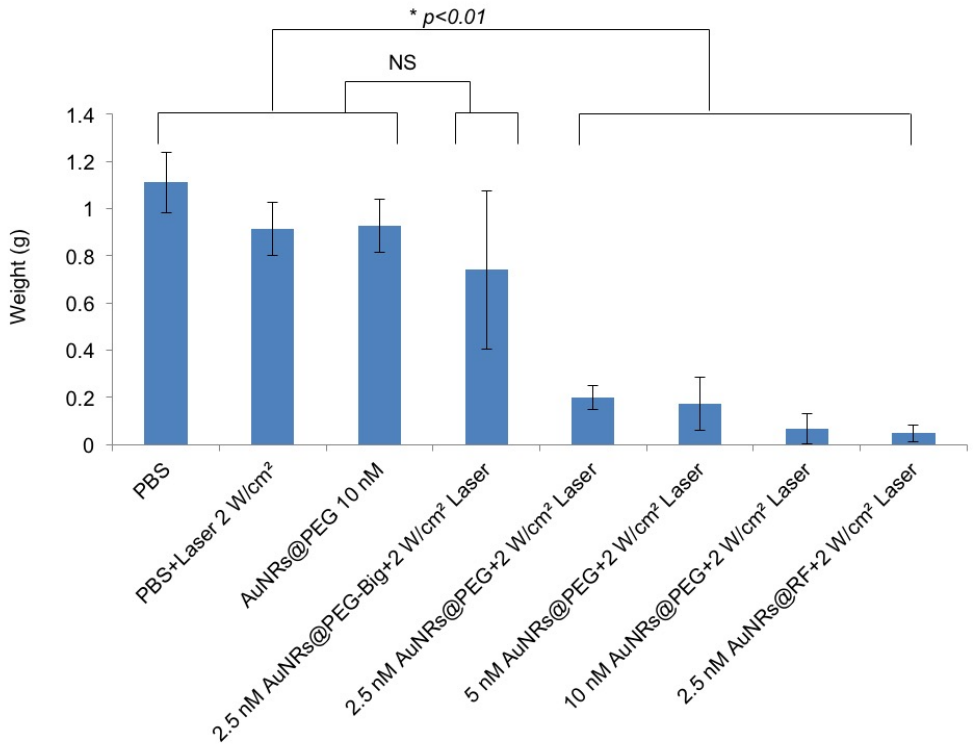

Figure B.6. Tumor weight of treated mice. Mice were sacrificed, tumors were collected from each treatment group on Day 25 and tumors were weighed (error bars are mean ±SD, n=5). Statistical analysis (t-test) shows that the difference between control (PBS, Laser, AuNRs@PEG) vs the big AuNRs@PEG treated group was not significant (NS), while control (PBS, Laser, AuNRs@PEG) vs other treated groups was $*p < 0.01$. For comparison with other studies, 5 nM = 1 O.D. (optical density) for small AuNRs (35).

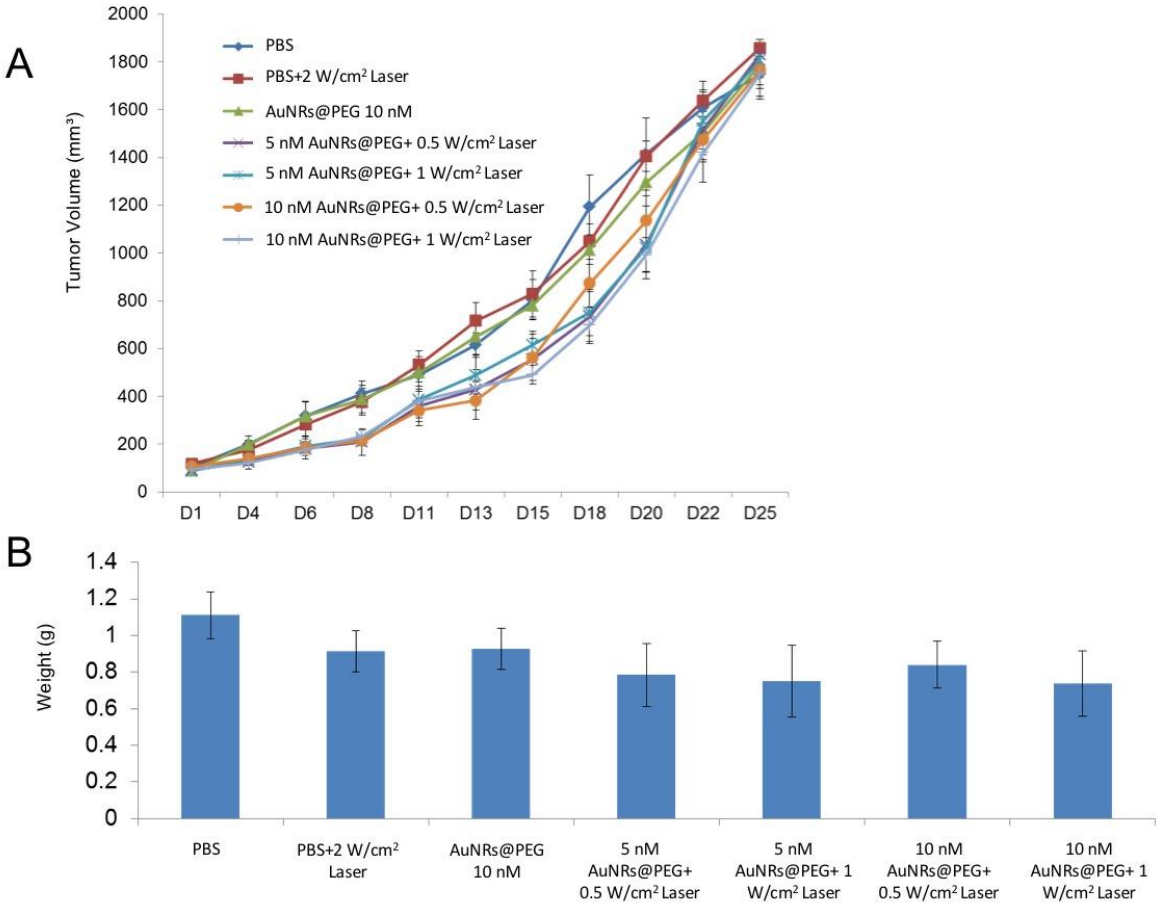

Figure B.7. Lower power of laser with AuNRs is unable to reduce tumor growth in a MDA686TU xenograft model. (A) Tumor growth (tumor volume = $0.5 \times l \times w^2$) progression in groups: PBS, 2 W/cm^2 laser, 10 nM small AuNRs as control groups; 5 nM, 10 nM small AuNRs with 0.5 and 1 W/cm^2 laser. First dose was given on Day 1 (tumor volume ~100mm^3) and tumor growth was monitored until Day 25 (endpoint of tumor volume 1800 mm_3) (error bars are mean ±SE, n=5); **(B)** Mice were sacrificed, tumors were collected from each treatment group on Day 25 and tumors were weighed (error bars are mean ±SD, n=5). For comparison with other studies, 5 nM = 1 O.D. (optical density) for small AuNRs (35).

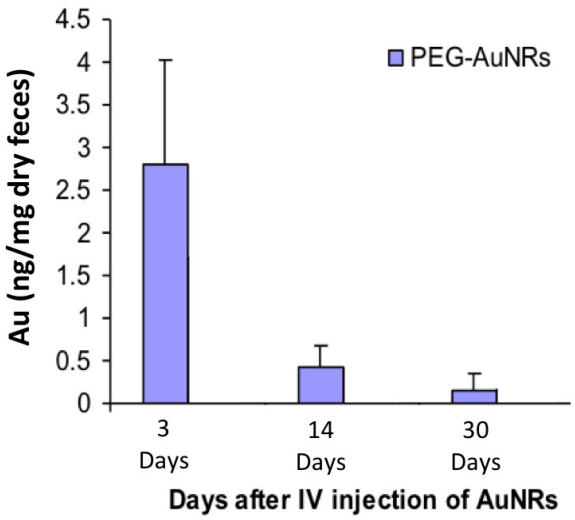

Figure B.8. Excretion of AuNRs in mice feces (Au 0.18mg/kg, 3 mice per group).

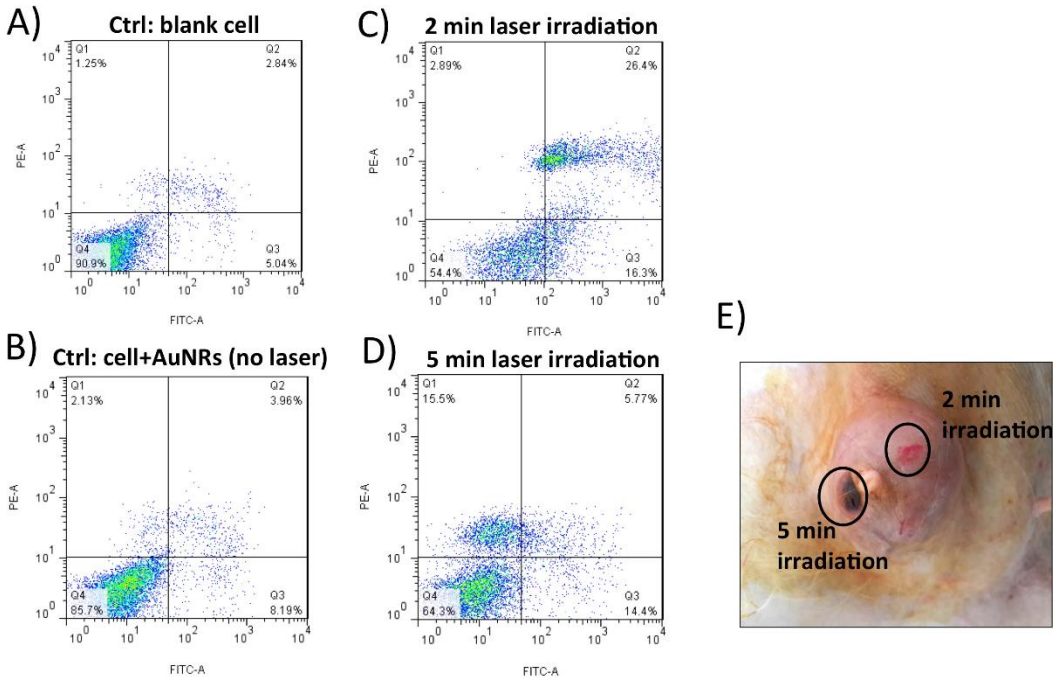

Figure B.9. Modulation of PPTT toward inducing cancer cell apoptosis.

Notes: (**A**–**D**) shows the MCF-7 cell apoptosis/necrosis states of the in vitro experiment. **(A)** Cells without AuNRs. **(B)** Cells incubated with AuNRs (no laser). **(C)** Cells incubated with AuNRs and 2 minutes laser irradiation. **(D)** Cells incubated with AuNRs and 5 minutes laser irradiation. **(E)** Laser irradiation spots of animals. The 5-minute irradiation caused burning of the tumor, whereas 2-minute irradiation shows no obvious change in appearance. The in vitro and in vivo experiments were conducted at the same condition.

Abbreviations: PPTT, plasmonic photothermal therapy; AuNRs, gold nanorods; ctrl, control.

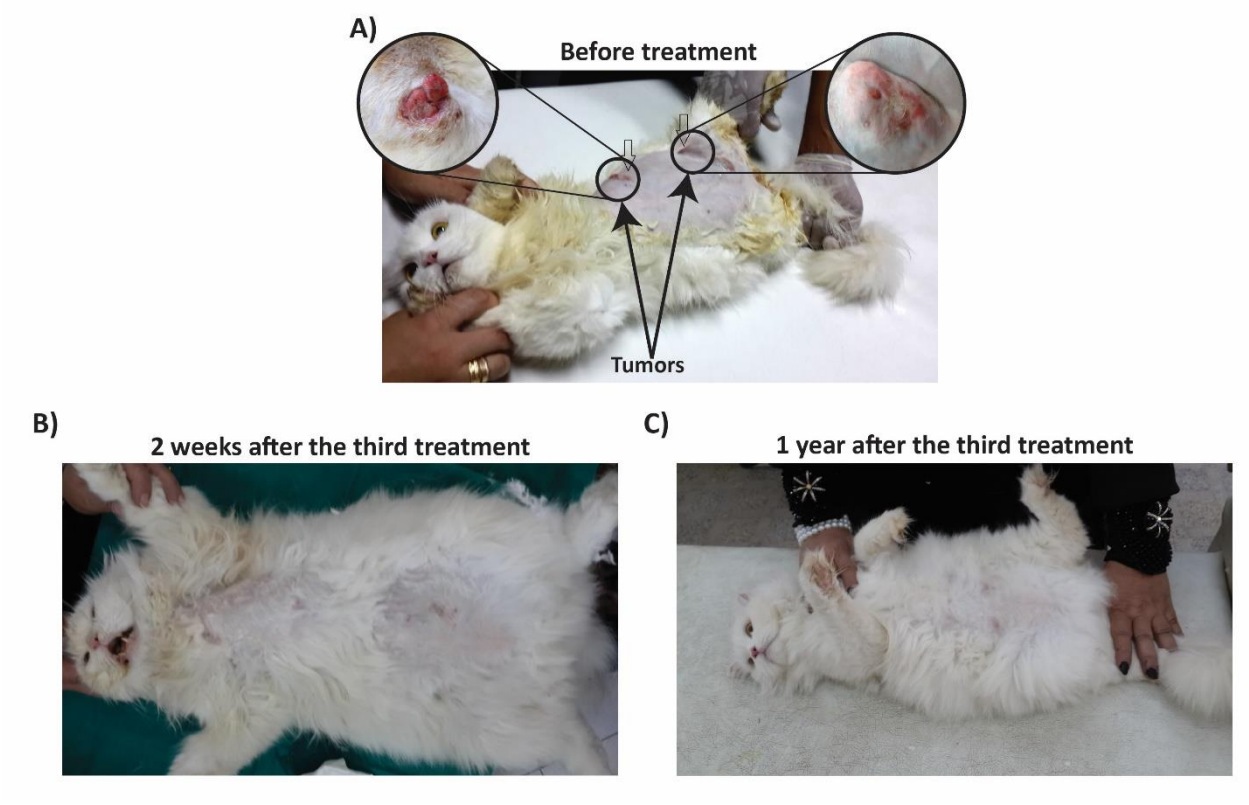

Figure B.10. (A–C) are photographs complete for Case 7 (Tumor 6: caudo-inguinal opened tumor and Tumor 10: anterior thoracic tumors) showing tumor regression after each treatment;

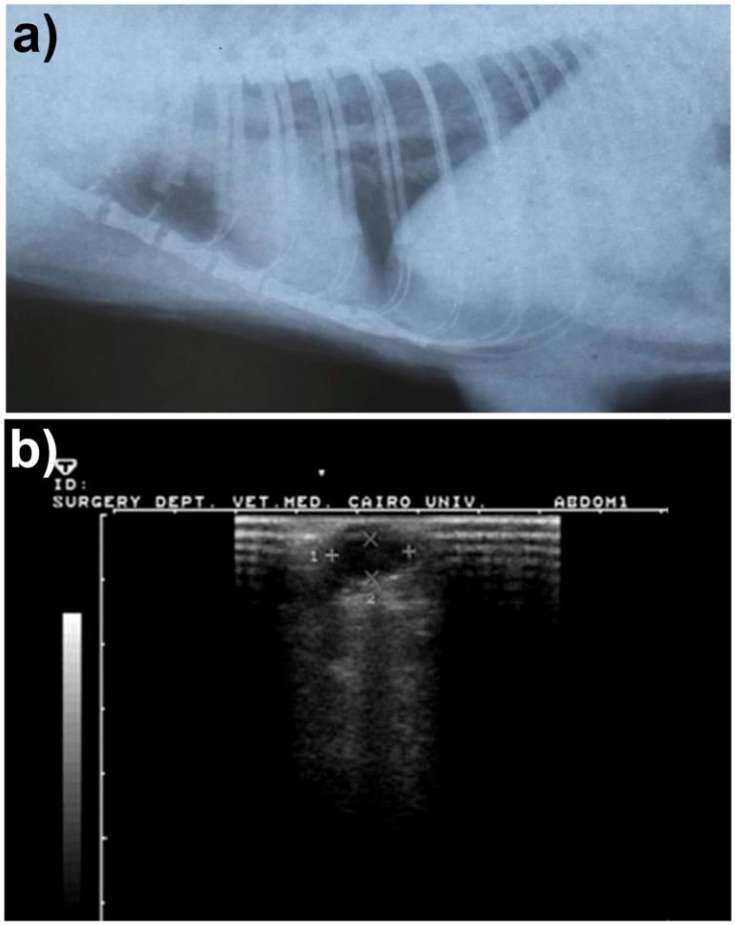

Figure B.11. Case 2 before treatment.

Notes: (A) The X-ray shows there is no metastasis in the internal organs. **(B)** Ultrasound shows the tumor location, shape, and dimensions.

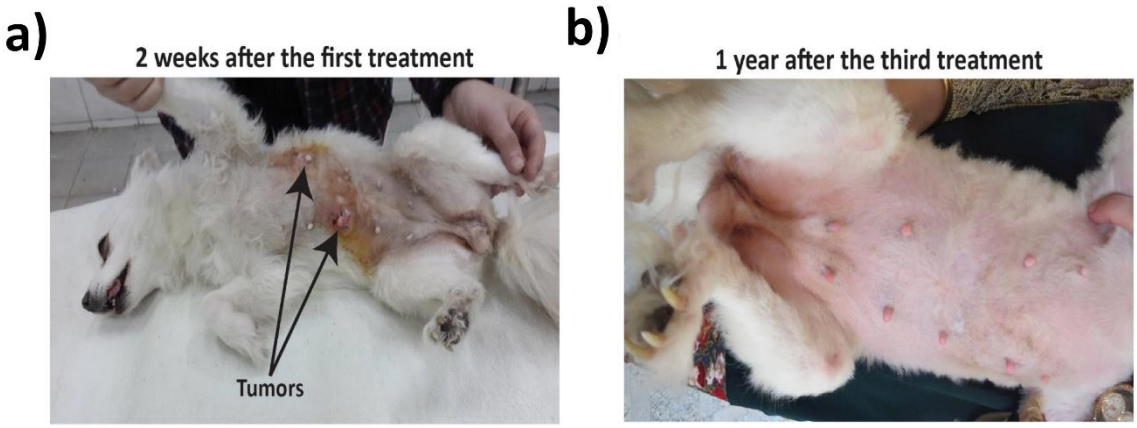

Figure B.12. Photographs for Case 2 (Tumor 4: left caudothoracic mammary gland and Tumor 9: right abdominal mammary gland) showing the tumor regression 2 weeks after first treatment.

Notes: (A) and **(B)**: after 1 year.

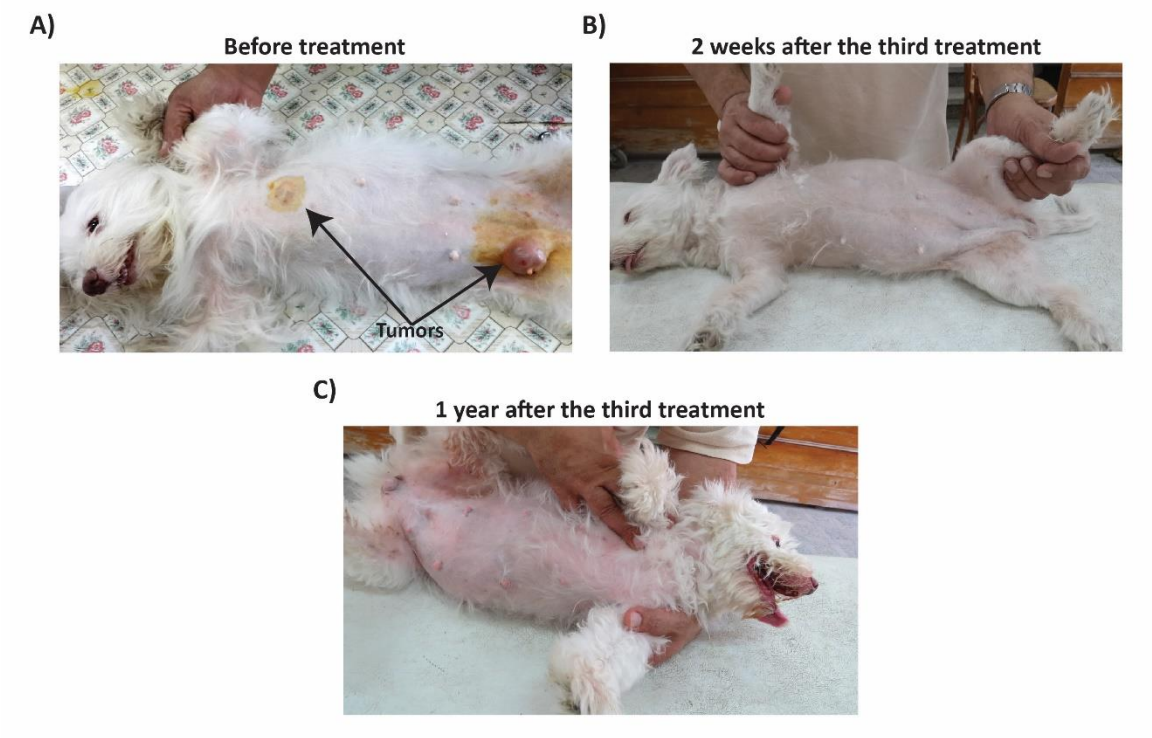

Figure B.13. (A–C) are photographs for case 3 (Tumor 2: left caudothoracic mammary gland and Tumor 13: right abdominal mammary gland) showing the tumor regression after each treatment; **(C)**: after 1 year.

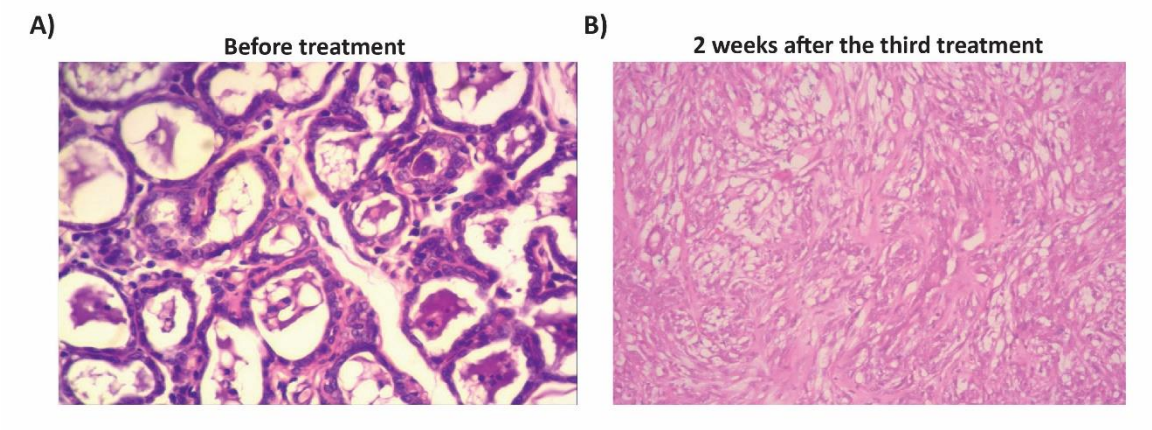

Figure B.14. Histopathology images (stained with H&E [×400]) for Case 3.

Notes: (A) Well-differentiated tubular adenocarcinoma before treatment. Carcinoma arranged in tubular pattern. Mass characterized by an intra-acinar deeply basophilic secretion and corpora amylecea. Connective tissue stroma infiltrated with mononuclear cells (tumor Grade III). (B) 2 weeks after the third treatment, there was absence of epithelial lining of acini and absence of acini and basement membrane. Also, loss of acinar pattern proliferation of fibrous connective stroma was seen (tumor Grade 0). Magnification of histopathology images stained with H&E: (A) ×200; (B) ×100.

Abbreviation: H&E, hematoxylin and eosin.

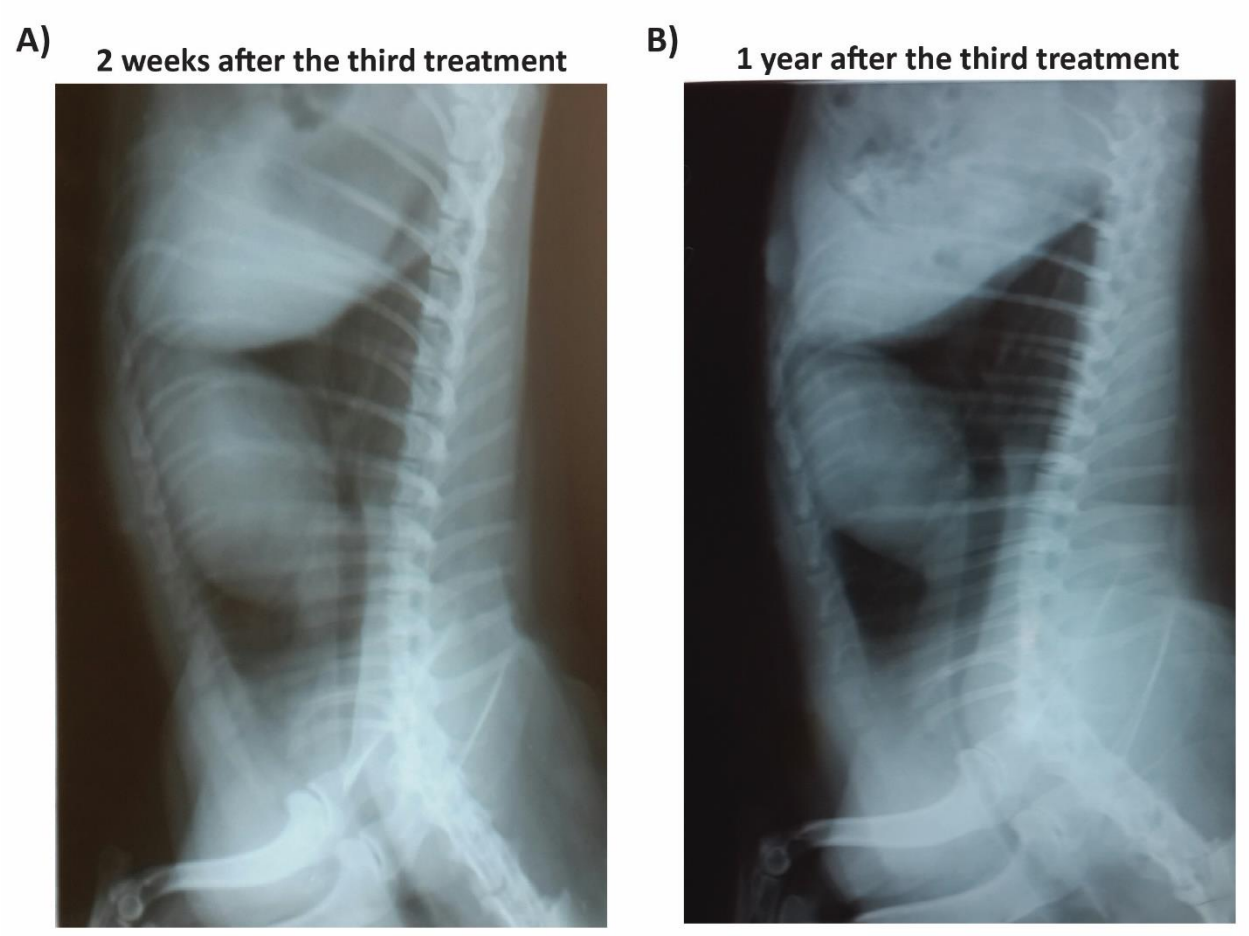

Figure B.15. X-ray lateral exposure for Case 3 after treatment.

Notes: (A) 2 weeks after third treatment, **(B)** 1 year after third treatment, showing there is no metastasis.

APPENDIX C: CHAPTER 4

ADDITIONAL FIGURES AND TABLES

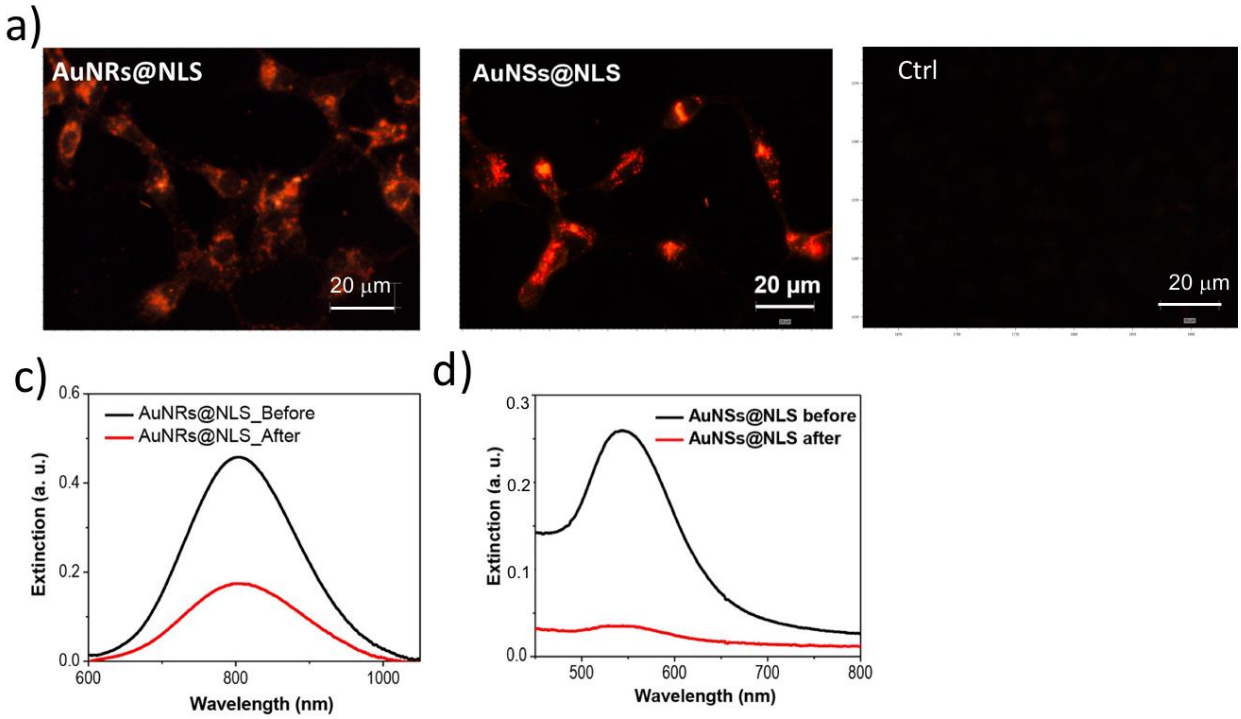

Figure C.1. HEY A8 cell uptake of AuNRs@NLS and AuNSs@NLS. (a) Dark field images of cells without AuNPs incubation (Ctrl), with 2.5 nM of AuNRs@NLS and 0.1 nM of AuNSs@NLS incubation. (c) UV-Vis spectra of 2.5 nM of AuNRs@NLS or 0.1 nM of AuNSs@NLS (d) in culture media before incubation with cells (black spectrum), compared with the ones after 24 h cell incubation (red spectrum).

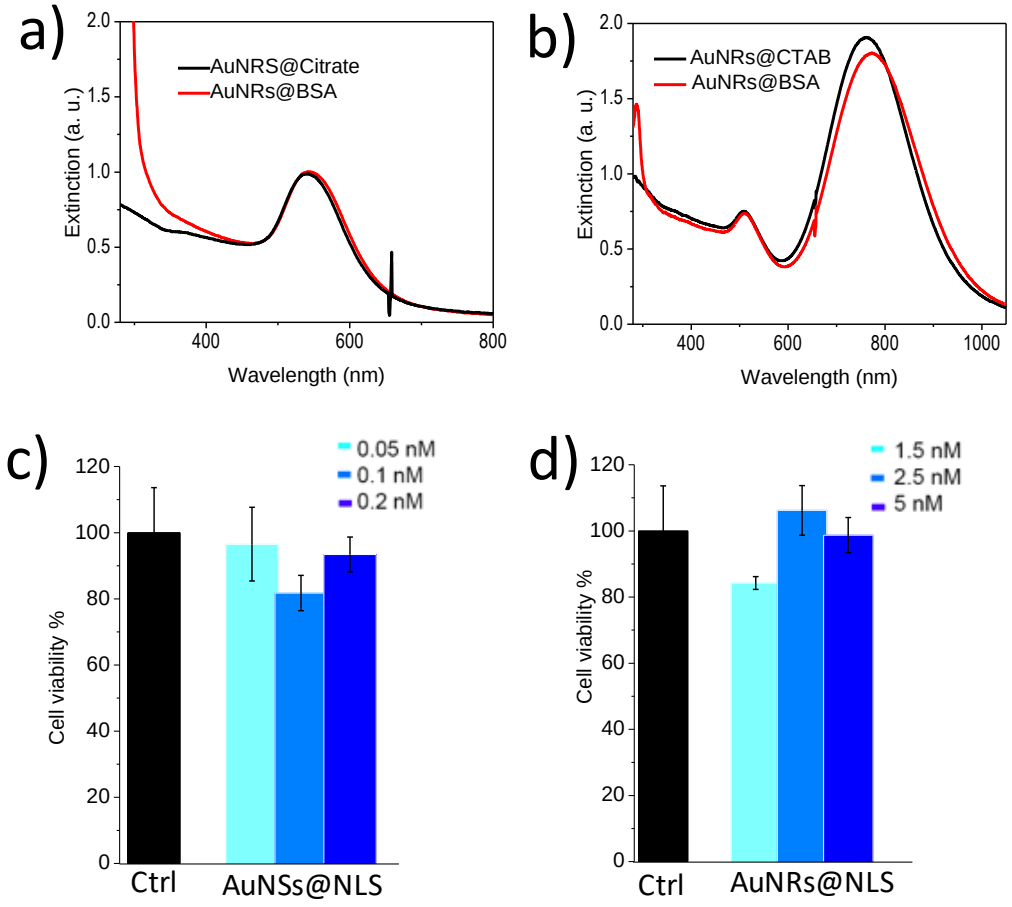

Figure C.2. Characterization for AuNPs@BSA and HEY A8 cell uptake. (a) UV-Vis extinction spectra of the unconjugated AuNSs@Citrate (black spectrum) and AuNRs@BSA (red spectrum). (b) UV-Vis extinction spectra of the unconjugated AuNRs@CTAB (black spectrum) and AuNSs@BSA (red spectrum). (c) XTT assay of HEY-A8 cells after 24 h incubation with AuNSs@NLS at concentrations 0.05 nM (light blue), 0.1 nM (medium blue) and 0.2 nM (dark blue), n=3. (d) XTT assay for cells after

1.5 nM (light blue), 2.5 nM (medium blue) and 5 nM (dark blue) of AuNRs@NLS incubation with HEY-A8 cells for 24h (n=3).

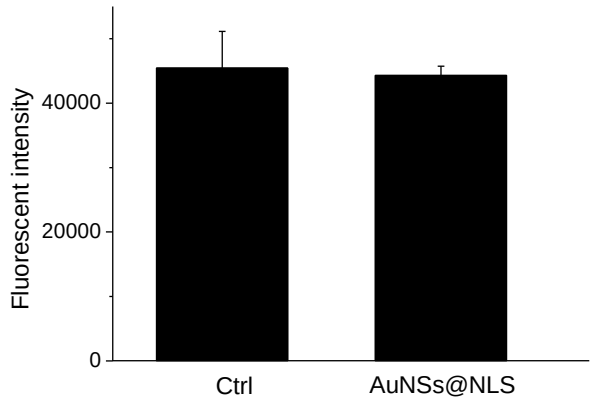

Figure C.3. The introduction of Au nanoparticles in cells does not affect the Fluorescent intensity of Calcein AM (n=3).

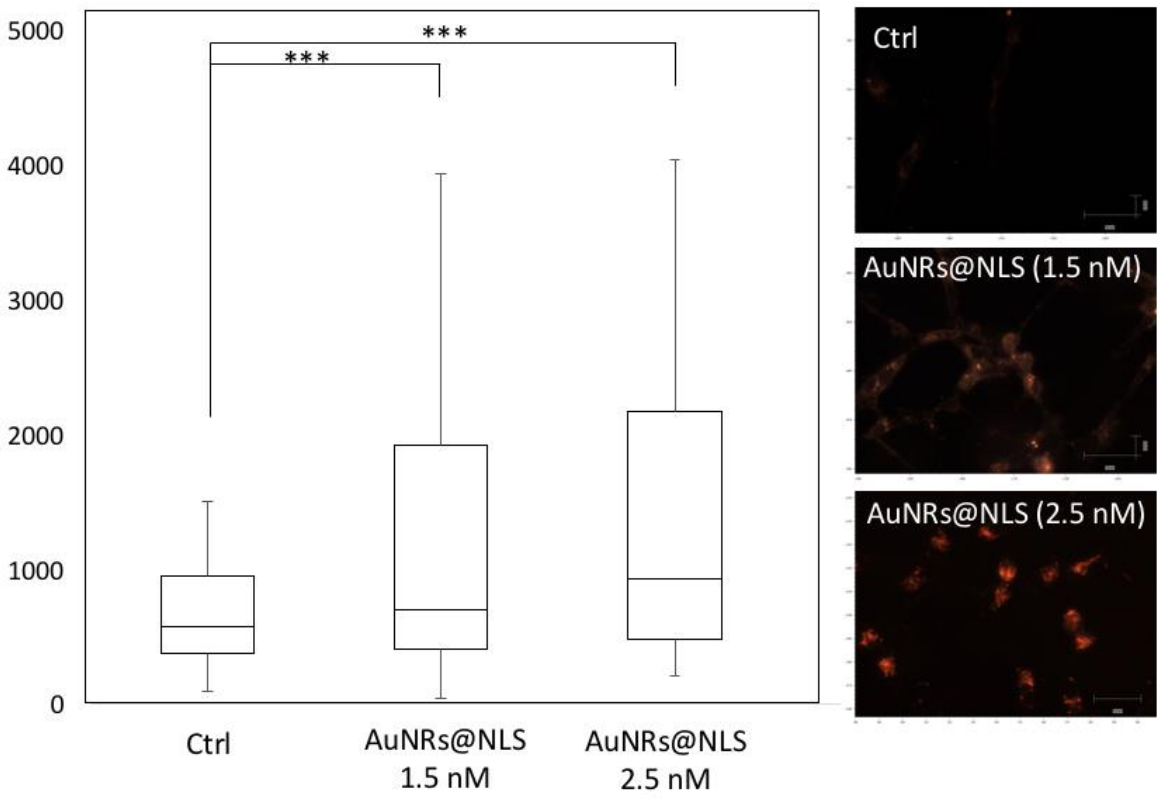

Figure C.4. Nuclear stiffness increase with the increased quantity of AuNRs. AFM result (left) and dark field images (right) show the stiffness and the nanoparticle uptake of AuNRs under different nanoparticle concentrations, respectively. n=3, cell counts>20 for each sample.

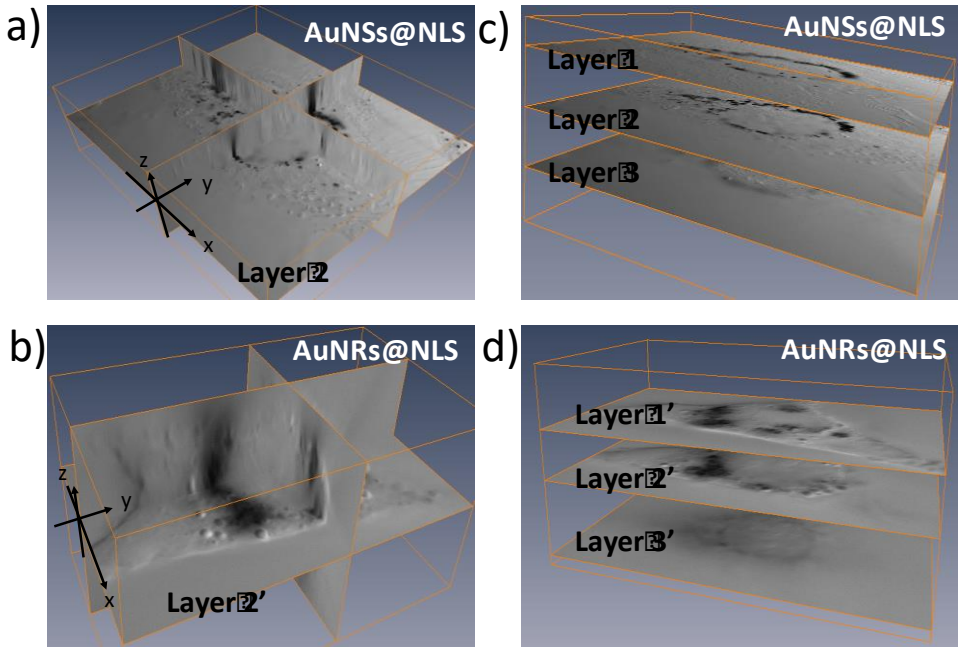

Figure C.5. Three dimensional (3D) view of HEY A8 cells incubated with AuNPs. (a and b) 3D figures of cells with 2.5 nM of AuNRs@NLS and 0.1 nM of AuNRs@NLS, showing xy, xz and yz planes (c and d) showing the z-stacking of 3 layers from the bottom of the cell (close to the attached glass surface as shown in the scheme), the middle of the cell, and the top of the cell, respectively, for AuNSs@NLS (c) and AuNRs@NLS (d).

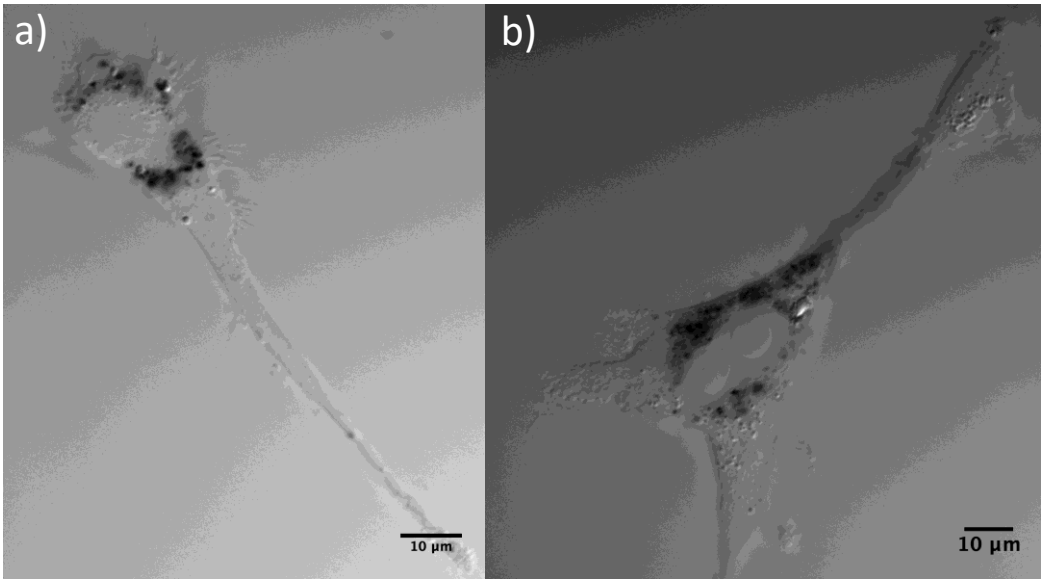

Figure C.6. The nuclear membrane targeting for AuNRs@NLS indicated by differential interference contrast (DIC) images.

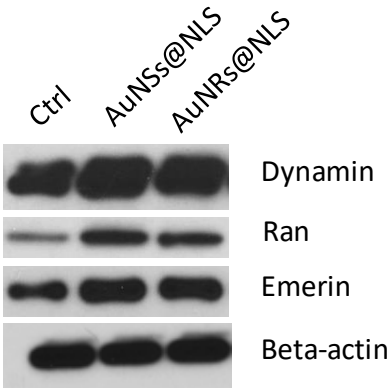

Figure C.7. Western blot of expression levels of Dynamin, Ran, emerin proteins and beta-actin from HEY-A8 cells (without AuNPs), HEY A8 cells with 0.1 nM of AuNSs@NLS and 2.5 nM of AuNRs@NLS treatment for 24 h.

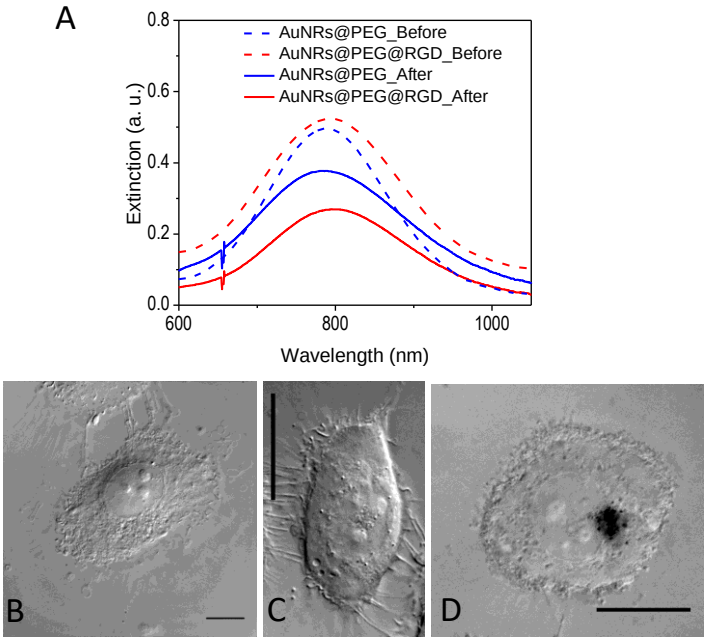

Figure C.8. HSC cell uptake of gold nanorods. (A) UV-Vis spectra of AuNRs before and after incubation with cells. (B-D) Differential interference contrast (DIC) microscopy images of cells without nanoparticle incubation (B), incubated with AuNRs@PEG (C), and incubated with AuNRs@RGD (D).

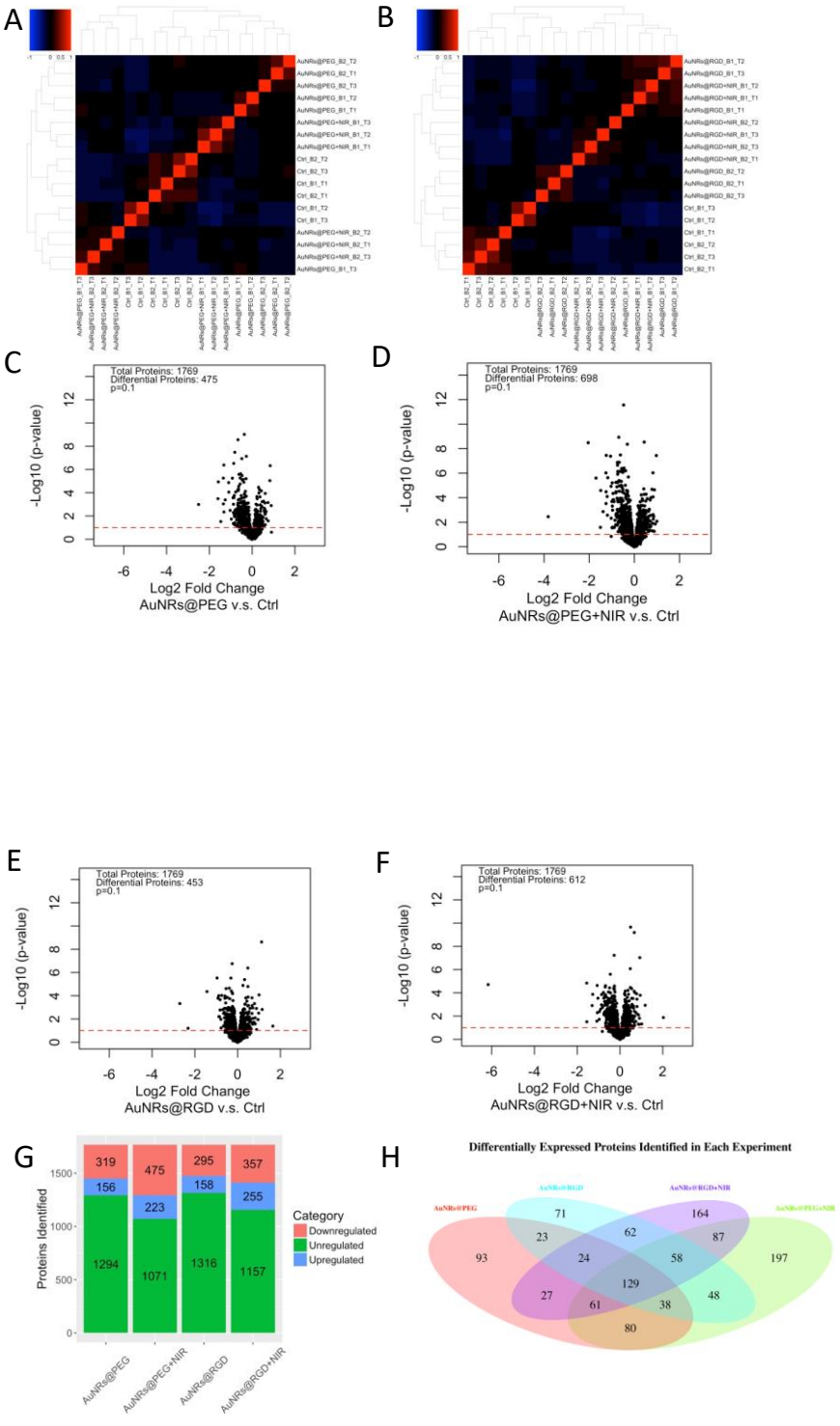
A
B
C
Total Proteins: 1769
Differential Proteins: 475
p=0.1
-Log10 (p-value)
Log2 Fold Change
AuNRs@PEG v.s. Ctrl
D
Total Proteins: 1769
Differential Proteins: 698
p=0.1
-Log10 (p-value)
Log2 Fold Change
AuNRs@PEG+NIR v.s. Ctrl
E
Total Proteins: 1769
Differential Proteins: 453
p=0.1
-Log10 (p-value)
Log2 Fold Change
AuNRs@RGD v.s. Ctrl
F
Total Proteins: 1769
Differential Proteins: 612
p=0.1
-Log10 (p-value)
Log2 Fold Change
AuNRs@RGD+NIR v.s. Ctrl
G
Proteins Identified
319
156
1294
475
223
1071
295
158
1316
357
255
1157
Category
Downregulated
Unregulated
Upregulated
AuNRs@PEG
AuNRs@PEG+NIR
AuNRs@RGD
AuNRs@RGD+NIR
H
Differentially Expressed Proteins Identified in Each Experiment
AuNRs@PEG
AuNRs@RGD
AuNRs@RGD+NIR
AuNRs@PEG+NIR
93
71
23
62
164
87
197
24
58
129
27
61
38
48
80

Figure C.9. Experimental results of proteomics. (A) Clustering analysis showing good reproducibility of proteomics experiments using AuNRs@PEG and corresponding NIR. (B) Clustering analysis showing good reproducibility of proteomics experiments using AuNRs@RGD and corresponding NIR. Volcano plot showing the differential protein under perturbation by (C) AuNRs@PEG, (D) AuNRs@PEG+NIR, (E) AuNRs@RGD and (F) AuNRs@RGD+NIR.

(G) Bar graph showing number of proteins identified in each experiment. (H) Venn diagram showing the comparison of differentially expressed proteins identified in each experiment.

A

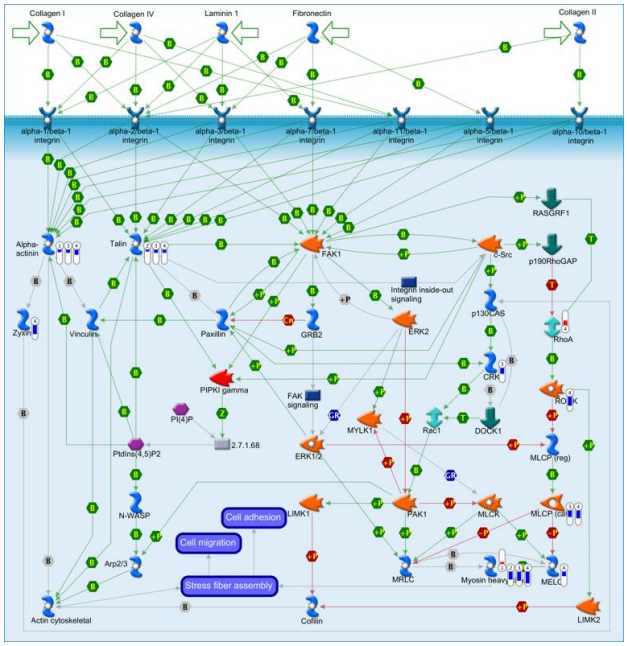
Collagen I
Collagen IV
Laminin 1
Fibronectin
Collagen II
alpha-1/beta-1 integrin
alpha-2/beta-1 integrin
alpha-3/beta-1 integrin
alpha-7/beta-1 integrin
alpha-11/beta-1 integrin
alpha-5/beta-1 integrin
alpha-10/beta-1 integrin
RASGRF1
Alpha-actinin
Talin
FAK1
c-Src
p190RhoGAP
Integrin inside-out signaling
Zyxin
Vinculin
Paxillin
GRB2
ERK2
p130CAS
RhoA
CRK
PIPKI gamma
FAK signaling
ROCK
PI(4)P
MYLK1
Rac1
DOCK1
2.7.1.68
ERK1/2
MLCP (reg)
PtdIns(4,5)P2
N-WASP
LIMK1
PAK1
MLCK
MLCP (cat)
Cell adhesion
Cell migration
Arp2/3
MRLC
Myosin heavy
MELC
Stress fiber assembly
Actin cytoskeletal
Cofilin
LIMK2

B

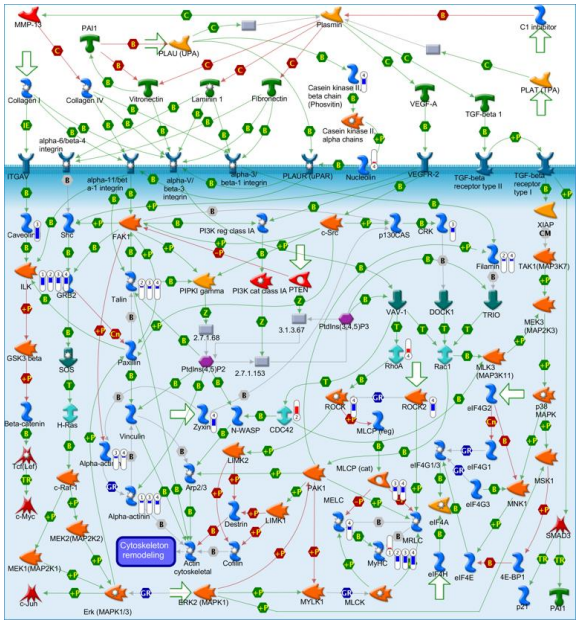
MMP-13
PAI1
Plasmin
C1 inhibitor
uPA
Collagen I
Collagen IV
Vitronectin
Laminin 1
Fibronectin
Casein kinase II beta chain (Phosvitin)
VEGF-A
TGF-beta 1
tPA
Casein kinase II alpha chains
alpha-6/beta-4 integrin
ITGAV
alpha-11/beta-1 integrin
alpha-V/beta-3 integrin
alpha-3/beta-1 integrin
PLAUR (uPAR)
Nucleolin
VEGFR-2
TGF-beta receptor type II
TGF-beta receptor type I
XIAP
Caveolin
Shc
FAK1
PI3K reg class IA
c-Src
p130CAS
CRK
Filamin
TAK1(MAP3K7)
ILK
GRB2
Talin
PIPKI gamma
PI3K cat class IA
PTEN
VAV-1
DOCK1
TRIO
MEK3 (MAP2K3)
3.1.67
PtdIns(3,4,5)P3
2.7.1.68
GSK3 beta
SOS
Paxillin
PtdIns(4,5)P2
2.7.1.153
RhoA
Rac1
MLK3 (MAP3K11)
ROCK
ROCK2
eIF4G2
p38 MAPK
Beta-catenin
H-Ras
Vinculin
Zyxin
N-WASP
CDC42
MLCP (reg)
Tcf/Lef
Alpha-actinin
LIMK2
MLCP (cat)
eIF4G1/3
c-Raf1
Arp2/3
PAK1
MELC
eIF4G3
MNK1
MSK1
c-Myc
Alpha-actinin
Destrin
LIMK1
eIF4A
SMAD3
MEK2(MAP2K2)
Cytoskeleton remodeling
Actin cytoskeletal
Cofilin
MRLC
MYPC
eIF4H
eIF4E
4E-BP1
MEK1(MAP2K1)
c-Jun
Erk (MAPK1/3)
ERK2 (MAPK1)
MYLK1
MLCK
p21
PAI1

C

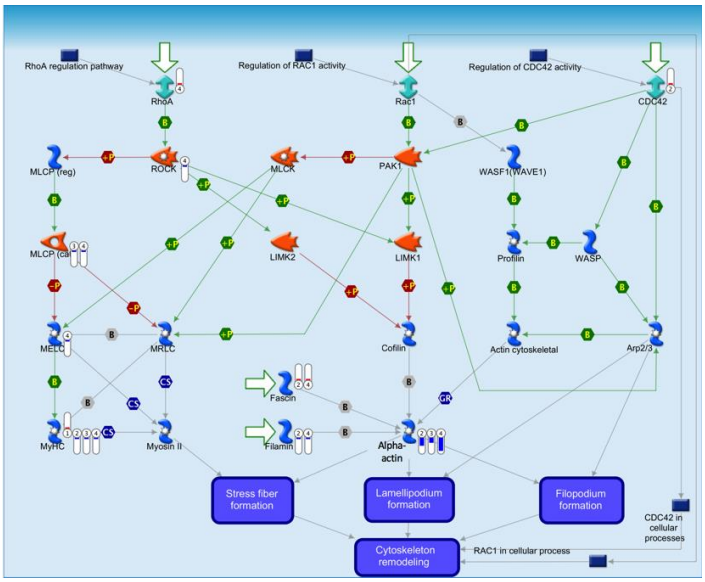
RhoA regulation pathway
RhoA
Regulation of RAC1 activity
Rac1
Regulation of CDC42 activity
CDC42
MLCP (reg)
ROCK
MLCK
PAK1
WASF1(WAVE1)
MLCP (cat)
LIMK2
LIMK1
Profilin
WASP
MELC
MRLC
Cofilin
Actin cytoskeletal
Arp2/3
Fascin
MyHC
Myosin II
Filamin
Alpha-actin
Stress fiber formation
Lamellipodium formation
Filopodium formation
CDC42 in cellular processes
Cytoskeleton remodeling
RAC1 in cellular process

D

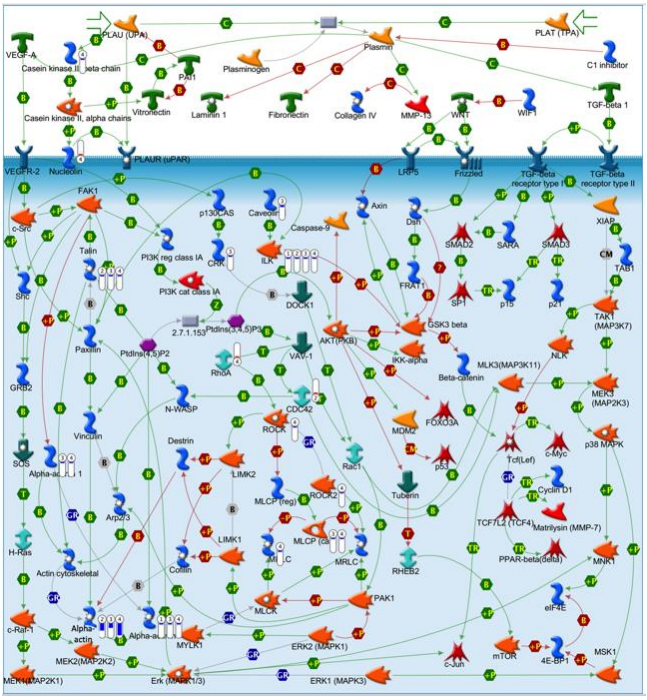
VEGF-A
PLAU (UPA)
Plasmin
PLAT (TPA)
Casein kinase II, beta chain
PAI1
Plasminogen
C1 inhibitor
Casein kinase II, alpha chains
Vitronectin
Laminin 1
Fibronectin
Collagen IV
MMP-13
WNT
WIF1
TGF-beta 1
VEGFR-2
Nucleolin
PLAUR (uPAR)
LRP5
Frizzled
TGF-beta receptor type I
TGF-beta receptor type II
FAK1
p130CAS
Caveolin
Caspase-9
Axin
Dsh
XIAP
c-Src
SMAD2
SARA
SMAD3
TAB1
Talin
PI3K reg class IA
CRK
ILK
FRAT1
Shc
PI3K cat class IA
DOCK1
SP1
p15
p21
TAK1 (MAP3K7)
2.7.1.153
PtdIns(3,4,5)P3
GSK3 beta
Paxillin
PtdIns(4,5)P2
AKT(PKB)
VAV-1
IKK-alpha
NLK
RhoA
Beta-catenin
MLK3(MAP3K11)
GRB2
N-WASP
CDC42
MEK3 (MAP2K3)
MDM2
FOXO3A
Vinculin
ROCK
Tcf(Lef)
c-Myc
p38 MAPK
SOS
Destrin
Rac1
Tuberin
Cyclin D1
LIMK2
MLCP (reg)
ROCK2
TCF7L2 (TCF4)
Matrilysin (MMP-7)
H-Ras
LIMK1
MLCP (cat)
MRLC
RHEB2
PPAR-beta(delta)
MNK1
Actin cytoskeletal
Cofilin
PAK1
eIF4E
c-Raf1
MLCK
Alpha-actin
MYLK1
ERK2 (MAPK1)
MSK1
MEK2(MAP2K2)
c-Jun
mTOR
4E-BP1
MEK1(MAP2K1)
Erk (MAPK1/3)
ERK1 (MAPK3)
å

Figure C.10. Key pathways perturbed by AuNRs related to cytoskeleton identified with MetaCore. (Red) means up-regulation compared to control; (blue) means down-regulation compared to control. In the thermometer sign, 1 refers to AuNRs@PEG; 2 refers to AuNRs@PEG+NIR; 3 refers to AuNRs@RGD; and 4 refers to AuNRs@RGD+NIR. The thermometers are filled to various degrees, corresponding to the amount by which the markers were up-regulated or down-regulated. (A) Pathway map of "Cell adhesion_Integrin-mediated cell adhesion and migration". (B) Pathway map of "Cytoskeleton remodeling_Cytoskeleton remodeling". (C) Pathway map of "Cytoskeleton remodeling_Regulation of actin cytoskeleton by Rho GTPases". (D) Pathway map of "Cytoskeleton remodeling_TGF, WNT and cytoskeletal remodeling".

Table C.1. Zeta potential of AuNPs with different surface ligands

Au nanoparticles with different surface ligands	Zeta potential (mV)
AuNRs@CTAB	50.9 ± 7.97
AuNRs@PEG	-13.6 ± 11.8
AuNRs@PEG@RGD@NLS	14.9 ± 3.13
AuNSs@Citrate	-29.7 ± 4.72
AuNSs@PEG	-12.1 ± 5.79
AuNSs@PEG@ RGD@NLS	18.3 ± 7.55
AuNRs@BSA	-19.6 ± 9.89
AuNSs@BSA	-15.2 ± 12.5

VITA

Moustafa Ali, joined the graduate program with B.Sc. and M.Sc. degrees from Cairo University, and has been the recipient of many awards and honors from Gerogia Tech, including the 2017 Suddath Award and the 2017 Petit Orientation-mentorship award. During his time at Tech, he has collaborated with investigators in several other universities, including Dr. Dong Shin at Emory University (animal testing of nanoparticles for anticancer activity) and Dr. Dawson at Brown University (cell imaging and migration). has focused on the use of gold nanorods and related materials to selectively kill tumor cells and inhibit cancer metastasis. Moustafa is currently a Ph.D. candidate in the School of Chemistry and Biochemistry at Georgia Institute of Technology, studying under Prof. Mostafa A. El-Sayed in the Laser Dynamics Laboratory (LDL). His current research interests include the fabrication and understanding of the exceptional physical, chemical, optical and biological properties of plasmonic nanoparticles specially for in plasmonic photothermal therapy for combating cancer. After earning the doctoral degree Moustafa will continue his post-doctoral study under Prof. Mostafa El-Sayed at the same group, and will continoue his focuse in the use of gold nanorods to selectively kill tumor cells and specifically inhibit cancer metastasis.

Moustafa enjoys sports such as boxing, lifting weights, and hanging out with his friends.